ESPOO 2003 VTT SYMPOSIUM 227

Plant Life Management

Progress for structural integrity

VTT SYMPOSIUM 227

Keywords:
service life, plant life, management, NPP, nuclear power plants, materials testing, ultrasonic testing, pipe vibrations, BWR, corrosion, pressure vessels, thermal ageing, stainless steel

Plant Life Management
Progress for structural integrity

Edited by

Jussi Solin

Organised by

VTT

ISBN 951–38–6280–1 (soft back ed.)
ISSN 0357–9387 (soft back ed.)

ISBN 951–38–6281–X (URL:http://www.inf.vtt.fi/pdf/)
ISSN 1455–0873 (URL: http://www.inf.vtt.fi/pdf/)

JULKAISIJA – UTGIVARE – PUBLISHER

VTT, Vuorimiehentie 5, PL 2000, 02044 VTT
puh. vaihde (09) 4561, faksi 456 4374

VTT, Bergsmansvägen 5, PB 2000, 02044 VTT
tel. växel (09) 4561, fax 456 4374

VTT Technical Research Centre of Finland
Vuorimiehentie 5, P.O.Box 2000, FIN–02044 VTT, Finland
phone internat. + 358 9 4561, fax + 358 9 456 4374

VTT Tuotteet ja tuotanto, Kemistintie 3, PL 1704, 02044 VTT
puh. vaihde (09) 4561, faksi (09) 456 7002

VTT Industriella System, Kemistvägen 3, PB 1704, 02044 VTT
tel. växel (09) 4561, fax (09) 456 7002

VTT Industrial Systems, Kemistintie 3, P.O.Box 1704, FIN–02044 VTT, Finland
phone internat. + 358 9 4561, fax + 358 9 456 7002

Otamedia Oy, Espoo 2003

Preface

A project on plant life management was started in 1999. The main activities during the two first project years were reported in VTT Research notes 2077 – Plant life management (XVO). Report 1999 and VTT Symposium 218 – Plant life management. Midtern status of a R&D project. This symposium describes subsequent results in 2001–2002. The research has been realised in annually modified sets of subsequent and parallel projects. The latest projects are: Rakenteellisen käyttöiän hallinta (XVO, Tekes decision 40342/02), Materiaalien vanhenemisen mekanismit energiateollisuudessa (MVM-RKK, Tekes decision 40519/01) and Rakenteiden käytettävyys ja käyttöiän hallinta (RKK, Tekes decision 541/02).

The papers in this symposium do not cover the project as a whole, but all research areas of the project are discussed in one or more papers. They are selected to give an overview of the main achievements and challenges within the project. The current compilation gives emphasis also to topics, which were not fully covered in the previous volumes.

Most papers have been presented in the project seminars in Olkiluoto, Loviisa, Helsinki and Porvoo during spring 2002. Additional papers have been edited on the basis of work reports and scientific publications prepared in this project. The first paper gives an overview of the project.

The authors and research teams have done a great job. This would not have been possible without a rigid funding basis and open communication between the researchers and experts in industry. The funding organisations, Tekes, TVO, Fortum Power and Heat, Fortum Nuclear Services, Neste Engineering, Fortum Oil and Gas, FEMdata and VTT, the project steering group chaired by Mr. Juho Hakala of TVO, all experts and altogether about hundred people are gratefully acknowledged of their valuable contributions.

Espoo 12.2.2003
Jussi Solin

Contents

Research for Plant Life Management

Jussi Solin and Rauno Rintamaa, VTT Industrial Systems, Espoo, Finland
Juho Hakala and Erkki Muttilainen, Teollisuuden Voima Oy
Antero Tamminen, Jyrki Kohopää and Kirsi Rintamäki, Fortum

Abstract

A joint project cluster of industry, VTT and other R&D suppliers is dealing with managing of lifetime of critical structures and components in energy and process industry. The research topics include systematic component lifetime management, data management, integrity and lifetime of pressure bearing components, non-destructive inspection, interactions of coolant and materials, environmentally assisted cracking and ageing of reactor internals. The volume is about 2 M€/a and about 100 experts contribute.

1. Introduction

Experimental and analytical research is being carried out in an industrially oriented project cluster on systematic component lifetime management, lifetime of pressure bearing components, piping vibrations and integrity management, management of materials ageing, non-destructive inspection, water chemistry, oxide films and their role in service reliability and build-up of activity levels, stress corrosion cracking in Inconel welds, irradiation assisted stress corrosion cracking of core components, development of crack growth testing methods as well as the mechanisms of environmentally assisted cracking. A majority of the funding and research challenges originate from nuclear industry, but in some subprojects the scope is generic or specific for other industry. Participation of Fortum Oil and Gas brings the oil refinery's point of view to the project.

Our aim is to combine and utilise knowledge into practice in an efficient way. All parallel disciplines shall be integrated such that quantitative assessments on remaining safe life and failure risks are possible. Knowledge is needed on

- relevant ageing mechanisms and their impact on the selected components,
- materials performance in the process environment under operational loads,
- condition of the materials and components,
- operational stressors[1] in normal steady state operation and in transients,
- service history of the particular component, and
- general industrial experience in similar plants.

The work is divided into parallel projects, subprojects and tasks. All of them aim to industrial applications, but with different time perspectives. The previous annual reports [1, 2], other papers in this proceedings and task reports provide the details and overviews on the major research topics. This paper gives a short summary of the project cluster and the technical challenges within it.

2. Background and motivation for this R&D

Capital intensive process and energy industry forms a significant part of Finnish economy. Reliability of operation and long life of investments can thus be considered even a national issue. Nuclear and oil refining industries are pioneers in this field – both internationally and nationally.

2.1 Industrial experience

All four Finnish nuclear plant units – two BWR's at TVO Olkiluoto plant and two VVER's at Fortum Loviisa plant – have operated for two decades with very few unplanned outages. The average load factors[2] have been 88.3% for the BWR's and 85.8% for the VVER's and the unit lifetime performances by end of year 2000 were ranked to positions 5, 6, 8 and 26 among the global NPP fleet. Furthermore, the powers of all reactors have been recently upgraded.

---

[1] "stressors" has a meaning broader than stresses: mechanical, thermal, chemical and other factors are included

[2] Average per MWh(gr) generated in 1977–2000

Unscheduled outages must be very rare events to keep the load factors on the current level. Component ageing shall be anticipated well in advance to develop mitigating measures and allocate future maintenance operations. Significant research efforts on ageing, structural integrity and lifetime management are thus justified to maintain the excellent load factors and to be able to continue operation long in future. National and international R&D collaboration is considered an important element behind the good performance.

2.2 Continuous improvement

In stead of getting a licence for 30 or 40 years in a time, the Finnish nuclear power plants operate on shorter operation licences. Each renewal of operation licence is based on a safety review. The regulatory body requires that the utilities follow the international state of the art and adopt all feasibly available means to maintain and improve the safety. A policy of continuous improvement has thus been included in the Finnish nuclear regulation principles and in the company strategies.

Continuous improvements for safety and plant life management are also needed for competitiveness. Reliable utilisation of the large primary capital investments to the plant and the deposited funds for waste management and decommissioning is a major concern to the utility.

The common interest to continuous improvements forms a good platform for co-operation between the authority and utilities. The continuous improvement strategy has already proven its benefits from both safety and operability points of view. The in-depth assessments and various safety improvements performed in relation to the Loviisa RPV safety case are good examples of this strategy [3].

3. Project management

The research was realised in three parallel projects:

- Rakenteellisen käyttöiän hallinta (XVO)
- Materiaalien vanhenemisen mekanismit energiateollisuudessa (MVM-RKK)
- Ydinvoimalaitosten rakenteellisen käytettävyyden kehittäminen (RKK).

The last one (RKK) was a joint industry group project led by TVO. It was the largest and contained most of the activities. The two other projects were smaller by an order of magnitude. In 2001 the XVO -project was focused in monitoring of water chemistry and behaviour of oxide films. It was realised by VTT in co-operation with a Japanese center of excellence in the Tohoku University, where a Finnish researcher stayed for an year. The MVM-RKK -project concentrated in studies on mechanisms of materials ageing. Helsinki University of Technology (HUT) was responsible of this project.

3.1 Industry group project

The key players behind the projects are the Finnish utilities TVO and Fortum together with VTT and the National Technology Agency. The industry group has been expanded along with time as the R&D activities have been planned, funded and executed through annual projects since 1999.

To keep the project in focus, the initial plans were based on current and anticipated challenges of the Finnish nuclear power plants. But technology transfer across the industry sectors is also considered important. Part of the advances in conceptual solutions, materials science and other generic technologies are directly transferable to other capital intensive industry sectors where avoiding of unplanned outages is equally important. On the other hand, nuclear industry can also benefit of adopting approaches tested in other industry. Therefore, the industry group has been expanded beyond the nuclear industry.

3.2 Research resources

The Helsinki University of Technology and some other research suppliers joined the team, but VTT still performs majority of the work. The total volume of work is about 2 M€ per annum. A few young researchers and students are occupied for the full time, but most of the work is shared between about 100 experts each contributing a couple of months, weeks or just days into the project. The distribution of manpower efforts in the largest project as shown in Fig. 1 clearly demonstrates the need of well established infrastructure and experienced research teams.

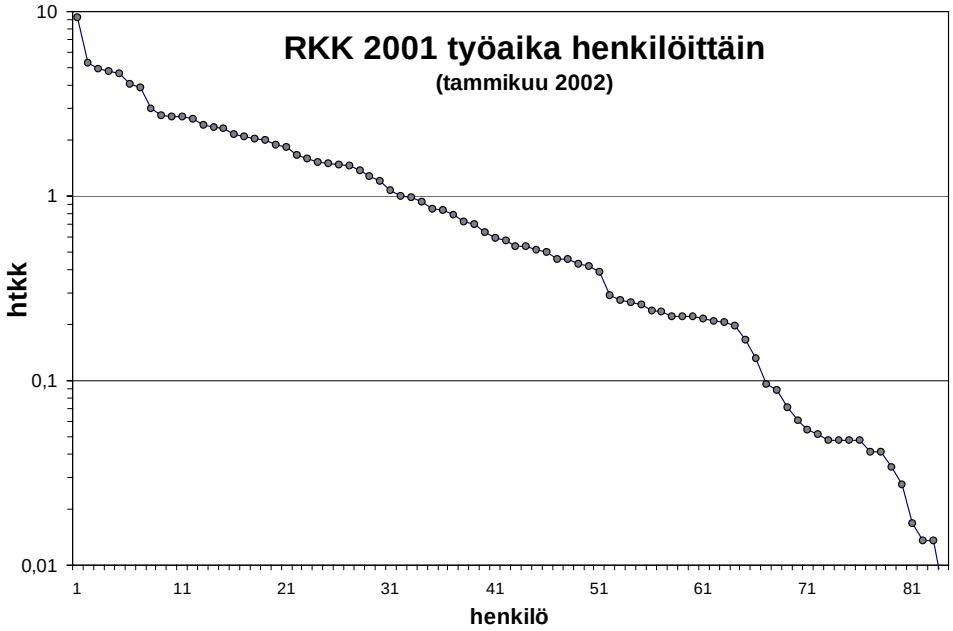

Figure 1. Distribution of research efforts in terms of VTT's manpower allocated to the RKK project in 2001.

1.3 Co-operation and networking

The research teams of VTT and HUT are continuously in close contact to the experts in industry. Open communication between the researchers and utility staff is an essential success factor. It helps to guide the work and to obtain a balanced mix of long term research and problem-solving activities. The innovations become focused to issues having direct relevance to practice and the experts in industry can utilise the results in real time.

Furthermore, the project has strong links to the national research programme on nuclear safety (Finnus) and the fifth framework programme of European Union, where generic technology is being developed from the safety point of view. Project specific co-operation agreements have been signed with Electric Power Research Institute, USA for the Co-operative IASCC Research program (CIR) and with Tohoku University for the Reliability centered life time prediction of environmentally assisted cracking research programme. Linking to the

international research community makes synergistic co-ordination possible and enables efficient technology transfer through intensive networking.

4. Overview of research topics

The project, as a whole, deals with many aspects of component lifetime management. The parallel disciplines shall be integrated such that quantitative assessments on remaining safe life and failure risks are possible. Fig. 2 shows a general scheme of component lifetime management followed in the current project.

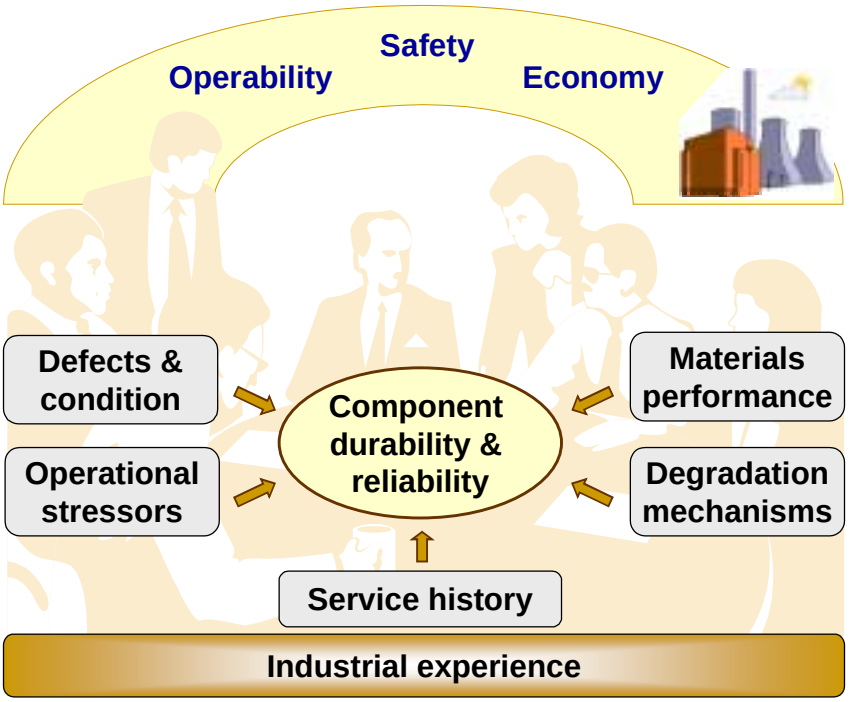

Figure 2. A general scheme for component lifetime management.

4.1 Developments in ultrasonic inspection and qualification of NDE

Reliability of non-destructive testing results has a direct influence on structural integrity assessment and safety of the inspected structures, e.g., NPP primary circuit pressure boundaries. Advanced technology together with highly skilled and experienced personnel is required.

One of the current trends is qualification, which aims to ensure that the inspection results are correct and fit for the purpose. The suitability and proper operation of equipment, methods and personnel, i.e. the whole chain, shall be proven. A round robin exercise was organised to obtain a deeper insight on suitability of different qualification samples and on critical issues in defect characterisation [4]. Two other papers in this proceedings concentrate on advances in defect sizing capabilities [5, 6].

4.2 Piping vibrations and piping integrity management

Traditional design and condition monitoring of piping is mainly based on postulated events and on the application of allowable vibration levels. This approach gives only indirect information on the loading at the critical locations and generally leads to over conservative assessments.

4.2.1 Integrated database system for managing piping integrity

The amount of input data necessary for fitness, safety and lifetime assessment of class 1 nuclear piping is considerable. It is essential that reliable and up-to-date data can be collected on a short notice. At the same time the same input data may be used in many different assessment modules, Fig. 3.

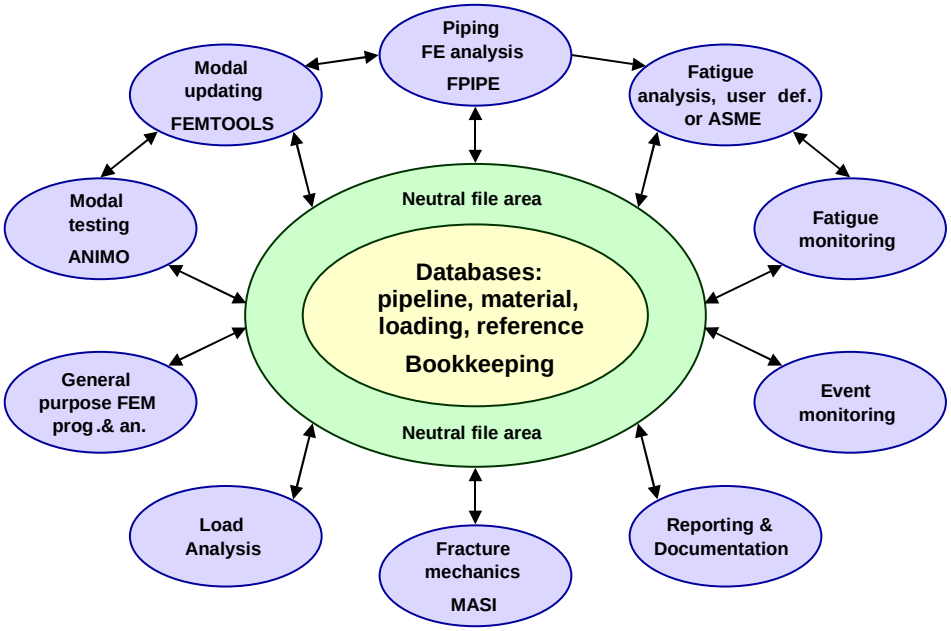

Figure 3. Relational database and program system being developed for TVO piping systems.

A relational database system, consisting of separate geometrical, material, loading and reference document databases is being developed by TVO and VTT. The system is developed to facilitate effective analyses of the piping and generation of the associated documentation. A general description of the database system as a whole was given in the previous annual report [7]. Organisation of the load cases and load combinations is discussed in this proceedings [8].

4.2.2 Piping vibration management

Relevant information about the actual loading state and condition of the piping could be obtained by comprehensive direct measurements, but in practice, the amount of measurement points must be strictly limited. Therefore, a practical method based on measurements accompanied by detailed finite element (FE) analyses is being sought for. The target is to be able to manage piping vibrations and related integrity concerns by using a minimum number of fixed continuous measurements and on an adequate numerical model [9].

Special purpose tools designed to update Finite Element analysis models with experimental data (modal correlation) are needed to obtain adequate agreement between the computational and experimental results [10].

The R&D work is realised through studying selected pipelines supported by the general development needed. The first case study was taken from the Olkiluoto NPP and the second from the Porvoo oil refinery. The third case study deals with a feed water line at the Loviisa plant. The Loviisa case is partially described in a paper included in this proceedings [11].

4.2.3 Development of FEA capabilities

New analysing possibilities were developed and improved within this project for the Finnsap programme, which is used for various strength analyses in Finnish industry. Development work resulted among other to new elements for modelling contacts and gaps, programmable support for weight optimising of profiles, integration of new non-linear beam elements and new solution method for stability assessment.

A preliminary capability to perform stress analysis according to the forthcoming Eurocode for pressure equipment was developed to the Fpipe programme on the basis of available drafts. Development of capabilities for taking into account the friction in piping supports was completed.

This subproject was performed by FEMdata Oy in close co-operation with the other activities for piping vibration management and development of the database system.

4.3 Water chemistry and corrosion R&D

Nuclear reactors are designed to last for decades. This is being achieved e.g. by selecting best materials and careful control of the water chemistry of the plant. Highly alloyed stainless steels and nickel-based alloys are employed for some of the reactor internal components to improve their corrosion resistance in high temperature water.

4.3.1 In situ monitoring of water chemistry

In situ monitoring cells have been developed and installed to primary circuits of both Finnish NPP's. The cells contain special probes capable to monitor essential corrosion related parameters in high temperature water. In addition, tens of material samples are deposited in another cell. The oxide films on the material samples are periodically investigated to clarify the oxide growth and properties together with the activity contamination during the plant operation cycles [12, 13].

4.3.2 Steam generators

Localised corrosion inside the oxide sludge piles on the bottom of the steam generator and in between the tubes is one possible concern at the Loviisa plant. The chemical conditions in these piles may differ markedly from the bulk water conditions. Due to the enrichment of anionic impurities the tube material is subjected to localised corrosion. But the results within this project suggest that this risk is not serious in the studied conditions [14].

4.3.3 Zircaloy 2 alloys

Corrosion properties of zirconium alloys used in the nuclear fuel cladding tubes in the demanding reactor core environment is of great interest. For estimation of corrosion rate and for determination of optimal content of the alloying elements and/or microstructure, a quantitative model for the behaviour of oxide films on the metal surfaces is needed. Laboratory tests methods suitable for other materials are not applicable for zirconium because of its very fast oxidisation to form an extremely thin oxide layer on the metal surface. The research is continued in order to find suitable methods for comparison and acceptance testing of different candidate fuel claddings [15].

4.3.4 Mechanisms of environment-assisted cracking

A quantitative kinetic model of oxide films has been developed. Among other things this corrosion model predicts transport of atomic holes (vacancies) into the metal. On the other hand, diffusion of vacancies plays an important role in

the crack growth according to the Selective Dissolution Vacancy Creep model of stress corrosion cracking. More recently, a great interest has been focused also to dynamic strain ageing and its role in SCC mechanisms. The role of vacancies and dynamic strain ageing in SCC mechanisms is discussed in two papers in this proceedings [16, 17].

4.4 Materials characterisation and ageing

4.4.1 Inconel alloys 82 and 182

Inconel alloy 182 has been widely used in welds of BWR and PWR reactors. The international experience has risen an issue of its susceptibility to stress corrosion cracking and alloy 82 is a candidate for replacing alloy 182, if repairs are needed. Sulphate concentrations that are high enough to change the pH to acidic are known to enhance SCC initiation and recent results have shown that sulphate enrichment rises the concentration in cracks is significantly. The effect of sulphate enrichment in BWR coolant on SCC initiation and propagation rate was studied for 182 and 82 alloys. The effect of sulphate addition was clearly demonstrated for alloy 182. But crack initiation was not observed in alloy 82 in conditions where crack was growing also in cold deformed 316 NG and sensitised 304 stainless steels [18].

4.4.2 Thermal ageing

Thermal ageing of cast Ti-stabilised stainless steels has been studied earlier. This year investigations were performed on a Ti-stabilised stainless steel pipe sections removed from the Sosnovy Bor NPP after 201 500 and 103 600 hours of operation. Both sections contain a weld. The studied material is similar to the steel and weld material used in VVER piping and the aim was to investigate the extent of thermal ageing in service. Another test steel was also studied as a reference, which is known sensitive to thermal ageing. The results of mechanical tests and microstructural investigations including a thorough study of transmission electron microscopy are summarised in this proceedings [19, 20].

4.4.3 Reactor internals

The mechanical and microstructural properties of irradiated Ti-stabilised 08X18H10T stainless steel absorber element bottom end material was studied. Two samples with different neutron fluences were received. The original aim was to study the sensitivity of the material to irradiation assisted stress corrosion cracking (IASCC), but the dislocation loop densities and mechanical properties revealed that the neutron fluences were smaller than assumed and the samples were not susceptible to IASCC. The fluence gradient turned out to be high at the location of absorber element bottom end and the fluence dose estimates were very sensitive to the accuracy of the absorber element position recordings. Refinement in the position history resulted to lower dose calculation results [21].

4.5 Life management of VVER reactor pressure vessels

Radiation embrittlement of RPV steels is a common problem in many pressurised water reactors (PWR), in particular in the Russian VVER designs from 70'ies. If suitable countermeasures were not introduced, embrittlement would become a life limiting factor for safe operation of the plant [3].

In light water reactors part of the fast neutrons escape outside the reactor core and hit the reactor pressure vessel (RPV) wall. These fast neutrons cause atomic scale defects in the crystallographic structure of the steel. The strength of the steel is increased, but simultaneously the ductility decreases. The formed vacancies and displaced atoms migrate and/or interact with the alloying elements and impurities present in the solution. Small precipitates, impurity clusters and grain boundary segregation may result.

The circumferential welds in the Loviisa RPV have significantly higher copper and phosphorus contents than the base metal. These impurities influence the embrittlement mechanism and rate. Unfortunately, one of these welds is near the reactor core area and gets a notable fluence of neutrons during normal operation, Fig. 4.

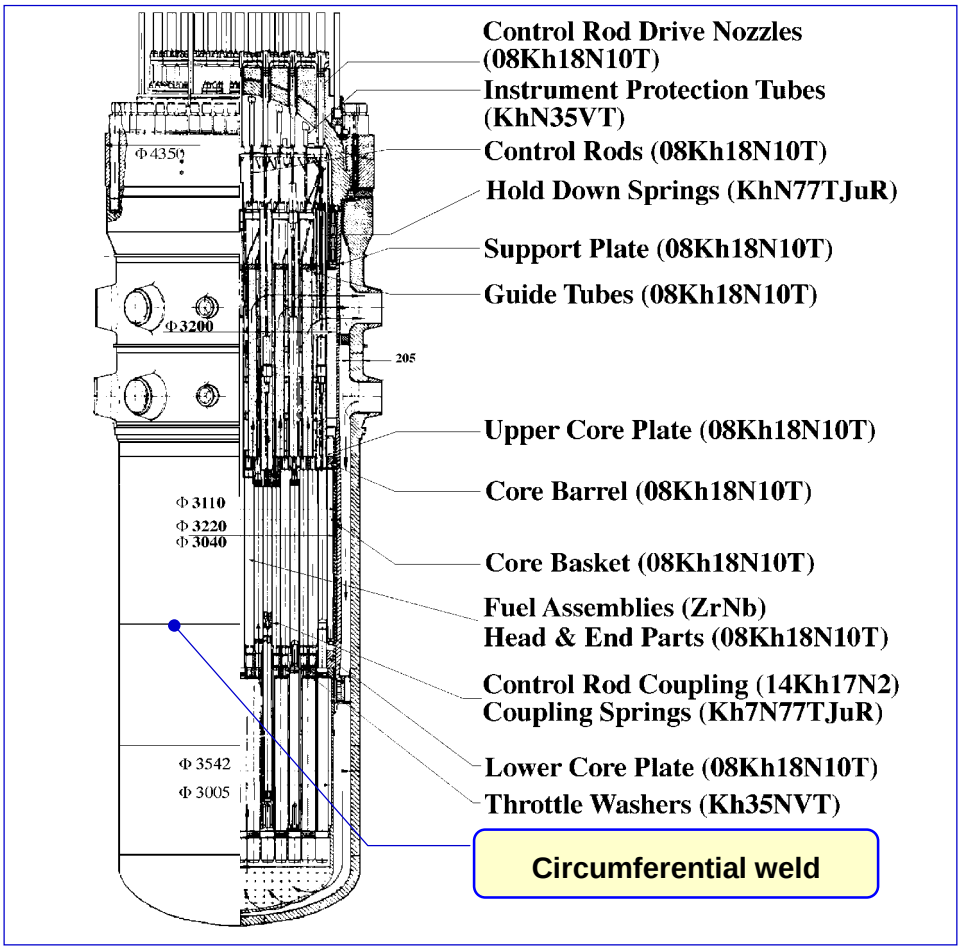

Figure 4. VVER 440 Reactor pressure vessel and location of the critical weld.

The core weld of Loviisa 1 was successfully annealed in 1996. Current concern is to verify the post-annealing embrittlement rate in order to enable safe and economic life management of the RPV.

The test results on re-embrittlement indicate that none of the currently used approaches for predicting the post-annealing re-embrittlement rate is physically correct. Further research is needed and parts of it are performed in this project. Plant specific testing and international co-operative research efforts are included. [22].

4.6 Risk informed life management for hydrotreating reactors

Hydrotreating is an important phase of the oil refining process. High temperature and pressure together with large size of the reactors set high safety and reliability requirements for these vessels. Ageing of the pressure vessel steel causes embrittlement, which has been followed by impact testing of surveillance material samples placed in the vessel. The empiricism in Charpy-V impact testing led to difficulties in quantifying the safety margins.

This study focussed on the introduction and verification of a new fracture mechanics based surveillance procedure for hydrotreating reactors. The aim was to quantify the present safety margins and life expectancy for the four studied reactors. The results and analyses validated the new surveillance procedure and verified the safety of the reactors for the next eight years [23].

4.7 Performance of non-metallic coatings in seawater tubes

Seawater pipe lines are made of large diameter carbon steel pipe coated with rubber or epoxy. Pipe material itself corrodes in seawater and is therefore protected by the coating. For assurance of operational reliability of seawater piping typical coating failures, guidelines for high quality coating, condition of the pipes and coating repair possibilities of the used pipes were studied. Some of the results are summarised also in this proceedings [24].

5. Conclusions

Condition and life management of power and process plant components is a broad topic requiring systematic research and development. The research shall be focused to obtain quantitative results to specific problems. On the other hand, multidisciplinary integrated approaches are a necessity to be able to utilise broad industrial and scientific experience and new innovations. The current project models are effective for planning and execution of such joint research.

Acknowledgements

This presentation is prepared within the project Structural operability and plant life management (RKK), which is coordinated by Teollisuuden Voima Oy. The work has been funded by the National Technology Agency (Tekes), Teollisuuden Voima Oy (TVO), Fortum Power and Heat Oy, Fortum Nuclear Services Ltd., FEMdata Oy, Neste Engineering Oy, Fortum Oil and Gas Ltd. and VTT. Their funding is gratefully acknowledged.

References

1. Solin, J. (ed.). Plant life management (XVO) report 1999. Espoo: VTT, Technical Research Centre of Finland, 2000. VTT Research Notes 2077. 68 p. + app. 3 p. (available at http://www.vtt.fi/vtt/results).

2. Solin, J. (ed.). Plant life management – Midterm status of a R&D project. Espoo: VTT, Technical Research Centre of Finland, 2001. VTT Symposium 218. 268 p. + app. 9 p. (available at http://www.vtt.fi/vtt/results).

3. Kohopää, J., Tamminen, A., Valo, M. and Solin, J. Innovations on life management of VVER reactor pressure vessels. In: Solin, J. (ed.) Plant life management – Midterm status of a R&D project. Espoo: VTT, Technical Research Centre of Finland, 2001. VTT Symposium 218. Pp. 107–126.

4. Sarkimo, M. and Api, M. Applicability of different artificial defects in qualification of ultrasonic testing method. In this proceedings, pp. 25–34.

5. Pitkänen, J. and Kauppinen, P. Experiences on Synthetic Aperture Focussing Technique (SAFT). In this proceedings, pp. 35–49.

6. Pitkänen, J., Kauppinen, P., Särkiniemi, P., Jeskanen, H., Vazquez, J. and Ojedo, F. Ultrasonic defect sizing with manual and semi-automatic system. In this proceedings, pp. 51–61.

7. Smeekes, P., Lipponen, A., Talja, H. and Raiko, H. Integrated Approach and Database System for Managing Load Cases and Integrity of Piping Systems. In: Solin, J. (ed.) Plant life management – Midterm status of a R&D project. Espoo: VTT, Technical Research Centre of Finland, 2001. VTT Symposium 218. Pp. 35–54.

8. Raiko, H., Lipponen, A., Smeekes, P. and Talja, H. Load-case and -combination database. In this proceedings, pp. 63–77.

9. Smeekes, P., Talja, H., Saarenheimo, A. and Haapaniemi, H. Piping Vibration Management Combining Measurements and Numerical Simulation. In: Solin, J. (ed.) Plant life management – Midterm status of a R&D project. Espoo: VTT, Technical Research Centre of Finland, 2001. VTT Symposium 218. Pp. 55–66.

10. Haapaniemi, H., Saarenheimo, A., Smeekes, P. and Talja, H. Numerical simulation of piping vibrations using an updated FE model. In this proceedings, pp. 79–98.

11. Saarenheimo, A., Haapaniemi, H., Luukkanen, P., Nurkkala, P. and Rostedt, J. Modal analysis of feed water pipe line RL61 at the Loviisa NPP. In this proceedings, pp. 99–120.

12. Bojinov, M., Kinnunen, P., Laitinen, T., Mäkelä, K., Saario, T. and Sirkiä, P. Monitoring of BWR water chemistry and oxide films on samples at Olkiluoto 1 during the fuel cycle 2000–2001. In this proceedings, pp. 121–136.

13. Bojinov, M., Kinnunen, P., Kukkonen, A., Laitinen, T., Mattila, M., Mäkelä, K., Saario, T. and Sirkiä, P. Activity incorporation into stainless steel samples in primary coolant at Loviisa 1 during the fuel cycle 2000–2001. In this proceedings, pp. 137–151.

14. Bojinov, M., Kinnunen, P., Laitinen, T., Mäkelä, K., Saario, T., Sirkiä, P. and Yliniemi, K. Corrosion of steam generator tube material – effects of chloride and sulphate ions. In this proceedings, pp. 153–164.

15. Bojinov, M., Hansson-Lyyra, L., Laitinen, T., Saario, T. and Sirkiä, P. Zircaloy-2 cladding materials – effect of microstructure on corrosion properties. In this proceedings, pp. 165–181.

16. Aaltonen, P., Yagodzinskyy, Y., Tarasenko, O. and Hänninen, H. Vacancy generation in electrochemical oxidation / dissolution of copper in $NaNO_2$ solutions and its role in SCC mechanism. In this proceedings, pp. 183–198.

17. Hänninen, H., Seifert, H.-P., Yagodzinskyy, Y., Ehrnstén, U., Tarasenko, O. and Aaltonen, P. Effects of dynamic strain aging on environment-assisted cracking of low alloy pressure vessel and piping steels. In this proceedings, pp. 199–221.

18. Toivonen, A., Moilanen, P., Aaltonen, P., Taivalaho, L. and Muttilainen, E. Effects of water chemistry transients on crack growth rate of nickel-based weld metals. In this proceedings, pp. 223–239.

19. Ehrnstén, U., Karjalainen-Roikonen, P., Nenonen, P., Korhonen, R., Timofeev, B. and Bloomin, A. Investigations on aged Ti-stabilised stainless steels. In this proceedings, pp. 241–251.

20. Nenonen, P. Thermal ageing of ferrite in cast stainless steel. In this proceedings, pp. 253–275.

21. Toivonen, A., Aaltonen, P., Nenonen, P., Ehrnstén, U., Käki, A. and Hietanen, O. Properties and IASCC susceptibility of austenitic stainless steel 08X18H10T. In this proceedings, pp. 277–308.

22. Valo, M. and Planman, T. Re-embrittlement of annealed pressure vessel, IAI_1-material condition of a Loviisa irradiated weld. In this proceedings, pp. 309–341.

23. Wallin, K., Laukkanen, A. and Nevasmaa, P. Risk informed plant life management – application of the Master-Curve approach for hydrotreating reactors in an oil refinery. In this proceedings, pp. 343–355.

24. Aho-Mantila, I. and Lahtinen, R. Paint and rubber piping coatings in seawater service. In this proceedings, pp. 357–361.

Applicability of different artificial defects in qualification of ultrasonic testing method

Matti Sarkimo and Marko Api
VTT Industrial Systems
Espoo, Finland

Abstract

Ultrasonic properties of real stress corrosion cracks and artificially produced defects were examined in a comparative round robin exercise. Seventeen professional ultrasonic testing (UT) examiners inspected eleven different defects. Detection and sizing results together with opinions about applicability of different reflector types were collected. The information was recorded to assess the detectability and sizing accuracy of reflectors and some insight was obtained on the indication features that inspectors use to examine the reflector properties.

Reflector properties that are typical for real defects were identified. The most important reflector characteristics were the stagger/specular of surface, echo dynamics generated and the influence of probe rotation (skew angle variation). It can be considered that the ultrasonic aspect is dominant and the geometric appearance of an artificial reflector does not need necessarily to be similar with the real defect.

1. Introduction

During the qualification process of a non-destructive testing (NDT) method the practical assessment has in many cases an important role. It is often required that the samples used are representative concerning e.g. the materials and geometry. A key requirement for the samples is also that they shall include reference defects that correspond the real defects and can be used to measure the performance of the inspection system. Only in few cases it is possible to use samples including real defects. Even if real defects are available the reliable definition of their actual size may be difficult. Therefore artificial defects produced using different techniques are often applied.

When ultrasonic testing method is applied the detection and sizing of defects is based on the signals (echoes) reflected by defects. Thus from the ultrasonic point of view the properties of the artificial defects should be as similar as possible to those of the real ones. Often the differences of these properties cannot be avoided and therefore it is important to recognise and to assess the influence of the differences to the final results. Sometimes the artificial defect may even be a very coarse simulation compared to the real defect but it may have certain ultrasonic properties that are quite sufficient to test the performance of some inspection aspects.

This study was made to examine the ultrasonic properties of different artificially produced defects and to compare them with real stress corrosion cracks. All these different defects that are later on called as reflectors were inspected by a rather large number of professional ultrasonic testing (UT) examiners. The goal of the study was to collect opinions of examiners about the applicability of different reflector types. On the other hand it was possible to compile information about the indication features that inspectors use to examine the reflector properties. Simultaneously a large amount of information was recorded that could be applied to assess the detectability and sizing accuracy of reflectors.

Complete reporting of the study is presented in the report Kuusinen et al. [1] and only main results are highlighted in this article.

1.1 Description of tests

There were altogether 11 reflectors included in the test samples. The reflectors were produced using different techniques e.g. electro-discharge machining (EDM), implanting, mechanical and thermal fatigue and special welding technique. Two of the reflectors were stress corrosion cracks that were initiated and grown up in a real process environment. The material of all samples was austenitic steel. A short description of the reflectors is given in Table 1.

The samples were covered before the start of examinations in such a way that only the surface necessary for the ultrasonic scanning was visible. In that way the locations of the reflectors were given to the examiners but no information of the type or size of the reflectors was given. There were altogether 17 UT

professionals (6 level III, 10 level II and 1 level I, according to EN 473) from three inspection companies examining manually the samples. Nearly all of the examiners had participated a special course and passed an examination concerning application of UT method on cracks in nuclear power plant components. All examiners had to use the same procedure, equipment and basic setting values during the testing. Four different probes were available for the examiners (Krautkrämer MWK 55-2, MWK 70-2, MWK 70-4 ja WSY 70-2).

Table 1. Description of the test reflectors.

ID	Reflector	Size (length × height) mm	Orien-tation	Location
1	A row of holes (12 holes with ∅ 0.5 mm) manufactured by EDM	11.5 × 2.8	Vertical	In base material, plate (thickness 30 mm)
2	Notch manufactured by EDM using disk shaped electrode	28 × 7	Tilt 8°	In base material, plate (thickness 30 mm)
3	Mechanical fatigue crack	15 × 5	Tilt 15°	At the root edge of the weld preparation (V), plate material (thickness 20 mm)
4	Real stress corrosion crack, cut out from process pipe	34 × c. 5	Approxi-mately vertical	At the root edge of the weld preparation (V), tube material (thickness 15 mm)
5	Real stress corrosion crack, cut out from process pipe	20 × c. 4.5	Approxi-mately vertical	At the root edge of the weld preparation (V), tube material (thickness 15 mm)
6	Welding defect, lack of fusion	11 × 2	Along weld pre-paration	At the root edge of the weld preparation (V), tube material (thickness 15 mm)
7	Stress corrosion crack, implanted	20 × 3	Vertical	In weld material, plate (thickness 30 mm), weld preparation (X)
8	Solidification crack along weld	39 × 12.5	Partly tilted	In weld material, plate (thickness 30 mm), weld preparation (X)
9	EDM notch fatigue crack (fatigue crack in front of the notch)	17 × 7.2 15 × 4	notch=0° crack=15°	At the root edge of the weld preparation (V), plate material (thickness 20 mm)
10	Thermal fatigue crack	8 × 4.0	Vertical	In base material, plate (thickness 15 mm)
11	Solidification crack along weld	44 × 5	Vertical	In weld material, plate (thickness 30 mm), weld preparation (X)

During the examination of the samples the examiners were asked to fill in forms their opinions and observation about the reflectors. Also they were asked to record measurement data e.g. the length, height (and technique to measure the height), maximum amplitude (and its location) and signal-to-noise ratio.

2. Results

The examiners expressed their personal opinions about how realistic or artificial the reflectors were. The overview of the distribution of opinions about the reflectors is given in Figure 1.

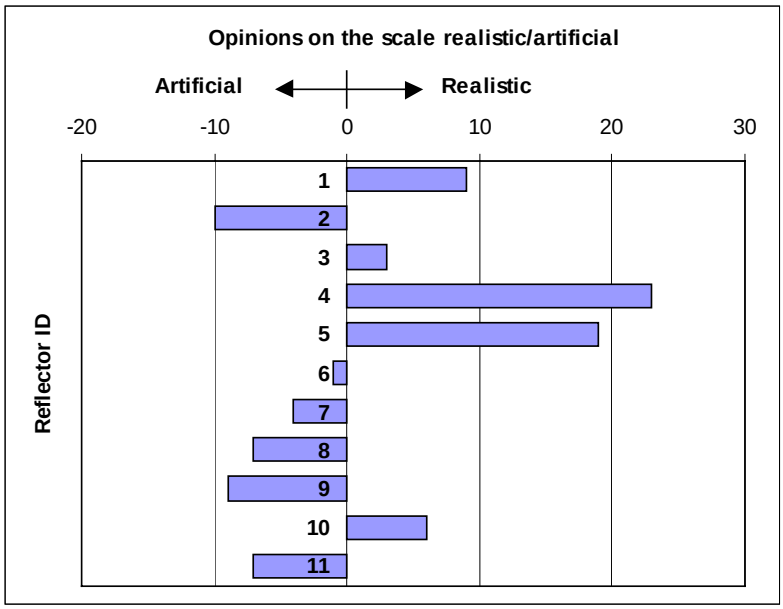

Figure 1. The distribution of the examiner opinions about how realistic or artificial they assessed the reflectors based on ultrasonic signals received.

The examiners recorded several different factors on which they based their opinions about the nature of the reflector. The most important factors identified were:

- the number of different reflector surfaces observed, artificial reflectors tend to have only one monotonic reflector surface but e.g. stress corrosion crack has many various reflector surfaces.

- the echo dynamic is clear and systematic for artificial reflectors and more varying for realistic defects. The starting points of the reflectors are easy to define at artificial reflectors because of the regularity of the geometric shape.
- real defects are often able to produce several echo amplitude peaks that can be detected in various locations along the reflector.
- the rotation of the probe (changing skew angle) decreases echo amplitude rapidly at specular reflector surface that is more typical for artificial defects.
- overall the real and realistic defects have typically more variability and irregularity compared to monotonous features of the artificial defects. These features can be seen in the UT signal behaviour.

It was noticed that examiners that had much experience could in many cases detect and identify many detailed features of the reflectors by analysing the echo dynamics and its behaviour. But finally there was not a clear difference between inspector groups of different experience levels when they classified the reflectors to real and artificial defects.

The examiners were asked to record several numerical values about the reflectors. As an example the measured signal-to-noise ratios are given in Figure 2 to describe the detectability of reflectors using different probes.

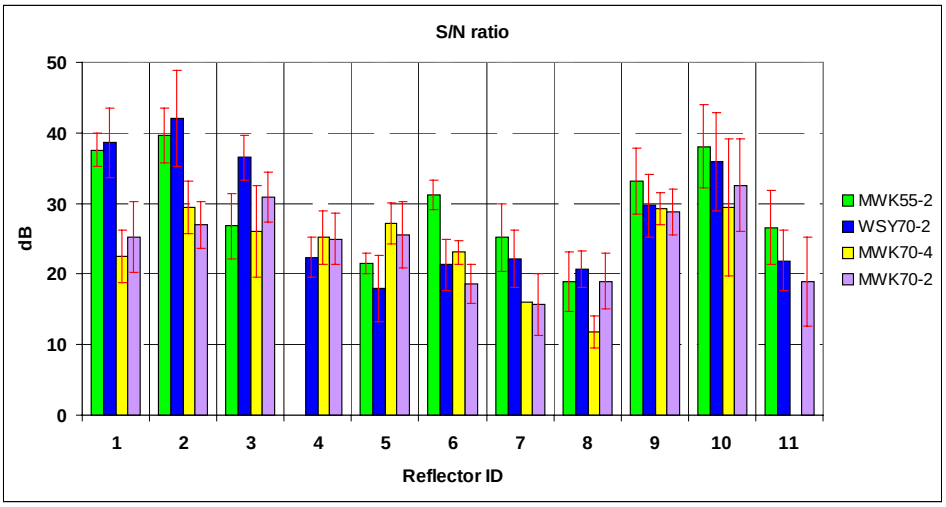

Figure 2. Signal-to-noise ratio of all reflectors measured with different probes. The columns show the average values of the measurements of all examiners. The lines at the top of the columns indicate the standard deviation.

The use of the crack tip signal is usually the most reliable way to define the through wall height of a defect. Unfortunately the detection of a crack tip signal is not always a straightforward task. The signal may be weak and specially in a noisy environment it may not be distinguished. Figure 3 shows the results of the answers when e examiners were asked about the detection of a crack tip signal. Only from reflector 2 (EDM notch in base material) all examiners declared a crack tip signal detection. On the other hand at the crack type reflector in the middle of weld material (number 8) hardly a third of examiners was sure about crack tip signal detection.

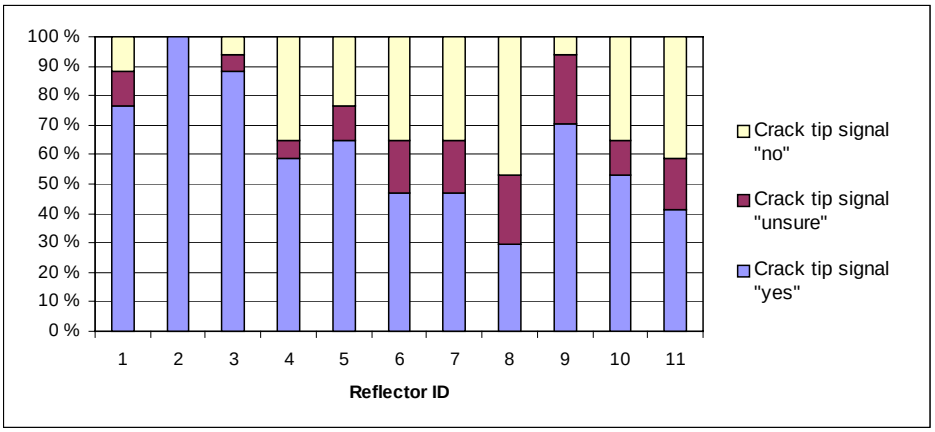

Figure 3. The distribution of the examiner answers on the question if they were able to detect crack tip signal.

As further examples of the measurement data recorded are some of the sizing results presented in Figures 4 and 5. The results of the through wall height measurements are given in Figure 4. In this figure are shown the average values achieved by all examiners and the standard deviation. For each reflector only the results of two probes that examiners preferred are included. The real height values indicated in the figure are not verified by destructive test but are based on the information given by reflector manufacturer or on the results from several special UT techniques.

The opinion of the examiners was that the through wall sizing of the reflectors was the most demanding part of their task. Weak crack tip signals or high noise level made the detection of the crack tip signal difficult and therefore also other methods were used to define the reflector height. It can be seen in the results of

Figure 4 that in some cases the difference between measured and real reflector height is rather large and also the standard deviation is quite significant.

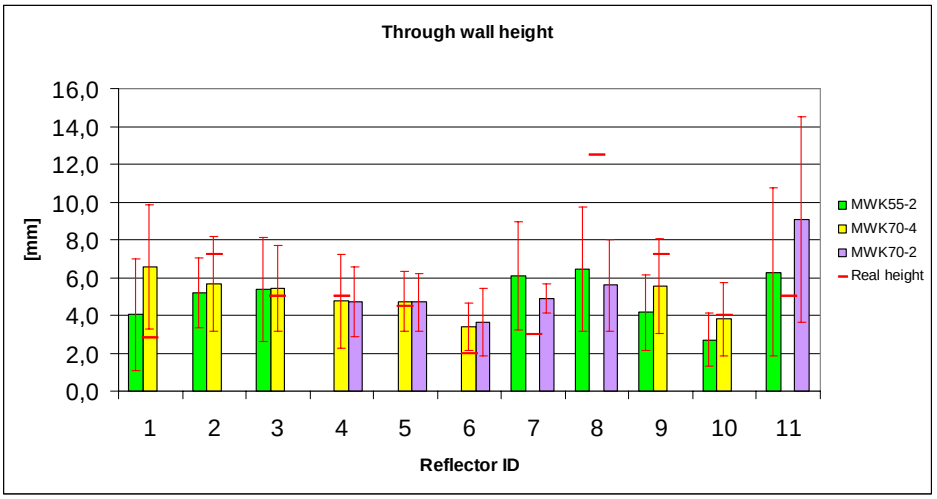

Figure 4. The results of reflector through wall height measurements. The columns show the average values of the measurements of all examiners. The lines at the top of the columns indicate the standard deviation.

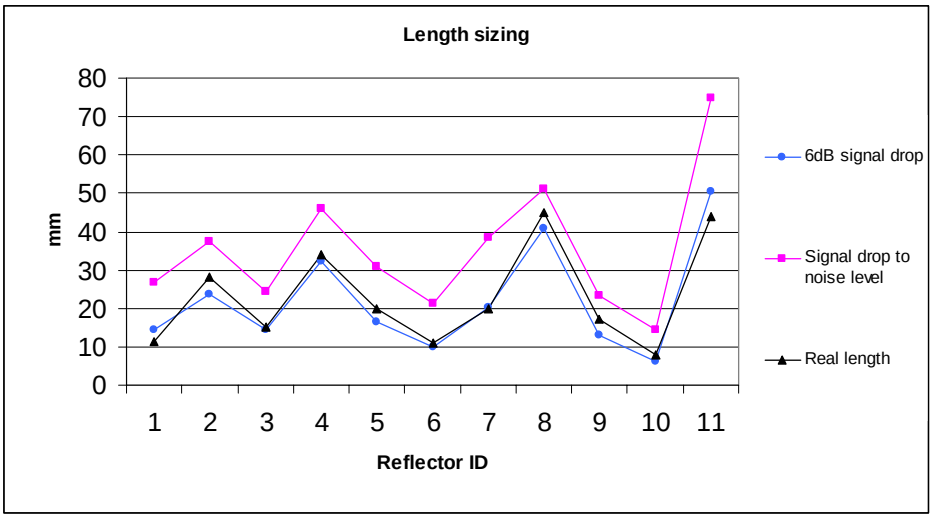

Figure 5. The results of the reflector length sizing with two different methods compared to the real length values. The measurement results are average values achieved by the examiners. The length sizing is performed using probe MWK70-4 at reflectors 4, 5 and 6 and otherwise using probe MWK55-2.

The examiners were asked to measure the reflector lengths using two methods: firstly dropping the signal amplitude -6 dB and secondly dropping the signal to the noise level. The average results of the examiners using the two methods compared to the real reflector length is shown in Figure 5. It seems that in this case the "-6 dB signal drop" -method resulted fairly accurate measures and the "signal drop to noise level" systematically oversized the length.

3. Discussion and conclusions

The real stress corrosion cracks included in the samples were easily recognised as cracks. These were rather long reflectors and had many reflector surfaces that produced signals typical for a non-specular crack. The amplitudes measured from these cracks were rather high. Also the signal-to-noise ratio was good despite of the vicinity of the weld. It is typical for these cracks that detection is possible even if the beam direction is not perpendicular to crack direction (they allow rather large skew angle variation). It was found that an artificial defect formed of a series of small holes could simulate in some extent the features of a stress corrosion crack.

The regular shape and specular reflectivity of an EDM notch was detected and identified easily. Similar features of ultrasonic behaviour were also found at fatigue cracks (reflectors 3, 9 and 10). All these reflectors produced large amplitude signals and their signal-to-noise ratio was high. This good detectability was also affected by the fact that the reflectors were located in the base material or in the front of the weld. In the most cases it was also possible to detect a crack tip signal at these reflectors.

One group of reflectors were located deep in the weld material (reflectors 7, 8 and 11). High noise level made the examination of these reflectors difficult. The detectability of reflectors was poorer compared to the other defects based on low defect signal amplitudes and high noise level originating from weld. Anyway some characteristics typical for cracks were detected. Based on the high noise level the examiners considered in many cases these reflectors as artificial.

The results identified reflector properties that are typical for real defects and thus important to be considered when they should be simulated with artificial reflectors. The most important reflector characteristics were the stagger/specular of surface, echo dynamics generated and the influence of probe rotation (skew

angle variation). The artificial defects should be able to reflect ultrasonic signals that simulate these characteristics of real defects. It can be considered that the ultrasonic aspect is dominant and the geometric appearance of an artificial reflector does not need necessarily to be similar with the real defect.

In this study it appeared that often the examiners could quite easily find out real and artificial reflectors. It can be considered that in a practical qualification situation this is not crucial. During the qualification process the practical trials using test samples should be able to produce evidence material about the performance of the inspection system. Thus it is most important that the reflectors have well defined sizes and can be located in appropriate positions and orientations. If it is assumed that the ultrasonic characteristics of the reflectors applied differ from the real defect, one should know the differences to assess the test results properly.

In the future it is important to compile and produce quantitative data about the reflector characteristics and their influence on reflected ultrasonic signal. This kind of information can be found in the literature as report of Wirdelius & Österberg [2] shows. The data available may depend on the measurement parameters and therefore one should always consider their applicability carefully.

A clear need to develop different types of reflectors can also be seen. It seems possible to produce reflectors that simulate many ultrasonic characteristics of the real defect types by combining different techniques.

4. Acknowledgements

This presentation is prepared for a joint Finnish industry group in a in a project on structural operability and plant life management (RKK). The project funding by the National Technology Agency (Tekes), Teollisuuden Voima Oy (TVO), Fortum Power and Heat Oy, Fortum Nuclear Services Ltd., FEMData Oy, Neste Engineering Oy, Fortum Oil and Gas Ltd. is gratefully acknowledged. The discussions with Kari Hukkanen of TVO and Raimo Paussu of Fortum Power and Heat and other partners in the consortium have been of great help in planning and execution of this work. Raimo Paussu deserves particular thanks of providing samples to the experiments.

References

1. Kuusinen, P., Api, M., Hakkarainen, T. and Sarkimo, M. Keinovikojen soveltuvuus ultraäänitarkastuksen pätevöintiin. Espoo: VTT Industrial Systems, 2002. Report BVAL65-011172. 30 p. + app. 17 p. (in Finnish).

2. Wirdelius, H. and Österberg, E. Study on defect characteristics essential for NDT testing methods ET, UT and RT. Swedish Nuclear Power Institute (SKI), 2000. SKI Report 00:42. 50 p.

Experiences on Synthetic Aperture Focussing Technique (SAFT)

Jorma Pitkänen and Pentti Kauppinen
VTT Industrial Systems
Espoo, Finland

Abstract

Imaging based on the synthetic aperture focussing technique (SAFT) improves the reliability of sizing and characterisation of structural discontinuities found in non-destructive testing of nuclear components. One of the main advantages of this technique is an improvement of signal-to-noise-ratio. The advantages are discussed in terms of practical applications and theory.

1. Introduction

The classical tasks of ultrasonic NDT are detection, sizing and characterisation of structural discontinuities like cracks or lack of fusion in welds, inclusions of foreign material or delaminations.

The imaging system applied to improve the reliability of assessment is based on the use of backpropagation of elastic waves in synthetic aperture focussing technique (SAFT). This technique is applicable to a wide range of ferritic and austenitic materials and is used for testing of pipes, turbines, plates, vessels or pump housings.

In this overview the main practical features of saft-inspection system are described and results from measurements performed on site are presented. The improvement of signal-to-noise-ratio (SNR) is one of the main advantages, which is considered in the theoretical background of saft. Saft-reconstruction is valid in the far field (Fraunhofer Region). This technique is mainly used for one crystal probes.

2. Inspection considerations

Important elements in practical saft measurements are following: The aperture for measurement can be calculated from a simple equation:

$$L = 2\frac{\lambda}{D_R * \cos\beta}S \tag{1}$$

where L [mm] is the aperture of measurement, λ [mm] is the wavelength of sound beam emitted by the probe, S [mm] is sound path, D_R [mm] is the crystal diameter and β [°] is the angle of incidence of the probe.

The resolution of the reconstruction is D/2, the half of crystal size of the probe. This is at the same time an advantage and also a disadvantage. With the small element size the near field is close to the probe and opening angle is large. Even though the resolution of small crystals is good, the power of ultrasonic signals is low. To increase the power especially with long sound paths, larger crystals are necessary. Thus the resolution is decreased. It is possible to increase the power by using as wide crystals as possible. Of course, the near field must be in between the probe and defect. The axial resolution is equal to the pulse length and is not related to the size of aperture.

Step-to-step distance parameter influences directly the SNR and herewith how clearly the image of a defect is displayed above the noise. This parameter does not influence directly the resolution of the image [5, 2]. It is recommended to select a probe step distance of 0.3 mm if the probe frequency lies between 1 MHz and 5 MHz (shear or long). In general, the maximum probe step distance should not exceed 1/5 of the effective crystal diameter of the probe. Sizing is independent from the selected probe step distance.

In conventional techniques using the DGS-diagram, amplitude variations influence immediately the equivalent flaw size: e.g. a drop of 6 dB would reduce the equivalent flaw size of 6 mm down to 4 mm. Therefore possible variations in coupling directly affect the reliability of inspection. Saft relies less on amplitude information but more on time-of-flight information. The image spots are formed by summing up information from different probe positions. As long as there are many probe positions the image intensity does not change much if there is loss

of coupling during some probe positions. Loss of amplitude influences the SNR in the image.

3. Characterisation and sizing of defects

Saft is a useful tool to determine whether a defect is planar or volumetric. Strong evidence for planar defect is the appearance of tip reflection echo(s). Especially in the case of large cracks the crack face can be seen in the SAFT reconstruction. Five different sizing techniques are generally used. In the following they are presented in the order of their field of application.

Sizing of cracks is based on tip reflection. Subsurface cracks are sized by measuring the vertical distance between the positions of tip echoes. Surface cracks are sized by measuring the position of crack tip or by determining the vertical distance between the corner and tip echoes. In Fig. 1 there is a corner reflection from a real IGSCC. The size of this crack is about 5–7 mm, depending on the spot, where measurement is taking place.

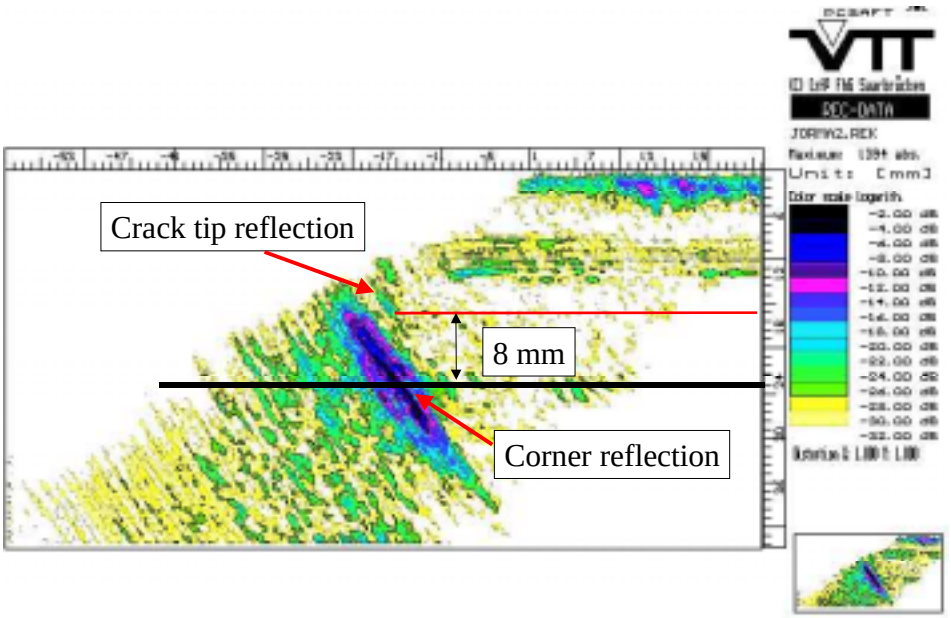

Figure 1. Saft reconstruction from an IGSCC.

The crack tip is not clearly seen in the reconstruction. It is quite normal that no clear reflection can be seen in the reconstruction. Corner reflection from a defect is very strong and the defect will be detected normally very easily, if it is on the outer or inner surface.

In Saft technique the beam diameter is the focussed diameter i.e. approximately half of the crystal size. Measurement is carried out simply by determining the vertical distance between points where the amplitude has dropped -6 dB. Method is applicable for both planar and volumetric inner defects. Half-amplitude method is demonstrated in Fig. 2.

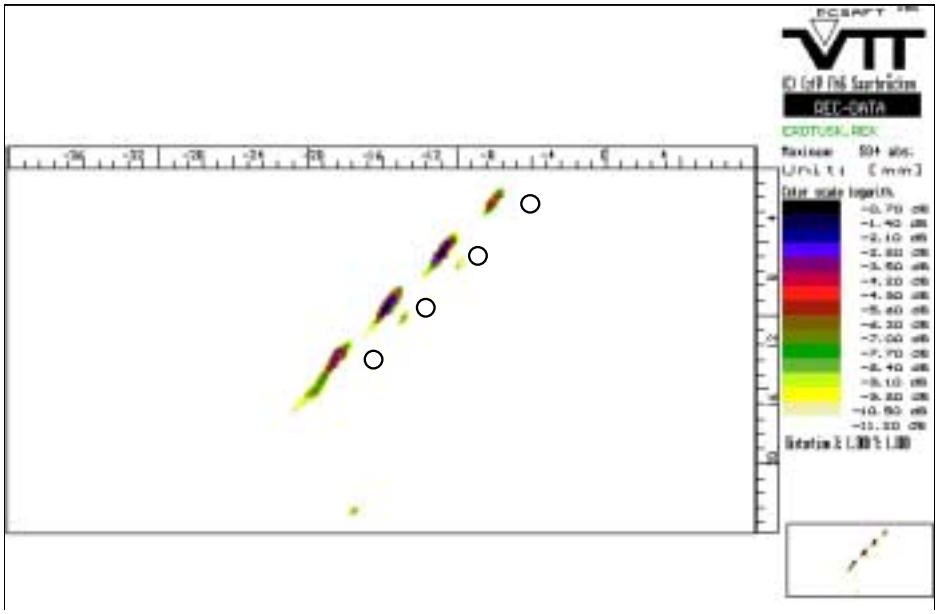

Figure 2. Demonstration of sizing capability with side-drilled holes.

Cracks can be sized also by measuring the extension of their face echo from the reconstruction. The height of a crack is supposed to be equal to the measured extension, see Fig. 3.

A volumetric defect gives generally strong main echo and weak creeping wave echo exactly on the beam central axis behind the main echo. Sometimes the main echo can be rounded in the reconstruction, see Fig. 4.

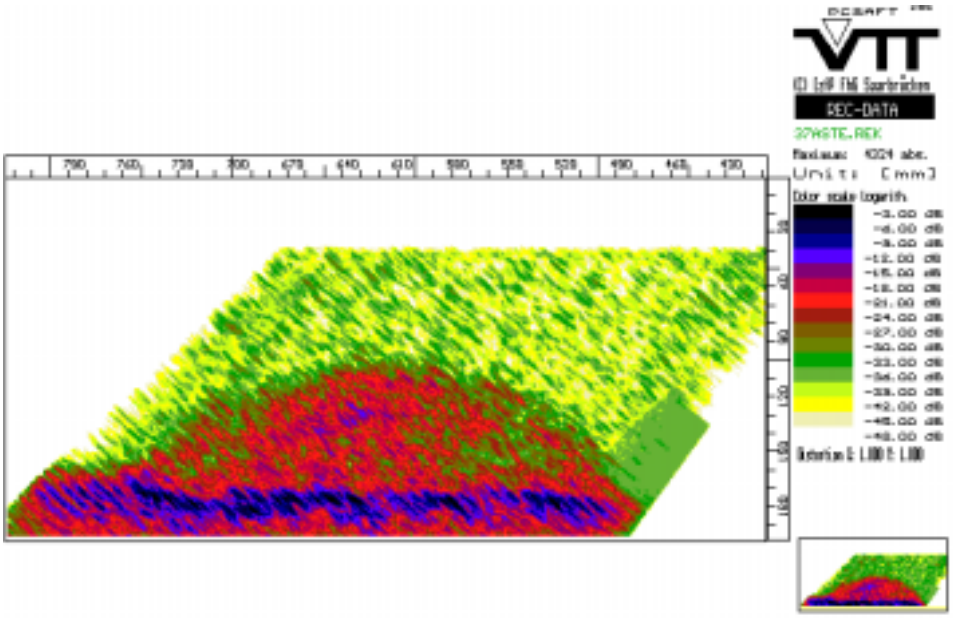

Figure 3. Demonstration of sizing capability from the crack face reflection (NESC-cylinder).

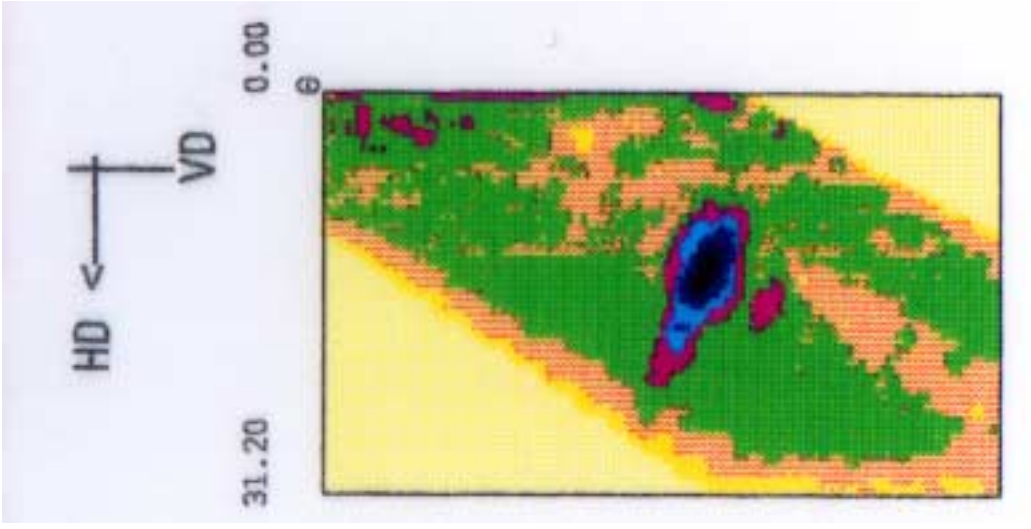

Figure 4. Saft reconstruction of a volumetric defect in RPV.

Round volumetric defects can be sized by measuring the sound path *S* between reflected and creeping echo, see Fig. 3. Diameter *D* of the defect is calculated by using equation

$$D = \frac{4S}{2+\pi} \tag{2}$$

Occasionally the use of shadow technique is a useful solution. It is a rather inaccurate technique when carried out by conventional manner but it has certain advantages. For instance, it is not sensitive to the orientation of the defect. Interpretation of the acquired data can be improved significantly by saft and the height of a defect will be evaluated from the reconstruction, see Fig. 5.

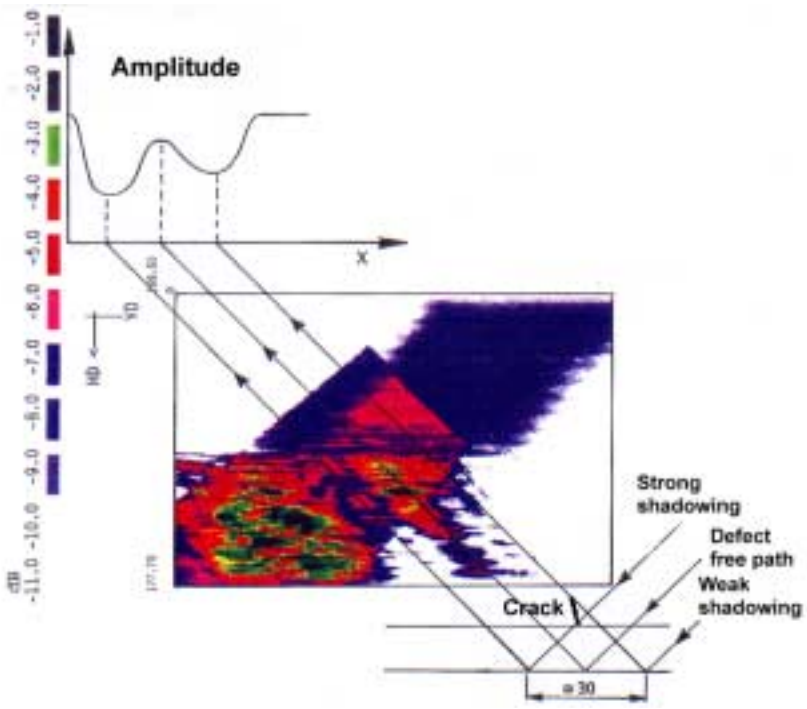

Figure 5. Shadow technique for using the saft method where crack diminishes sound pressure in the reconstruction figure.

4. Applications of SAFT

One example of application is the inspection of welds in main gate valves. A scanning manipulator is placed on the nozzle between the main cooling pipe with a diameter of 500 mm and the valve. The geometry did not allow direct insonification of the weld, but full skip (reflection from the backwall) had to be used. Therefore the sound path was more than 300 mm and because of the strong attenuation of the ultrasonic pulse in austenitic forging, the SNR was not sufficient to make a satisfying evaluation of the indications.

In Fig. 6 there is a saft reconstruction of a calibration defect (a) in size of 20 mm in through wall direction. It is difficult to detect a defect behind the weld in normal A-scan due to the low SNR. In Fig. 6 the real size and location of the calibration defect is marked with a white rectangular. In Fig. 6b there is a real indication, which could be divided in two different indications with the help of saft reconstruction.

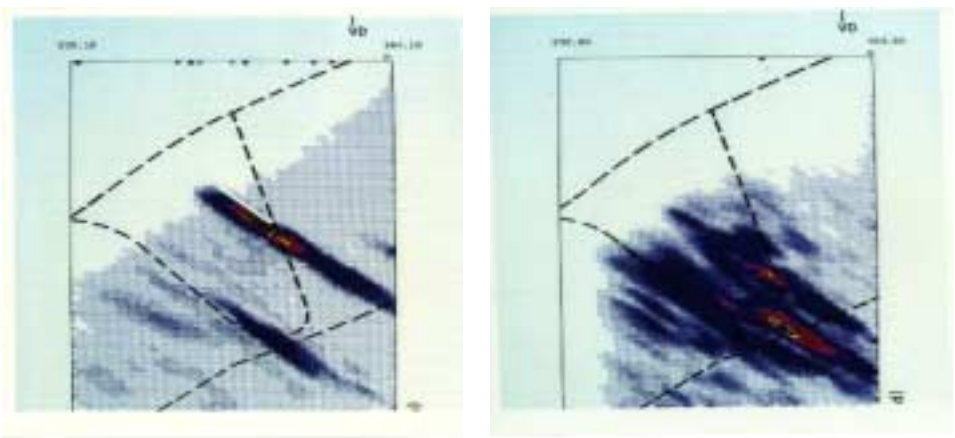

a) *b)*

Figure 6. Saft reconstruction of a calibration defect from a real size mock up (a) and real defect (b) in the weld of main gate valve.

Saft measurements have been performed to the dissimilar weld of the emergency cooling nozzle. The aim of the saft measurement was to distinguish the geometrical indications from the real defect indications. In Fig. 7 clear geometrical indications in the geometry of the component can be seen. The

indications are caused by a notch, by a side drilled hole and by the counterbore surface and corners.

Threaded holes in a flange of primary circuit pump casing were examined by eddy current testing in 1993 and an indication was detected at the bottom of one thread which was at the depth 60–70 mm from flange surface. However, the inspector was not able to asses the size of this indication. The indication was analysed with saft by scanning in two directions. One direction was radial backward from the edge of hole. Another direction was circumferential so that the probe was moved along the edge of the hole. The result was 13 mm × 15 mm respectively. The indication was analysed again in 1996 and the result showed that the size of the defect was not increased. The deviation from the previous result was less than 5%.

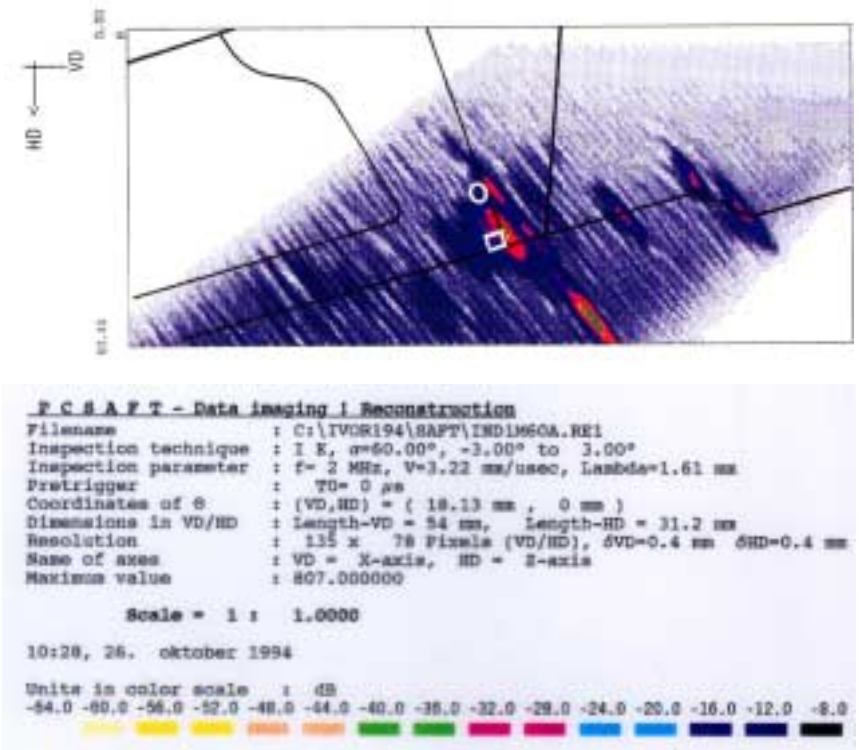

Figure 7. Saft reconstruction from emergency cooling nozzle.

For accurate sizing it is necessary to find the echo from crack tip. Fig. 9 shows a crack tip front measured from a crack in a reference block during the manufacture of the block and the corresponding measurement of the crack front with 0°L probe from the base material side. The crack tip front is clearly seen from the data. The same testblock measurements have been made with saft, see Fig. 10.

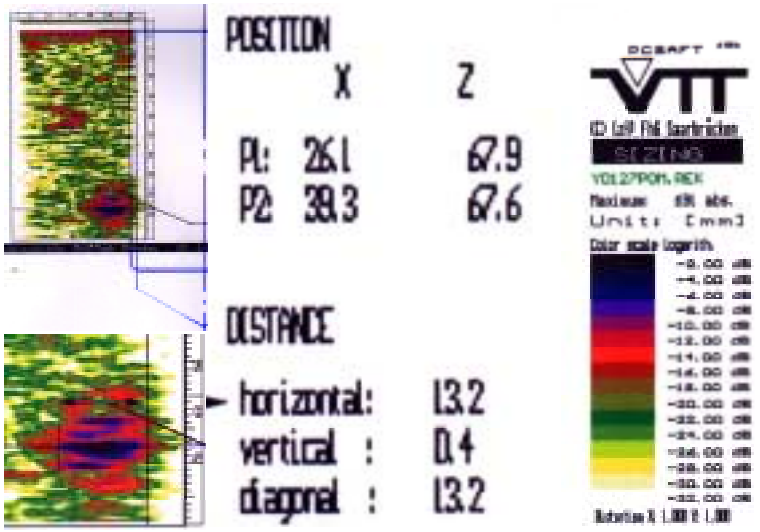

Figure 8. Saft-reconstructions from primary circuit pump showing indication originating from thread surface.

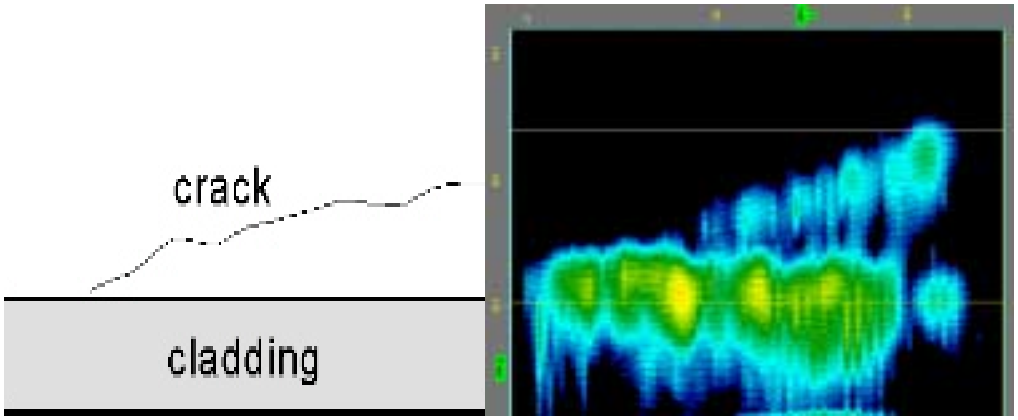

a) *b)*

Figure 9. Crack tip front of a sub cladding defect in the test block PS 13 and corresponding measurement with 0°L probe (b).

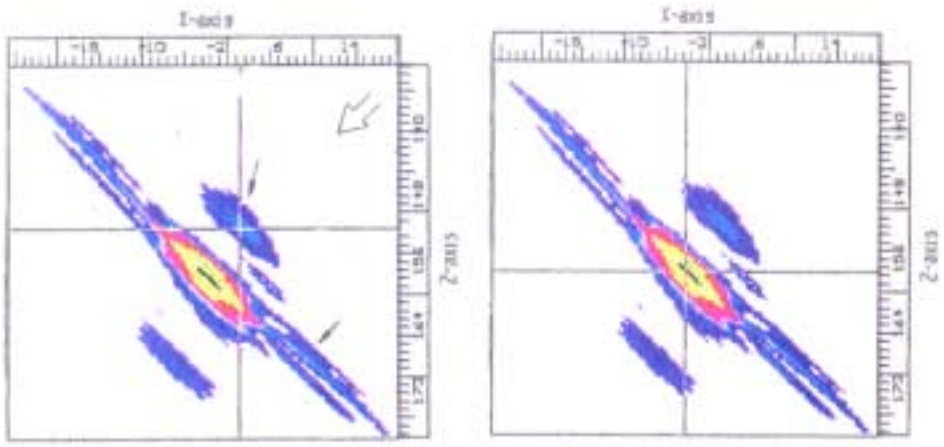

Figure 10. Saft measurement from a subcladding defect located in test block PS13. Crack tip echo is above the corner reflection.

In the saft measurements tip signals were used for sizing of defects. With 1 MHz 45°T probe the estimated height of the defect was: 3.6 mm and with 2 MHz 45°T probe 3.0 mm. According to the surface wave measurements carried out before welding of the cladding the estimated crack size was in this area 5.0 mm.

In practical inspections large defects are very seldom met and sized. In the round robin test of the international NESC-project this was possible. In the following two examples are presented showing the results from defects B and R of the test cylinder. In normal testing it was difficult to detect the crack tip from normal data of defect B. It means that the crack tip was quite tight, see Fig. 11a. However, in one of the measurements performed by VTT the noise from the face of the crack was seen in the data. With the help of this saft reconstruction the size of the defect B was determined. The comparison to the metallography gave a sizing error of about 2.7%. In the post test same defect tip was detected with 0°L-probe, see Fig. 11b. No saft measurement was performed in this phase.

For the post test phase one new fatigue crack (R) was manufactured. This defect was measured with a normal multichannel ultrasonic equipment and with saft-equipment. With normal ultrasonic measurement it is difficult to detect the crack tip profile, Fig. 12a. In the saft reconstruction the crack tip profile can be followed more precisely, Fig. 12b. The error in flaw size measured ultrasonically

with saft-recontruction was about 2.3% based on the metallography. In the Nesc cylinder there was also one multi-branch defect, which was not included in the comparison of results of round robin test. This defect was also a large defect of similar size than the two defects mentioned above.

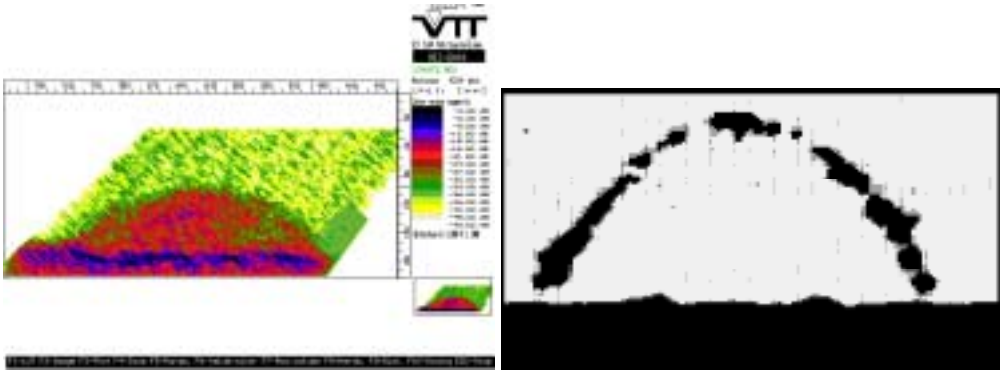

a) *b)*

Figure 11. Defect B measured in the pretest phase with saft (a) and in the post test phase with 0°L probe (b). In figure a) the crack characteristics are shown and in b) the crack tip profile.

In the radial support of RPV some slaglines were detected during manufacturing. Based on the fracture mechanics analysis there are also some stress concentrations in this area. Because of the radiation embrittlement a recovery annealing was performed and stress concentrations during annealing were higher than normally. Because of these causes the radial support welds were inspected with saft technique. No indications growing towards the reactor pressure vessel were found. Figure 13 shows the saft reconstruction from radial support area with some geometrical indications.

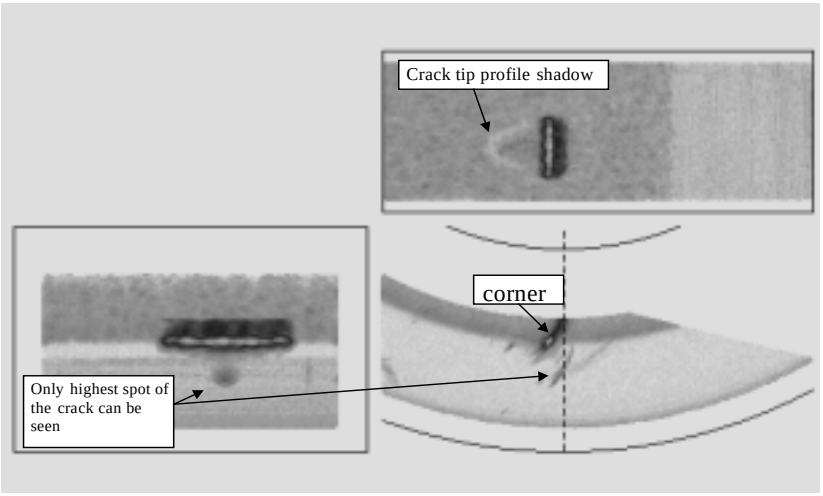

a)

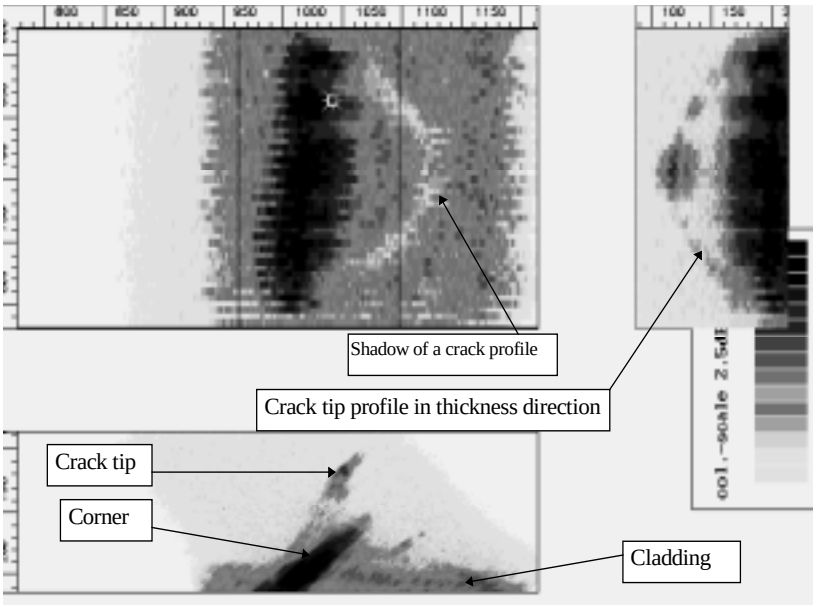

b)

Figure 12. Defect R measured with normal multichannel equipment and with one-channel saft-equipment.

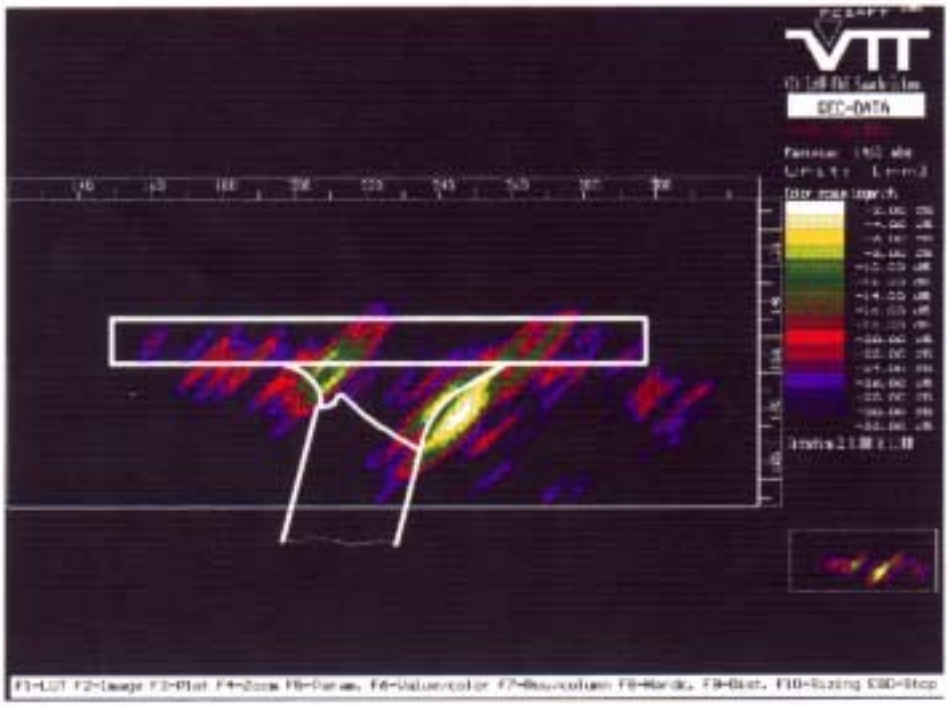

Figure 13. Saft measurement from a radial support using saft.

5. Conclusions

Saft reconstruction can be used in many applications in nuclear power plant to evaluate the defects detected in components. Saft-measurement can be especially applied to inspections where sound paths in ultrasonic testing are long. This includes pressure vessel, thickwalled pipings, main gate valves etc. Saft method is mainly intended to be used for characterisation and sizing of defects. With saft it is often possible to size the defects more precisely but it is not the only correct method. In general, the best result is based on the estimates achieved by different methods together. The following tables (Figures 14 and 15) show data from some inspections, data from Erhard *et al.* [1] and data from the NESC trial. It can be seen that the error of saft measurement is normally less than 2 mm from the real value. In three cases the error is 3 mm or more. Of course the values tend to increase in percentages when the defects are smaller but the absolute value seems to be about the same. These values are only giving a tendency noticed in sizings performed with saft-method. The accuracy is depending on

many factors and not only the physical resolution of the method is decisive. Coupling, ultrasonic probe, sizing technique, human factors etc. affect also the accuracy.

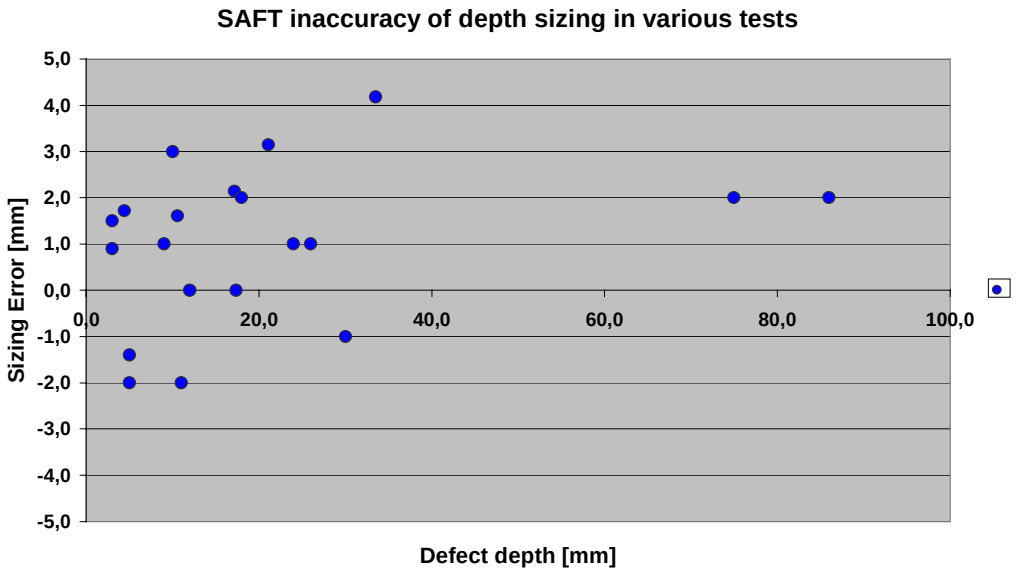

Figure 14. Sizing error using saft measurement with different defect sizes.

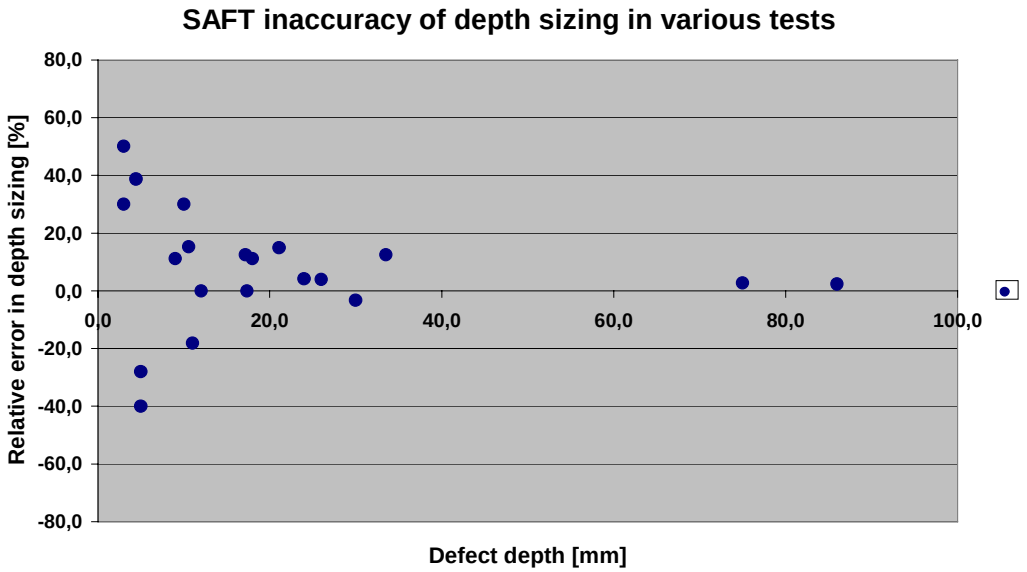

Figure 15. Relative error using saft measurement with different defect sizes.

Acknowledgements

This presentation is prepared for a joint Finnish industry group in a project on Structural operability and plant life management (RKK). The project funding by the National Technology Agency (Tekes), Teollisuuden Voima Oy (TVO), Fortum Power and Heat Oy, Fortum Nuclear Services Ltd., FEMdata Oy, Neste Engineering Oy, Fortum Oil and Gas Ltd. is gratefully acknowledged.

References

1. Erhard, A., Schulz, E., Brekow, G., Wüstenberg, H. and Kreier, P. Critical assessment to the TODF approach for ultrasonic weld inspection, 7th ECNDT European Conf. on Non-destructive Testing, Copenhagen, 26–29 May 1998. Pp. 1236–1242.

2. Kauppinen, P., Jeskanen, H. and Schmitz, V. Analyse von Primärkreis-ventilen mittels PCSAFT, DGZFP-Jahrestagung, Garmisch-Partenkirchen, 17–19 May 1993. Berlin: Deutsche Gesellschaft für zerstörungsfreie Prüfung. Pp. 659–663.

3. Pitkänen, J., Särkiniemi, P. and Jeskanen, H. The underclad defect detectability in ultrasonic testing. Espoo, Finland: VTT Metals Laboratory, 1992. Report VTT-MET-B199.

4. Pitkänen, J., Kauppinen, P., Jeskanen, H., and Schmitz, V. Evaluation of ultrasonic indication by using synthetic aperture focusing technique (PC-SAFT). Proc. of Int. Conf. Computer Methods and Inverse Problems in Non-Destructive Testing and Diagnostics, CM NDT-95, November 21–24, 1995, Minsk, Belarus. Pp. 291–302.

5. Pitkänen, J., Kauppinen, P., Jeskanen, H., Särkiniemi, P., and Schmitz, V., Evaluation of ultrasonic indication by using synthetic aperture focusing technique (PC-SAFT). 14th Int. Conf. NDE in the Nuclear and Pressure Vessel Industries, 24–26 September 1996, Stockholm, Sweden. ASM International. Pp. 459–463.

Ultrasonic defect sizing with manual and semi-automatic system

Jorma Pitkänen, Pentti Kauppinen, Pauli Särkiniemi and Harri Jeskanen
VTT Industrial Systems
Espoo, Finland

Jesus Vazquez and Fernando Ojedo
Tecnatom S.A.
Madrid, Spain

Abstract

In the outages of nuclear power plants, conventional power stations and oil refineries the majority of defect sizing is carried out manually, because the installation time for mechanised inspection system is high and the result of inspection is not shown to be more accurate in general.

This review discusses defects sizing and compares sizing performed manually and with a semi-automated system. With the help of the semi-automated system described here it is possible to collect the inspection data in a computer and to analyse it more accurately after inspection.

The advantages and disadvantages of this system are discussed. The system can be used as a defect sizing tool in manual inspections as well as to complete mechanised ultrasonic inspection of objects which can be inspected with a mechanised system only partly or not at all.

1. Introduction

Ultrasonic testing can be divided in three categories: manual, semi-automatic and automatic testing. If automatic testing is considered strictly, it means a system where decision making during inspection is included. In this survey mainly some differences between manual and semi-automatic system are

considered. In normal manual ultrasonic testing the inspector makes decision about indications during the inspection. Possibly only the A-scan is saved into the equipment. At the moment the majority of ultrasonic inspections is still made by this way. With a semi-automatic system the measured data can be stored into the equipment. The evaluation and decision making can be performed after inspection. This sets requirements on the quality of the measured data.

At first the quality of data acquisition must be high. This means that the acoustic contact during the inspection must be sufficient. One of the main tasks of the operator is to assure this. Another task is to vary the skew angle of the probe during scanning as in manual inspection.. Without the possibility to change the skew angle the system is only a poor mechanised system with variable step to step distance and with variable distance between the scanning lines. In the semi-automatic system it is important to determine and evaluate in advance the volume to be inspected. This assures the reliability and sufficient resolution of the inspection. There are two possibilities to check the volume inspected: (1) to draw in advance on the screen the planned volume, which disappears during inspection, (2) to draw during inspection on the screen the volume measured.. With the semi-automatic system the analysis carried out afterwards gives the possibility to get more precise results from thickness measurements, defect sizing and detection.

2. Equipment

Measurements have been carried out with a multichannel ultrasonic data acquisition system SUMIAD, version 4. The probe positioning system BAT has been attached to this system. BAT system is based on low frequency ultrasonic sensors. Before inspection all the positioning sensors must be calibrated. This is at the moment made simply with the help of one emitter and 3 receivers, see Figure 1. With this configuration it is not possible to measure the skew angle of the ultrasonic probe. This is at the moment a clear disadvantage. In near future this will be improved by increasing the number of receivers and emitters.

The calibration of the position of the ultrasonic probe is very simple. First the distances between the receivers and the origin of the co-ordinate system will be introduced to the software. By using the receivers and the emitter each co-

ordinate axis will be calibrated separately and the origin of the measurement axis will be determined. In Figure 1 the principle of positioning one emitter and 3 receivers is shown.

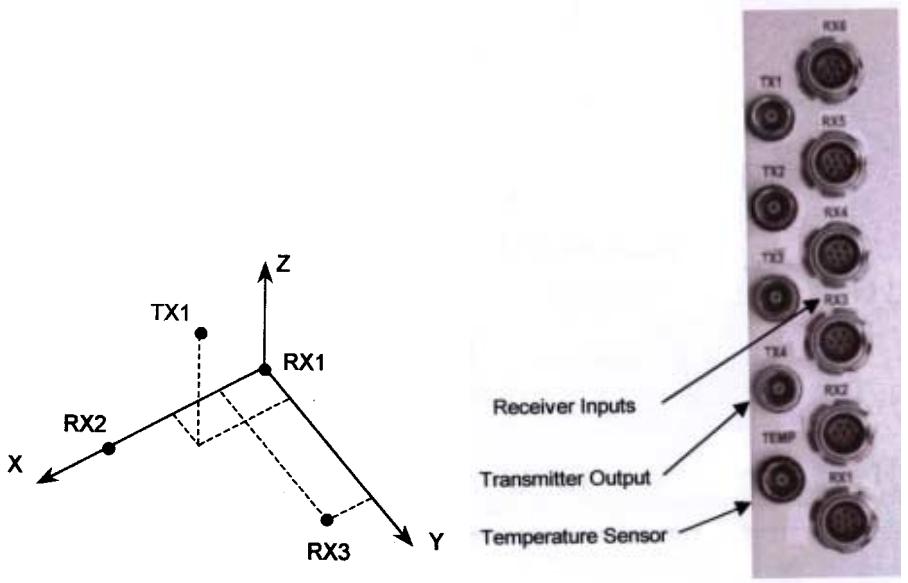

Figure 1. Positioning principle and the receiver (6) and emitter (4) plugs of the BAT-system.

After calibration of the positioning system, the calibration of the ultrasonic probes can be made in the calibration menu of SUMIAD. Also the inspection volume and the type of probe holder (one or more probes) will be given during calibration.

When the ultrasonic equipment is calibrated the data acquisition is a very simple process. After releasing the position measurement system by pushing the button the measurement begins. The scanning is performed manually and all data is simultaneously stored on the hard disk. The size of the measurement file depends on the size of the measured A-scans and if they are in RF-mode, as rectified A-scans or in peak mode, Figure 2. The rectified A-scans can be stored either in logarithmic or in linear mode. In linear mode the dynamic range is 48 dB and in logarithmic mode 80 dB with 8 byte.

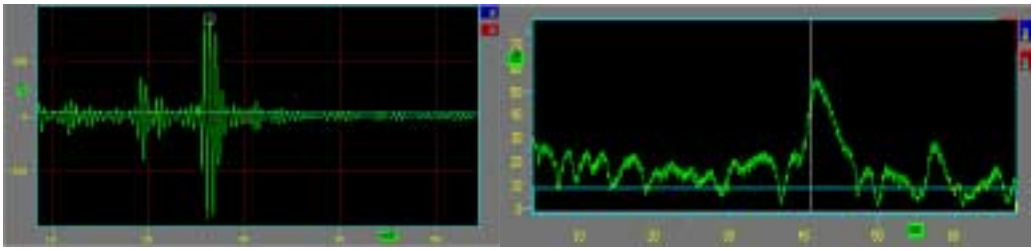

Figure 2.Data from a crack corner echo and from a crack tip echo saved in RF-mode (left) and from a thermal crack corner echo saved in logarithmic A-scan mode (right).

The analysis of data can be carried out in Sumiad EDIT mode or in Windows NT Masera analysis software.

3. Applications

Following simple applications will be discussed here: defect detection, defect sizing and wall thickness measurement. Especially in difficult geometrical objects or in cases where sizing is made manually the BAT system can improve the reliability of sizing. In hazardous environment (radiation, high temperature) the measurement can be performed quickly on site and the results can be analysed afterwards in office.

3.1 Defect detection

During manual inspection a lot of information passes through the brains of the ultrasonic operator. With the system described here the same data is stored in the equipment and different B-scans can be produced both during the inspection and afterwards during the analysis. One example shown here is an austenitic pipe containing thermal fatigue cracks [1]. In the measured data shown in Figure 3 the cracks can be clearly detected and the analysis of cracks can be performed properly afterwards based on the data. The resolution of the positioning is about 1 mm. This sets the limits on the measurements. Different crack lines are shown slightly round, which is caused by an error in the positioning due to the curvature of the pipe. This does not affect the detection of defects but causes

some errors in the positioning of defects. In Figure 4 the result of inspection of a plate with two welds is shown. The inspection is carried out properly but the cracks existing in the plate are not detected. This means that the semi-automatic system does not guarantee good inspection results if the ultrasonic technique is not properly selected.

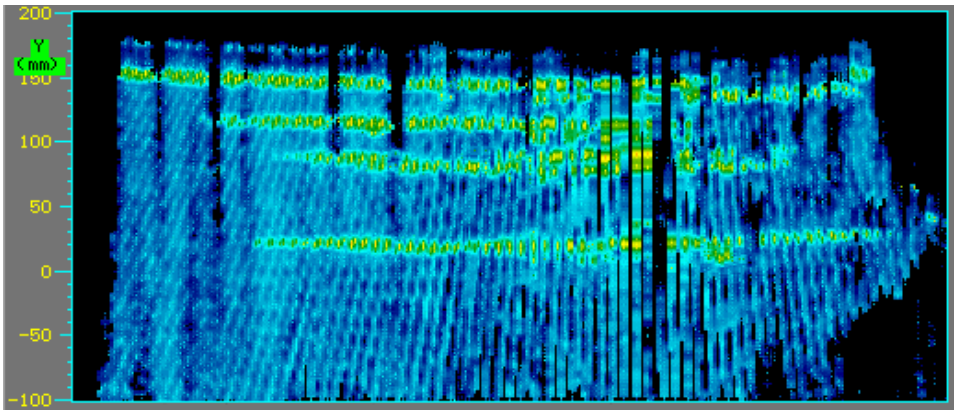

Figure 3. In-service induced thermal fatigue cracks in austenitic pipe.

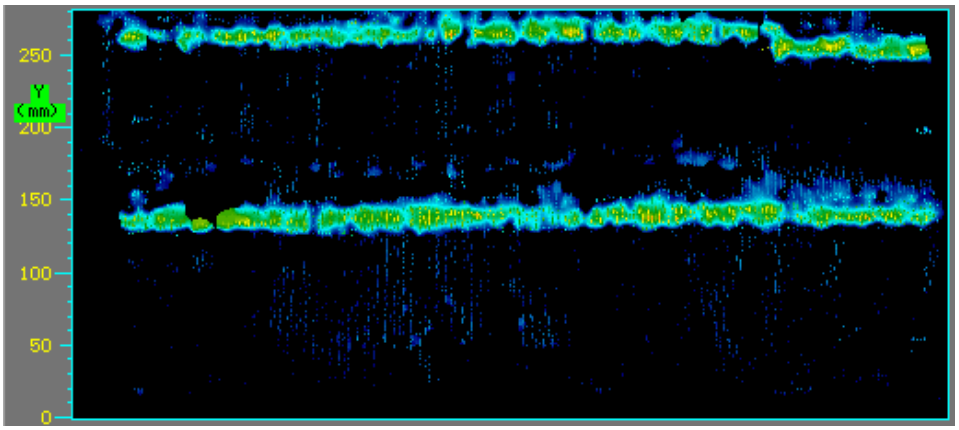

Figure 4. Cracked welds in an austenitic plate.

From the measurement of test specimen shown in Figure 4 the resolution of the positioning system can be estimated based on the ultrasonic results presented in Table 1.

Table 1. Accuracy of the positioning system.

Reference distance [mm]	Real distance [mm]	Distances measured [mm]	
		70°T4MHz composite	70°T2MHz composite
weld to weld	**119**	**118**	**121,5**
weld to specimen corner	**275**	**273**	**276**
notch to specimen corner	**34**	**34**	**32**
specimen width	**284**	**282**	

3.2 Defect sizing

Defect sizing can be carried out in similar way as in the data evaluation of mechanised inspection. The results can reproduced reliably if the measured data fullfills following four quality factors:

1. Contact has been sufficient during inspection
2. The ultrasonic inspection technique used is properly selected
3. The calibration is performed in proper way (positioning, ultrasonic equipment, inspection volume, probeholder)
4. The operator controls that whole inspection volume is sufficiently covered in inspection.

Defect sizing is one of the most difficult tasks of the ultrasonic operator. If all measured data is stored e.g. the crack tip echoes can be easily detected. As well known the crack tip echo is sometimes not received from tight cracks and sometimes the crack tip echo is very clear. The following cases have been measured with BAT system and the advantages of evaluation made by the computer is clearly seen. The stored distances can be measured exactly, which is manually not always possible. The sound velocity can be changed which means that the wave mode can be changed and different wave modes in data can be analysed.

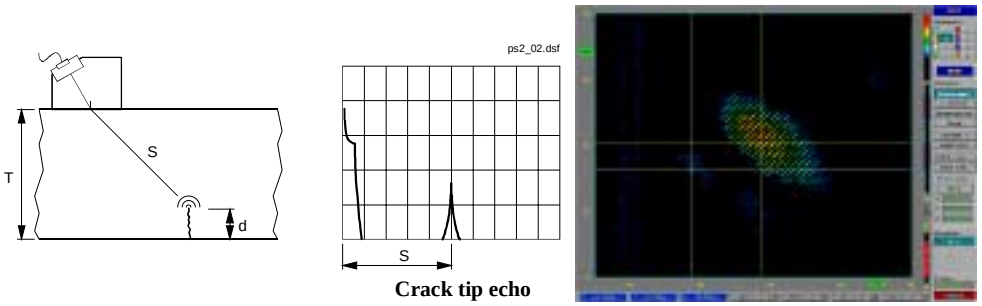

Figure 5. Inservice induced thermal fatigue crack in an austenitic block detected with 45°T 2 MHz composite probe.

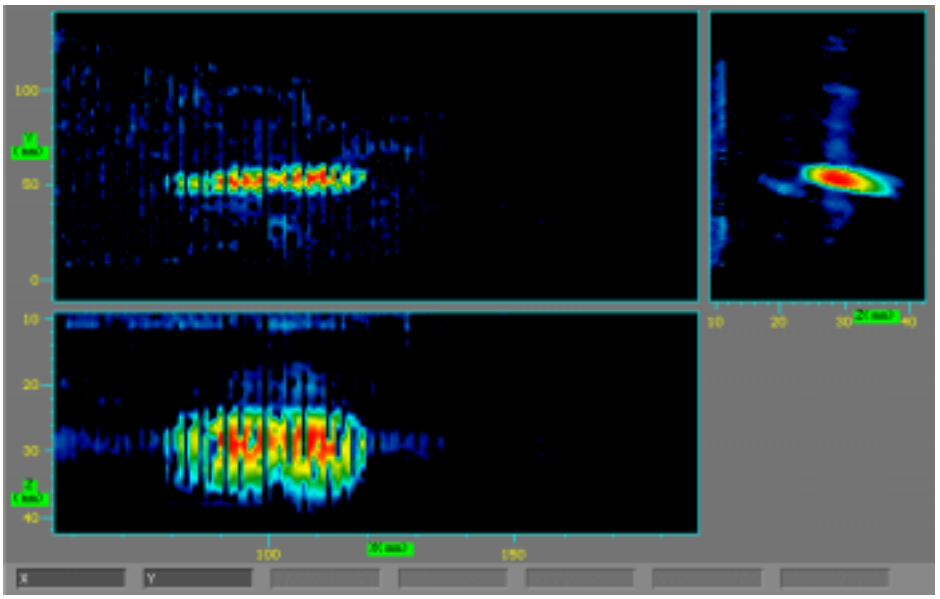

Figure 6. Artificial produced circumferential thermal fatigue crack in an austenitic block detected with 45°T 2 MHz composite probe.

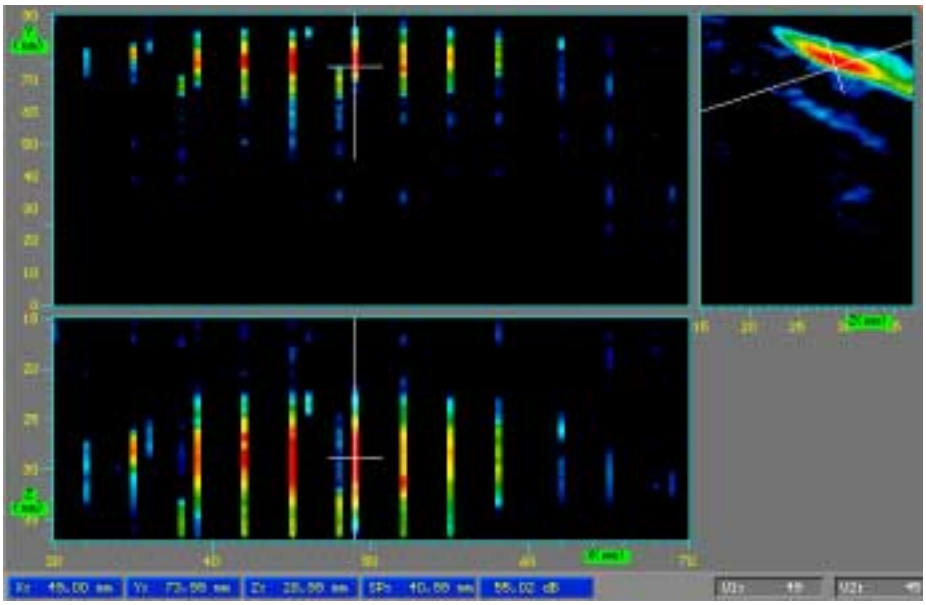

Figure 7. Artificial produced axial thermal fatigue crack in an austenitic block detected with 45°T 2 MHz composite probe.

In Figure 5 the simple principle of crack sizing with help of crack tip echo is shown. The size of a real in-service induced thermal fatigue crack was evaluated and the size (depth) was estimated to be. about 10 mm. In the highest spot the crack depth was 12 mm but this was not inside the evaluation area. In Figures 6 and 7 the ultrasonic evaluation results from artificial produced axial and circumferential fatigue cracks are shown. In these cases the sizes of cracks were evaluated to be from 6 to 8 mm.

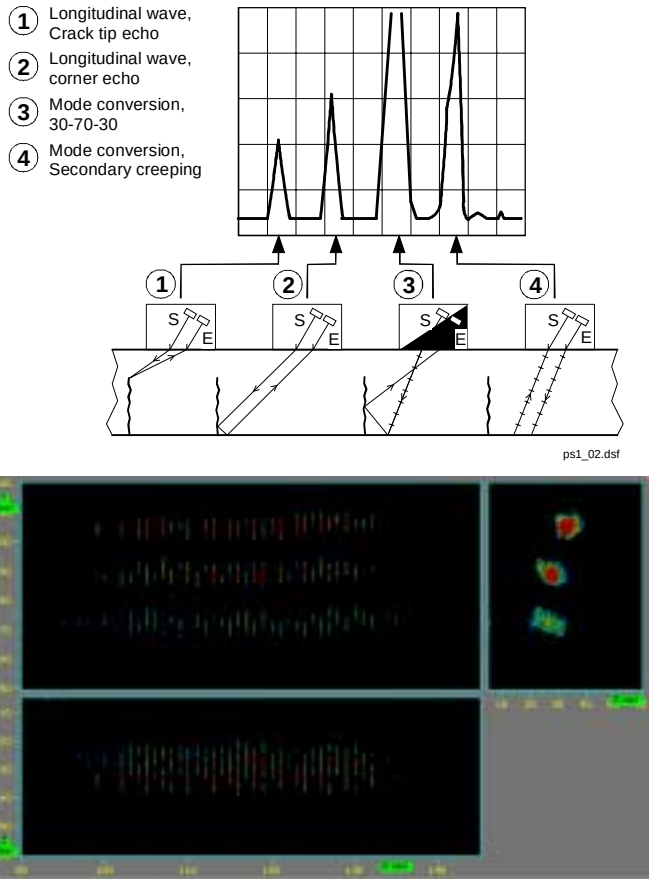

Figure 8. Artificial produced circumferential thermal fatigue crack in an austenitic block with ADEPT 60°L 5 MHz.

The evaluation of the crack can be performed with many different types of probes. In Figure 8 the special probe ADEPT 60 and the principle of detecting echoes from the crack is shown. The results of this probe are more difficult to evaluate than the results of normal angle probes. By using a PC-based system better tools for evaluation of complicated wave modes and echoes is available. In Figure 8 data measured with BAT system from a crack is shown. In the data echoes 1, 2 and 3 are seen.. The analysis of results of this type of probe needs on site more time than the simple analysis by PC. Other complicated probe types are mode conversion probes (for instance WSY) and SLIC-probes. In the analysis of results many wave modes have to be taken into account.

3.3 Thickness measurement

The BAT-system can be used also in very simple wall thickness measurement. The first application is designed for aerospace industry. When using normal incidence probe in thickness measurement the skew angle has no effect on ultrasonic result. This makes BAT system very applicable in thickness measurement. The system can handle several ultrasonic probes at the same time. This gives possibility to inspect more quickly and with high reliability.

4. Discussion and conclusions

The BAT system shows clear potential in defect detection, sizing and in thickness measurement. In manual inspection more tools in evaluation of defects are needed. BAT provides to manual scanning tools which are normally included only in mechanised systems. It can also complete the mechanised systems in cases where objects with difficult geometry have to be inspected.

BAT system will be improved in near future by measuring the skew angle of the probe and by applying better software in pipe inspections. The curvature of the pipe causes slight bending of the echo if it is long. This does not affect the sizing of defects but positioning will have an error of about 2−3 mm depending on the diameter of the pipe.

There are some disadvantages like the system is sensitive to any objects like extra cables between the emitter and receiver of the positioning system. These disadvantages will hopefully be at least partly avoided in the future.. After improving the software for pipe inspection semi-automatic system provides a good tool both for helping manual and mechanised inspections.

5. Acknowledgements

This presentation is prepared for a joint Finnish industry group in a in a project on structural operability and plant life management (RKK). The project funding by the National Technology Agency (Tekes), Teollisuuden Voima Oy (TVO), Fortum Power and Heat Oy, Fortum Nuclear Services Ltd., FEMData Oy, Neste Engineering Oy, Fortum Oil and Gas Ltd. is gratefully acknowledged. the discussions with Kari Hukkanen of TVO and Raimo Paussu of Fortum Power and Heat and other partners in the consortium have been of great help of planning and execution of this work.

Reference

1. Pitkänen, J., Särkiniemi, P., Kauppinen, P. and Jeskanen, H. Ultrasonic measurement of a thermal fatigue crack field manually and with simple handscanner. 7th European Conference on Non-Destructive Testing, Copenhagen 26–29 May, 1998. Pp. 746–750.

Load-case and -combination database

Heikki Raiko[1], Aarne Lipponen[2], Paul Smeekes[3] and Heli Talja[2]
[1]VTT Processes, Espoo, Finland
[2]VTT Industrial Systems, Espoo, Finland
[3]Teollisuuden Voima Oy (TVO), Olkiluoto, Finland

Abstract

The loading database is part of the pipeline analysis and monitoring system that will be used for nuclear power plant piping systems and connected equipment at two Finnish nuclear power plants. These plants are situated in Olkiluoto and operated by Teollisuuden Voima Oy (TVO). For a start the system will be used for class 1 piping systems only, but later on it may be extended to other systems where it is useful. The system will comprise a large set of process systems and components. Piping components, geometry, materials and systems are defined in an associated pipeline database [1]. Like the pipe-line database, also the load-database will have a combined alphanumerical and graphical user-interface to show the user what the actual state is and what changes are made. The database system runs on a PC using commercially available database software [3].

This paper outlines the contents of the loading database system, which is being developed by TVO and VTT to facilitate the condition monitoring, aging and thermal transient follow-up, load history bookkeeping, documentation for component load specifications and related analyses for class 1 piping.

Basic dimensioning and necessary checks are made according to design standards like the ASME Code. This code defines allowable stress/strain levels in applicable service limits and rules how to estimate the usage factor of the cyclic loads. Normally those standards are applied that were valid when designing the plant or component. When ordering new components, they have to be compatible with the rules valid at that moment. This is the practice, at least in Finland. This means that in one plant different acceptance systems may exist simultaneously. This makes it difficult to find the applicable load data at a time.

The load database is designed to:

1. Contain and document the actually valid design load specification for any component or system inclusive service limits
2. Act, as far as possible, as an input database to perform stress, flexibility, fatigue and/or crack analyses for the piping components or systems under consideration
3. Monitor and document the annual cumulative thermal transient events
4. Perform bookkeeping of the load-cases and -combinations that are valid at a time and contain the connection between old and new data
5. Give the structure for the result database where the significant results of analyses are stored.

Load-cases and -combinations are fully user configurable. In the present application either static or dynamic pressures, temperatures, weights, and forced displacements can be included as basic loads. These are included in the database or coupled as structured files in case of large data quantities. Presently, the database structure has been designed and is implemented. The items 1, part of item 2 and item 3 of the above list are implemented and test runs have been made for a piping system for at least part of the analysis types described under item 2. Most of the basic programming work will be finalized within one year. During the presentation the present status of the databases and program modules will be described.

1. Introduction

In the design analyses and safety assessment of nuclear power plant (NPP) components the loads are perhaps the most complicated input data to determine. The original design basis consists of a certain set of loads, which may also be applied in the case of component replacement. This set is formed by basic loads (load types or components), which then are combined and superimposed to combinations. Load combinations or operational events correspond to normal operation conditions, anticipated transients, incidents or accidents according to certain, conservative rules. The component replacement can also affect the loads on the system and often it must be demonstrated that the loads have not increased due to changes in the process or in the hardware. At the TVO

Olkiluoto plant, the loads also have been reassessed due to power uprate. So far, power uprate has been realized twice during the operational lifetime of the plant. The actual loads/events occurring at a plant may, on the other hand, differ significantly from the design load cases.

To keep track of all the data needed for piping analyses, loading events and to ensure that up-to-date information is easily accessible TVO has decided to organize it in a database system [1]. The loading database, which is part of this system, will contain as well design loads as information on actually occurred transients, preferably inclusive detailed information with regard to process parameters during the event.

The load database is aimed to be a practical tool for bookkeeping of documentation of the design load specification for any component or system comprised. Thus it can be utilized in the case of making specifications for component replacement. It also shall act as a data source to perform stress, flexibility, fatigue and/or crack sensitivity or crack growth analyses for the piping components or systems. In this context the connection to a general piping database is an essential feature. Further, the database shall serve as bookkeeping and reporting tool for the annual cumulative thermal transient events and the follow-up of the rate between cumulative events and specified design events.

2. Organization of the loads and load combinations at TVO

In the sections below the organization of the loads and load combinations as used at TVO is shortly described. This is necessary to understand the section on the database content and organization. As can be seen the present organization of the loads and load combinations, as was defined in the TVO plant modernizing project MFSAR (modernization of the FSAR), is based on the ASME design principles. In that project the loads and load combinations were updated, modernized and organized in such a way that subsequent computer aided engineering is made possible. Below parallels will be drawn between the ASME rules and the MFSAR project. Later on, in the database contents chapter, parallels will be drawn between the MFSAR project and the actual database, thus establishing the connection between the database and the ASME.

2.1 Design loads

According to the design practice, the design loading used in basic dimensioning shall be established on the highest pressure, temperature and coincidental design mechanical loads in operational conditions. Design loads for a mechanical NPP component or system is a set of simplified load cases and more complex load combinations that, in the plant design phase, are used for dimensioning and lifetime assessments. Basic dimensioning and necessary checks are made according to design standards like the ASME Code [2].

2.2 Basic load cases

The load specification system is described in Fig. 1. An important part of the basic loading definition is the definition of piping sections where identical loading conditions prevail. The piping sections are defined on the base of system flow diagrams, see Fig. 5.

According to the Code [2], at least the following load types have to be taken into account when designing a component:

- Internal and external pressure;
- Impact loads, including rapidly fluctuating pressures;
- Weight of component and normal contents under operating or testing condition, including additional pressure due to static and dynamic head of liquids;
- Superimposed loads such as other components, operating equipment, insulation, corrosion resistant or erosion resistant linings, and piping;
- Wind loads, snow loads, vibration, and earthquake loads where specified;
- Reaction of supporting lugs, rings, saddles, or other type of supports;
- Temperature effects.

For many of the above mentioned loads a separate load analysis has to be performed in order to determine the numerical load data that can be applied to the piping system finite element model.

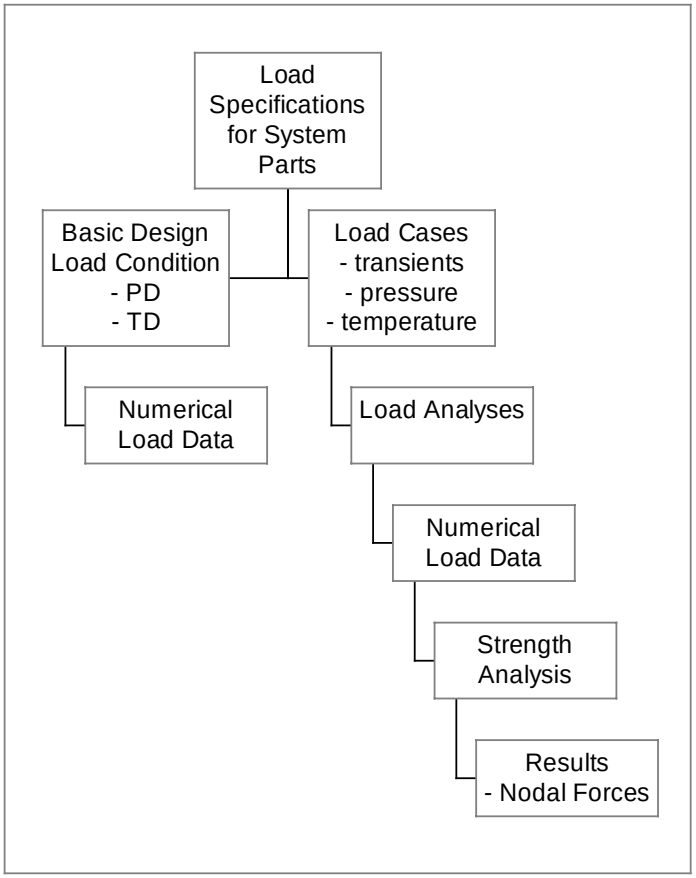

Figure 1. Load specifications for piping sections and system parts, the hierarchy of load cases, load analyses, load data, strength analysis, and nodal results from the strength analysis.

2.3 Plant events and load combinations

Definitions of coincidental load combinations for each system section are specified for all designed plant events. The load combination has an event identifier and it is defined as a sum of different loads. Each load combination belongs to certain service limit (A-D) and the service limit specifies the applicable stress limit rule according to [2]. Description of how the load combination results are derived from plant events is given in Fig. 2.

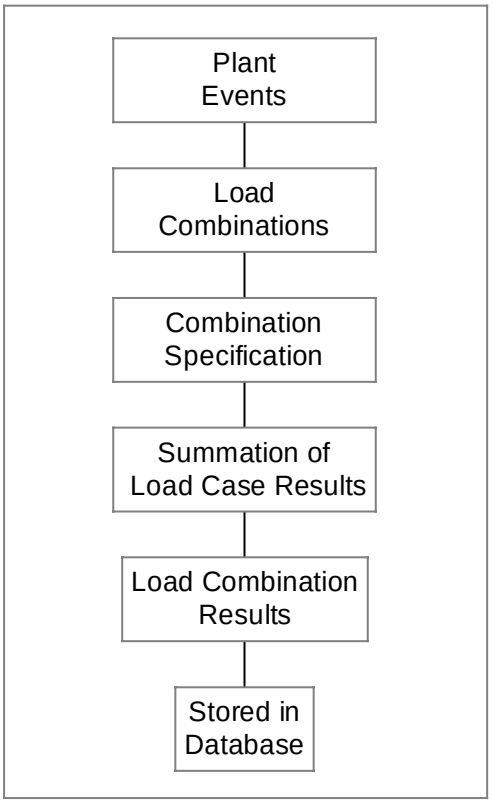

Figure 2. Load combinations are derived from plant event descriptions. The effect of the load combination is summed from the elementary results of the specified load case analyses, which results are stored in the database.

2.4 Cyclic loading

The load combinations for service limit A and B have a specified number of cycles that is specified in the design phase. The fatigue lifetime of a component is assessed on the base of these cycles. Level C and D loads are not included in fatigue assessment due to the very low frequency of these events. Instead, in the event of level C or D incidents, inspection, testing and possible repair in plant systems and a possible shutdown is required.

2.5 Plant operational history

The design lifetime of the plant has been assessed by making a cumulative fatigue assessment on the base of the specified number of the designed plant events. The actual cumulative usage factor can be calculated for any component or part of system at any time on the base of actual stored operational history of the plant. Accordingly, the operational history can be followed by collecting the operational data and storing it in chronological sequence in the database. Figs 3 and 4 give the sequence for assessing design cumulative usage factor and actual cumulative usage factor.

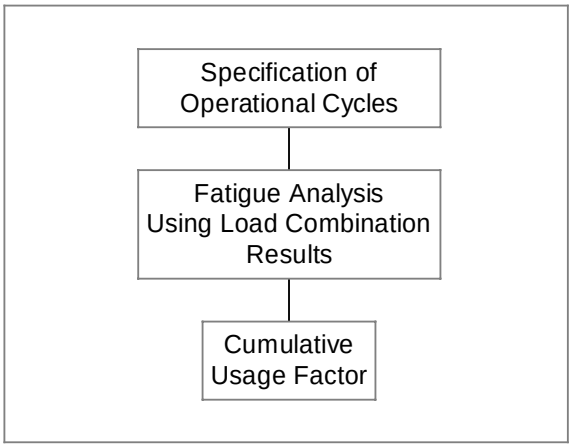

Figure 3. Assessing of a design usage factor.

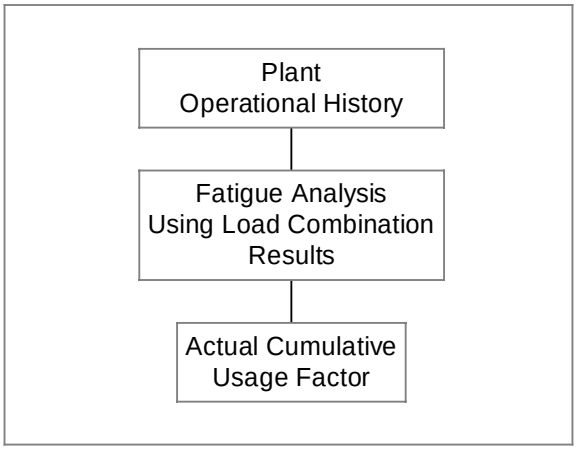

Figure 4. Assessing of an actual usage factor.

3. Database contents

3.1 General properties

The system design load database contains the following information in applicable format: definition of piping sections, load cases, design base loads, coincidental load combinations and their area of influence and data related to cyclic loads. A reference to the applicable level of the service limit of the loading event is also given. Below these items are described in more detail. Some typical examples of loads, load cases and plant events are listed in Table 1.

Table 1. Examples load types, Table 1a, load cases, Table 1b, and load combinations (events), Table 1c.

Load types	**Load cases**	**Load combination (events)**
PRESSURE	Design pressure (PD)	Basic dimensioning design condition (01)
TEMPERATURE	Design temperature (TD)	Normal operation (03a)
FLOW (mass)	Dead weight (DW)	Anticipated thermal transients (03b)
FLOW (velocity)	Operating pressure (PO)	Reactor overfilling (04)
DISPLACEMENT	Operating temperature (TO)	Periodic testing of pressure relief system (07a)
VELOCITY	Temperature transients (TT_A, TT_B) (A = operational, B = anticipated)	Actuation of pressure relief system (08a)
ACCELERATION	Steam hammer from closing steam line isolation valve (SH)	Pump transients (09a), water hammer (09b), steam hammer (09)
FORCE (F_x, F_y, F_z)	Water hammer from pump stop transient (WH/PT)	Pipe break outside containment (11)
MOMENT (M_x, M_y, M_z)	Water hammer from steam condensation during pump start (WH/SC)	Pipe break inside containment (16)
	Reaction force from pipe break outside containment (RF)	Condensation pool phenomenon after a LOCA (13, 14)

3.2 Definition of piping sections and system parts

An important part of the loading definition is the definition of piping sections where identical loading conditions prevail. Accordingly, the database contains definitions of system parts, for which the definition of load combinations is identical. A system part consists of one or, in most cases, more piping sections. A systematic naming procedure is applied throughout the database. The load specification for each piping section is separately defined and included in the database. And, respectively, the load combinations are defined and included in the database. An example of the piping section definition in a flow diagram is shown in Fig. 5.

The definition of piping sections and system parts is based on the use of the separate piping geometry database. This contains the piping geometry, welds, supports and piping components including the piping sectional properties in numerical form. Thus the actual geometry and the load and load combination areas are connected to each other.

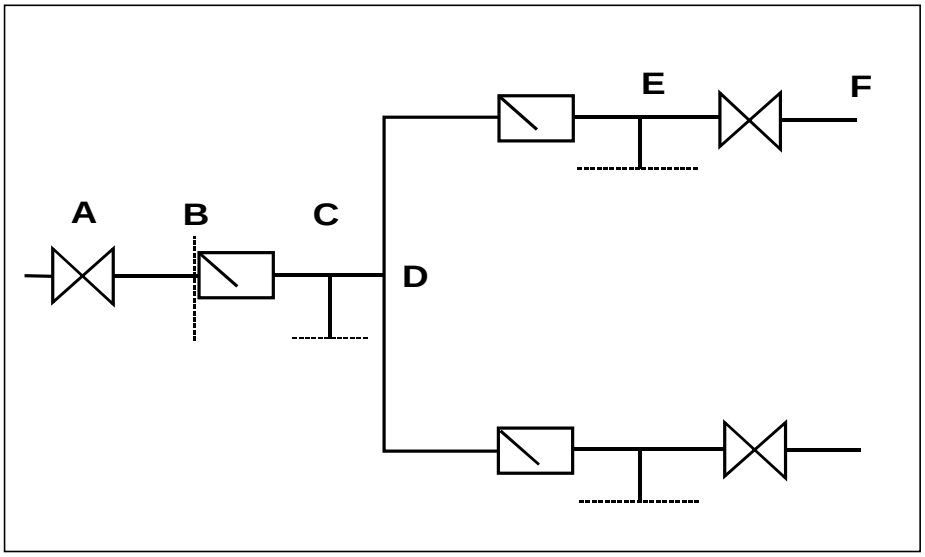

Figure 5. Example of piping section definitions, sections A–B, B–C, etc.

3.3 Definition of loads for piping sections

All the loads are identified with a string and the related numerical information is stored in the database in one or more alternatives of the following:

- Numerical value of a constant load
- Time history of a variable function load
- Definition of a dynamic response spectra (acceleration, frequency, damping)
- Reference to a separate file of numerical load definition.

Examples of load types and cases are given in Tables 1a and 1b above. A load definition in the database is accompanied by a reference to a load descriptive document. The reference documents are archived in a separate document database in TVO. An example of a visualization of time-dependent load definition in the database is shown in Fig. 6, below.

Figure 6. Example of visualization of the pressure-temperature load in the database.

3.4 Load combinations

Load combinations are derived from plant operational events. An operational event is a chain of incidents in the NPP, which all cause different loading consequences in different system parts. In addition, during an operational event the systems interact in many ways in loading sense. Some interactions are direct and some are consequential. And some are coincident, some random and some are delayed (non-coincident). In loading database, the load combinations for system parts are defined as a direct or root-sum-square value sum expression of the predefined load cases, depending on the type of nature or origin of the load case.

Some typical examples of plant events in BWR-type NPP are given in Table 1c. Defined load combination can be grouped in following categories according to design rules:

- Definition of design pressure and design temperature of the system part. Each load has an abbreviation for easier identification (for ex. system xx load case A01 = PD + DW, design condition, whereas A is the designation of the system part)
- Definition of operation condition loads (service limit A) of the system part, operation pressure, operation temperature, operational mechanical loads (for ex. system yy load case B03a = PO + DW + TTA + D/B, service limit A, whereas B is the designation of the system part)
- Definition of anticipated operational transient loads (service limit B) of the system part, specified time histories for pressure, temperature, flow and mechanical loads, global vibration (for ex. system yy load case A09a = PO + DW + yyWH/PT & B09a = 0, service limit B, whereas A and B are the designation of the system part)
- Definition of minor accident loads (service limit C) of the system part, specified time histories for pressure, temperature, flow and mechanical loads, global vibration (for ex. system xx load case A09b = 0 & B09b = PO + DW + yyWH/SC, service limit C, whereas A and B are the designation of the system part)
- Definition of design base accident and hypothetical accident loads (service limit D) of the system part, specified time histories for pressure, temperature, flow and mechanical loads, global vibration.

3.5 Cyclic loading

The number of design operational cycles for plant events is stored in the database and the number can be used in making fatigue analyses and lifetime estimates. The number of design cycles is used as a reference when making the annual summary report of the cumulated annual events and a comparison to the design thermal and pressure transient events for lifetime follow-up. An example of definition of a complete thermal transient cycle is shown in Fig. 7, below.

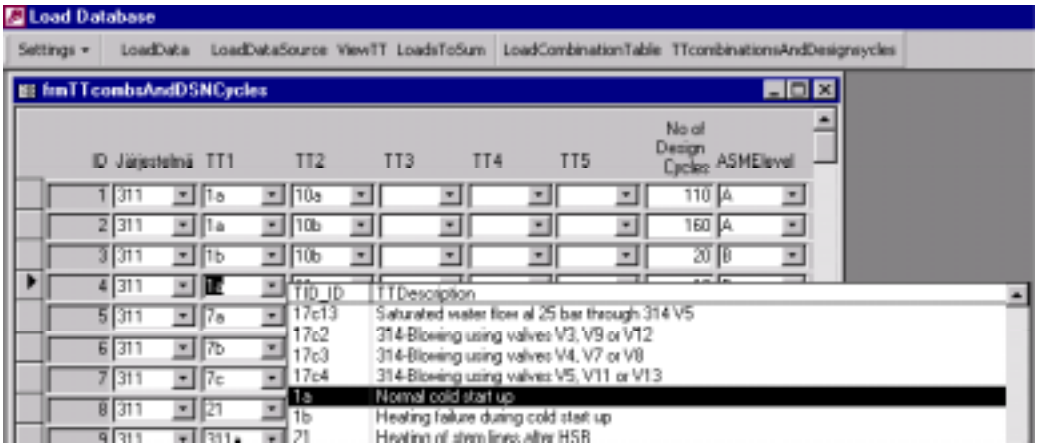

Figure 7. Definition of thermal transient cycle in the database.

3.6 Plant operational history

The NPP operational events must be monitored and annually reported to the licensing authority. In the report, the cumulative number of each event type will be compared to the designed number of the respective event. This kind of monitoring is required to ensure that the designed number of cyclic load transients is not exceeded. The bookkeeping of actual plant events and cyclic loads in chronological sequence including registered associated process parameters and the instant of time of the event will in the future be made using the load database system.

3.7 Results for load cases

The loading database gives a structure also for the associated result database where the significant FE analysis results of load, stress and fatigue analyses are stored for post processing purposes according to corresponding logic. This system is also partly described above in Figs. 1 to 4.

4. Database operations

4.1 Storing of data

The loading database shall be able to keep track of the following:

- Definition of load data for the piping sections and system parts for the different system parts affected by the load
- The load cases for piping sections and load combinations for system parts that are valid at a time and the connection between old and new load data
- The number of design operational cycles for plant events
- The bookkeeping of actual plant events and cyclic loads in chronological sequence including registered associated process parameters and the instant of time of the event
- Numerical data from load analyses
- Numerical data from strength analyses
- Numerical data from load combination analyses
- Numerical data from fatigue analyses.

In addition to storing the data, the database system can visualize the data in the form of data graphs, as shown in Fig. 6, or in the form of loading in a piping isometric drawing. The visualizing system is an important tool for validation of the manually entered data.

4.2 Reporting capabilities

The database system shall be able to make the following operations:

- Collect the loading data from the stored database for a piping system analysis and formulate it in an input-file for a piping analysis program
- Make a complete design load specification document for a specific piping component, line or system to be used, for instance, as load specification for piping component renewal
- Make an annual summary report of the accumulated annual events and a comparison to the design thermal and pressure transient events. This is to be used for lifetime monitoring.

To make safety, fitness and lifetime-related assessments for nuclear power plant components the necessary input data has to be reliable and up-to-date and it often has to be collected in a very short time. This might, for instance, be to assess the need for component repair during the annual outage, or for a temporary license application for continued operation for a damaged component.

5. Summary

This paper outlines the contents of the loading database system, which is being developed by TVO and VTT to facilitate the condition monitoring, aging and thermal transient follow-up, load history bookkeeping, documentation for component load specifications and related analyses for class 1 piping. The loading database is operated in conjunction with other databases, namely, the piping geometry database, the reference report database, and the material database. All the analyses needed for assessments are made outside the database system using normal commercially available computer codes for load, stress, deformation, dynamics, or fatigue analysis. However, the results of the mentioned analyses can be stored in the data-base system for combination and archiving purposes. The database system is run on a PC using commercially available data-base software.

Acknowledgements

This presentation is prepared for a joint Finnish industry group in a project on Structural operability and plant life management (RKK). The project funding by the National Technology Agency (Tekes), Teollisuuden Voima Oy (TVO), Fortum Power and Heat Oy, Fortum Nuclear Services Ltd., FEMdata Oy, Neste Engineering Oy, Fortum Oil and Gas Ltd. is gratefully acknowledged.

References

1. Smeekes, P., Lipponen, A., Raiko, H. and Talja, H. The TVO Pipeline Analysis and Monitoring System. SMiRT 16, Paper 1868, 2001.

2. ASME Boiler and Pressure Vessel Code, Section III, Nuclear Power Plant Components, Division 1, Subsection NB, Class 1 Components.

3. Microsoft® Access 2000, Relational Database Management System for Windows.

Numerical simulation of piping vibrations using an updated FE model

Heikki Haapaniemi[1], Arja Saarenheimo[1], Paul Smeekes[2] and Heli Talja[1]
[1]VTT Industrial Systems, Espoo, Finland
[2]Teollisuuden Voima Oy, Olkiluoto, Finland

Abstract

Traditional design and condition monitoring of piping is mainly based on postulated events and on the application of allowable vibration levels. This approach gives only indirect information on the loading at the critical locations and generally leads to over conservative assessments. It is essential that developing piping failures can be anticipated and/or monitored and that any repair work is carefully planned ahead and carried out during regular outages. In an ongoing project a practical method is being developed to monitor the condition and remaining lifetime of process piping. This method combines both measurements – using a minimum number of fixed continuous measurements – and an adequate computational model.

Relatively simple piping in a NPP was chosen as the first pilot case. Measured modal shapes of the structure were excited using an impact hammer and a shaker. Results from experimental modal analysis were used in finite element (FE) model validation and updating process carried out using the FEMtools [1] code. This paper outlines the project and describes the main experiences and results of the model updating work.

Nomenclature

EMA	Experimental modal analysis
$\{\psi_a\}$	Analytical mode shape vector
$\{\psi_e\}$	Measured mode shape vector
T	Superscript: Transpose of vector

H_{ij}	Response function, which expresses the response at DOF i if excitation is at DOF j
ω	Frequency
r	Subscript: mode number
N	Number of modes
ψ_{ir}	Eigenvector value at DOF i corresponding to the r^{th} mode
ψ_{jr}	Eigenvector value at DOF j corresponding to the r^{th} mode
ω_r	r^{th} natural frequency
ζ_r	Modal damping ratio for the r^{th} mode.

1. Introduction

Condition monitoring and damage detection by means of monitoring modal parameters is based on the principle, that changes in modes are sensitive indicators of changes in the physical integrity of any mechanical structure [2]. Vibration testing offers an opportunity for different inspection techniques that may be able to detect structural failures and local structural damages, which can e.g. effect the stress fields of the structure.

Normally condition monitoring and damage detection, when done by monitoring modal parameters such as eigenfrequencies, mode shapes and damping ratio, has been based on comparison of results from experimental modal analysis of undamaged structure and damaged structure. These measurements can be made either with artificial excitation, e.g. with shakers or impact impulses or with ambient excitation in operational conditions [2–4].

Instead of using the modal properties of an undamaged structure as a reference baseline for comparison, modal properties of an updated FE model can also be used as a baseline. A verified, validated and usable mathematical model is the best knowledge base for the system under investigation [5]. In this work the aim was to create such an updated FE model which could later be used as a reference baseline and also to learn about appropriate modelling techniques and identify the difficulties concerning modelling of a pipeline and its components.

In the FE model updating phase a somewhat larger amount of measurements will probably be necessary than is possible in normal condition monitoring. Probably

several iteration cycles are needed to come up to an adequately working FE model. This process is described in Fig. 1.

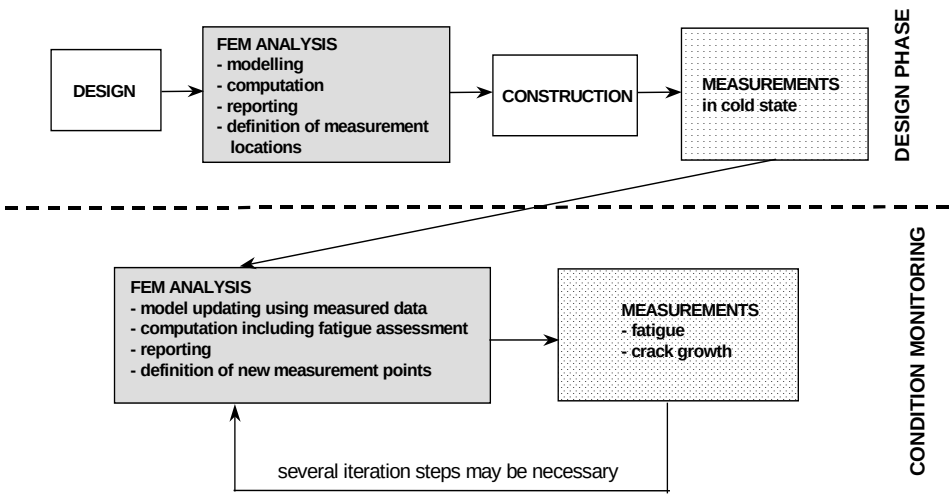

Figure 1. The approach to come to an adequate model to monitor the vibration behaviour of a piping system, starting from the piping design phase [6].

2. General description of the structure

The first pilot system, part of the auxiliary feed water system piping at the Olkiluoto NPP (OL1) was chosen based upon the following requirements:

- Reasonable in size
- Cold in operation condition, no temperature effects nor insulation
- Easy to access and measure in both operational and standstill condition (modal analysis),
- A clearly defined excitation (reciprocating pump).

During normal operation the auxiliary feed water system is not in use except for the periodically performed tests lasting for five minutes each month. The expected – and measured – vibration amplitudes were so small that no integrity problems are anticipated due to this vibration.

The part of the piping system being under consideration is located on the outside of the containment between the containment penetration and the auxiliary feed water system pumps. The pumps are 3 piston plunger pumps running at a frequency of 4 Hz. The length of the modelled part of the pipeline is about 56 meters including two major branches attached to it. The length of the measured part of the pipeline is about 44 meters. There are also 17 supports and three different actuators (valves or restrictors) in the measured part of the pipeline. Support locations and general description of the pipeline can be seen in Fig. 2.

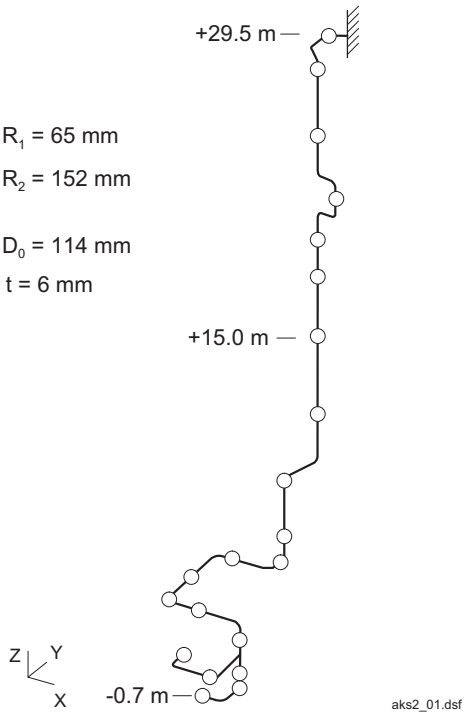

Figure 2. FE model and support locations.

This pipeline is made from DN 100 stainless steel pipe with nominal diameter of 114.2 mm and wall thickness of 6.02 mm. The design pressure, which is effective during the use of the pump, is 90 bar and the design temperature is 100^{o}C. However, the piping is filled with water that does not exceed the room temperature during any anticipated transient. This means that the piping is not insulated and that temperature is not an issue.

There were basically four different types of piping supports, which were modified depending on their position and/or purpose. The purpose of supports was either to act as a support in all loading conditions or act as a support in case of a piping or neighbouring support failure. In latter case, the design drawings usually indicated a gap between pipe and support structure. During walkdown inspections it was found out, that visible gaps seldom existed between pipe and support structure.

3. Measurements

Modal testing was done using both impact hammer [7] and shaker excitation [8], based upon 29 measurement locations and 76 measured DOFs. These measurement locations are shown in Fig. 3 along with the FE model. Modal testing was performed to experimentally characterise the dynamic behaviour of the piping. The mode shapes and associated frequencies were determined both during operation and in standstill condition. Thus, both operational and natural mode shapes were obtained.

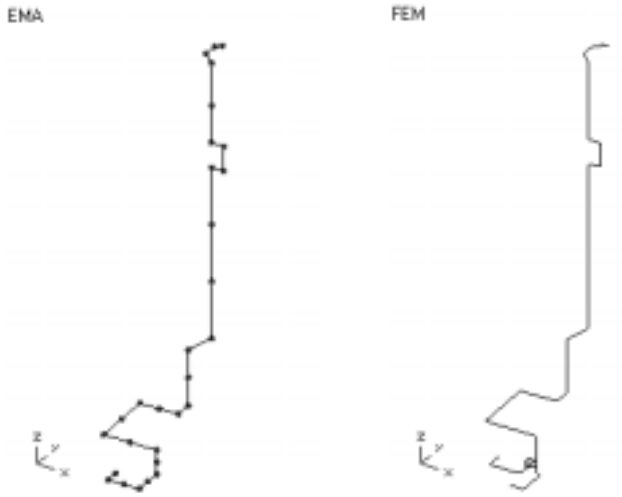

Figure 3. Measurement points (left) and the FE model (right).

3.1 Natural mode shapes

The natural mode shapes were excited, in case of impact test, with hammer impacts causing short time impulses with more or less uniform energy input over the significant frequency band [9]. The mode shapes themselves were then recorded but the data immediately after the impulses was neglected. The data, after the direct influence of the excitation has become negligible, were used to determine the modes and associated frequencies.

In case of shaker excitation a random noise signal was used to control the shaker output. Mode shapes were calculated with the Rational-Fraction-Polynomial-curve fitting method [8]. All measured FRFs were used together during this so-called global curve fitting.

Most significant (i.e. lowest) eigenfrequencies from both impact and shaker measurements are listed in Table 1, excluding the lowest measured eigen-freguency (19.0 Hz) from impact tests due to measurement errors connected to that mode shape.

Table 1. The most significant eigenfrequencies from impact and shaker measurements.

Impact (Hz)	27.1	32.4	38.4	40.9	
Shaker (Hz)	27.2	32.7	39.2	40.8	42.3
Impact (Hz)	56.5		71.6	77.6	82.0
Shaker (Hz)	56.4	57.7	71.2		81.2

The mode shapes with hammer impact measurements and with the shaker excitations were quite close to each other and it seemed that in this case results were not dependent of the type of excitation (impact or shaker) used. It should also be noted that some of the deviation in the results could be explained by the fact that the water height in the piping was not necessarily the same during these tests.

4. FE models

The FE models were originally generated with FPIPE [10] program and the models were translated into ABAQUS [11], which was then used as a solver. These analyses were conducted as a MSc. thesis [12].

The first FE model, referred here as Case 1, was modelled according to design drawings. This would also be the normal approach in the design phase and this model would also be used in first pretest analysis when the first measurements are planned. Of course, it was clear from the beginning that there are always differences between the actual structure and the ideal design drawing.

Properties of the FE model were varied in order to find out how different modifications affect the behavior of the model. Because it was known on beforehand that the critical aspect was to find suitable stiffness values for the piping supports, mainly their spring constants were modified. The stiffness values for the supports were estimated by using very simple FE models loaded by unit forces and moments. Also, more relevant information concerning the actual piping geometry was obtained by direct measurement and so-called walk down inspections made to the piping. This information was then applied in further analysis based on updated input data (Case 2 and Case 3).

The FE model used in the ABAQUS [11] analyses, main dimensions of the pipe line and support locations are shown in Fig. 2. The model consists of 180 elbow and pipe elements, 3 beam elements and 123 spring elements. Both pipe bends and adjacent straight segments are modeled with ELBOW31 elements and the bends were modeled with 2 elements. There are 5 integration points through the wall thickness and 20 integration points around the circumference of the section; six ovalization modes are used. The middle segments of long, straight pipe runs are modeled with PIPE31 type elements. To join the pipe segments modeled with different element types, warping of the ELBOW31 elements is prohibited at the nodes connecting the ELBOW31 elements to the PIPE31 elements. 1-dimensional spring elements are used in the appropriate directions to model the supports. Six SPRING1 elements with different stiffness values (one for each degree of freedom) are needed to describe one pipe support. One B31 element was needed to model an extension attached to the pipeline and two B31 elements were needed to model beam connecting two different pipe segments.

The locations and stiffness values of the supports as well as the pipe wall thickness values were modified according to inspection and measurements in Cases 2 and 3. In Cases 1 and 2 the pipe is assumed to be completely filled with water whereas in Case 3 the pipe is assumed to be filled only up to +15.00 m (see Fig. 2). This is done because, if the system has a height of more than 10 meters and the isolation valves at the top of the piping are perfectly tight, one may assume that there will be a vacuum in the upper part of the piping.

The material properties used in Cases 1–3 are listed in Table 2 and general descriptions of Cases 1–3 are listed in Table 3.

Table 2. Material properties.

Property	Case 1–3
Young's modulus	206 GPa
Steel density	7850 kg/m^3
Water density	1000 kg/m^3
Poisson's ratio	0.3
Temperature	20°C

Table 3. Analysed basic cases.

Property	Case 1	Case 2	Case 3
Supports	design documents	measured	measured
Supports	simple FE models	simple FE[1] models	simple FE[1] models
Gaps	low stiffness[1]	updated spring[2] stiffness	updated spring[2] stiffness
Wall thickness	nominal	measured	measured
Water level	full	full	level +15 m

1) Gaps in supports according to design documents are described using spring elements with low stiffness value.

2) Observed gaps in supports are described using spring elements with low stiffness value.

5. Correlation analysis between original FE models and experimental data

In order to validate the FE models, their correlation against experimental results needs to be evaluated and their quality must be reviewed numerically. Also, if results of correlation analysis are not satisfactory models must be modified and updated. Prior to any updating correct mode pairs must be identified, which can be a very problematic task.

The correlation was evaluated by comparing results from an impact hammer test [7] against the results from FE analysis. These analyses were conducted as a part of MSc. thesis [12].

As a first task the correlation between experimental and numerical results was evaluated in terms of modal assurance criterion (MAC) values and MAC matrices. In the beginning it was decided to filter terms with a value less than 15% of maximum displacement from experimental eigenvectors and also to use 5% double frequency tolerance. Filtering focuses the correlation analysis to areas where major modal displacements take place and double frequency tolerance enables combining frequencies within this tolerance limit. Correlation evaluations were mainly performed with the FEMtools [1] code. The following equation is used for evaluating MAC values:

$$MAC(\psi_a, \psi_e) = \frac{\left|\left(\{\psi_a\}^T \{\psi_e\}\right)\right|^2}{\left(\{\psi_a\}^T \{\psi_a\}\right)\left(\{\psi_e\}^T \{\psi_e\}\right)} \quad (1)$$

In general higher MAC value indicates better correlation between modes, although it is difficult to provide precise values that the MAC should take in order to guarantee good results. Ewins [13] has suggested following interpretation for the MAC values value less than 5% indicates uncorrelated mode shapes and value higher than 90% correlated mode shapes. Another estimate provided by Ingemansson Education [14] in their course material is that the MAC value below 50 % indicates poor correlation and values higher or equal as 70% good correlation. This latter suggestion may also be reasonable in case of piping systems, where it may be difficult to define the actual measurement

locations and directions accurately and where distances between measurement locations may be large.

Here the mode pair selection is based on visual inspection of mode shapes, MAC values and frequency errors. Usually the mode pairing is based on maximising MAC values and minimising frequency errors but in some cases this is not a feasible approach because it may cause mode pairing problems as described in reference [15]. Note, that experimental mode 1 is left out of all comparisons due to a measurement error in it's mode shape. Mode pairs for Cases 1–3 are presented in Tables 4–6.

Table 4. Mode pairs for Case 1. The average frequency error and MAC value are presented in the last line.

	Case 1		EMA			
Pair	Mode	[Hz]	Mode	[Hz]	Err (%)	MAC
1	18	25.15	2	27.13	–7.28	90.8
2	31	43.27	3	32.38	33.66	47.9
3	37	53.32	4	38.38	38.93	83.1
4	45	60.05	5	40.88	46.91	75.9
5	39	54.77	6	56.50	–3.07	41.1
6	43	57.76	7	71.63	–19.35	96.8
7	56	80.57	8	77.64	3.78	87.1
8	54	76.44	9	82.00	–6.79	53.9
		Average			20.0	72.1

From Table 4 it can be seen that even if there are some acceptable mode pairs like pair 2 and 8 this model is not acceptable and it needs further refinement. This was not a surprise because the model used in Case 1 was based solely on design drawings, which were not always as accurate as hoped. During visual inspection of the pipeline and measurement of the support locations it was found out that the actual support locations differed sometimes significantly from locations suggested by design drawings. Also some of the supports have been altered from original design drawing. So it is extremely important, that design drawings used during the modelling phase are correct and up to date.

From the results presented in Tables 4–6 it is easy to conclude that both Case 2 and Case 3 have an improved situation over the original Case 1. Generally, results are better although in some mode pairs significant trade off has occurred between frequency errors and MAC values. Especially the largest frequency errors are reduced and the lowest MAC values improved while the highest MAC values have slightly deteriorated due to the trade off mentioned earlier.

In view of these results it is still somewhat unclear which one of the models, Case 2 or Case 3, would eventually provide the best possible base for further model updating. Also, it is impossible to determine with any certainty the actual water level in the piping from these results.

The selection to use Case 3 in model updating is based mainly on two factors:

1) knowledge that it is not likely that the piping is completely filled with water and
2) on engineering judgement based on marginally better correlation provided by Case 3.

Table 5. Mode pairs for Case 2.

	Case 2		EMA			
Pair	Mode	[Hz]	Mode	[Hz]	Err (%)	MAC
1	17	26.26	2	27.13	–3.17	90.4
2	25	37.95	3	32.38	17.21	32.1
3	29	43.05	4	38.38	12.17	56.8
4	31	44.48	5	40.88	8.81	83.5
5	38	54.92	6	56.5	–2.79	66.1
6	42	57.35	7	71.63	–19.93	94.5
7	44	61.66	8	77.64	–20.57	81.2
8	49	68.97	9	82	–15.89	72.1
Average					12.6	72.1

Table 6. Mode pairs for Case 3.

	Case 3		EMA			
Pair	Mode	[Hz]	Mode	[Hz]	Err (%)	MAC
1	15	25.21	2	27.13	–7.05	90.4
2	16	26.26	3	32.38	–18.88	57.5
3	28	43.68	4	38.38	13.82	56.8
4	30	44.48	5	40.88	8.81	83.5
5	36	54.65	6	56.5	–3.27	67.3
6	40	58.73	7	71.63	–18	94.5
7	60	94.25	8	77.64	21.4	84.3
8	56	86.14	9	82	5.05	71.9
		Average			12.0	75.8

6. Results from model updating

The Case 3 was selected as base model for the updating process and the main focus was concentrated to piping supports which were known as the most uncertain and ambiguous part of the pipeline. The updated version of Case 3 is referred as Case 4. All translational support spring constants were selected to be alterable parameters and experimental frequencies from 2 to 9 as well as corresponding modes were selected to act as responses. Later also the Young's modulus was also chosen as a parameter to be modified in order to improve the updating results.

So-called automated model updating was in this case impossible due to incorrect stiffness matrix, caused by use of the SPRING elements. This caused some serious difficulties to the updating procedure, which could be described as a loop, where certain steps were performed as follows:

(i) Importing of the ABAQUS [11] results into the FEMtools [1].
(ii) Performing correlation analysis and mode pairing in the FEMtools [1].
(iii) Sensitivity and updating analysis performed by FEMtools [1].

(iv) Re-editing of the original ABAQUS [11] input with the modifications suggested in previous step.
(v) Re-run of updated input in the ABAQUS [11].

Due to the incorrect stiffness matrix this loop was required to run several times and in order to avoid instability during the updating analysis the FEMtools [1] was allowed to make only small changes to the updating parameters.

Main changes caused by the updating analysis were in the stiffness of the translational spring supports, which were increased in some cases several hundred percent. Also the Young's modulus was increased in the lower (below level +15.00) part of the structure from 206 GPa to 210 GPa.

The mode pairing table of updated model Case 4 and experimental results based on 15 % filtering and 5 % double frequency tolerance can be seen Table 7. This table indicates improvement in the frequency correlation in general and also slight improvement in the lowest MAC values (mode pairs 2 and 3) over the situation with Case 3 (see Table 6). If mode pairs in Tables 6 and 7 are compared it can noticed that there has been some trade-off between frequency error and MAC values in pairs with high MAC values in Case 3 (Table 6).

Table 7. Mode pairs for Case 4.

	Case 4		EMA			
Pair	Mode	[Hz]	Mode	[Hz]	Err (%)	MAC
1	14	25.31	2	27.13	–6.7	88
2	19	30.11	3	32.38	–6.98	61.3
3	25	43.46	4	38.38	13.25	58.1
4	27	44.78	5	40.88	9.55	80.7
5	37	56.33	6	56.5	–0.31	54.8
6	48	74.9	7	71.63	4.57	88.8
7	54	83.72	8	77.64	7.83	86
8	52	80.59	9	82	–1.72	71.2
		Average			6.4	73.6

6.1 Introducing damping

In order to evaluate possible effects caused by damping following procedure was performed:

(i) Analytical FRFs were synthesised from natural frequencies and corresponding mode shapes obtained from FE model used in Case 4 with the FEMtools [1] code. Here modal damping model with 1.5 % modal damping ratio was used and the FRF synthesis was performed according to following equation:

$$H_{ij}(\omega) = -\omega^2 \sum_{r=1}^{N} \frac{\psi_{ir}\,\psi_{jr}}{\omega_r^2 - \omega^2 + 2\,i\omega\,\omega_r\zeta_r} \tag{2}$$

(ii) Resulting FRFs were imported into I-DEAS Test [16] software was used to perform modal analysis to the analytical FRFs obtained from previous step. This new model with damping is referred as Case 5.

(iii) Resulting natural frequencies and corresponding mode shapes were imported in to the FEMtools [1] for new correlation analysis.

The FRF synthesis was made by using three excitation co-ordinates (all three directions x, y and z were used) and by using all nodes of the FE modes as response co-ordinates. Modal analysis was performed with I-DEAS Test [16] by using so-called polyreference technique for extraction of the modal parameters (natural frequencies, damping and residue) and corresponding mode shapes were extracted with the frequency polyreference technique. Both techniques can be found summarised in I-DEAS Test [16]: Theory manual.

The resulting mode pairs for the new model, referred as Case 5, is presented in Table 8. Also here 15% filtering was used and 1.85% was used as a double frequency tolerance for mode pairs 1–5 and 4% for mode pairs 5–8.

Table 8. Mode pairs for Case 5.

	Case 5		EMA			
Pair	Mode	[Hz]	Mode	[Hz]	Err (%)	MAC
1	11	24.71	2	27.13	–8.9	84.3
2	15	30.11	3	32.38	–6.98	74
3	19	44.6	4	38.38	16.23	58.4
4	21	46.16	5	40.88	12.92	90.1
5	26	56.33	6	56.5	–0.31	69.6
6	34	74.9	7	71.63	4.57	95.7
7	36	78.21	8	77.64	0.74	83.1
8	38	80.59	9	82	–1.72	74.2
		Average			6.5	78.7

The frequency error is presented in Fig. 4 in terms of a 45° line where in the ideal situation all markers indicating mode pairs should lie on this line. These results indicate better frequency correlation for the updated Cases 4 and 5 than for the original Cases 1, 2 and 3. The Case 4 produces best results in mode pairs 2, 5, 6 and 8 along with Case 5. In mode pair 1 there is very little difference between different cases. In mode pairs 3 and 4 the best results is achieved with Cases 2, 4 and 5. Cases 3 and 4 gives the best results for mode pair 4 and for mode pair 7 the best result is achieved with Case 5.

Both the actual frequency errors for all mode pairs in Cases 1–5 and the average frequency errors for individual cases are presented in Fig. 5. Also in Fig. 6 all the MAC values for mode pairs in Cases 1–5 as well as the average MAC values for individual cases are shown.

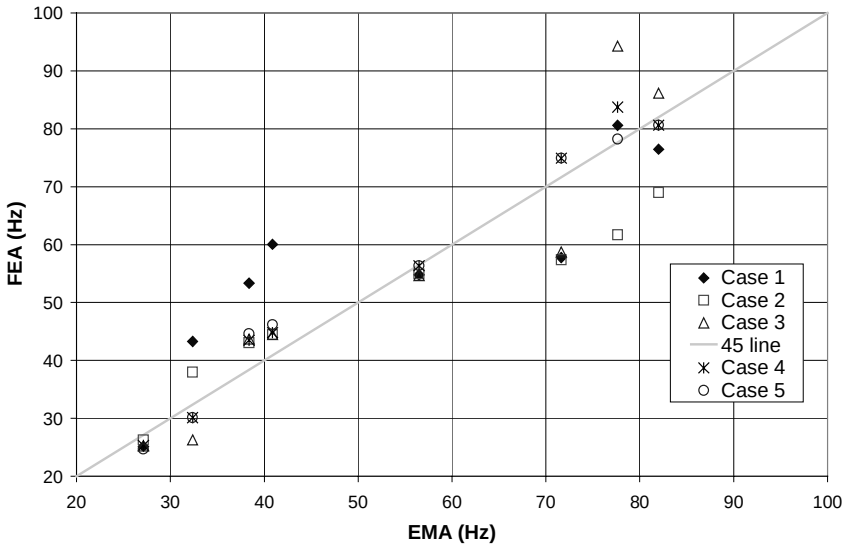

Figure 4. 45°-line comparison for eigenfrequencies in Cases 1–5.

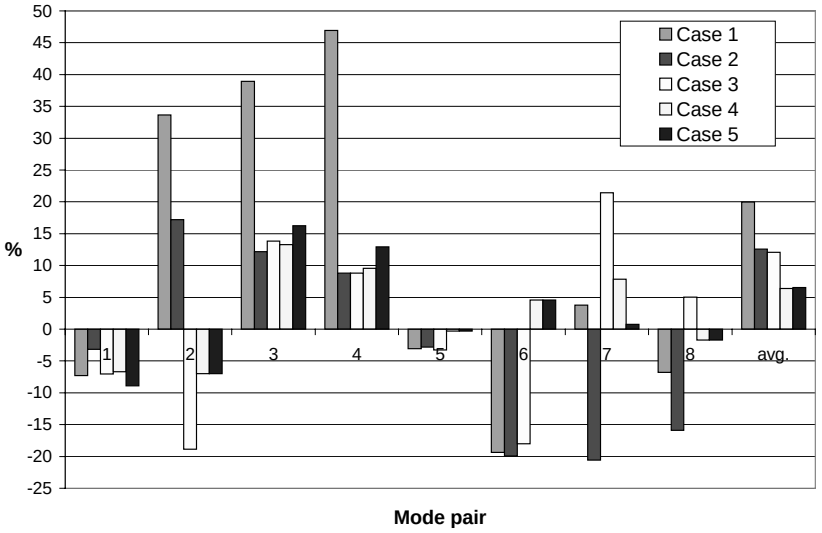

Figure 5. Frequency errors for mode pairs in Cases 1–5 and average errors in percentages.

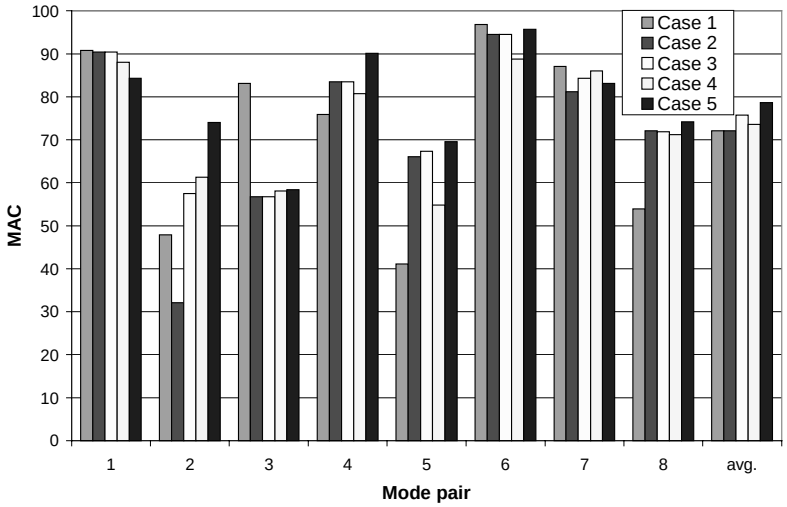

Figure 6. MAC values for mode pairs from Cases 1–5 and average MAC values.

Figures 5 and 6 as well as Table 7 confirm the improvement of the FEA results in Case 4 over the original Cases 1–3 especially in view of the frequency error. In case of MAC values the situation is not so clear due to the trade-off mentioned earlier. In general updating of the FE model improved the MAC values in mode pairs with low original MAC values and in mode pairs with high original MAC values some loss of correlation did occur.

When the damping was introduced into the FE model in Case 5 also the MAC values improved as can be seen from Figures 5 and 6 and Table 8. On the other hand this caused some growth in the frequency errors, especially in mode pair 3. In general the average frequency error did not deteriorate significantly if compared with situation in Case 4.

7. Conclusions

It is fairly clear that the discrepancy, in case of piping with several supports, between FE models and real man made structures comes mainly from the uncertainties of the pipe supports. So from this point of view they are also the most suitable parts for modifications for updating a FE model. In order to

enhance the possibilities of successful model updating some measurements should also be made from the supports and corresponding locations of the pipe. These measurements may reveal important information about the dynamic behaviour of the supports and about the interactions between the pipe and it's supports.

Special attention should be given to locating the actual measurement points accurately from the real structure. Also it is important to ensure, as carefully as possible, that the actual measurement directions are correct. If the planned measurement direction is X then it is important that the measurement sensors are set in this direction. Both of these seemingly simple tasks can be extremely difficult in case of complex piping systems and some discrepancies and errors will always exist, which may cause serious and unexpected problems in correlation analysis and in later model updating.

During the FE modelling phase of a pipeline enough emphasis should be given to the boundary conditions, like supports or pipe-ends, and it should be remembered that a pipeline seldom ends with really rigid boundary conditions. When the FE model (geometry) ends, the effect of masses beyond this end point should also be taken into consideration if the pipeline is not rigidly anchored in this point.

Introduction of damping into the FE model had some improving effect to the modal correlation but these effect should be studied more carefully and with some other damping model like structural damping model before any conclusions can be drawn.

During the updating process it must be remembered that, although the updating is usually based on modifying some physically realisable properties such as Young's modulus, cross-section area, density, etc., there is no one-to-one correspondence between experimental and analytical models. In other words, the actual modelling errors are in fact compensated by adjusting design parameters selected for updating, rather than actually identifying and eliminating these modelling errors.

Acknowledgements

This presentation is prepared for a joint Finnish industry group in a project on Structural operability and plant life management (RKK). The project funding by the National Technology Agency (Tekes), Teollisuuden Voima Oy (TVO), Fortum Power and Heat Oy, Fortum Nuclear Services Ltd., FEMdata Oy, Neste Engineering Oy, Fortum Oil and Gas Ltd. is gratefully acknowledged.

References

1. FEMtools User's Guide. Version 2.0.4. Dynamic Design Solutions N.V. (DDS). Leuven, Belgium, June 2000.

2. Mannan, M. A., McHargue, P. and Richardson, M. H. Continuous Monitoring of Modal Parameters to Quantify Structural Damage, Proc. of IMAC XII, 1993. 6 p.

3. Mattheis, A., Trobitz, M., Kussmaul, K., Kerkhof, K., Bonn, R. and Beyr, K. Diagnostics of Piping by Ambient Vibration Analysis, Nuclear Engineering and Design, 2000. Vol. 198, pp. 131–140.

4. Mevel, L., Hermans, L. and Van Der Auweraer, H. Application of a Subspace-based Fault Detection Method to Industrial Structures, Mechanical Systems and Signal Processing, 1999. Vol. 13, No. 6, pp. 823–838.

5. Natke, H. G. Problems of Model Updating Procedures: A Perspective Resumption, Mechanical Systems and Signal Processing, 1998. Vol. 12, No. 1, pp. 65–74.

6. Smeekes, P., Talja, H., Saarenheimo, A. and Haapaniemi, H. Piping Vibration Management Combining Measurements and Numerical Simu–lation, Proc. of Baltica Conference 2001. 12 p.

7. Rostedt, J. Description of the Dynamic Properties of Pipeline 327 with Help of Vibration Animation. Kankaanpää: J. Rostedt Oy. 2000. Report RR000712.Doc. 5 p. + app. 21 p. (in Finnish)

8. Nuutila, O. and Rostedt, J. OL1, – Modal Analysis of a Part of System 327 Using Shaker Excitation. Kankaanpää: J. Rostedt Oy. 2001. Report 010328r.Doc. 5 p. + app.

9. Smeekes, P., Talja, H., Saarenheimo, A. and Haapaniemi, H. Numerical Simulation of Piping Using Modal Correlation. Transactions of the 16th International Conference on Structural Mechanics in Reactor Technology, SMiRT 16, Washington DC, USA, 2001.

10. FPIPE User's Manual, FEMdata oy, Espoo 1999.

11. ABAQUS Theory Manual, Version 5.8. (1998). Hibbit, Karlsson & Sorensen Inc. RI.

12. Haapaniemi, H. A Case Study for Validating and Updating the Dynamic FE Model of a Pipeline. MSc. Thesis. Helsinki University of Technology, 2001. 101 p.

13. Ewins, D. J. Modal Testing: Theory and Practice, Research Studies Press Ltd. Letchworth, Herts, U.K, 1986. 269 p. ISBN 0-86380-036-X

14. Ingemansson Education. LMS Gateway, Correlation and Updating Course Book, Held at Gothenburg 27–29.06.2000.

15. Möller, P. W. and Friberg, O. An Approach to the Mode Pairing Problem. Mechanical Systems and Signal Processing, 1998. Vol. 12, No. 4, pp. 515–523.

16. I-DEAS Test: Modal Analysis User's Guide. I-DEAS Master Series 7, Structural Dynamics Research Corporation, USA, 1998.

Modal analysis of feed water pipe line RL61 at the Loviisa NPP

Arja Saarenheimo and Heikki Haapaniemi
VTT Industrial Systems, Espoo
Pekka Luukkanen, Fortum Power and Heat, Loviisa NPP
Pekka Nurkkala, Fortum CMC, Helsinki
Jaakko Rostedt, J. Rostedt Ltd, Kankaanpää

Abstract

The main aim of this project is to develop a practical method for monitoring the condition and remaining lifetime of process piping. The computational model is updated through measurements, but in practice both measurements and testing are often quite limited. Numerical pre-analyses were performed to optimise the use of resources available for testing. Optimal locations for the transducers and the shaker were predicted numerically using the ABAQUS Finite Element (FE) and FEMtools programs. It is important to select the optimal measurement method for each case. Both hammer excitation and shaker excitation were used when analysing modal shapes by measurement. Some preliminary evaluations of these results are presented here.

1. Introduction

The feed water pipeline RL61 of the VVER 440 type PWR plant Loviisa 1 is the third pilot case in this ongoing research project. Numerical pre-test analyses were carried out to aid the planning of modal tests. Both impact hammer and shaker excitation were used in modal testing.

The main dimensions of the pipeline are shown in Fig. 1. The outer radius of the pipe is 324 mm and the pipe bend curvature 600mm. The thickness of the pipe is generally 20 mm, except for the vertical part, which has a wall thickness of 17.5 mm.

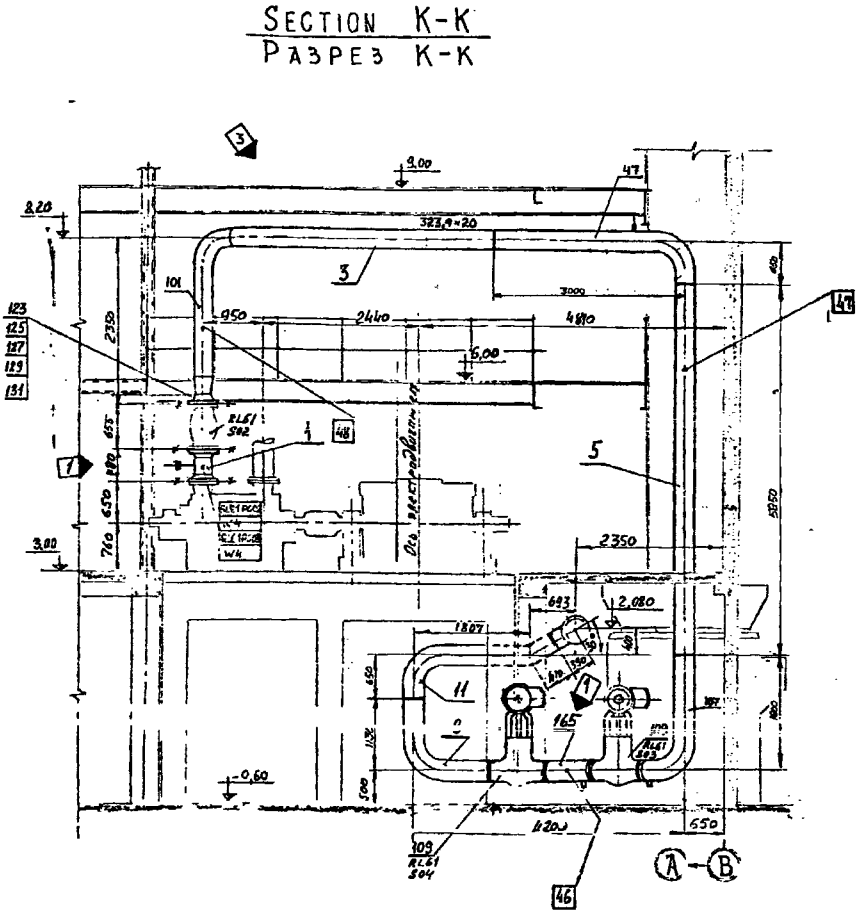

Figure 1. Feed water line RL61.

2. Pre-test analyses

Pre-test analyses were carried out using the FEMtools program (FEMtools Theoretical Manual Version 2.1.0 2001). The optimal locations for excitation of the structure were identified. Also, the numerically predicted mode shapes can be used to select the optimal minimum set of DOF (Degrees Of Freedom) where measurements are required to enable pairing with calculated mode shapes. The ABAQUS/Standard [1] code was used for finite element analyses.

2.1 Optimal Exciter and transducer location

Driving point residues (DPR) are equivalent to modal participation factors. They are proportional to the magnitudes of the resonance peaks when measuring FRF at a driving point. A driving point is defined as any point in the structure where the excitation DOF and the response DOF are equal. A shaker or a reference accelerometer is usually located at a driving point. The driving point residues (DPR) for all the DOFs in an FE model can be computed as

$$DPRj(i,i) = \frac{\Psi_j(i)^2}{\omega_j}$$

where i is the degree of freedom, ψ the eigenvector, ω the circular frequency, and j the mode shape number. DPRs are a measure of how much each mode is excited, or has participated in the overall response, at the DPR [5].

The driving point residues are normalised and compared with a range of mode shapes of interest. The Normalised Modal Displacement (NMD) is used as a criterion and can be calculated using minimum, maximum, averaged maximum or combined weighted maximum and averaged maximum values. In order to get the best point and direction for exciting, the case in which the DPRs for all modes of interest are as high as possible should be chosen. In a case where excitation of certain modes is unfavourable, the driving point should be chosen with the minimal DPRs for those modes.

A certain minimum number of DOFs is needed in an FE model to obtain sufficient accurate results. Also, there is a minimum number of test DOFs needed to model the mode shapes and to distinguish one mode shape from another.

In this study, the optimal exciter locations for RL61 measurements were predicted using weighted NMDs, which are defined as follows:

$$NMD(i) = [\max_{j=1}^{M}(\overline{DPR}_j(i,i))][\frac{1}{M}\sum_{j=1}^{M}(\overline{DPR}_j(i,i))]$$

where M is the number of mode shapes of interest [2].

The pipeline was modelled with straight pipe elements of type PIPE31 and special purpose pipe bend elements of type ELBOW31, which allow cross-sectional ovalisation and warping, where as the PIPE31 type beam element expands only radially. There are six elbow elements modelling one pipe bend of 90 degrees. All elbow elements used in the analyses incorporate six circumferential Fouries modes for ovalisation, seven integration points through the wall thickness, one integration point in the axial direction and 18 circumferential integration points.

In this preliminary study, the connection to the pump and the downstream end of the model were modelled as fully fixed. This pipeline is supported by three spring hangers. The locations of the spring hangers referred to in the following as S1, S2 and S3 are shown in Fig. 1, numbered 46, 47 and 48 respectively. The spring constant of S1 is 660 N/mm and the corresponding value for springs S2 and S3 is 446N/mm. There are two valves, V1 and V2, each weighing 978 kg.

First, the pipe was assumed to be non-insulated, cold and empty. The weighted NMD values in relation to the global X-, Y- and Z-axes are shown as coloured vectors in Figs 2 a–d. The NMDs were calculated also assuming that the pipeline is filled with water, but non-insulated and cold. The mass of the water was included in the equivalent density of the pipe cross-section. The corresponding vector plots are shown in Figs 3a–d.

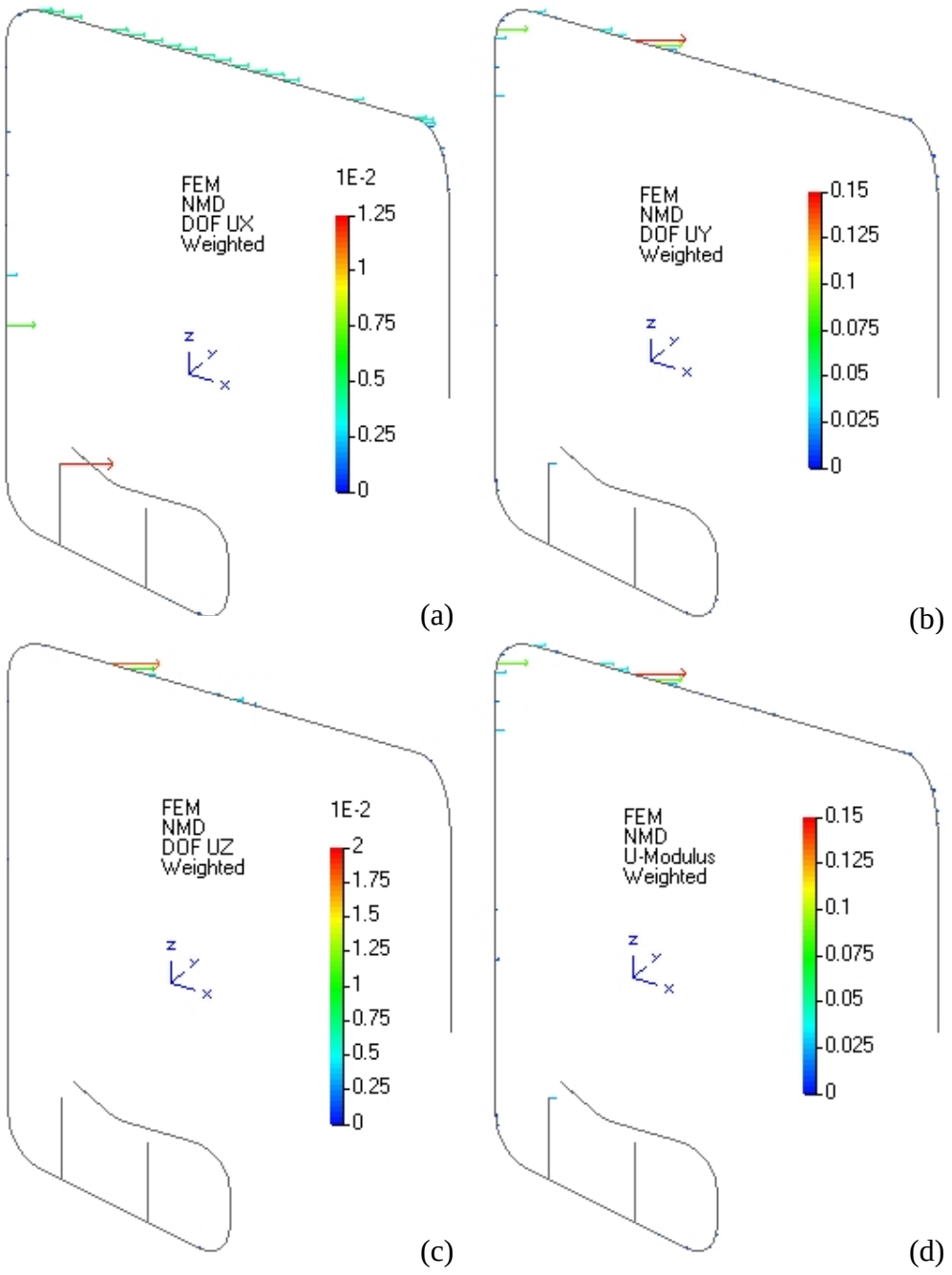

Figure 2. Weighted NMDs related to (a) global X-direction, (b) global Y-direction, (c) global Z-direction and (d) summarised NMDs, empty pipeline.

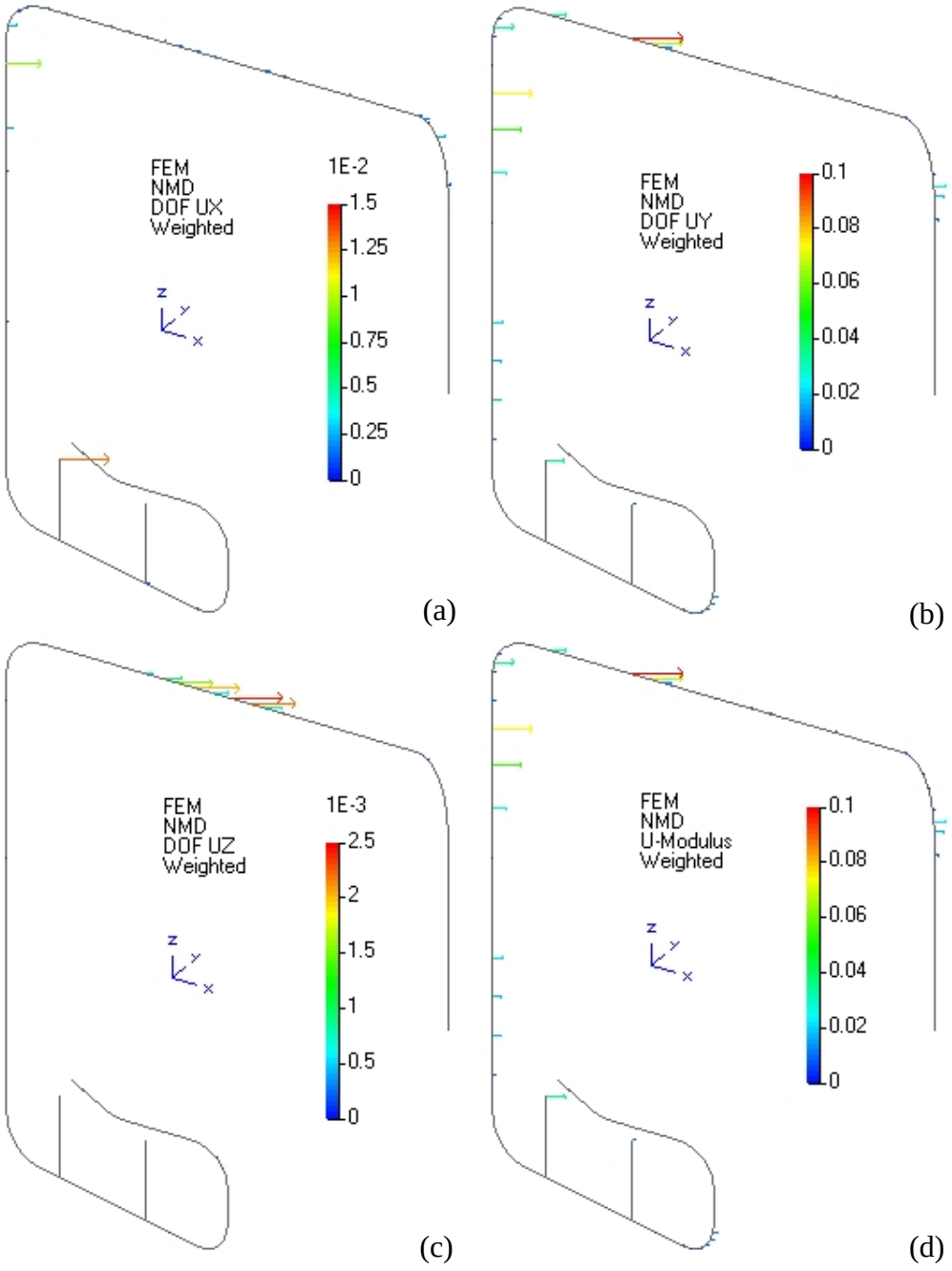

Figure 3. Weighted NMDs related to (a) global X-direction, (b) global Y-direction, (c) global Z-direction and (d) summarised NMDs, pipeline filled with water.

3. Modal analysis using shaker excitation

Modal testing with shaker excitation was performed during the outage [3]. The pipeline was tested first as non-insulated, cold and empty (Case 1). In the second case (Case 2) the insulation was added and in the third case (Case 3) the pipe was filled with hot water. The pre-analyses described above were used in planning the modal testing.

The model used in modal testing and the numbers of measurement points are shown in Fig. 4. The responses were measured at all the measurement points in all three global co-ordinate directions. For practical reasons excitation at point 114 was done in the global negative Z-axis and global negative Y-axis directions. These global co-ordinate axes are shown in Figs 2 and 3. The Excitation was given in one direction at a time. A servohydraulic exciter was used for excitation. The mass of the exciter was 400 kg and maximum nominal dynamic force 11 kN. The choice of frequency range was based on pre-analyses and the number of available transducers. The frequency range used in these measurements was 0–100 Hz.

The modal indication function method (MIF) was used in evaluating the measured data. The MIF value is a sum function of measured frequency response functions measured using one single point and one single direction for excitation.

$$MIF = \frac{\sum(|\mathrm{Re}(H)||H|)}{\sum(|H|^2)}$$

where H is a frequency response function. MIF has a maximum value of unity. Eigenmodes of the structure exist in local valleys (minima).

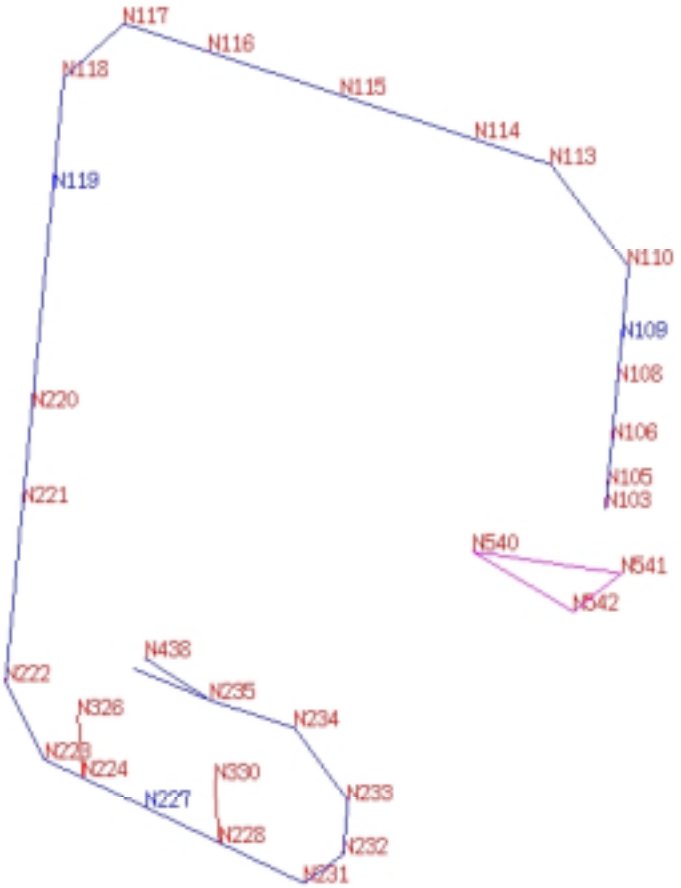

Figure 4. Modal testing model, measurement points.

The MIF value calculated in Case 1, using excitation in the global negative Z-direction, is presented as a function of frequency in Fig. 5. The eigenfrequencies are denoted by '+'. There seem to be two eigenfrequencies at the frequency value of 21 Hz (IDEAS Test 1998).

The effect of the insulation layer is considered in Figs 6–8, which compares the frequency responses of Cases 1 and 2 with each other. Figure 6 shows the measured frequency response function at measurement point 220 in the negative Y-axis direction. Corresponding values evaluated at measurement points 110 and 233 in the positive Z-axis direction are shown in Figs 7 and 8, respectively. The numbering of these measurement points is shown in Fig. 4.

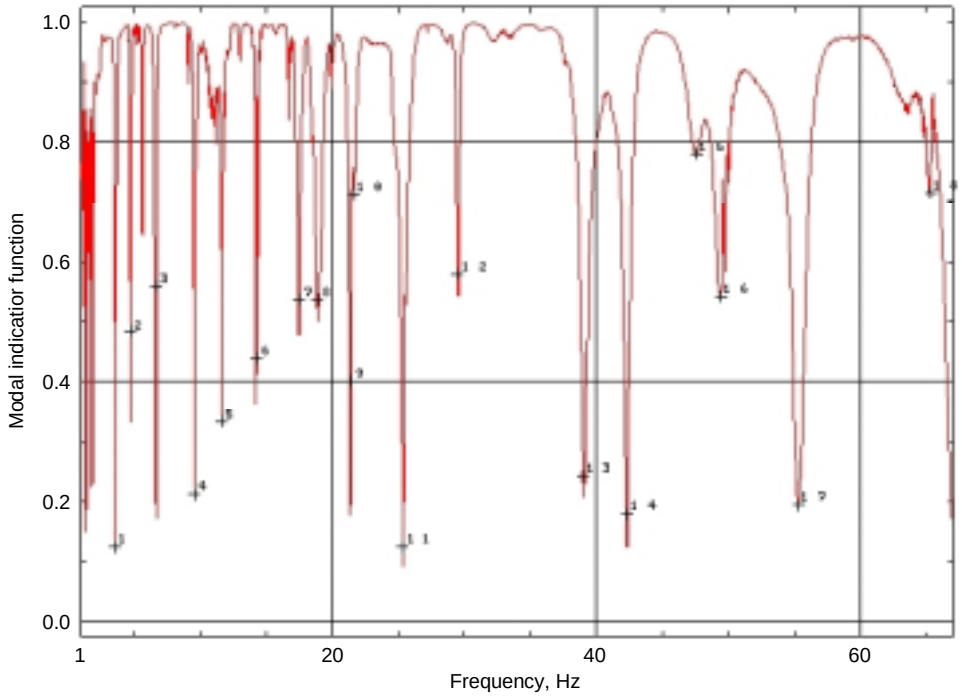

Figure 5. Modal indicator function (MIF) in Case 1.

The effects caused by insulation can clearly be seen in the frequency response measured at point 220 outside the frequency range from 5 Hz to 20 Hz.

In the response at point 110 the effect of the insulation is clearly visible throughout the measured frequency range (Fig. 7). The same phenomena can be seen in the response measured at point 233, mainly at frequencies below 4 Hz and again above 24 Hz (Fig. 8).

The effect of the insulation layer was further considered using the Cross Signature Assurance Criterion (CSAC) and the Cross Signature Scale Factor (CSF) functions. By means of these correlation functions the level of correlation can be evaluated.

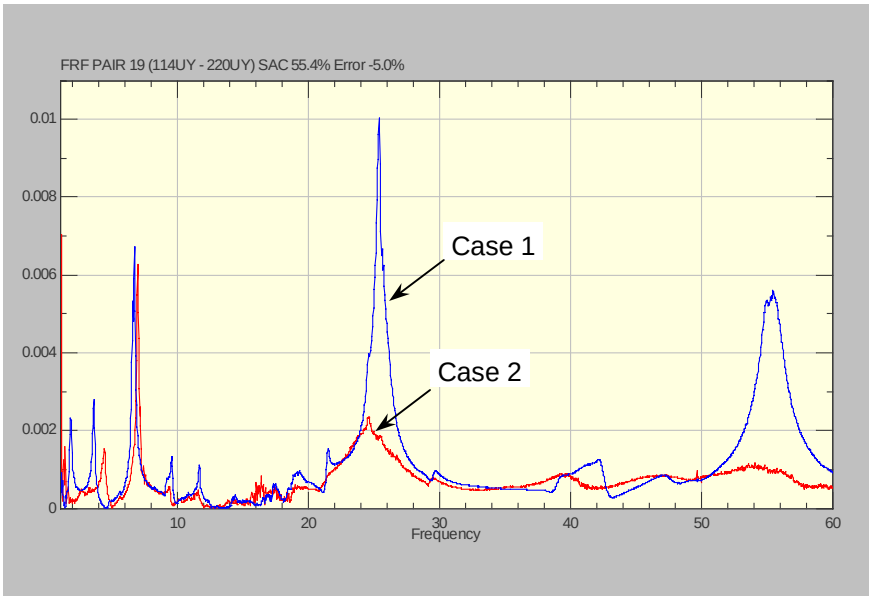

Figure 6. Frequency response in the negative Y-axis direction at point 220, excitation at point 114 in the negative Y-axis direction, Case 1 blue, Case 2 red.

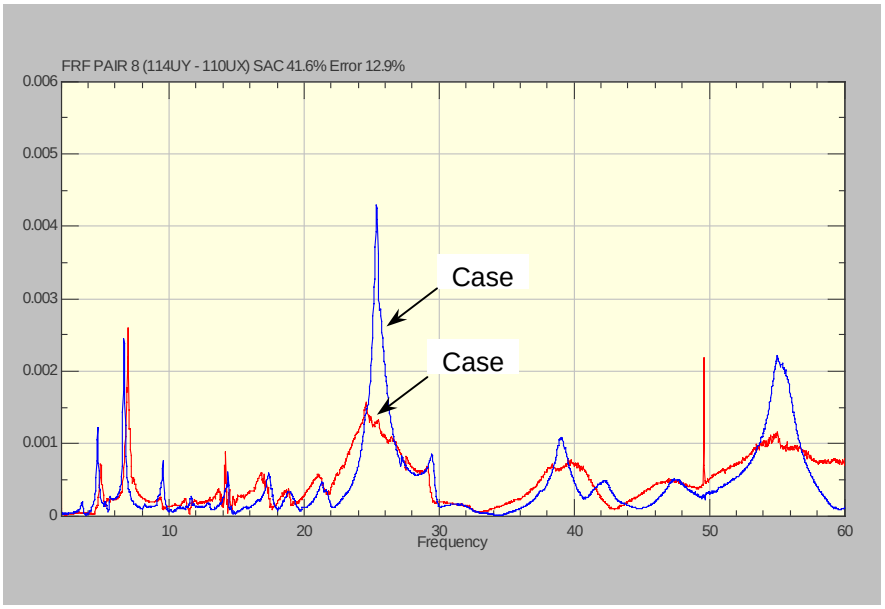

Figure 7. Frequency response to the positive Z-axis direction at point 110, excitation at point 114 to the negative Y-axis direction, Case 1 blue, Case 2 red.

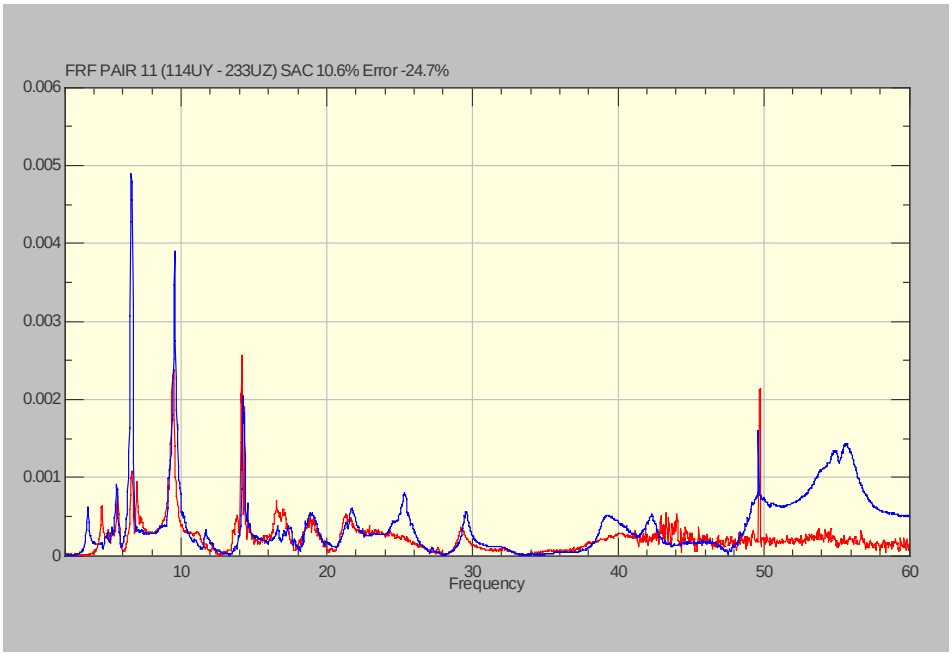

Figure 8. Frequency response in the positive Z-axis direction at point 233, excitation at point 114 in the negative Y-axis direction, Case 1 blue, Case 2 red.

The CSAC function evaluates the shape of a FRF, which is mainly determined by the position and amount of resonance peaks. As can easily be seen, this function is sensitive to errors in mass and stiffness. CSAC can be written as

$$CSAC(\omega_k) = \frac{\left|\alpha_{X_i}^H(\omega_k)\alpha_{A_i}(\omega_k)\right|^2}{\left(\alpha_{X_i}^H(\omega_k)\alpha_{X_i}(\omega_k)\right)\left(\alpha_{A_i}^H(\omega_k)\alpha_{A_i}(\omega_k)\right)}$$

where ω_k is the frequency at point k. The frequency range considered is divided into a certain number of frequency points (Nf); k=1,2,...Nf. In this study, (α_X) is the measured FRF in Case 1, and (α_A) is the measured FRF in Case 2 (insulated). Subscript i is the number of DOFs in the system considered. The value of CSAC varies from zero to one. Usually, there are three DOFs at each measurement point. Superscript H stands for the Hermitian transpose and is determined as follows:

$[A]^H = ([A]^T)^*$

where * denotes the complex conjugate. The complex conjugate of z = x+iy is graphically simply the reflection of z about the real axis, $z^* = x-iy$.

Because FRF is not only defined by its shape, it is necessary to apply another correlation function which evaluates the discrepancies in amplitude. The CSF function is defined as

$$CSF\ (\omega_k) = \frac{2\left|\alpha^{H}_{X_i}(\omega_k)\alpha_{A_i}(\omega_k)\right|}{\left(\alpha^{H}_{X_i}(\omega_k)\alpha_{X_i}(\omega_k)\right) + \left(\alpha^{H}_{A_i}(\omega_k)\alpha_{A_i}(\omega_k)\right)}$$

Because CSF evaluates the amplitude, it is more sensitive to errors in damping, [2].

In order to study the effect of insulation, CSAC functions were calculated using FRFs measured in Cases 1 and 2. CSAC functions in the frequency range 1–30 Hz are presented in Fig. 9 and the corresponding functions for the frequency range 30–60 Hz in Fig. 10. The value of 100% indicates similar FRFs in these two cases considered. Similarities can be found when considering the values at single measurement points. However, CSAC values calculated using seven points (110, 113, 115, 118, 220, 223 and 233) and 21 their DOFs, available in the measurement model, are considerably lower when compared with the CSAC values calculated at some single point. All three DOFs are taken into account also when calculating CSAC values presented at these single points.

In order to compare the amplitudes in the non-insulated case (Case 1) and insulated case (Case 2), the CSF functions were calculated at the same points where the CSAC values were considered.

CSF values in the frequency range 1–30 Hz are presented in Figure 11. The corresponding values for the frequency range 30–60 Hz are shown in Figure 12, respectively. Especially in the lower frequency range the amplitudes are quite similar at points 113 and 233. Point 113 is located close to the excitation point, and point 233 is located on the vertical part of the pipeline between the valve and the connection to the downstream pipeline.

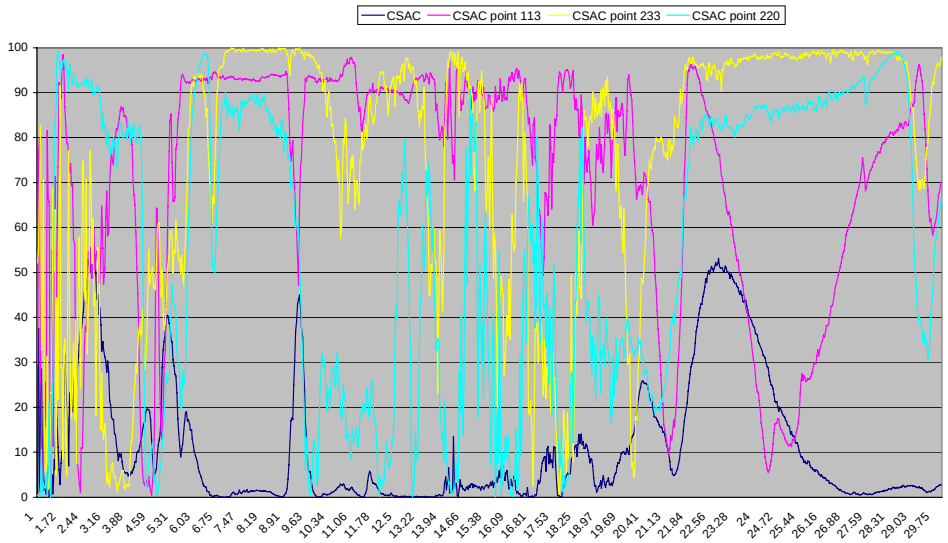

Figure 9. Eeffect of insulation, CSAC functions in the frequency range 1–30 Hz.

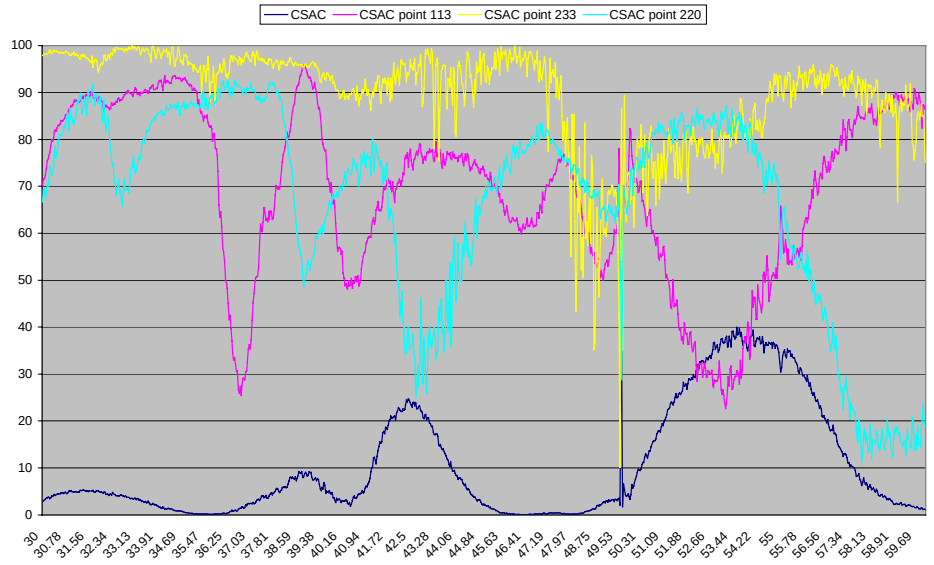

Figure 10. Effect of insulation, CSAC functions in the frequency range 30–60 Hz.

The insulation had a remarkable effect on the dynamic behaviour of the pipeline. Especially in the frequency range over 20 Hz the damping effect of the insulation was considerable. One explanation for this phenomenon might be one

additional support due to the contact of the insulation and cable shelter. More research on this subject is urgently needed!

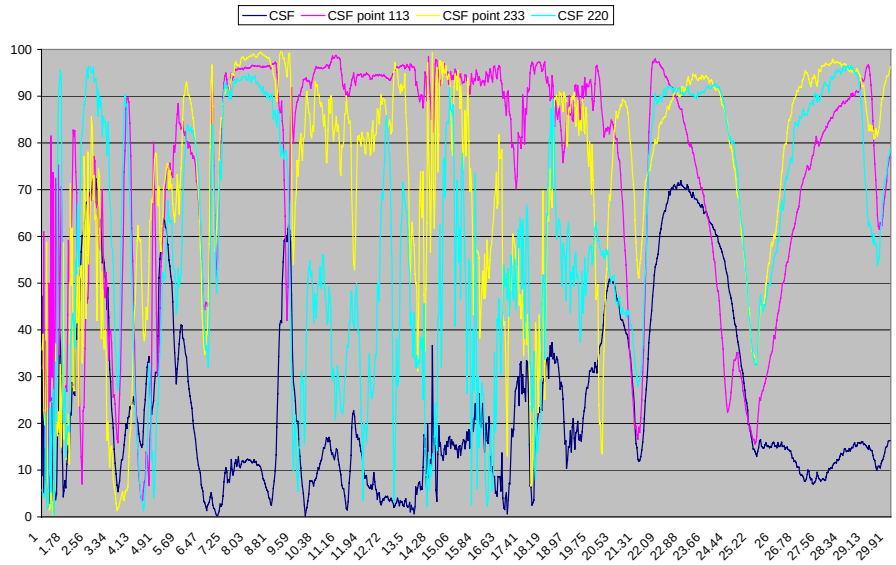

Figure 11. Effect of insulation, CSF functions in the frequency range 1–30 Hz.

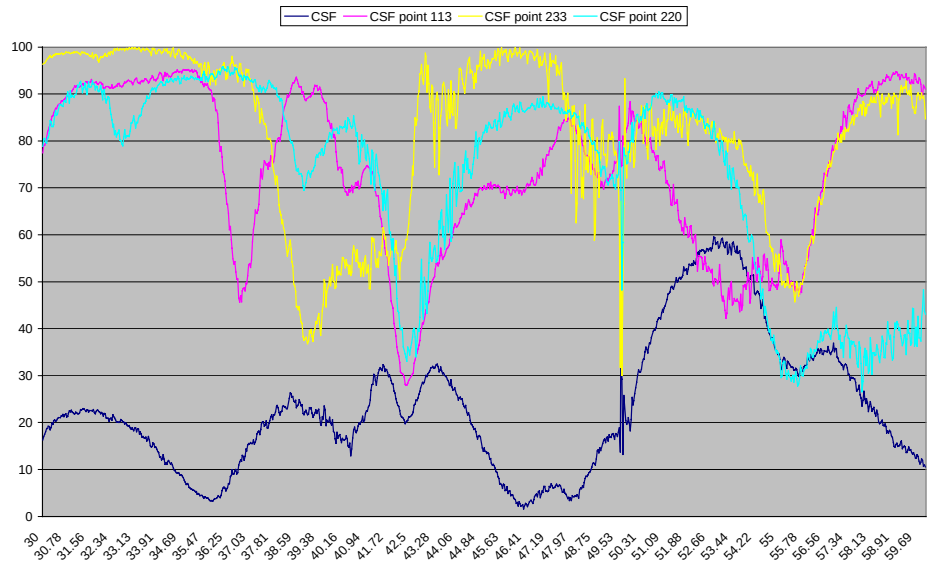

Figure 12. Effect of insulation, CSF functions in the frequency range 30–60 Hz.

4. Modal analysis using hammer excitation

In the non-insulated case (Case 1), modal testing was done also using an impact hammer [4]. The measurement points used in this study are shown in Fig. 13. The location of the excitation point is also indicated. Hammer excitation was performed at the same location as with the shaker. The weight of the hammer is 22.3 kg.

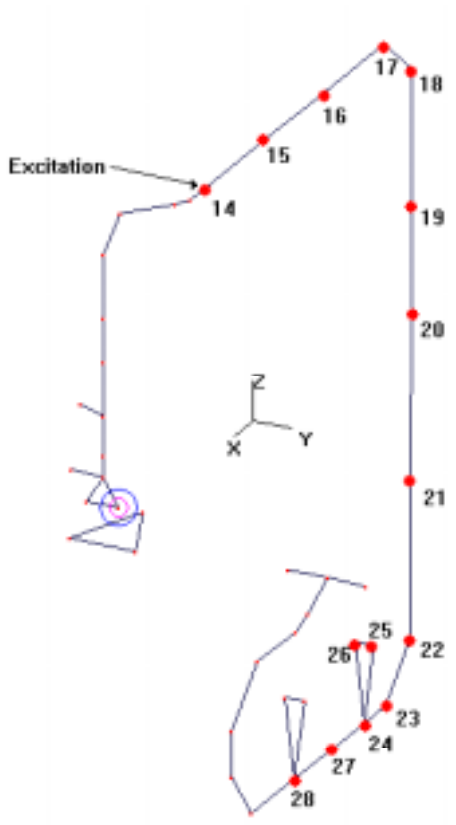

Figure 13. Model used in modal testing carried out with impact hammer.

The averaged FRFs are shown over the frequency range of Figure 14.

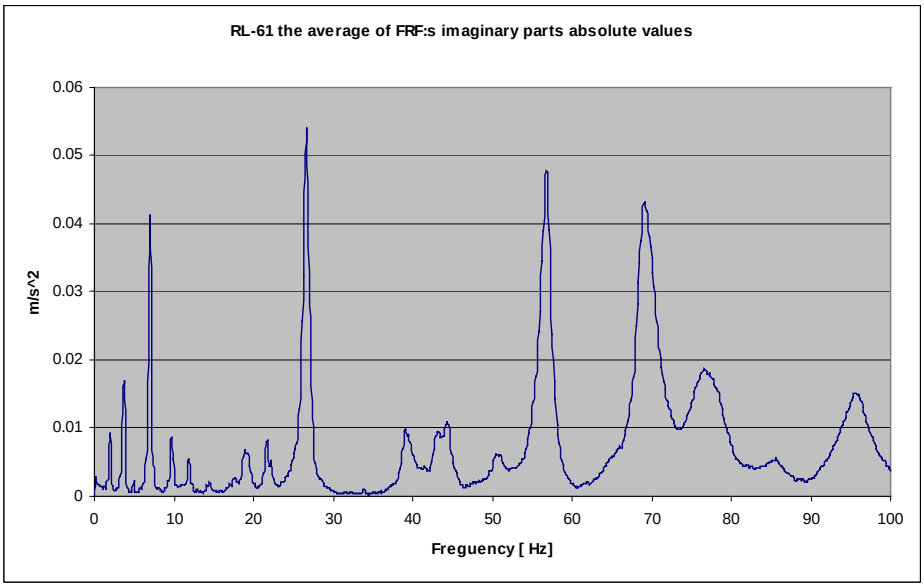

Figure 14. Averaged FRFs, Case 1.

No curve fitting method was used; the eigenfrequencies were determined by visual investigation of the frequency-response functions. The frequencies of the mode shapes are listed in Table 1, whereas the most significant modes are underlined.

As the force transducer suffered damage during the hammer tests, excitations in the X- and Z-directions were measured with the help of an accelerometer instead, causing some unreliability to the three-dimensional modes.

5. Discussion

The eigenvalues predicted numerically in Case 1 using shaker excitation and an impact hammer are listed in Table 1.

Table 1. Mode shapes of pipeline RL-61.

Mode	FE result	Shaker	Hammer
number	[Hz]	[Hz]	[Hz]
1	1.9	1.812	2.0
2	3.6	3.594	3.75
3	3.7	4.718	7.125
4	6.2	5.599	9.625
5	7.6	6.551	11.875
6	8.1	6.68	19.25
7	12	9.752	21.5
8	16.7	11.67	26.5
9	19.5	14.272	39.125
10	22.5	17.451	43.25
11	24.4	18.961	44.5
12	25.9	21.4	51.0
13	31.2	21.672	56.875
14	45.1	25.384	69.25
15	48.3	25.986	77.0
16	53.4	29.544	95.875
17	55	39.07	
18	57.2	41.6	
19	63.6	42.109	
20	65	47.418	
21		49.539	
22		55.087	
23		55.526	
24		65.322	
25		66.118	
26		67.255	

The evaluation of results is an ongoing process. Model test data will be used in updating the numerical model.

The numerical correlation between shaker excitation and impact hammer excitation results are shown in Fig. 15 for the frequency range 2–20 Hz and in Fig. 16 for the frequency range 20–60 Hz. These results are based on both CSAC and CSF analyses done in case of reference co-ordinate (excitation) 114 Y and response co-ordinates (measurement points) 115, 118, 220 and 223 (i.e. 12 DOFs).

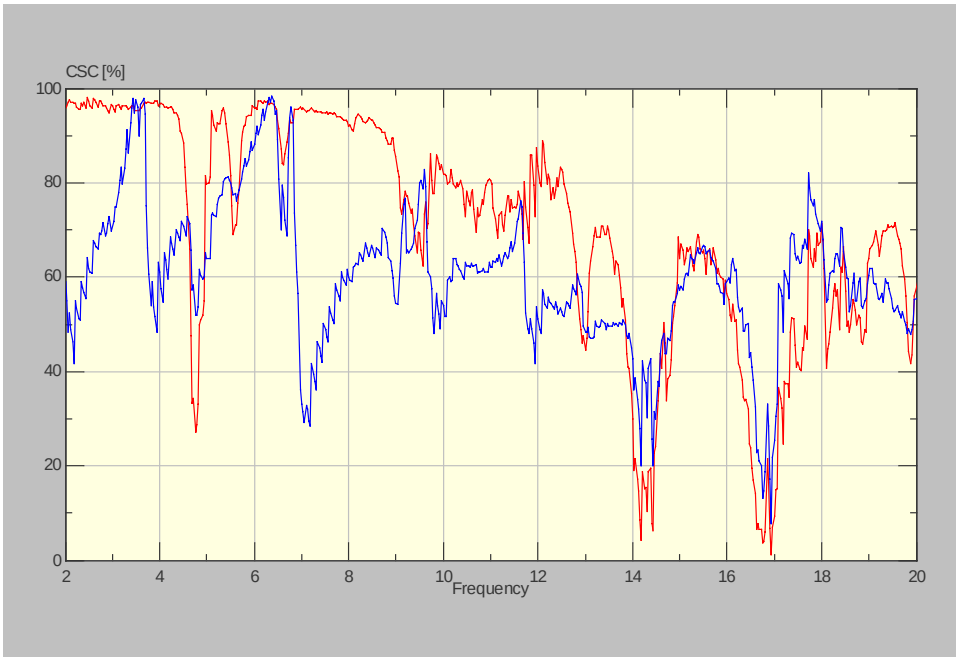

Figure 15. Comparison between impact hammer excitation results and shaker excitation results in respect of CSAC (red line) and CSF (blue line) in the frequency range 2–20 Hz.

These correlation analysis results show that there is good correlation in frequencies from 2 to 13 Hz, 23 to 42 Hz and 51 to 60 Hz in view of the CSAC values. This means that the measured FRFs are similar in shape, i.e. there are roughly the same number of resonance peaks and these are similarly positioned. As expected, the CSAC correlation is not as good as expected in the frequency ranges 13–23 Hz and 42–51 Hz. The reason for lower CSAC correlation in these two frequency ranges can be seen by comparing the obtained eigenfrequencies in Table 1. Table 1 suggests that within these frequency ranges impact hammer testing failed to excite some modes that were excited with a shaker.

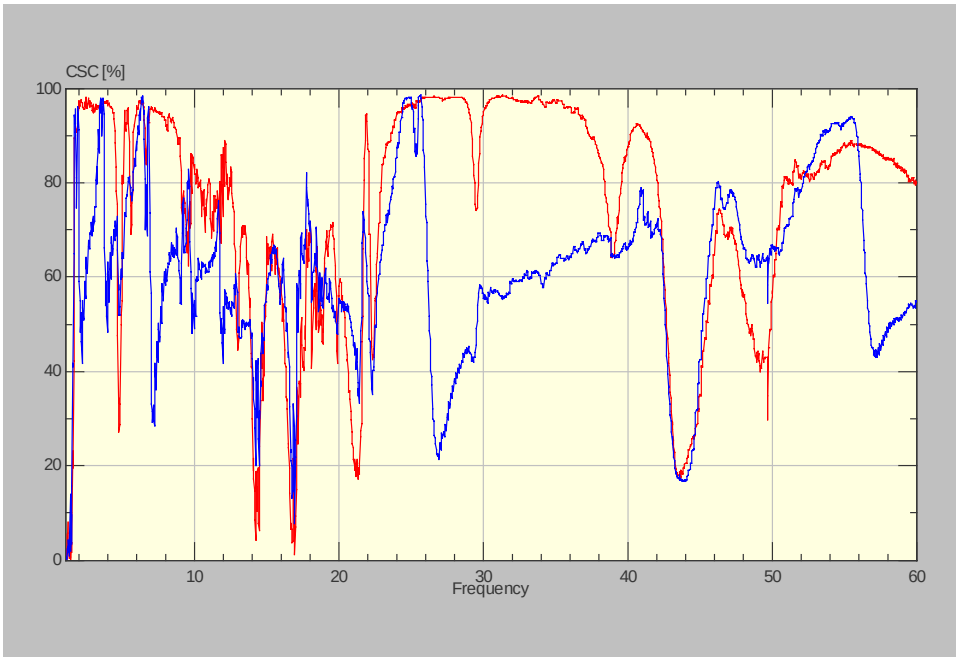

Figure 16. Comparison between impact hammer excitation results and shaker excitation results in respect of CSAC (red line) and CSF (blue line) in the frequency range 20–60 Hz.

The CSF correlation does, on the other hand, show some discrepancies between these two experimental models. This means that there are some discrepancies in the amplitudes of these resonance peaks, which may suggest that there are some differences in damping levels between these two experimental models. These discrepancies cannot yet be explained unambiguously and would require further study. One explanation could be that there is some damping phenomenon taking place which is somehow dependent on the excitation force levels used.

It must of course be remembered that these correlation analysis results may vary if more DOF is introduced into the analyses. Especially areas of good correlation may vary (in the case of CSAC) or the level of correlation change if more DOFs are included.

The FRF pairs shown in Figs 17 and 18 also confirm the earlier correlation analysis results, and show that there are similarly positioned resonance peaks especially at lower frequencies, although their amount varies, and that there are

clearly some differences in the amplitudes of resonance peaks throughout the frequency range.

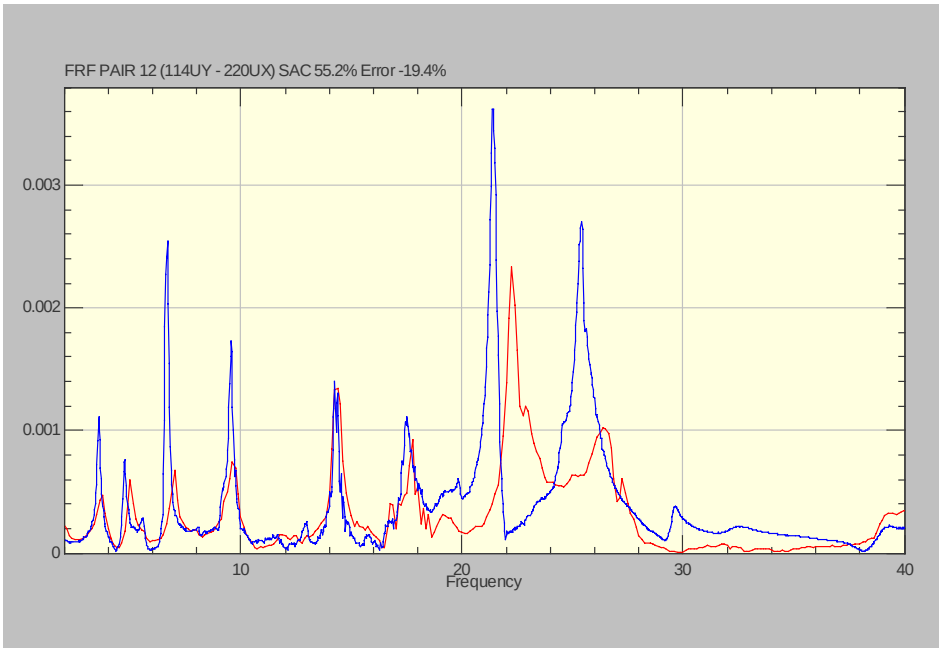

Figure 17. Frequency response in the positive X-axis direction at point 220, excitation at point 114, shaker results in blue, impact hammer in red.

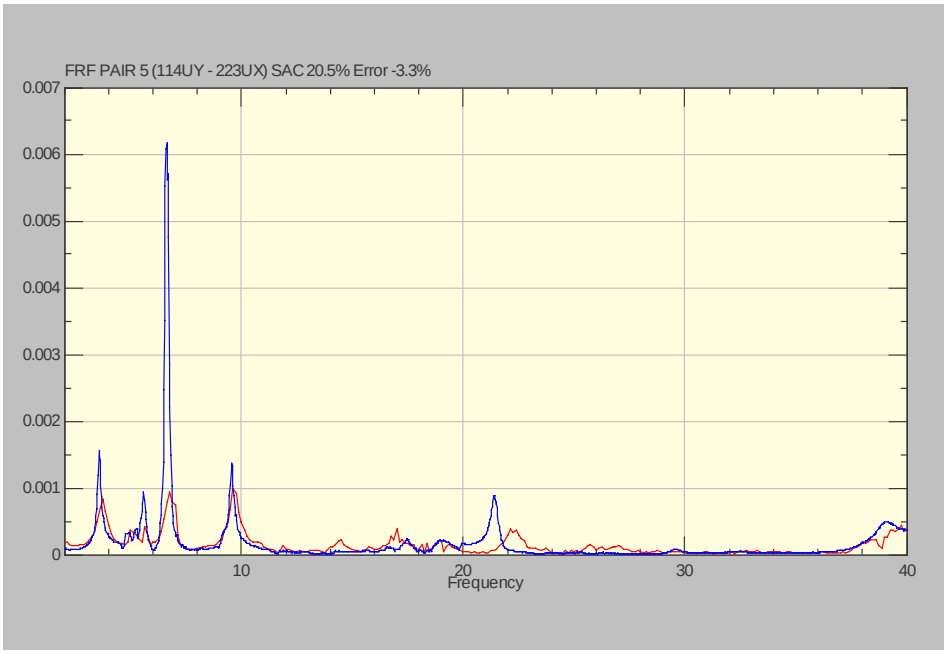

Figure 18. Frequency response in the positive X-axis direction at point 223, excitation at point 114, shaker results in blue, impact hammer in red.

Acknowledgements

This presentation was prepared for a joint Finnish industry group as part of a project on Structural Operability and Plant Life Management (RKK). The project funding by the National Technology Agency (Tekes), Teollisuuden Voima Oy (TVO), Fortum Power and Heat Oy, Fortum Nuclear Services Ltd., FEMdata Oy, Neste Engineering Oy, Fortum Oil and Gas Ltd. is gratefully acknowledged. The authors are indebted to Mr Aimo Tuomas and to Mr Timo Krouvi from Fortum Loviisa NPP for their contribution during this work.

References

1. ABAQUS Theory Manual, Version 5.8. 1998. Hibbit, Karlsson & Sorensen Inc. Rhode Island.

2. FEMtools Theoretical Manual Version 2.1.0. 2001. Dynamic Design Solutions N. V. (DDS). Leuven, Belgium.

3. Nurkkala, P. Loviisa 1 syöttövesilinjan painepuolen RL61 putkiston moodianalyysi kolmella eri reunaehdolla elokuussa ja lokakuussa 2001. Fortum CMC. Työseloste CMC-201. 2002.

4. Rostedt, J. Fortum Power and Heat Oy, Loviisa Power Plant-MODAL ANALYSIS OF PIPELINE RL-61 USING HAMMER EXCITATION. Research Report 020301.doc. J. Rostedt Ltd, Kankaanpää, Finland, 2001.

5. Van Lagenhove, T. and Brughmans, M. Using MSC/Nastran and LMS/Pretest to find an optimal sensor placement for modal identification and correlation of aerospace structures. Presented at the 2nd MSC Aerospace Conference, June 1999. 12 p.

Monitoring of BWR water chemistry and oxide films on samples at Olkiluoto 1 during the fuel cycle 2000–2001

Martin Bojinov, Petri Kinnunen, Timo Laitinen,
Kari Mäkelä, Timo Saario and Pekka Sirkiä
VTT Industrial Systems
Espoo, Finland

Abstract

A flow-through cell unit has been installed in the shutdown cooling system 321 at Olkiluoto 1 in May 2000 in order to collect the data needed for establishing the correlations between rate of activity incorporation, water chemistry data and the properties of oxide films formed on material samples.Observations and correlations related to susceptibility to stress corrosion cracking and other forms of corrosion are also looked for. The monitoring unit provides relevant high-temperature water chemistry information that can be well used both for assessing long-term trends and for sensitive detection of rapid changes in the coolant environment. Also the material sample cell has been verified to give a representative view of activity incorporation and oxidation of construction materials in the primary coolant.

The results have indicated marked differences between the behaviour of different isotopes and different materials. It has become evident that he thickness of the oxide film is not the only factor that correlates with the extent of activity build-up.

1. Introduction

The susceptibility of structural materials in a nuclear power plant to stress corrosion cracking and to other forms of corrosion, as well as the extent of activity incorporation on primary circuit surfaces, are closely connected to the chemical parameters of the coolant water and to the properties of oxide films on

material surfaces [1]. Changes in operational conditions are likely to induce changes in corrosion susceptibility and rate of activity incorporation. To predict these changes, experimental correlations between water chemistry, oxide films, corrosion behaviour and activity incorporation, as well as mechanistic understanding of the related phenomena need to be established.

A flow-through cell unit has been installed in the shutdown cooling system 321 at Olkiluoto 1 in May 2000 in order to collect the data needed when searching for such correlations. The unit is being used for the following major purposes:

- Monitoring of the corrosion potentials of relevant material samples, the redox potential, the conductivity and the pH_T of the primary coolant at high temperature.

- Observation of the growth, structure, properties and activity levels of oxide films formed on material samples exposed to the primary coolant.

- Establishing correlations between the observations about water chemistry, activity levels, material behaviour and the abundant chemical and radiochemical data on coolant composition, dose rates etc. collected routinely by the plant.

The monitoring of high-temperature water chemistry was started after the refuelling outage of Olkiluoto 1 in 2000, i.e. in the beginning of June 2000. The obtained data has been continuously compared to related data obtained in room-temperature measurements performed in the laboratory at the plant. The first material samples have been removed from the cell before and during the refuelling outage of 2001, and they have been subjected to activity analysis and to a variety of *ex situ* instrumental analyses.

This presentation summarises the results of high-temperature water chemistry monitoring and material sample analysis at Olkiluoto 1 during the fuel cycle June 2000 – May 2001. A comple description of the test materials, procedures and results can be found in a separate report [2].

2. Experimental

2.1 High-temperature cells and sensors

The flow-through cells for monitoring the corrosion and redox potentials, conductivity and pH_T at high-temperature and for exposing material samples to the primary coolant have been connected to the shutdown cooling system 321 at Olkiluoto 1. The mass flow-rate through the cells is ca. 0.4 kg s^{-1}, corresponding to a nominal flow-rate of ca 0.3 m/s. During normal operation the system is thermally insulated to ensure a constant and relevant temperature in the cells.

The coolant enters first the lower cell and flows further to the upper cells. The lower cell contains two AgCl/Ag reference electrodes filled with 0.005 M KCl, one conductivity electrode, one pH_T electrode, two Pt samples for measuring the redox potential and eight separate samples for measuring the corrosion potential (ECP) of AISI 304 and AISI 316 L(NG) stainless steels, as well as that of Inconel alloys 82 and 182, Fig. 1.

The four-plate high-temperature conductivity sensor has been recently developed at VTT to improve the quality of conductivity measurements in plant conditions.

2.2 Material samples

Material samples made of AISI 304 stainless steel, AISI 316L(NG) stainless steel, Inconel alloy 82 and Inconel alloy 182 have been installed in the two upper cells in order to simulate the exposure of plant component surfaces to the primary coolant. The samples are removed from the cell at pre-scheduled intervals, and the oxide films formed on their surfaces are analysed, and the results are correlated with other observations of the plant operation. The two material sample cells contain altogether 80 samples.

The first set of samples has been removed from the material sample cell on May 8th 2001, i.e. during power operation before the shutdown preceding the refuelling outage of 2001. The second set of samples has been removed after the

shutdown during the refuelling outage in May 2001. At that time the activity levels of most of the samples in the cells have been measured to ensure a statistical significance of the activity measurements in the future.

The sampling schedule is shown in Table 1. The pre-scheduled dates for the sample removal during the cycle June 2001 – May 2002 are also given.

The pickup of activity on the sample surfaces is linked to the composition, structure and thickness of the oxide film. To be able to establish correlations between the structure and measured activity levels, the various techniques have been used to characterise the oxide films after the exposure to the BWR coolant. They are described in previous reports [2, 3, 4].

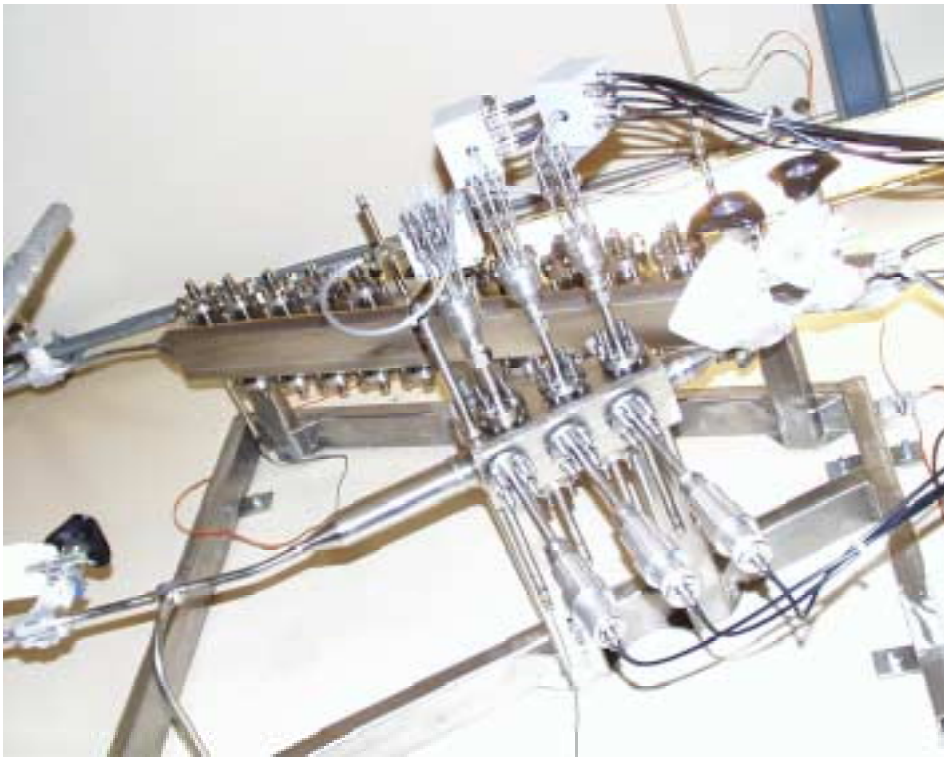

Figure 1. The flow-through cells with high temperature water chemistry sensors and 80 material samples in the shutdown cooling system 321 at Olkiluoto 1.

Table 1. Sampling schedule for the material samples. Future dates in italics.

Period of exposure	Time of exposure
5.6.2000 – 8.5.2001	11 months
5.6.2000 – 22.5.2001	11.5 months
5.6.2000 – 20.4.2002	*22.5 months*
5.6.2000 – 25.7.2002	*25.5 months*
etc.	

2.3 Operation of the plant

The temperature of the cell has been in the range 270–273 °C for the most part of the monitoring period. A few excursions to higher temperatures have occurred. According to plant reports, these excursions have taken place during reduced power output on June 22th – 25th, 2000, on August 20th, 2000, etc. The temperature in the shutdown cooling system 321 increases during a period of reduced power output because of the reduced cooling effect of the coolant circulation in the primary circuit.

The level of oxygen content determined by manual measurements corresponds to ca. 300 ppb, decreasing slightly towards the end of the fuel cycle. The oxygen level of 300 ppb can be considered to be close to expected values in a BWR plant with normal water chemistry (NWC). The on line results of oxygen measurements are not reported in the present report because of problems in the calibration of the equipment.

3. Results

The results of corrosion potential monitoring are summarised in Fig. 2 and the results of ex-situ analyses of the material samples are summarised in Figs 3 to 10. A summary and short discussion of the main observations is given thereafter.

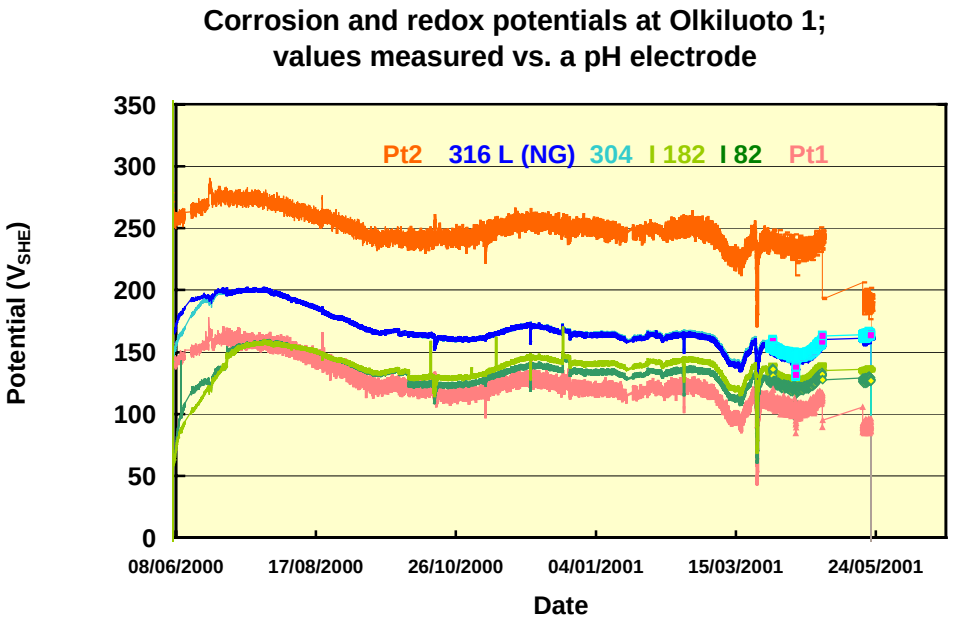

Figure 2. Corrosion potential (ECP) of AISI 304 stainless steel, AISI 316L(NG) stainless steel, Inconel alloys 82 and 182, and redox potential of the coolant measured with two different Pt sensors in the OL1 shutdown cooling system 321. Potentials determined vs. a pH electrode assuming a constant pH in the coolant.

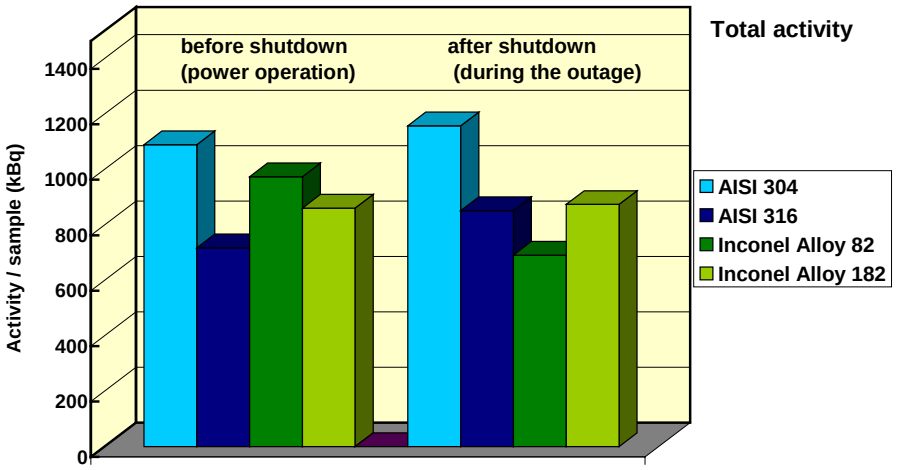

Figure 3. Total activity in material samples removed from the cell before and after the shutdown in May 2001, i.e. during power operation and outage.

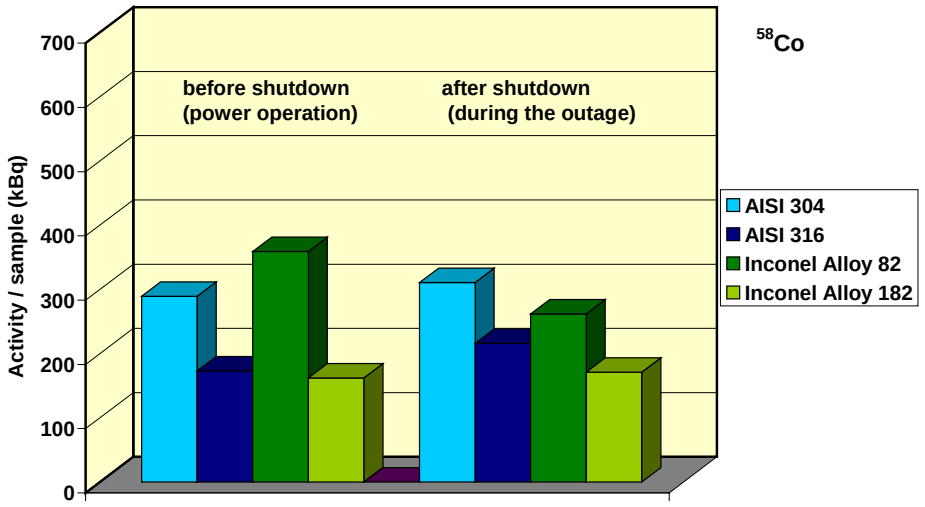

Figure 4. Activity due to ^{58}Co inmaterial samples removed from the cell before and after the shutdown in May 2001.

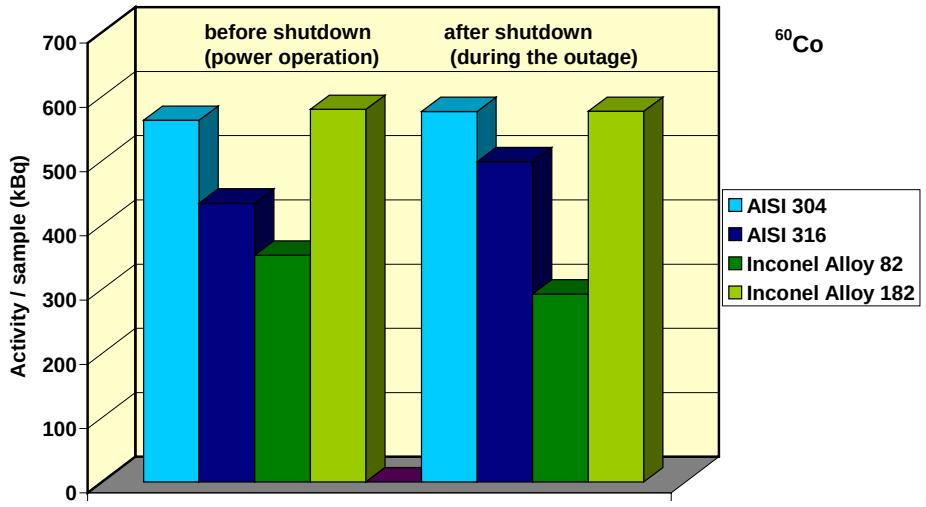

Figure 5. Activity due to ^{60}Co in material samples removed from the cell before and after the shutdown in May 2001.

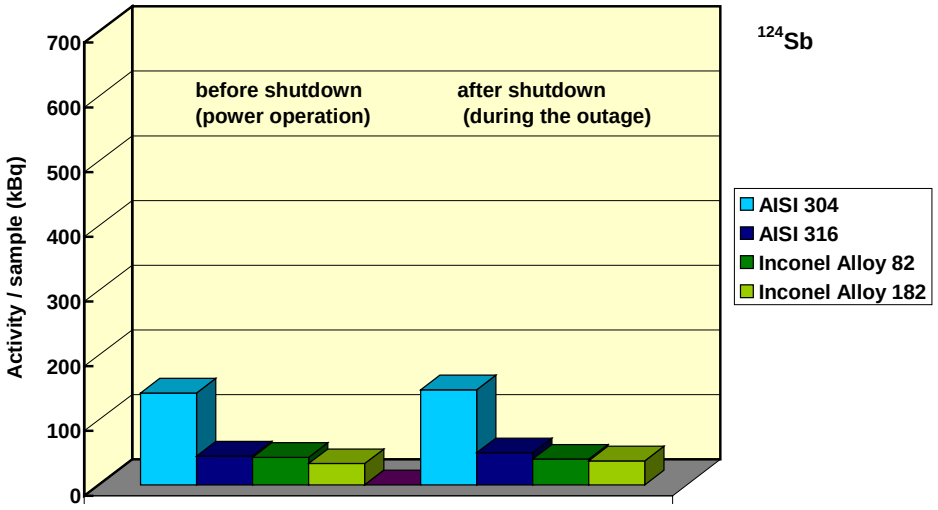

Figure 6. Activity due to ^{124}Sb in material samples removed from the cell before and after the shutdown in May 2001.

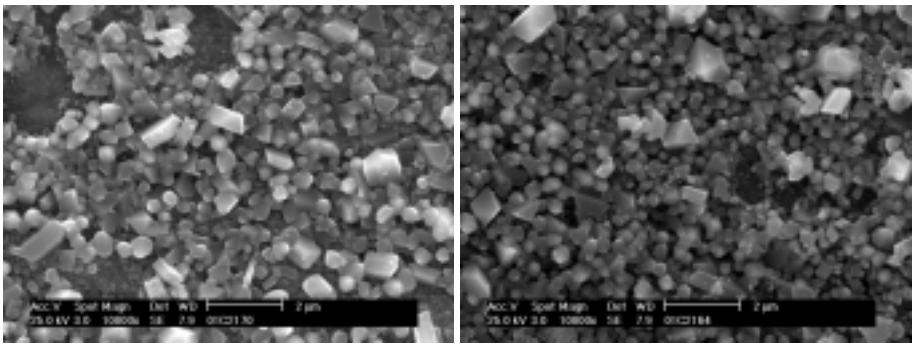

(a) (b)

Figure 7. Scanning electron microscopic (SEM) images of the surface of the AISI 316L(NG) sample removed from the cell (a) during power operation before the shutdown in May 2001 and (b) during the outage after the shutdown in May 2001. A layer with smaller-sized crystals and slightly larger crystals on top of it can be observed. Some hole-like forms can also be seen.

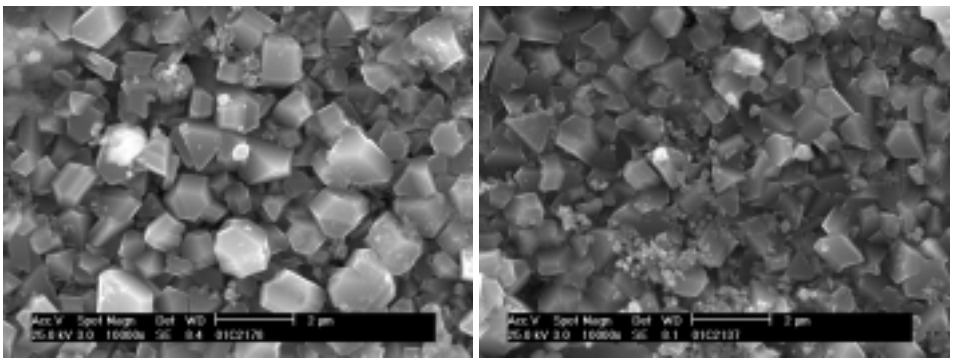

(a) (b)

Figure 8. Scanning electron microscopic (SEM) images of the surface of the Inconel alloy 82 sample removed from the cell (a) during power operation before the shutdown in May 2001 and (b) during the outage after the shutdown in May 2001. A layer with with a relatively uniform crystal size can be seen.

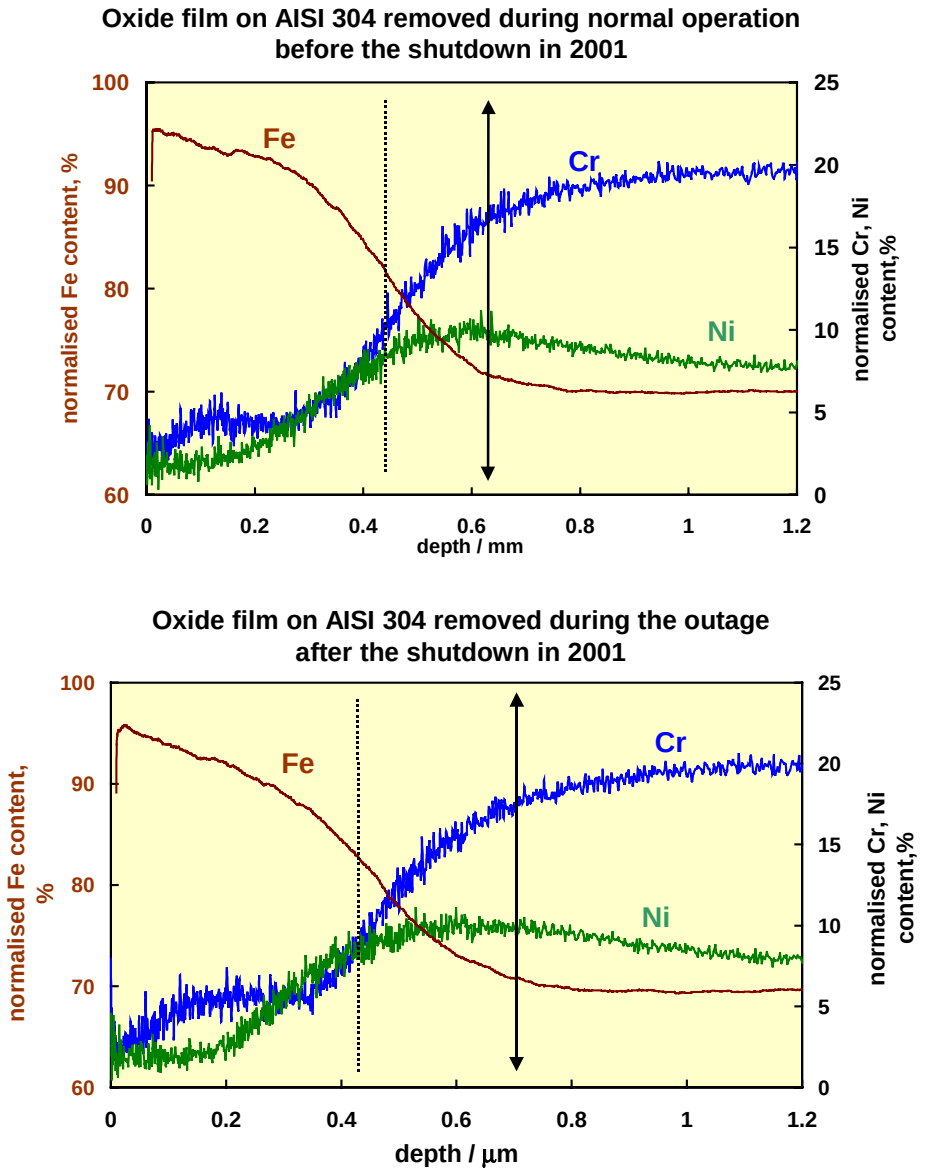

Figure 9. Normalised depth profiles of Cr, Fe and Ni in the oxide film on the AISI 304 sample removed during power operation (a) and outage (b) May 2001. Estimated boundary between the oxide film and the substrate metal indicated by the vertical solid line, while the dashed line is used as an indication of the boundary between the innermost Cr-rich part and the rest of the oxide film.

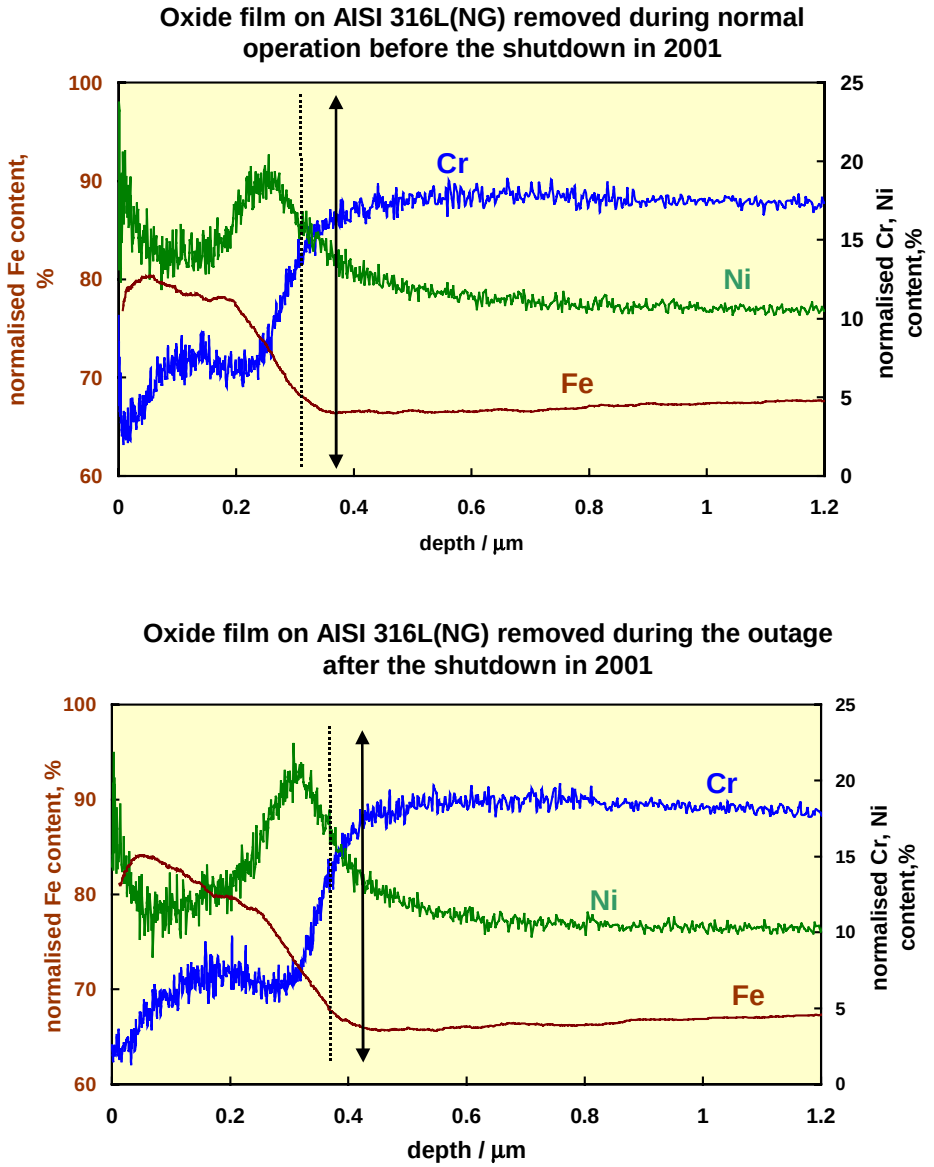

Figure 10. Normalised depth profiles of Cr, Fe and Ni in the oxide film on the AISI 316 L(NG) sample removed during power operation (a) and outage (b). Estimated boundary between the oxide film and the substrate metal indicated by the vertical solid line, while the dashed line is used as an indication of the boundary between the innermost Cr-rich part and the rest of the oxide film.

4. Summary of main observations

The following main observations have been made during the first full fuel cycle of monitoring high-temperature water chemistry in the shutdown cooling system 321 at Olkiluoto unit 1:

- The corrosion potentials of AISI 316 L(NG) stainless steel, AISI 304 stainless steel, Inconel alloy 182 and Inconel alloy 82 are in the range 0–200 mV, which is typical for these materials in BWR plants under normal water chemistry (NWC) conditions.
- Thus the materials are subject to a certain risk for environmentally assisted intergranular stress corrosion cracking.
- The corrosion potentials are not very sensitive to the excursions of SO_4^{2-} and NO_3^- contents in the coolant.
- The high-temperature conductivity of the coolant has proven to be a sensitive indicator of changes in the anionic impurity content and temperature variations of the coolant.
- Decrease of the power output of the plant leads to an increase of the temperature in the cells of the shutdown cooling system 321.
- Repeated maxima in the high-temperature conductivity of the coolant occur because of the release of impurities from ion exchange resins.
- The high-temperature conductivity of the coolant may also partly reflect the changes in the chromate content of the coolant.

During almost the whole monitoring period June 2000 – May 2001, the following general trends have been observed:

- The potentials decrease with time.
- The high-temperature conductivity decreases with time.

The decrease of potentials may be partly related to changes in the chromate content of the coolant, and also the decrease in conductivity could be partly correlated with the chromate content. It is, however, more likely that the observed trends are mainly associated with the operational features of the reference electrode, and probably also of the conductivity electrode.

Concerning the samples in the material sample cell, the following main observations have been made about activity incorporation and the oxide films formed on material surfaces:

- The main contributors to the total activity measured in material samples are isotopes ^{54}Mn, ^{58}Co ^{60}Co and ^{124}Sb that have also been found to be present in the coolant.
- The position of the sample in the material samples cell has been found not to have a significant influence on the incorporation of radioactive species which may be regarded as a verification of the experimental arrangement.
- The compositions of the films on stainless steel samples and on the Inconel alloys are significantly different:
  - the films on stainless steel samples comprise of an outer part rich in Fe, a middle part rich in Ni and an inner part rich in Cr.
  - the films on Inconel alloy 82 comprise of an outer part rich in Ni and an inner part rich in Cr.
  - the films on Inconel alloy 182 comprise of an outer part rich in Ni and Fe and an inner part rich in Ni and Cr.
- The films on AISI 304 and Inconel alloy 182 tend to incorporate more ^{60}Co than the films on AISI 316 L(NG) and Inconel alloy 82.
- The films on AISI 304 and Inconel alloy 82 tend to incorporate more ^{58}Co than the films on AISI 316 L(NG) and Inconel alloy 182.
- The different behaviour of the isotopes ^{58}Co and ^{60}Co can only be explained if they are present in different forms, e.g. as dissolved ions and as colloids or particles, in the coolant. Such differences may be an indication of the different origin of the two isotopes.
- The lower amount of Co incorporation into the films on AISI 316L(NG) may be connected with the minimum of Cr content and the maximum in Ni content in the middle part of the film.
- The films on AISI 304 incorporate more ^{124}Sb than the other alloys.
- The thickness of the films on Inconel alloy 82 is slightly higher and that of the films on Inconel alloy 182 considerably higher than that of the films on the stainless steel samples.

- The higher thickness of the oxide film on Inconel alloy 182 compared to the thickness of the film on Inconel alloy 82 coincides with the higher level of activity due to ^{60}Co measured on Inconel alloy 182. The level of ^{124}Sb incorporation is however similar on both materials.
- The effect of the shutdown on activity incorporation is relatively small: The activity levels in stainless steel samples tend to increase slightly during the shutdown while an opposite trend is observed for Inconel alloy 82.
- The thickness of the oxide films on AISI 304, AISI 316L(NG) and Inconel alloy 182 increases during the shutdown, but an opposite trends is observed for the film on Inconel alloy 82.

To summarise, marked differences have been observed in the incorporation of different radioactive isotopes in the oxide films on different materials. The higher extent of incorporation of ^{60}Co in Inconel alloy 182 than in Inconel alloy 82 may be connected with the considerably higher film thickness on the former material. However, the ^{124}Sb content in the oxide films on these two Inconel alloys is similar. In addition, the total activity levels as well as the levels of ^{60}Co and ^{124}Sb in the oxide films on AISI 304 are higher than what is measured on AISI 316L(NG) samples, even though no clear difference in oxide thickness can be found. These observations indicate that the film thickness is not the only factor determining the amount of incorporation of different nuclides into the films. The incorporation of Sb may for instance be highly related to phenomena at the very surface of the oxide film. In addition, the largely different composition of the films on stainless steels and on the Inconel alloys is likely to influence significantly the incorporation of radioactive isotopes.

5. Conclusions

The monitoring unit employed at Olkiluoto 1 provides relevant high-temperature water chemistry information that can be well used both for assessing long-term trends and for sensitive detection of rapid changes in the coolant environment.

Also the material sample cell at Olkiluoto 1 has been verified to give a representative view of activity incorporation and oxidation of construction materials in the primary coolant.

The results have indicated marked differences between the behaviour of different isotopes and different materials. It has become evident that the thickness of the oxide film is not the only factor that correlates with the extent of activity build-up. The different composition and structure of the films on stainless steels and Inconel alloys, as well as differences at the very surface of the oxide film may have a significant influence on the activity incorporation.

An interesting phenomenon that certainly deserves further investigations is the minimum in the Cr content and the maximum in the Ni content in the middle of the films on AISI 316L(NG) and their possible connection to the lower amount of Co incorporation when compared to AISI 304.

More detailed conclusions about the factors contributing to the differences in activity incorporation require, however, experimental data collected during several fuel cycles. Probably also the application of more sophisticated techniques for oxide film analysis have to be looked for or developed.

One additional future prospect is to utilise the cell at Olkiluoto 1 to study the rate of activity incorporation after subjecting part of the material samples to alternative decontamination treatments.

Acknowledgements

This presentation is prepared for a joint Finnish industry group in a project on Structural operability and plant life management (RKK). The project funding by the National Technology Agency (Tekes), Teollisuuden Voima Oy (TVO), Fortum Power and Heat Oy, Fortum Nuclear Services Ltd., FEMdata Oy, Neste Engineering Oy, Fortum Oil and Gas Ltd. is gratefully acknowledged.

The pleasant co-operation with Anneli Reinvall, Erkki Muttilainen and Mika Helin (Teollisuuden Voima Oy, Olkiluoto) is gratefully acknowledged. The valuable contribution of Pekka Nousiainen (Teollisuuden Voima Oy, Olkiluoto) has facilitated significantly the work and arrangements done at the plant. In addition, the efforts of Olli Taivainen, Risto Sillanpää and Seppo Salonen during the activity measurements at the Olkiluoto plant have been of great value.

The *ex situ* analyses would not have been possible without the contributions and expertise of Ulla Ehrnstén, Arto Kukkonen and Marketta Mattila of VTT Industrial Systems, Juha Siiriäinen of Stresstech Oy and Aulis Hakkarainen and Kaarina Myllykangas of Rautaruukki Steel.

References

1. Laitinen, T., Bojinov, M., Betova, I., Mäkelä, K. and Saario, T. The properties of and transport phenomena in oxide films on iron, nickel, chromium and their alloys in aqueous environments, Radiation and Nuclear Safety Authority, STUK-YTO-TR 150, January 1999. 79 p.

2. Bojinov, M., Kinnunen, P., Laitinen, T., Mäkelä, K., Saario, T. and Sirkiä, P. Monitoring of high-temperature water chemistry and characterisation of oxide films on material samples exposed to BWR coolant at Olkiluoto 1 during the fuel cycle 2000–2001. VTT Industrial Systems, Research Report BVAL67-021204, Espoo 2002.

3. Bojinov, M., Kinnunen, P., Laitinen, T., Mäkelä, K., Saario, T. and Sirkiä, P. Monitoring of high-temperature water chemistry and charactterisation of oxide films on material samples exposed to BWR coolant at Olkiluoto 1. VTT Manufacturing Technology, Research Report BVAL67-011125, Espoo 2001.

4. Solin, J. (ed.) Plant life managemet. – Midterm status of a R&D project. VTT Symposium 218, VTT, Technical Research Centre of Finland, Espoo 2001. 268 p. + app. 9 p. (available at http://www.vtt.fi/vtt/results)

Activity incorporation into stainless steel samples in primary coolant at Loviisa 1 during the fuel cycle 2000–2001

Martin Bojinov, Petri Kinnunen, Arto Kukkonen, Timo Laitinen,
Marketta Mattila, Kari Mäkelä, Timo Saario and Pekka Sirkiä
VTT Industrial Systems
Espoo, Finland

Abstract

Increased activity incorporation in primary circuit oxides increases the risks of radiation exposure to the maintenance personnel. In order to find out the factors contributing to activity incorporation and to be able to control them, stainless steel samples with different pre-treatments are exposed to the primary coolant at the cold-leg temperature at Loviisa unit 1 since February 2000. Since then, samples have been regularly removed and replaced with new samples. The activity of the removed samples has been determined, and the oxide films on the samples have been analysed in order to find correlations between the properties of the oxide films and activity incorporation. SEM, SIMS and GDOES techniques have been used for the analysis. An additional task of the project is to find the most suitable surface analysis method for oxide films formed in VVER coolant conditions. In this report the analysis results are given together with the HTWC monitoring data obtained at the plant during the fuel cycle 2000–2001.

High-temperature potential and conductivity monitoring data are in agreement with the coolant chemistry during the fuel cycle. They indicate no deviations from normal plant operation. The main contribution to the activity levels in the studied samples is due to the ^{124}Sb and ^{110m}Ag isotopes. In addition to these two isotopes, also the activity of ^{60}Co is of outmost importance, because of the long half life. Incorporation of ^{60}Co, ^{58}Co, ^{54}Mn and ^{110m}Ag does not seem to depend on the pre-treatment of the sample. On the other hand, incorporation of ^{124}Sb is much more pronounced into the ground samples than into the pre-oxidised samples. For ^{60}Co, the activity increases mainly during the period including the outage, the subsequent start-up and the first five months of operation. The most

significant variations in the rate of activity increase during the whole period are observed for ^{124}Sb.

SEM micrographs from the top of the samples indicate that pre-treatment has an impact on the appearance of the oxide films. The oxide films on the surfaces of ground samples exhibit a larger number of small crystals than those on the surfaces of the pre-oxidised samples. On pre-oxidised samples also some fairly large crystals exist. The results indicate that the activity levels do not directly correlate with the thickness of the film. On the other hand, the composition and distribution of alloying elements seem to have a significant impact on the activity incorporation. The enrichment of Co seems to be correlated with the presence of Cr and probably also Ni in the films.

In order to obtain more information of the possible influence of the start-up period and of other stages involving significant changes in the chemistry of the coolant, sample sets have to be removed at more frequent intervals in the future. In addition, data from several fuel cycles are needed to establish reliable correlations between the trends in activity incorporation and the history of the plant over the years. Such correlations will facilitate the prediction of possible increase in activity levels on the basis of analysis data from the material sample cell.

1. Introduction

Increased activity incorporation in primary circuit oxides increases the risks of radiation exposure to the maintenance personnel in a nuclear power plant. The extent of activity incorporation on primary circuit surfaces is closely connected to the chemical composition of the coolant water and to the structure and properties of oxide films formed on material surfaces. Changes in operational conditions may change the structure of the oxide films and the rate of activity incorporation. To predict these changes, experimental correlations between water chemistry, oxide films and activity incorporation, as well as mechanistic understanding of the related phenomena need to be established.

A unit consisting of three flow-through cells has been installed in the sampling line of Loviisa unit 1 in order to collect the data needed when looking for such correlations. The cells are being used for two major purposes:

- Observation of the growth, structure and activity incorporation levels of oxide films formed on material samples exposed to the primary coolant at the cold-leg temperature.

- Correlating these observations with chemical and radiochemical data collected by the plant, as well as with high-temperature water chemistry monitoring data such as the corrosion potentials of relevant material samples, the redox potential and the high-temperature conductivity of the primary coolant.

The exposure of stainless steel samples in the present cell unit as well as the monitoring of high-temperature water chemistry at the cold-leg temperature has been started at Loviisa unit 1 on the 7th of February, 2000.

The test materials, procedures and results are described in detail in the report [2]. Previous data can be found in references [3–6].

2. Experimental

2.1 High-temperature cells and sensors

The flow-through cells for monitoring the high-temperature water chemistry and for exposing material samples to the primary coolant have been connected to the sampling line of the primary circuit of Loviisa unit 1 as shown in Fig. 1. The linear flow-rate through the cells is roughly 0.02 m s^{-1}, corresponding to a volume flow rate of 2 l min^{-1}. The photograph shown in Fig. 1 has been taken before the system was insulated thermally to ensure a constant temperature corresponding to the cold-leg temperature of the plant. Due to proper insulation of the sampling line, there has been no need for extra heating of the cell by the electrical heaters connected to the flow-through cell.

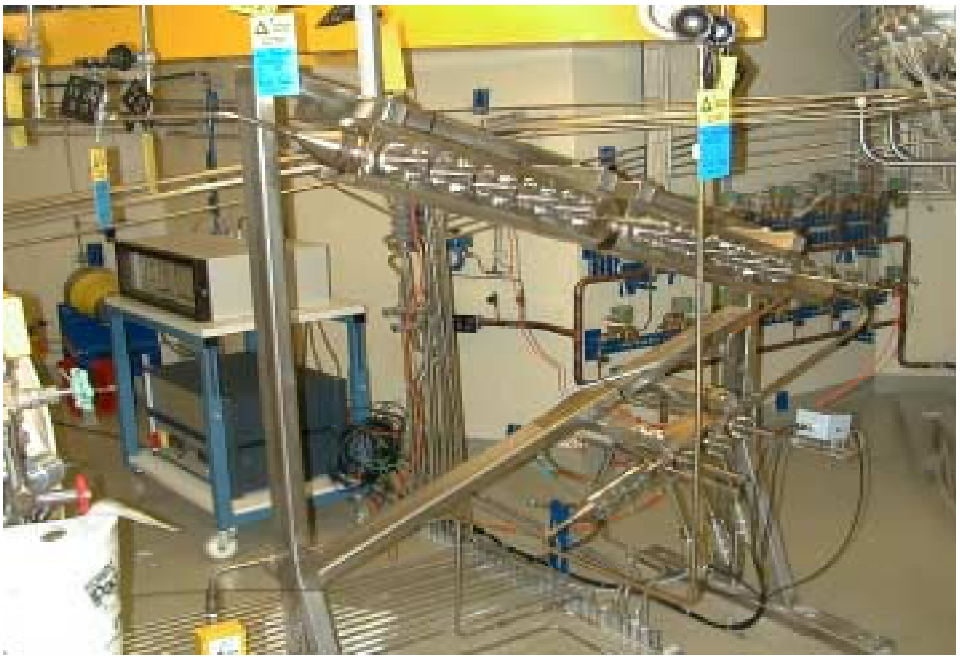

Figure 1. The flow-through cells with high temperature water chemistry sensors and 80 material samples at Loviisa 1 plant.

The coolant enters first the lower cell that contains two AgCl/Ag reference electrodes filled with 0.1 M KCl, one conductivity electrode, one pH electrode, a Pt sample for measuring the redox potential and two separate samples for measuring the corrosion potential (ECP) of AISI 316L stainless steel. The material samples are in the two upper cells that have been positioned close to each other.

2.2 Material samples

Material samples made of 08X18H10T stainless steel and of AISI 316L stainless steel have been installed in the two upper cells in order to simulate the exposure of plant components to the primary coolant. Samples are removed from the cell at pre-scheduled intervals, and the oxide films formed on their surfaces are analysed. The results are correlated with the abundant chemical and radiochemical data such as coolant composition, dose rates etc. measured and

collected routinely at the plant over the years. The two material sample cells contain altogether 80 samples.

The elemental composition of 08X18H10T was determined using optical emission spectrometer (Spectrolab S), resulting in the following composition: 18 wt.% Cr, 10.4 wt.% Ni, 0.05 wt.% C, 0.47 wt.% Ti, 0.15 wt.% Co and balanced with Fe. The composition of AISI 316L is 18 wt.% Cr, 10 wt.% Ni, 3 wt.% Mo, < 0.02 wt.% C balanced with Fe.

The samples have been placed in 20 sample holders each containing two samples of OX18H10T and two samples of AISI 316L with two different pre-treatments as follows:

- Ground samples
  These samples have been cut from a 08X18H10T or an AISI 316L rod and wet ground using 600 grade emery paper and washed with water purified in a Milli-Q® purification system.
- Pre-oxidised samples
  The samples have been first wet ground using 600 grade emery paper and then pre-oxidised in high purity water in a re-circulation autoclave. During the one week pre-oxidation period at 297 ^{o}C, the oxygen content in the re-circulation loop has been kept at 300 ± 30 ppb.

The samples in the sample holder are electronically insulated from the body of the flow-through cell and from each other. Furthermore, the design of the sample holder and the flow-through cell has been optimised to guarantee as similar flow conditions on the surfaces of all the 80 samples as possible.

3. Results

The results of water chemistry monitoring are summarised in Figs 2 to 4 and the results of ex-situ analyses of the material samples are summarised in Figs 5 to 10. A summary and short discussion of the main observations is given thereafter.

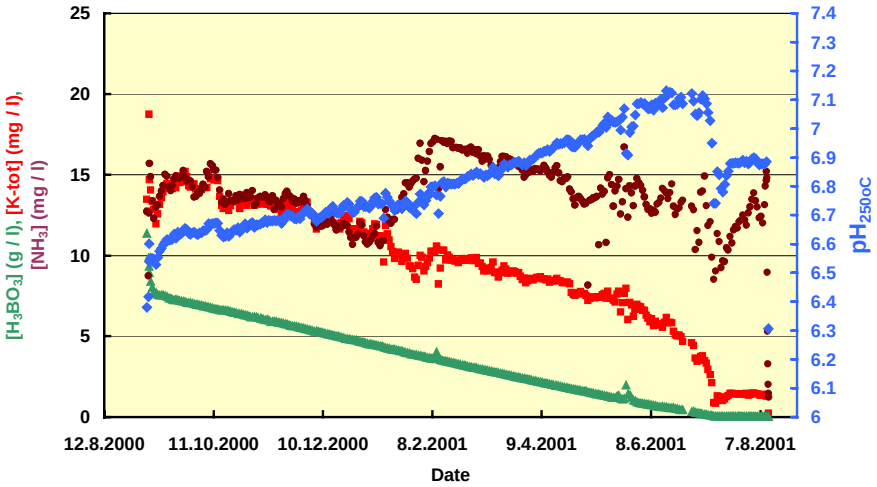

Figure 2. Chemical analysis of the main components of the primary coolant at Loviisa unit 1. The theoretical pH at 250 ℃ is also given, corresponding to the temperature in the monitoring cell.

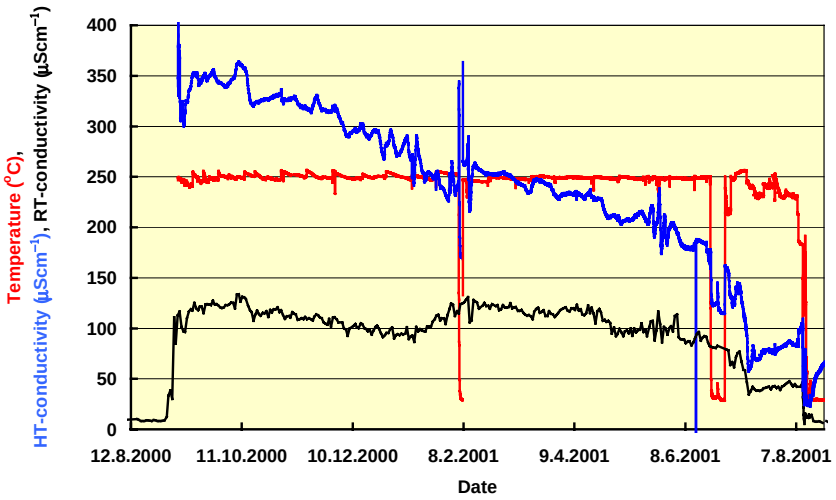

Figure 3. Measured high-temperature and room-temperature conductivities.

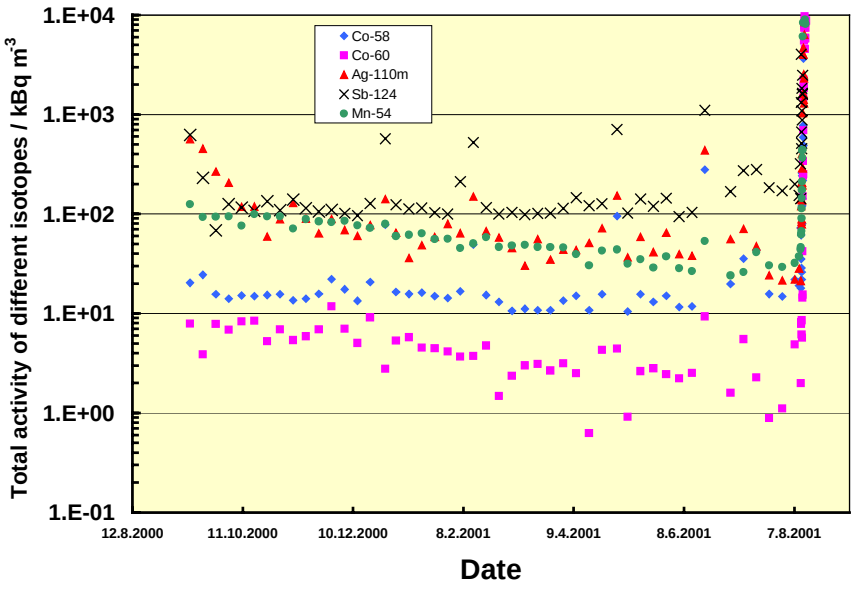

Figure 4. Activity levels of the major isotopes in the primary coolant of Loviisa unit 1 during the previous monitoring period 2000–2001.

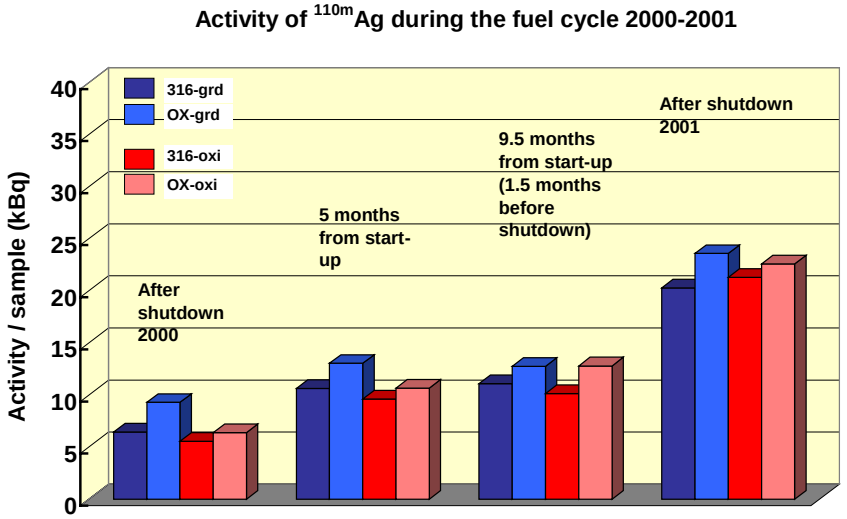

Figure 5. Activity of ^{110m}Ag in samples removed from the material sample cell at different times during the fuel cycle.

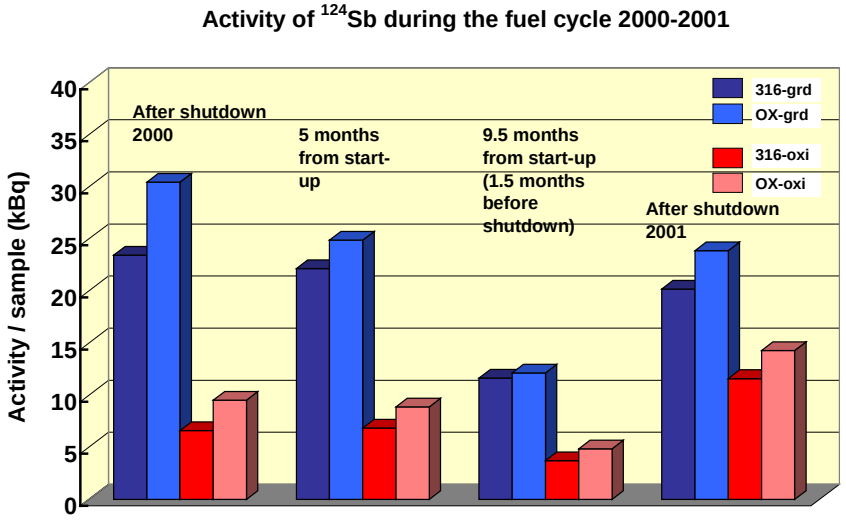

Figure 6. Activity of ^{124}Sb in samples removed from the material sample cell at different times during the fuel cycle.

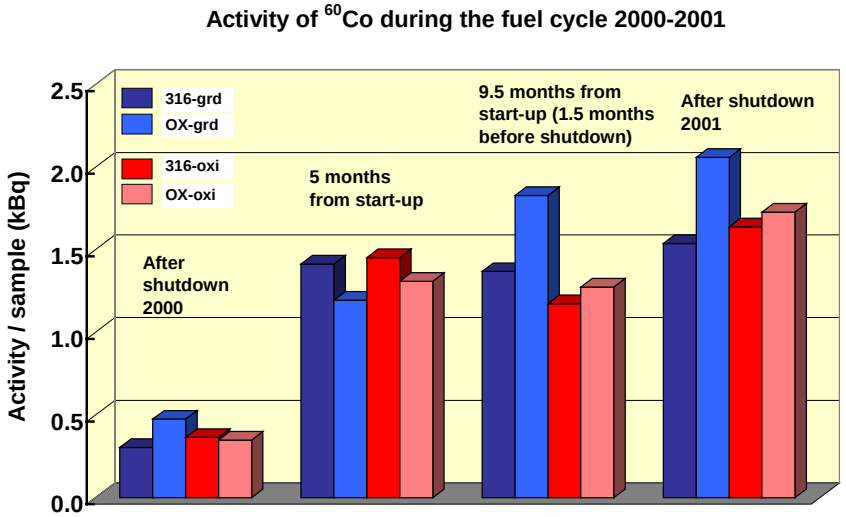

Figure 7. Activity of ^{60}Co in samples removed from the material sample cell at different times during the fuel cycle.

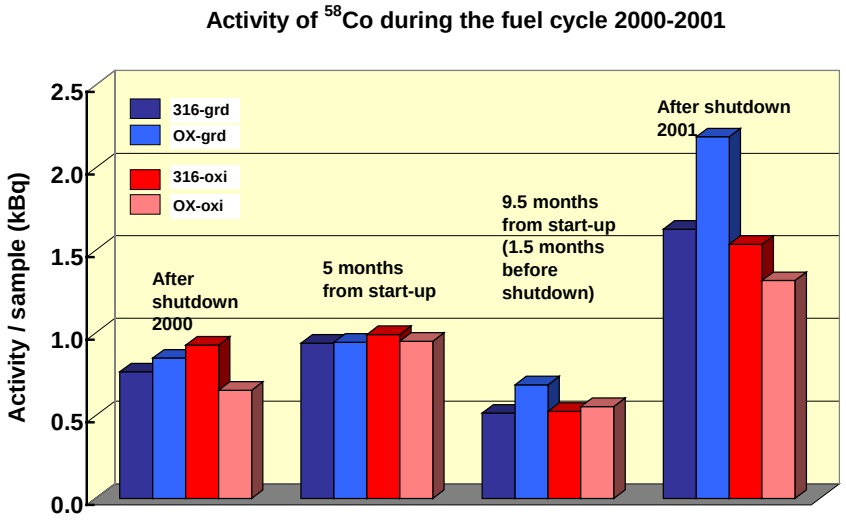

Figure 8. Activity of ^{58}Co in samples removed from the material sample cell at different times during the fuel cycle.

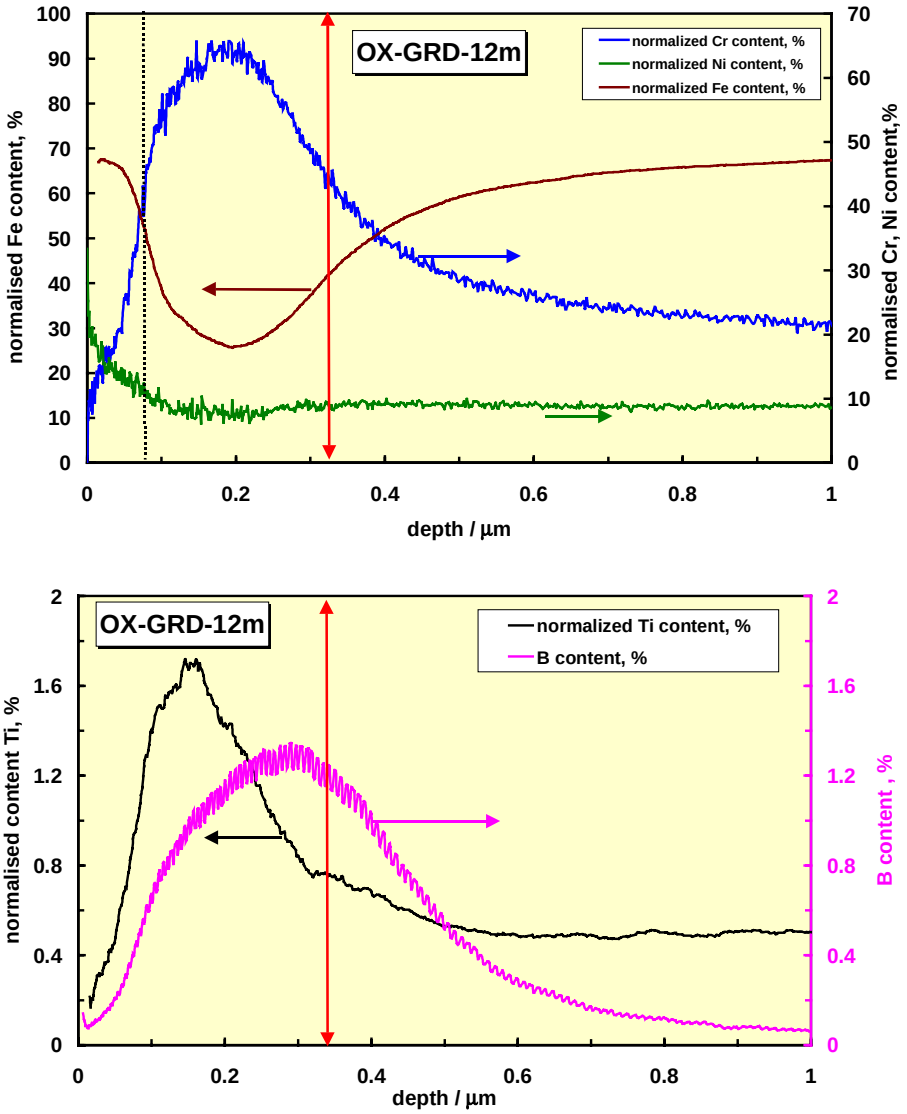

Figure 9. Normalised contents of Fe, Cr, Ni (a) and Ti, B (b) in the ground O8X18H10T sample removed from the sample cell after 5 months from the start-up from the refuelling outage. Estimated boundary between the oxide film and substrate metal is indicated by the vertical red arrow.

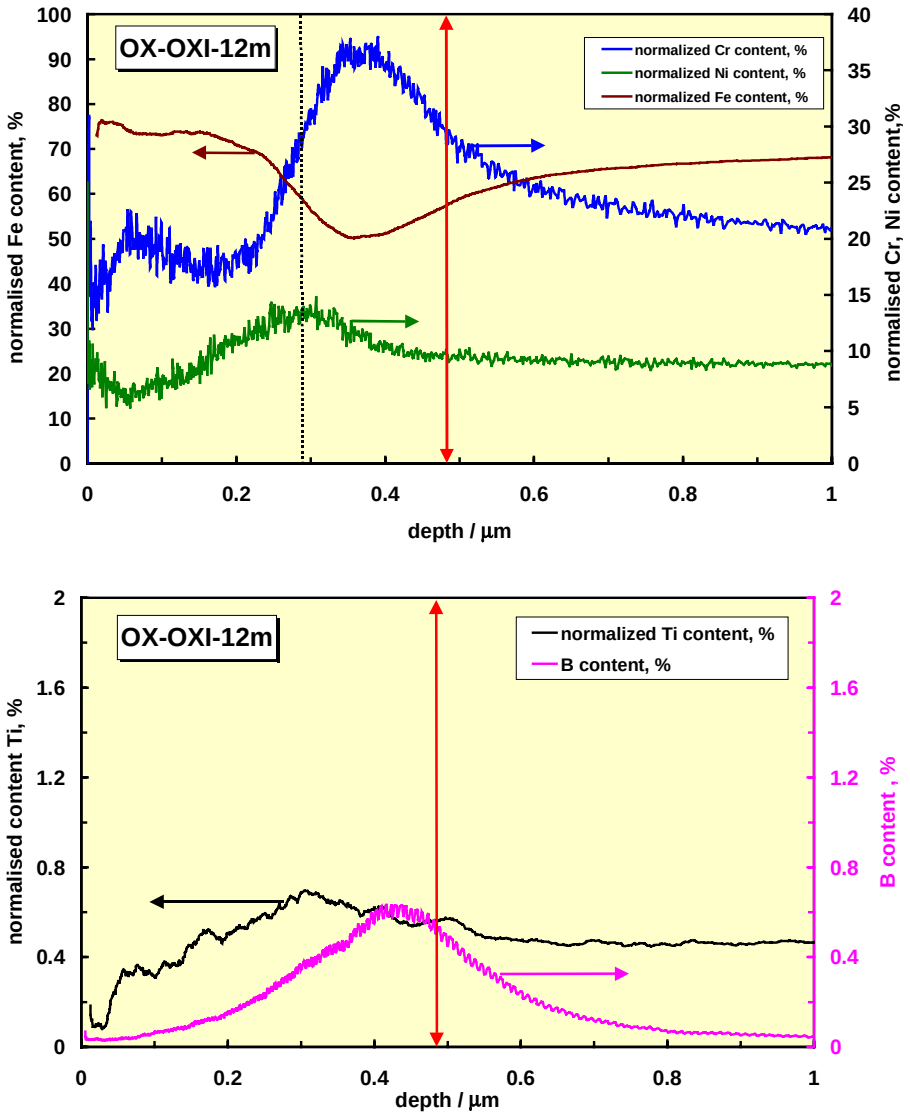

Figure 10. Normalised contents of Fe, Cr, Ni (a) and Ti, B (b) in the pre-oxidised O8X18H10T sample removed from the sample cell after 5 months from the start-up from the refuelling outage. Estimated boundary between the oxide film and substrate metal is indicated by the vertical red arrow.

4. Summary of main observations

The main observations made in this study can be summarised as follows:

- The monitoring of potential and conductivity at high temperature at Loviisa unit 1 correlates well with the data collected routinely at the plant and has indicated a very stable operation with only small variations. It has thus shown that the data collected in this work are relevant to a steady-state operation of a VVER plant and can be used to assess the impact of water chemistry on activity incorporation in such plants.

- SEM micrographs of the top of the samples indicate that the oxide films on ground samples exhibit a larger number of small crystals than those on the pre-oxidised samples. The thickness of the films on pre-oxidised samples is slightly higher than that on the ground samples. The films on all other samples except on pre-oxidised O8X18H10T seem to become thinner during the period including the shutdown, which may be related to reductive dissolution of iron from the film.

- The main sources of activity in the samples are ^{110m}Ag and ^{124}Sb, which is a typical phenomenon on fresh surfaces. In addition to these two isotopes, also ^{60}Co is of outmost importance, because of its long half life.

- The incorporation of antimony into the oxide films on ground samples is significantly higher than into the films on pre-oxidised samples and seems to be a surface related phenomenon as the ground surfaces have a larger number of small crystals and thus a higher surface area. Moreover, thicker films do not incorporate more antimony than thin films.

- The incorporation of ^{124}Sb seems to be highest during the period including the shutdown to refuelling outage, which is in agreement with previous observations [3].

- The rate of increase of the ^{60}Co content in the oxide films is the highest in the beginning of the fuel cycle including the start-up, when compared to the other isotopes, which is also in agreement with previous observations [3]. This behaviour may be due to changes in oxide film composition.

- The profile of Co correlates with the profile of Cr and partly also with that of Ni in the film, exhibiting a maximum close to the metal/film interface.

- Even though the oxide film thickness does not increase markedly during the shutdown period, the higher ^{60}Co content in the coolant during this period results in slightly increased ^{60}Co values.

- The increase in the activity due ^{60}Co is, however, relatively low during the period including the shutdown to refuelling outage.

5. Conclusions

The goal of this ongoing study is to estimate the factors, which affect activity incorporation into oxide films during the different stages of the fuel cycle. In addition, a great deal of effort has been put to search for possible correlations between activity build-up and different pre-treatment of the surfaces of different construction materials. The following conclusions can be drawn on the basis of the existing results:

- The data for the high-temperature water chemistry (HTWC) at Loviisa unit 1 are characteristic of a steady-state operation of a VVER plant and can be used to assess the impact of water chemistry on activity incorporation in such plants.

- A still more efficient use of the HTWC monitoring can probably be obtained during the shutdown and following start-up periods, as well as during possible unscheduled transients. Detailed investigation of HTWC together with on-line measurement of soluble and insoluble species in different time frames of these transients could provide valuable information, because these species may influence significantly the amount of activity incorporated into the films.

- The incorporation of ^{60}Co seems to be strongest during the period including the outage in 2000, the start-up and 5 months of operation. A more efficient removal of ^{60}Co during the start-up period might lead to a general decrease of ^{60}Co levels. The increase of ^{124}Sb levels is associated with phenomena at

the very surface of the oxide film. This can be affected by different surface treatments of the plant components. Possibly samples with for instance electropolished surfaces should be incorporated into the test matrix.

- More detailed and reliable information of the composition and thickness of the film is needed to draw conclusions on the mechanism of and factor affecting the incorporation of different species. This means development of the existing techniques or finding new ways to analyse samples *ex situ*.

- In order to obtain more information of the possible influence of the start-up period and of other stages involving significant changes in the chemistry of the coolant, sample sets are planned to be removed at more frequent intervals during the next fuel cycle.

- Data from several fuel cycles are needed to draw more definite conclusions. Data from a longer period will make it possible to correlate the trends in activity incorporation with the history of the plant over the years. This will facilitate the prediction of possible changes in activity levels on the basis of analysis data from the material sample cell.

- In order to influence the incorporation of radioactive isotopes and to remove them from the surfaces of the primary circuit during different stages of the fuel cycle, more mechanistic understanding of the incorporation of different isotopes is needed. It will be one of the main focuses in future work.

Acknowledgements

This presentation is prepared for a joint Finnish industry group in a project on Structural operability and plant life management (RKK). The project funding by the National Technology Agency (Tekes), Teollisuuden Voima Oy (TVO), Fortum Power and Heat Oy, Fortum Nuclear Services Ltd., FEMdata Oy, Neste Engineering Oy, Fortum Oil and Gas Ltd. is gratefully acknowledged.

References

1. Laitinen, T., Bojinov, M., Betova, I., Mäkelä, K. and Saario, T. The properties of and transport phenomena in oxide films on iron, nickel, chromium and their alloys in aqueous environments, Radiation and Nuclear Safety Authority, STUK-YTO-TR 150, January 1999. 79 p.

2. Bojinov, M., Kinnunen, P., Kukkonen, A., Laitinen, T., Mattila, M., Mäkelä, K., Saario, T. and Sirkiä, P. Activity incorporation into the oxide films on stainless steel samples exposed to primary coolant in Loviisa 1 unit during fuel cycle 2000–2001. VTT Industrial Systems, Research Report BVAL67-021199, Espoo 2001. 52 p. + app.

3. Bojinov, M., Ehrnsten, U., Kinnunen, P., Laitinen, T., Mäkelä, K., Saario, T., Sirkiä, P. and Taivalaho, L. Activity incorporation into the oxide films on stainless steel samples exposed to primary coolant in Loviisa 1 unit. VTT Manufacturing Technology, Research Report BVAL67-011113, Espoo 2001.

4. Sirkiä, Pekka, Saario, Timo, Mäkelä, Kari, Laitinen, Timo and Bojinov, Martin. Changes in oxide films on Ti-stabilised stainless steel samples during exposure to primary coolant at Loviisa units. VTT Manufacturing Technology, Research Report VAL67-001323, Espoo 2000.

5. Mäkelä, K. and Aaltonen, P. X-ray diffraction characterisation of oxide films on primary circuit surfaces at Loviisa unit 2. VTT Manufacturing Technology, Research Report VAL62-980928, Espoo 2001.

6. Solin, J. (ed.) Plant life managemet. – Midterm status of a R&D project. VTT Symposium 218, VTT, Technical Research Centre of Finland, Espoo 2001. 268 p. + app. 9 p. (available at http://www.vtt.fi/vtt/results)

Corrosion of steam generator tube material – effects of chloride and sulphate ions

Martin Bojinov, Petri Kinnunen, Timo Laitinen, Kari Mäkelä,
Timo Saario, Pekka Sirkiä and Kirsi Yliniemi
VTT Industrial Systems
Espoo, Finland

Abstract

Localised corrosion may lead to unscheduled shutdowns and repairs in steam generators in PWR-type nuclear power plants. One possible concern at the Loviisa power plant has been the occurrence of localised corrosion inside the oxide sludge piles on the bottom of the steam generator and in between the tubes within the tube bundle. The sludge piles are formed due to the flaking off the oxide films from the tube surfaces. The chemical conditions within these sludge piles may differ markedly form the bulk water conditions in the steam generators. An important feature of the special conditions is the enrichment of anionic impurities in the pores and crevices inside the sludge piles. Anionic impurities are likely to subject the tube material to localised corrosion.

Our earlier work has shown that the sludge pile material at Loviisa NPP acts as an impurity trap for anions and may thus pose a serious risk for localised corrosion phenomena. The goal of this work has been to assess the effect of high concentrations of anionic impurities (Cl^-, SO_4^{2-}) on the corrosion behaviour of Ti-stabilised stainless steel SG tubes. Experiences and interpretations of the effect of anionic impurities on the corrosion of stainless have been collected from recent literature. Experiments to assess to effect of different anion contents have been carried out in a static Ni autoclave at temperatures corresponding the temperatures at Loviisa SGs. Electrochemical techniques by means of a controlled distance electrochemistry (CDE) arrangement have been used to study the corrosion behaviour of Ti-stabilised stainless steel SG tubes in simulated bulk coolant and in a solution containing high content of chlorides and sulphates, simulating crevice conditions or other environments with high enrichment of impurities. The results of the laboratory experiments show that:

- No features of localised corrosion of 08X18H10T stainless steel are detected in the voltammetric and impedance measurements in solutions containing up to 5000 μg l^{-1} sulphates, chlorides or both of the anions.

- Features of localised corrosion are detected in a solution containing 1000 mg l^{-1} chlorides + 1000 mg l^{-1} sulphates at potentials roughly 1 V more positive than the potential range in the secondary side of Loviisa nuclear power plant during steady state operation.

- Sulphate ions seem to be more aggressive than chloride ions towards the primary passive film on 08X18H10T stainless steel.

The results suggest that the risk of localised corrosion in the studied conditions is not serious. It has to be considered, however, that any factors leading to more oxidative conditions may change the situation significantly.

1. Introduction

Fouling, i.e. the accumulation of sludge has been one of the major failure modes of the vertical steam generators (SG) in PWRs and in horizontal SGs in VVER type reactors. The detrimental role of sludge piles is closely connected with the accumulation of anionic impurities and subsequent formation of an aggressive environment. Green and Hetsroni [1] have studied the phenomena inside a sludge pile and divided the pile into three regions*:* 1) wetted region, 2) alternate wetting and drying region and 3) steam blanketed region, in this order from the top of the pile. They have postulated that the concentration of impurities inside the sludge is high in the region of alternate wetting and drying. The boiling water withdraws the impurities into this area but the bubbles hinder the impurities to flow away. Therefore the impurities accumulate in the area and form an aggressive environment, leading thus to increased risk of localised corrosion [2]. Ösz et al. [3] have investigated the composition of sludge and water impurities and their contribution to the plugging of 837 tubes in the four SG units of PAKS PWR. According to them it is evident that fouling has been a reason for the occurrence of stress-corrosion cracking. The amounts of copper, chloride and sulphate ions in sludge (consisting mainly of Fe_3O_4) removed from the Paks nuclear power plant by chemical cleaning have been found to be:

copper 3–8 g / kg (Fe_3O_4), chloride ions 1–4 g / kg (Fe_3O_4) and sulphate ions below 2 g / kg (Fe_3O_4).

Both units at Loviisa PWR originally started to operate using neutral water chemistry in the secondary side. The oxygen-free feed water and low impurity concentrations resulted in a good condition of the steam generator stainless steel tubes. On the other hand, the low oxygen content of the water in combination with neutral pH caused some erosion corrosion problems in the feed water lines. Thus a decision was made to increase the pH of water by hydrazine injections. During the application of the neutral water chemistry the outermost part of the oxide films at Loviisa SGs were fairly porous and thick. Since the introduction of hydrazine water chemistry in 1994–1995 the oxide films have become thinner and harder. During the last years sludge piles have been found in between the tubes within the tube bundle, particularly near the hot collector areas [4]. Parts of the sludge piles have been mechanically removed during the outage periods. In addition to the introduction of hydrazine water chemistry, changes in the feed water distribution pipe and the increased power output of the plant may have affected the nature of the oxide films. The major concern has been the possibly high concentrations of anionic impurities inside the sludge pile and the effects they may have on the corrosion resistance of the SG stainless steel tubes.

The aim of the present work has been to clarify whether the conditions that may prevail in the steam generators at Loviisa nuclear power plants may pose a hazard to the tubes made of Ti-stabilised stainless steel, 08X18H10T. The main part of the work has been carried out as a diploma thesis. Some parts of the literature survey of the thesis are first summarised below. The main focus of the present report is on the experimental determination of the influence of different anion contents on the behaviour of the Ti-stabilised stainless steel 08X18H10T in simulated secondary side water.

Literature data and comprehensive description of the current results are given in the report [5].

2. Experimental

To demonstrate how features of localised corrosion can be detected in measurements with electrochemical techniques, we show and discuss below a cyclic voltammogram and an impedance spectra of a system undergoing localised corrosion.

2.1 Cyclic voltammetry

The typical potential programme for the detection of stable pit propagation is as follows: first, the specimens are left at their open circuit potential (OCP) for 15 min. Pits are then initiated by a cyclic polarization test conducted above OCP, and their generation starts to dominate the current vs. potential curve at the potential E_{gp} (pit generation potential). When the current density reached a predefined critical value (typically 50–200 $\mu A\ cm^{-2}$), the potential is reversed in the negative sweep direction. During the negative sweep, the current density still increases and stabilizes typically at values between 1–10 $mAcm^{-2}$ due to stable pit growth.

Summarising, two main features in a cyclic voltammogram indicate the occurrence of pitting corrosion: a sharp increase of the current at a certain critical potential (usually statistically distributed around a mean value) and a continuing significant increase of the current after the reversal of the sweep direction from positive to negative.

1.2 Electrochemical impedance spectroscopy

In the presentation of results of electrochemical impedance measurements, the magnitude of impedance, |Z|, and the phase angle between the potential and current, ϕ, can be plotted against the measurement frequency, f. This is the so-called Bode plot. Another possibility for plotting is the complex-plane plot in which the real part of impedance, ReZ, is plotted versus the imaginary part of impedance, ImZ, so that frequency, f, is a parameter.

If the curve of the Nyquist plot is completed to a semi-circle, the high frequency intersection of the ReZ-axis and the curve would give the resistance of the electrolyte and the diameter of the circle gives the charge transfer resistance. At high frequencies the reaction is controlled by the kinetics of the electron transfer reaction. The line approximately at an angle of 45º "after" the semi-circle shows that the reaction is controlled totally by linear diffusion at low frequencies.

1.3 Test conditions, electrodes and materials

All the measurements have been done in an autoclave made of nickel. The test temperature was 250ºC and pressure 50–60 bar. The system was bubbled with pure nitrogen gas (99.999%, AGA) for an hour to remove oxygen from the electrolytes.

The solutions used to simulate secondary side coolant with different anion contents were made using solid NaCl (Baker, The Netherlands) and Na_2SO_4 (Baker, The Netherlands) dissolved in MQ purified water. The pH of all electrolytes was adjusted to 9.2 at room temperature either by 25% NH_3 (Merck, Germany) or 25% NH_4OH (Baker, The Netherlands). The theoretical pH value is between 8–9 in pure ammonia water at 250 ºC.

The experiments can be divided into four parts: measurements a) in water containing only ammonia, b) in NaCl solutions, c) in Na_2SO_4 solutions and d) in solutions containing both NaCl and Na_2SO_4. All the solutions were made in water containing ammonia.

3. Results

A complete description of the results is given in the report [5]. As examples, two voltammograms are shown in Fig. 1, four Nyquist plots in Figs 2–3 and SEM micrographs in Fig. 4.

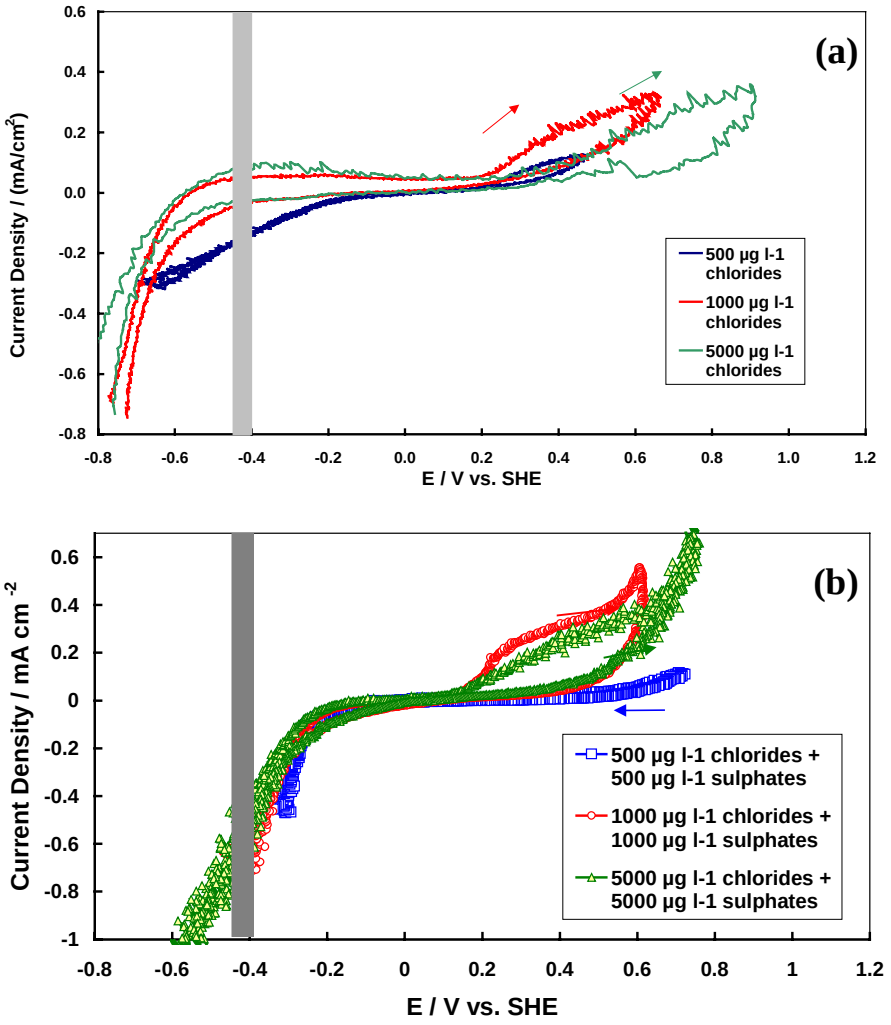

Figure 1. The voltammograms of 08X18H10T in ammonia solutions containing only chloride ions (a) and both chloride and sulphate ions (b) at 250 ^{o}C. Sweep rate is 1 mVs^{-1}. The grey area is the potential range of operation conditions in Loviisa nuclear power plant.

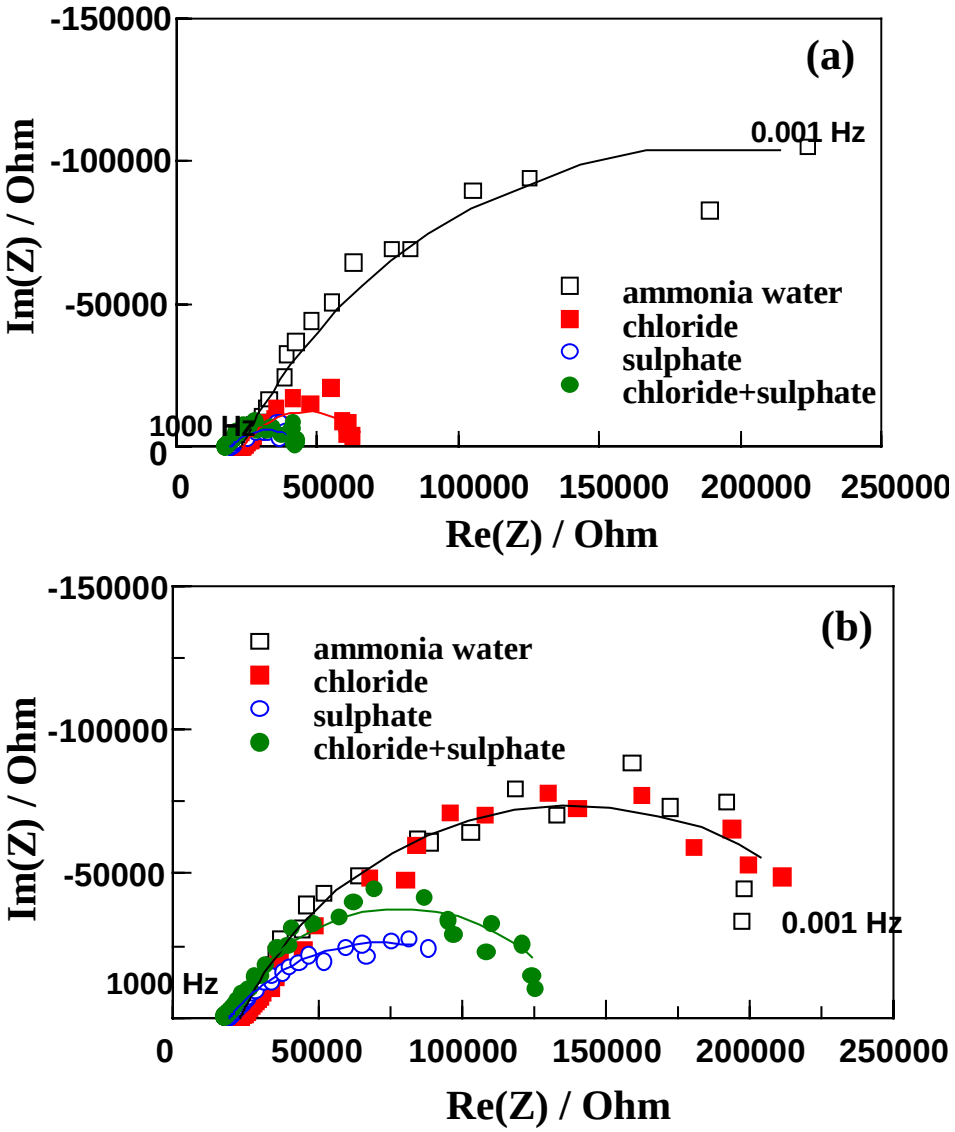

Figure 2. The Nyquist plots of 08X18H10T in water containing only ammonia, 500 μg l^{-1} Cl^- + ammonia, 500 μg l^{-1} SO_4^{2-} + ammonia and 500 μg l^{-1} Cl^- + 500 μg l^{-1} SO_4^{2-} at –0.2 V_{SHE} (a) and 0 V_{SHE} (b).

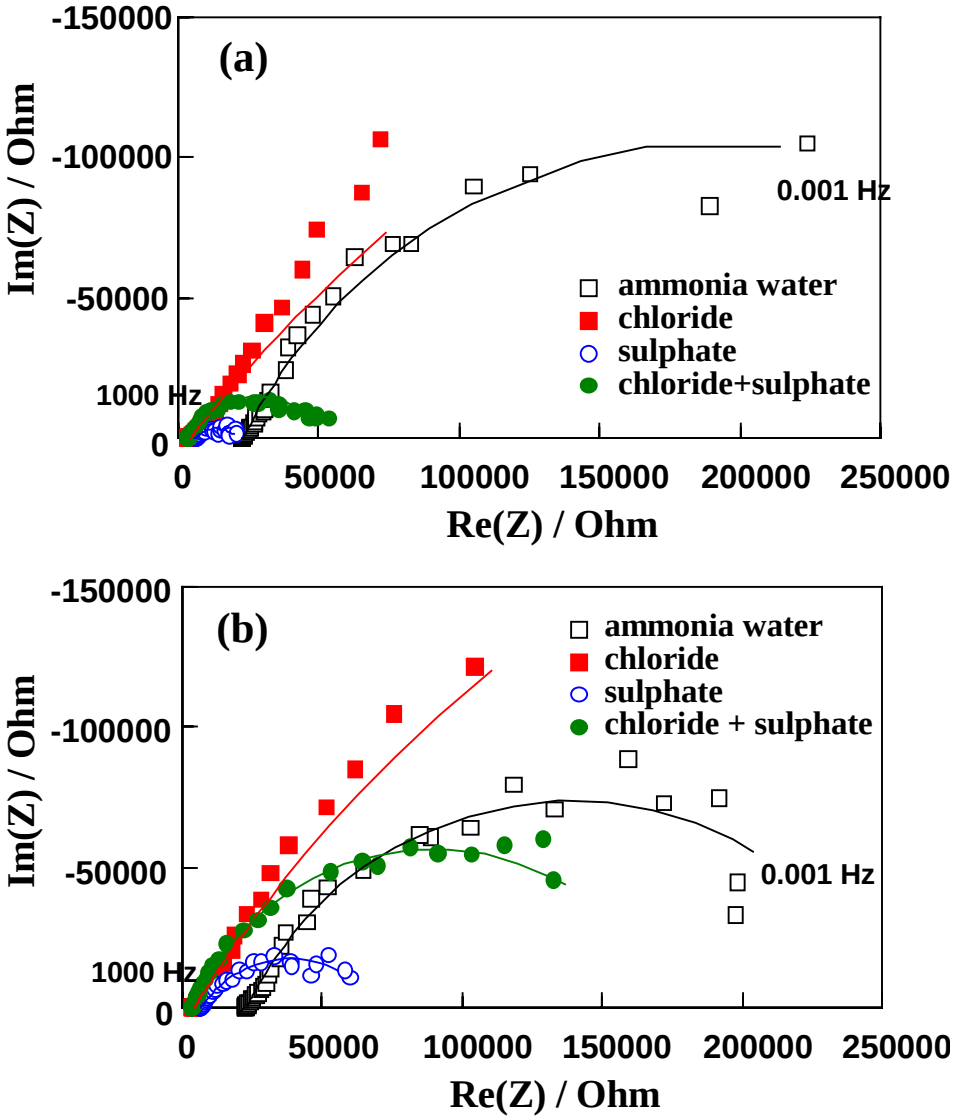

Figure 3. The Nyquist plots of 08X18H10T in water containing only ammonia, 5000 μg l^{-1} Cl^- + ammonia, 5000 μg l^{-1} SO_4^{2-} + ammonia and 5000 μg l^{-1} Cl^- + 5000 μg l^{-1} SO_4^{2-} at –0.2 V_{SHE} (a) and 0 V_{SHE} (b).

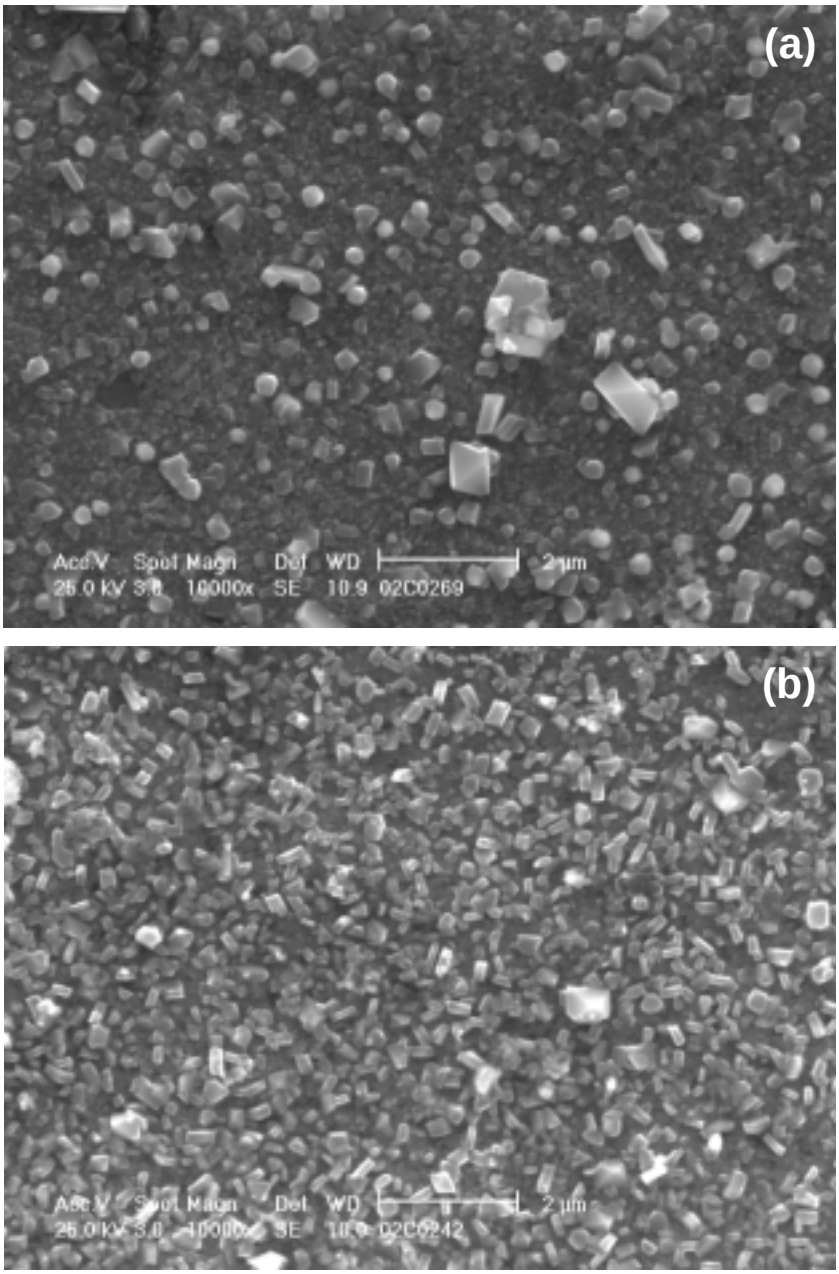

Figure 4. SEM micrographs of the top of the 08X18H10T samples after exposure to ammonium water containing a) no anions (78 hrs), b) 5000 µg l^{-1} Cl^- (141 hrs), c) 5000 µg l^{-1} SO_4^{2-} (95 hrs) and d) 5000 µg l^{-1} Cl^- + 5000 µg l^{-1} SO_4^{2-} (118 hrs) at 250 °C. The exposure time is shown in brackets.

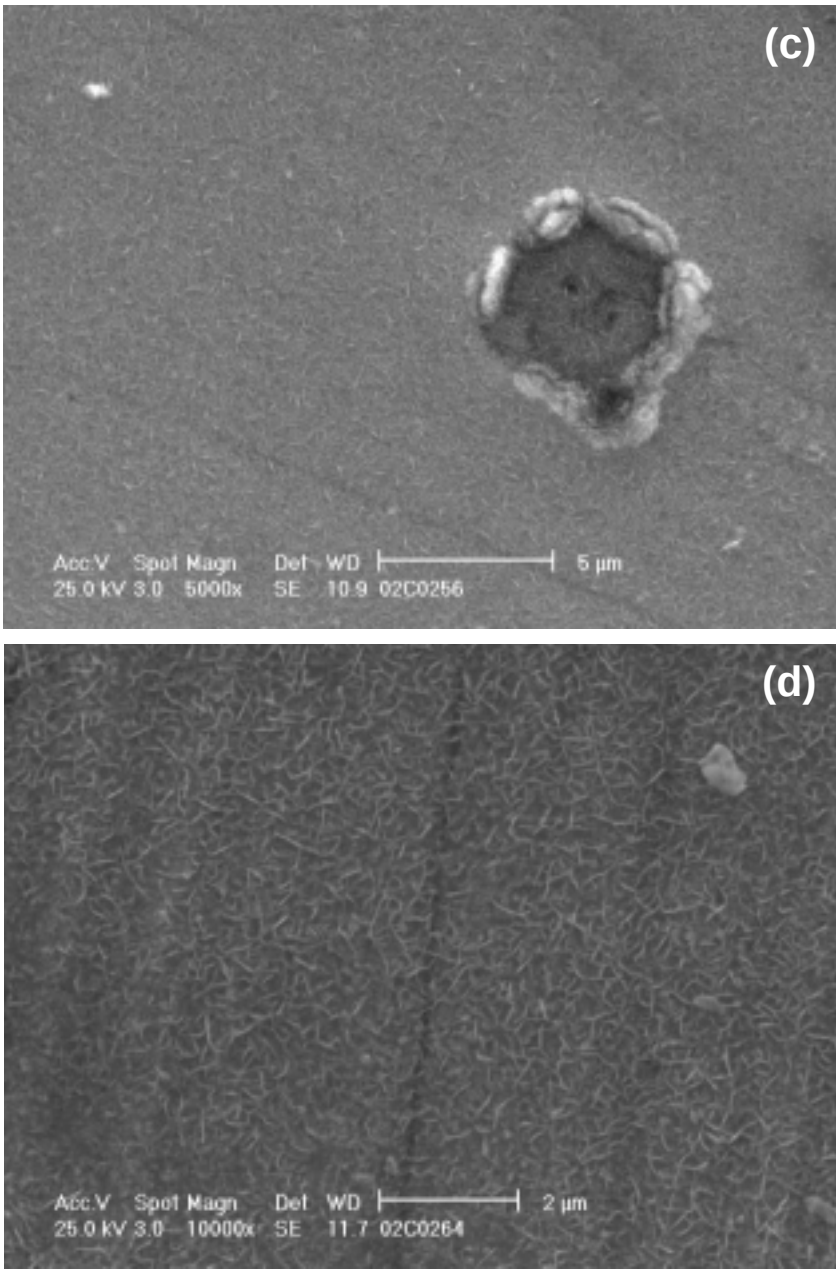

Figure 4 (continued). SEM micrographs of the top of the 08X18H10T samples after exposure to ammonium water containing c) 5000 µg l^{-1} SO_4^{2-} (95 hrs) and d) 5000 µg l^{-1} Cl^- + 5000 µg l^{-1} SO_4^{2-} (118 hrs) at 250 °C.
The exposure time is shown in brackets.

4. Conclusions

The following conclusions concerning the basic understanding of the effect of anionic impurities on corrosion can be drawn on the basis of the present study:

- Chloride ions seem to hinder the secondary passivation but sulphate ions are more aggressive towards the primary passive film.

- The presence of chloride ions together with sulphate ions eliminate the most aggressive behaviour of sulphate ions towards austenitic stainless steel.

- Chloride ions change the potential region of primary passivity in a negative direction and sulphate ions in a positive direction.

- Even though the electrochemical measurements do not show any serious risk of localised corrosion, SEM micrographing showed pit-like features on some sample surfaces. Thus the electrochemical methods are not sufficient to totally exclude the possibility of localised corrosion on 08X18H10T in solutions containing chlorides or sulphates.

At the practical level following conclusions about the effect of anionic impurities on 08X18H10T can be made:

- Chloride ions and sulphate ions have a corrosive effect on 08X18H10T but no serious localised corrosion was observed.

- Sulphate ions seem to be more aggressive than chloride ions towards the primary passive film on 08X18H10T. Therefore a low concentration of sulphate ions in secondary side water is more crucial than a low concentration of chloride ions when considering corrosion phenomena in steam generators.

- When concerning the stability of 08X18H10T the presence of chloride ions together with sulphate ions in the secondary side water is more beneficial than the presence of only one of them.

Acknowledgements

This presentation is prepared for a joint Finnish industry group in a project on Structural operability and plant life management (RKK). The project funding by the National Technology Agency (Tekes), Teollisuuden Voima Oy (TVO), Fortum Power and Heat Oy, Fortum Nuclear Services Ltd., FEMdata Oy, Neste Engineering Oy, Fortum Oil and Gas Ltd. is gratefully acknowledged.

Co-operation with Thomas Buddas, Magnus Halin and Kimmo Tompuri (Loviisa Power Plant) is gratefully acknowledged.

References

1. Green, S. J. and Hetsroni, G. PWR Steam Generators. *Int. J. Multiphase Flow* **21** (1995), pp. 1–97.

2. Strikantiah, G. and Chappidi, P.R. Particle deposition and fouling in PWR steam generators. *Nuc. Eng. Des.* **200** (2000), pp. 285–294.

3. Ösz, J., Salamon, T., Nagy, O. and Tilky, P. Results of Secondary Side Water Regime Modifiacation in Nuclear Power Plant Paks. 5th International Seminar on Primary and Secondary Side Water Chemistry of Nuclear Power Plants, Eger 2001.

4. Bojinov, M., Buddas, T., Halin, M., Kinnunen, P, Laitinen, T., Mäkelä, S., Saario, T., Sirkiä, P. and Tompuri, K. Corrosion of steam generator tubes inside the horizontal SGs in Loviisa PWR, a paper proposed to *4th CNS International Steam Generator Conference.*

5. Bojinov, M., Kinnunen, P., Laitinen, T., Mattila, M., Mäkelä, K., Saario, T., Sirkiä, P., Yliniemi, K. Corrosion of tube material of steam generators at Loviisa NPP – effects of chloride and sulphate ions. VTT Industrial Systems, Research Report BVAL67-021200, Espoo 2002. 35 p.

Zircaloy-2 cladding materials – effect of microstructure on corrosion properties

Martin S. Bojinov, Lena Hansson-Lyyra, Timo Laitinen,
Timo Saario and Pekka Sirkiä
VTT Industrial Systems
Espoo, Finland

Abstract

The earlier results obtained in the controlled distance electrode (CDE) arrangement showed that the thin-layer electrochemical impedance and the contact electric impedance measurements provided similar information of the corrosion reactions of the oxide films of different types of Zircaloy-2 specimens. To gain information on the properties of the zirconia corrosion films only, the corrosion reactions taking place in the water was eliminated. To improve the statistical reproducibility of the impedance measurements, a new disc type specimen was introduced. The specimens made of Zr and of Zircaloy-2 tube materials were exposed to simulated BWR water at 300°C for four days, after which their thin oxides were measured by performing the contact impedance measurements in the water. Therefore, the autoclave was evacuated at 300ºC and filled with nitrogen. The additional contact impedance measurements in N_2 were performed at temperatures ranging from 300°C down to 100°C. As a result of the measurements in N_2, the contribution of the conductivity of the oxide film could be distinguished from the impedance spectrum measured in the water. The thickness of the oxide films was determined later from metallographic samples using scanning electron microscope (SEM). However, the observed difference between the conductivity of the oxide films of the two Zr and Zircaloy-2 specimens were not larger than the accuracy of the impedance measurements.

1. Introduction

The experiments performed last year using the controlled distance electrode (CDE) arrangement and five different types of Zircaloy-2 specimens indicated that the electrochemical thin layer measurements and contact electric resistance measurements provided basically similar information of the transport processes and corrosion reactions of the four-day oxide films formed on the specimens [1]. Therefore, it was not possible to distinguish between the electronic properties and the corrosion reactions of the oxides formed on the individual Zircaloy specimens, in spite of their different second phase particle structures and hydride contents. This was not an expected result, since local variations of the second phase particles in the base materials are expected to affect the electrical resistance of the oxides films. To obtain information on the electrical properties of the oxide films alone, and to eliminate the contribution of the corrosion processes, the contact impedance spectra of one of the specimens was measured also in N_2 atmosphere. A new disc type specimen made of Zr and Zircaloy-2 tube materials was introduced.

2. Experimental

2.1 Test specimens

New disc type specimens were made of zirconium tube (99.8% Zr) supplied by Goodfellow and Zircaloy-2 (Zr/1.5Sn-0.17Fe-0.10Cr-0.07Ni) cladding tube material supplied by ANP Framatome. The discs having diameters roughly 5 mm were cut from the tubes by a diamond saw and the edges were rounded with a side cutter. To prepare the working electrodes for the electrochemical measurements a zirconium wire connected to a silver-plated copper wire with a screw connection was spot welded to both specimens. The electrical connections were insulated by PTFE tape.

2.2 Simulation of coolant conditions

The tests were carried out using the CDE arrangement inserted into an autoclave. The details of the electrochemical measurement system have been described in the previous report [1]. The autoclave was connected to a high-temperature re-circulation loop simulating BWR coolant conditions at 300°C and at 10 MPa. The measurements were carried out at the open circuit potential. The measured inlet oxygen content of the water was slightly less than 300 ppb and the conductivity of the water less than 0.2 μScm^{-1}.

2.3 Gaseous atmosphere

After the electrochemical impedance measurements in the water the autoclave was drained off while simultaneously filling it up with pure nitrogen at 300°C. The subsequent contact impedance measurements of the Zircaloy-2 specimen were performed in the gas atmosphere at temperatures ranging from 300°C down to 100°C.

2.4 Electrochemical measurement techniques

The autoclave was equipped with a Zr or Zircaloy-2 working electrode, an Ir quasi-reference electrode and a Pt counter electrode. The measurements were started by increasing the temperature of the water to 300°C. The contact electric resistance CER measurements during the initial fast growth of the oxide were performed by moving the electrodes periodically apart to expose the specimen to the water. For Zircaloy-2 specimens the time to reach the maximum resistance is typically few hours, after which the growth of the oxide is so slow that it is assumed to stay in an unchanged state during subsequent measurements. After a four-day exposure the oxide films of the specimens were measured using thin layer electrochemical impedance spectroscopy and contact electric impedance spectroscopy. The autoclave was evacuated and the following contact impedance measurements of the Zircaloy-2 specimen were carried out in dry nitrogen, assuming that the oxide growth does not take place in the nitrogen. A Solartron 1287 / 1260 system (galvanostatic zero dc current mode, amplitude 30 μA rms) was used for the TLEIS and CEI measurements.

3. Results

3.1 SEM and oxide thickness

After the electrochemical measurements the specimens were removed from the autoclave. To prepare metallographic samples they were coated with gold, hot mounted in phenolic mounting resin, ground and finally polished with 3 μm diamond paste. To determine the thickness of the four-day oxide films formed on the specimens during their 4-day exposure to simulated BWR water, the cross-section surfaces of both metallographic samples were examined using a Philips XL30 ESEM scanning electron microscope (SEM). The thickness of the oxide films on the specimens were determined directly from the cross-sectional SEM images.

The oxide film formed on the Zr specimen during the four-day exposure is shown in Fig. 1. The oxide was very uneven and the film thickness varied from less than 1 μm up to 3 μm, the average value being roughly 2 μm. Fig. 2 shows a micrograph of the relatively uniform oxide film formed on Zircaloy-2 during the four-day exposure. The oxide thickness values varied from roughly 0.2 μm to 0.4 μm and the average value was 0.30 μm.

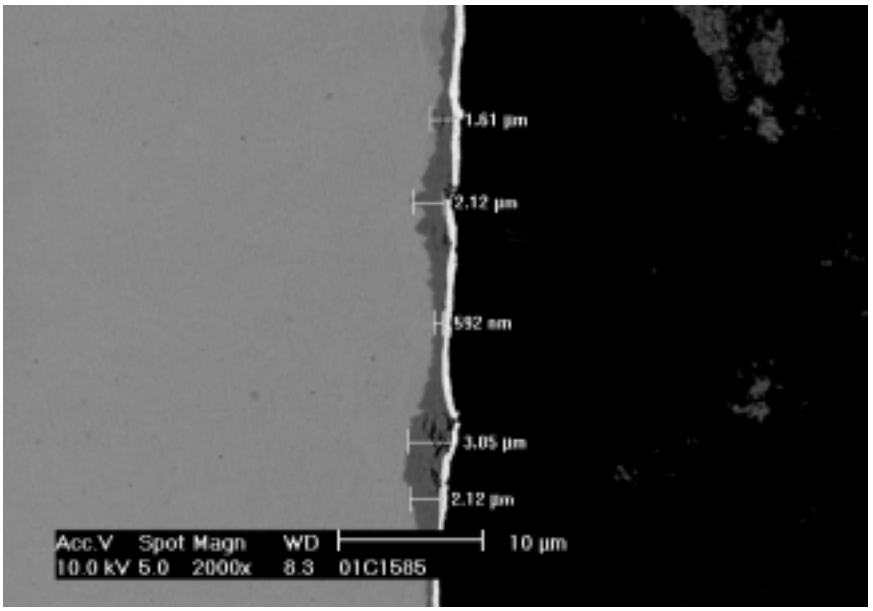

Figure 1. SEM micrograph of the cross-section surface of Zr disc specimen after four-day exposure to simulated BWR water (gold plating on the dark grey oxide shown as a white layer), magnification 2000X.

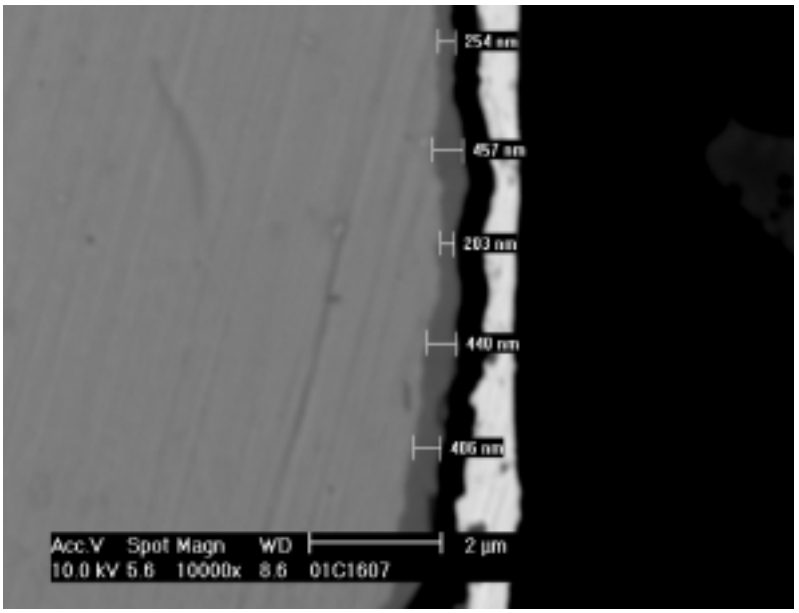

Figure 2. SEM micrograph of the cross-section surface of Zircaloy-2 disc specimen after four-day exposure to simulated BWR water (gold plating detached from the oxide, resin shown as a black layer between gold plating and oxide layer), magnification 10000X.

3.2 TLEIS measurements

The thin-layer impedance measurements were performed after the four-day exposure of the specimens. The impedance spectra for the combined system of the electrolyte and the oxide film of the Zr disc specimen are shown in Fig. 3 and those for the Zircaloy-2 disc specimen in Fig. 4.

As in the case of earlier results [1], two time constants at around 1 kHz and 1 Hz can be observed in the impedance spectra shown in Figs 3 and 4. The high-frequency time constants at approximately 1 kHz shown in the complex plane presentations can be related to the dielectric properties (capacitance) and resistivity of the barrier film. The low-frequency time constants at approximately 1 Hz are assumed to be related to diffusion-limited transport of ionic defects through the oxide film. From the relative magnitude of the resistances associated with the two time constants, it can be suggested that the latter transport process is a rate-limiting step of zirconium oxidation.

The low-frequency intercept of the impedance spectrum, i.e. the impedance magnitude at frequencies decreasing towards zero is assumed to be inversely proportional to the rate of the corrosion reaction, i.e. the higher the magnitude of the impedance, the lower the corrosion rate. It is noticeable again that the impedance spectra are considerably "flattened", which most probably infers to a range of local reaction rates related to the detectable corrosion processes of Zr and Zircaloy-2 in the simulated BWR coolant [2].

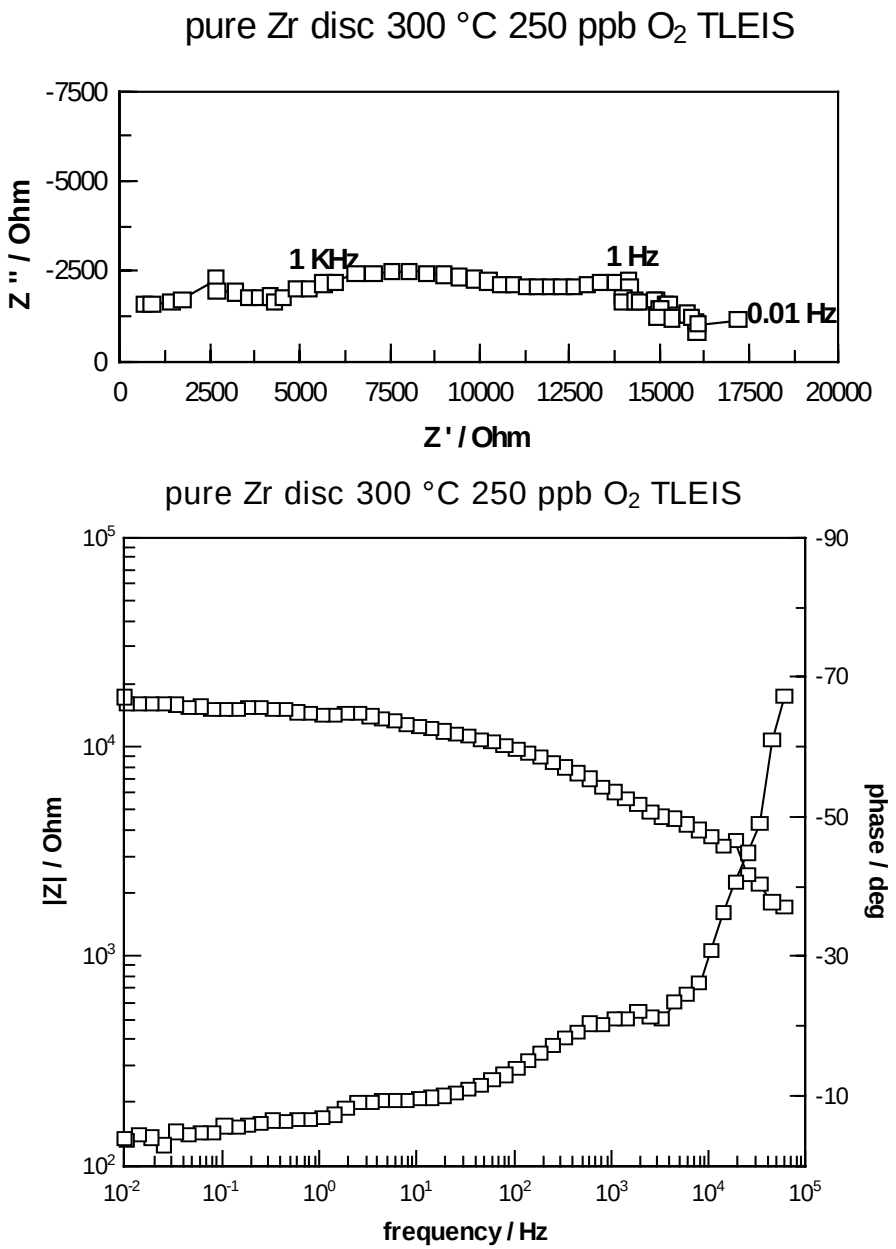

Figure 3. A complex plane presentation (above) and a Bode-plot presentation (below) of the thin-layer electrochemical impedance spectra (TLEIS) of the Zr disc specimen. The measurement was performed in the high temperature water after a 4-day exposure to simulated BWR coolant at 300°C, 7 MPa. Distance between the Ir-reference and Zr-working electrode 5 µm.

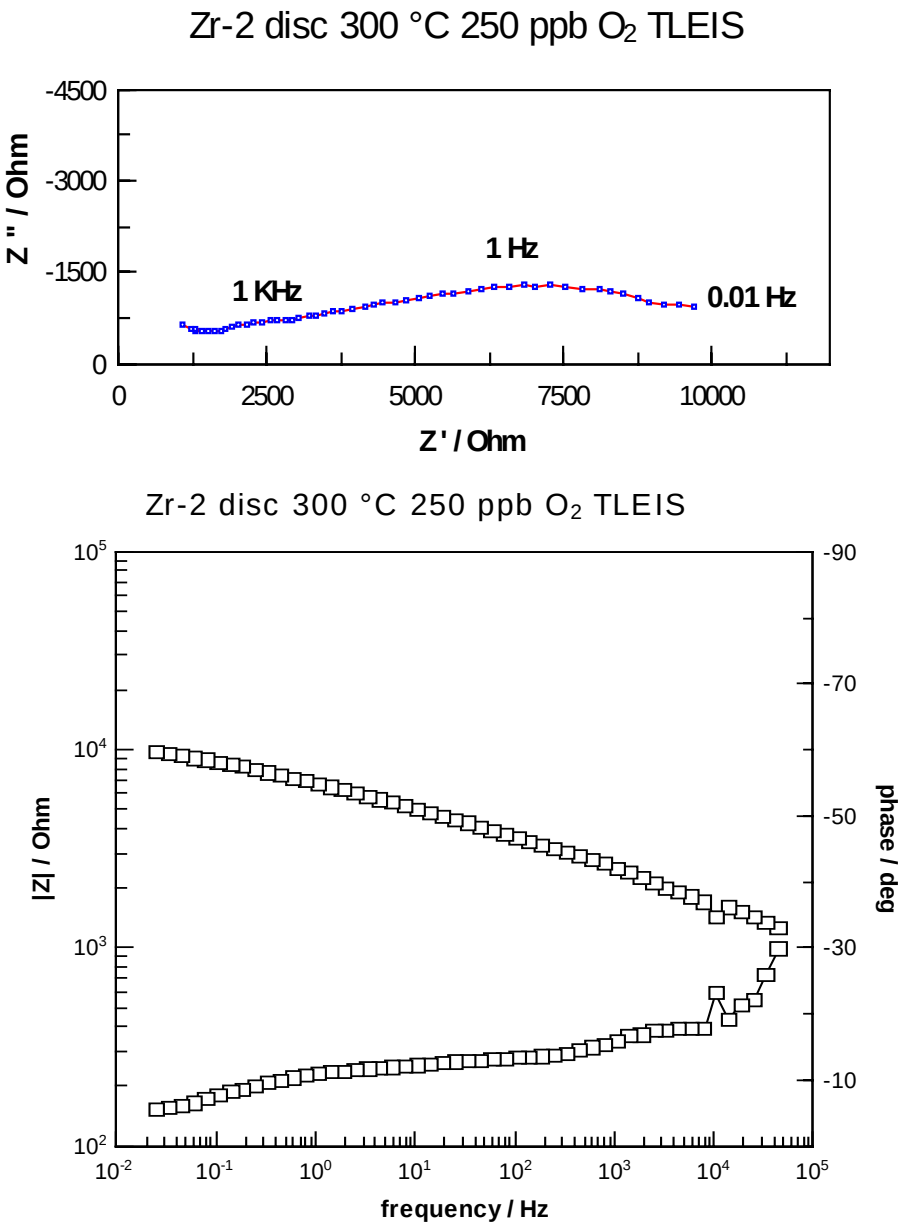

Figure 4. A complex plane presentation (above) and a Bode-plot presentation (below) of the thin-layer electrochemical impedance spectra (TLEIS) of the Zircaloy-2 disc specimen. The measurement was performed in the high temperature water after a 4-day exposure to simulated BWR coolant at 300°C, 7 MPa. The distance between the Ir-reference and Zr-working electrode 5 µm.

3.3 CEI measurements

3.3.1 Simulated coolant

The measurements in the thin layer configuration were followed by contact electric impedance measurements. The measured CEI spectra of the Zr disc specimen are shown in Fig. 5 and those of the Zircaloy-2 disc specimen in Fig. 6. In analogy to the TLEIS results, the two time constants of the CEI spectra suggest that the rate limiting step of the oxide growth is a transport process, probably due to mixed ionic-electronic conduction through the oxide film.

The close correspondence between the TLEIS and CEI spectra is probably an indication of the two types of impedance responses being largely controlled by same phenomena, as discussed earlier [1, 2]. The difference between the measured TLEIS and CEI spectra of the pure Zr and the Zircaloy-2 specimen is only quantitative, the magnitude of the contact electric impedance being roughly twice of that measured in the TLEIS mode. The higher magnitude of the contact impedance is probably due to the high resistance of the thin zirconia layer on the specimens. This leads to a situation where current passes through a reduced surface area, i.e. through a thin solution layer of electrolyte remaining between the surfaces of the sample and the Ir tip in contact with each other.

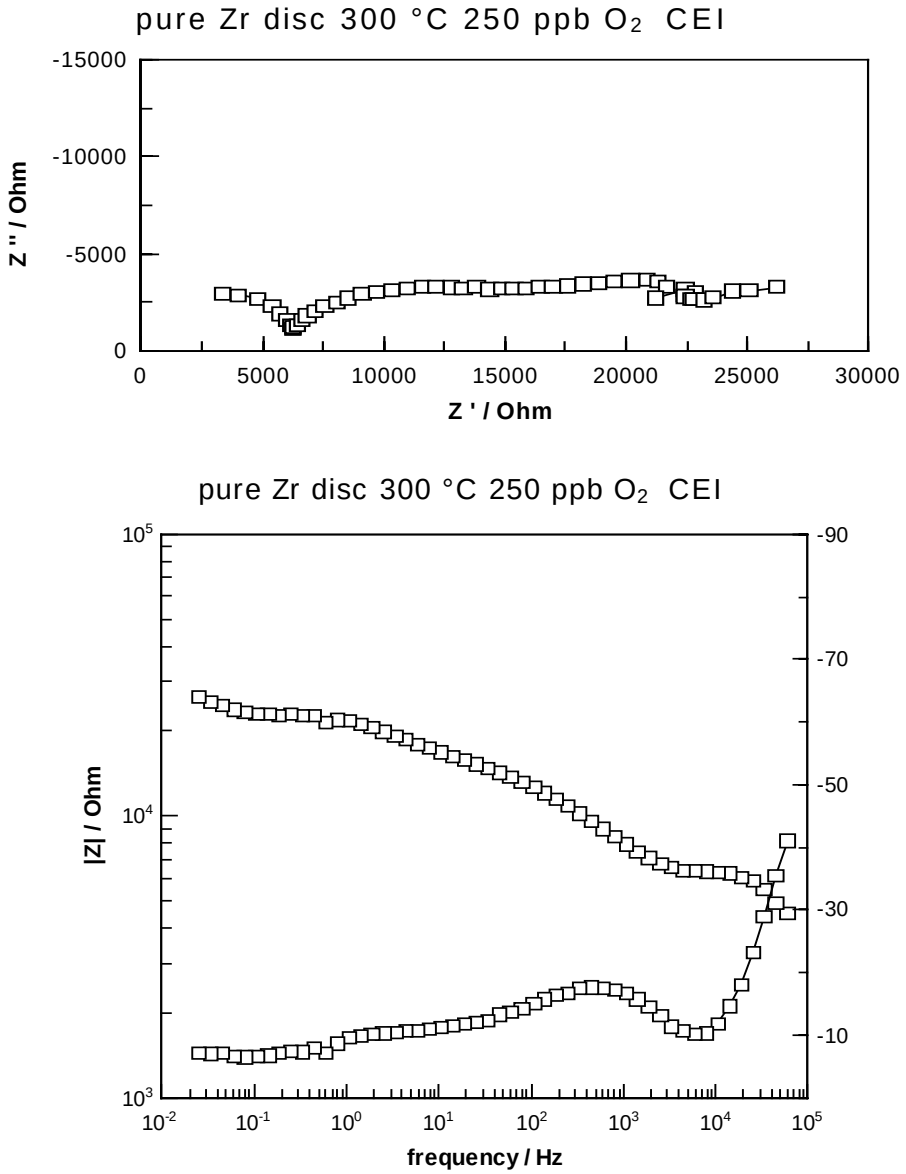

Figure 5. A complex plane presentation (above) and a Bode-plot presentation (below) of the contact electronic impedance spectra (CEI) of the Zr disc specimen. The measurement was performed in the high temperature water after a 4-day exposure to simulated BWR coolant at 300°C, 7 MPa. Contact pressure of the Ir-reference on the Zr-working electrode less than 0.3 MPa.

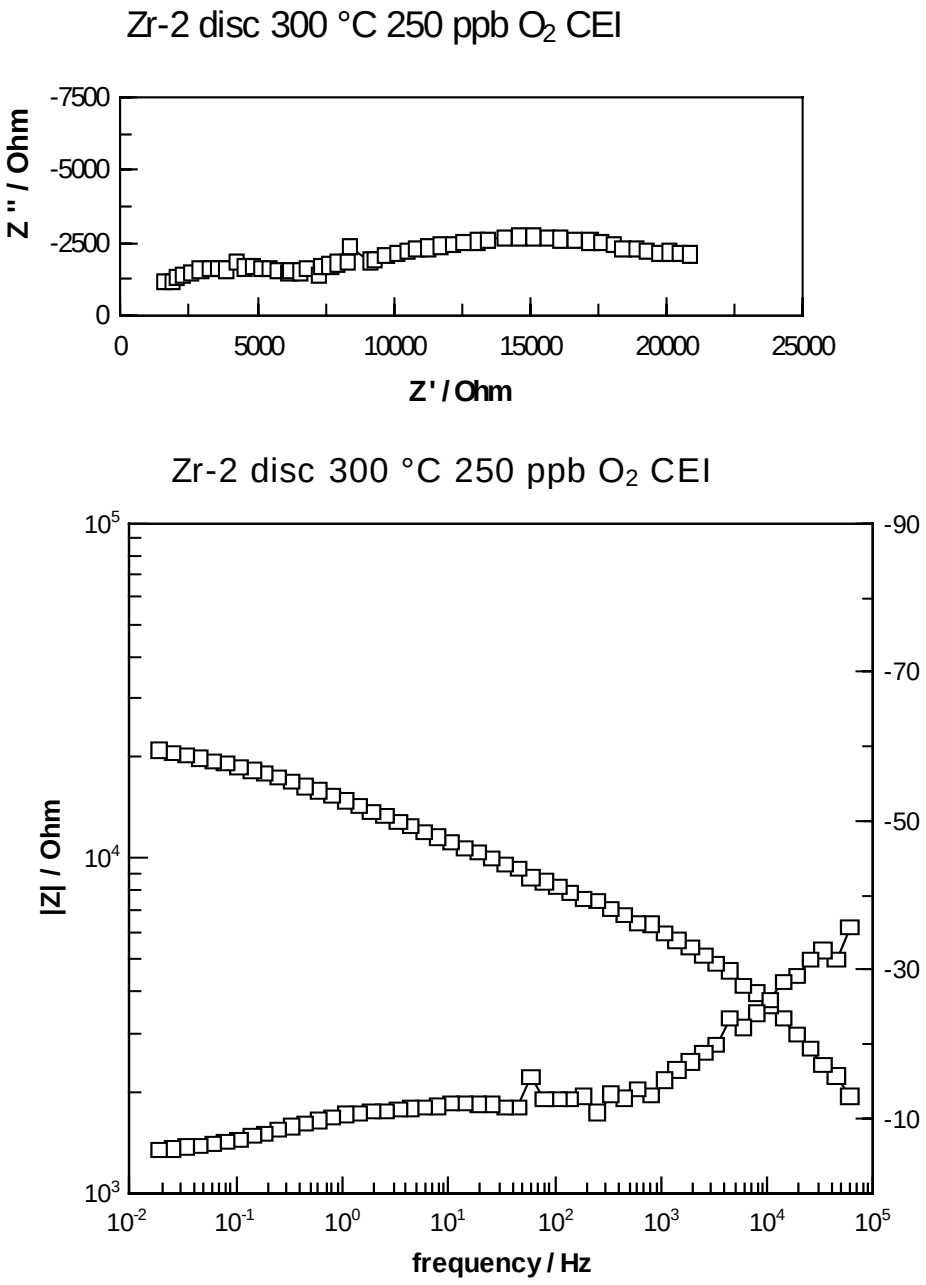

Figure 6. A complex plane presentation (above) and a Bode-plot presentation (below) of the contact electronic impedance spectra (CEI) of the of Zircaloy-2 disc specimen. The measurement was performed in the high temperature water after a 4-day exposure to simulated BWR coolant at 300°C, 7 MPa. Contact pressure of the Ir-reference on the Zr-working electrode less than 0.3 MPa.

3.3.2 Nitrogen atmosphere

To focus on the properties of the oxide film alone, i.e. to eliminate the effect of the corrosion reaction on the impedance spectra, the CEI measurements of the specimens were also performed in an inert N_2 atmosphere at temperatures ranging from 300°C down to 100°C. The results of the measurements for the Zr specimen are presented in Fig. 7 and those for the Zircaloy-2 specimen are shown in Fig. 8. There is only one time constant to be observed in the impedance spectra shown in these figures. These high-frequency time constants are related to the electrical properties of the barrier film. Since corrosion is not assumed to take place in dry nitrogen the low-frequency time constant related to diffusion-limited transport of ionic defects through the oxide film is missing from these spectra.

The magnitude of the contact impedance measurements in the gas were significantly temperature dependent only at temperatures above 200 °C. The spectra of the specimens in the range of 100° to 200°C were identical with each other within the experimental error. This fact suggests a very low activation energy for the conduction process in the oxide. Direct current measurements of oxide films formed on Zircaloy-2 specimens in steam at 400–500°C carried out by Howlader et al. [3] using deposited zirconium contacts have demonstrated that the electrical conductivity is almost constant at temperatures ranging from 25 to 150°C but increases thereafter. Moreover, investigations of electrical conductivity of stabilised zirconia have shown that when the electronic conductivity is a dominating conduction process, the activation energy is 0.03 to 0.06 eV up to approximately 200°C [4].

To be able to obtain a correlation between the impedance parameters, film thickness and corrosion rate of pure Zr, the parasitic high-frequency time constant can be subtracted from the CEI spectrum of the Zr disc specimen shown in Fig. 7. The corrected CEI spectrum measured in nitrogen gas at a temperature of 200°C is shown in Fig. 9 in Bode co-ordinates.

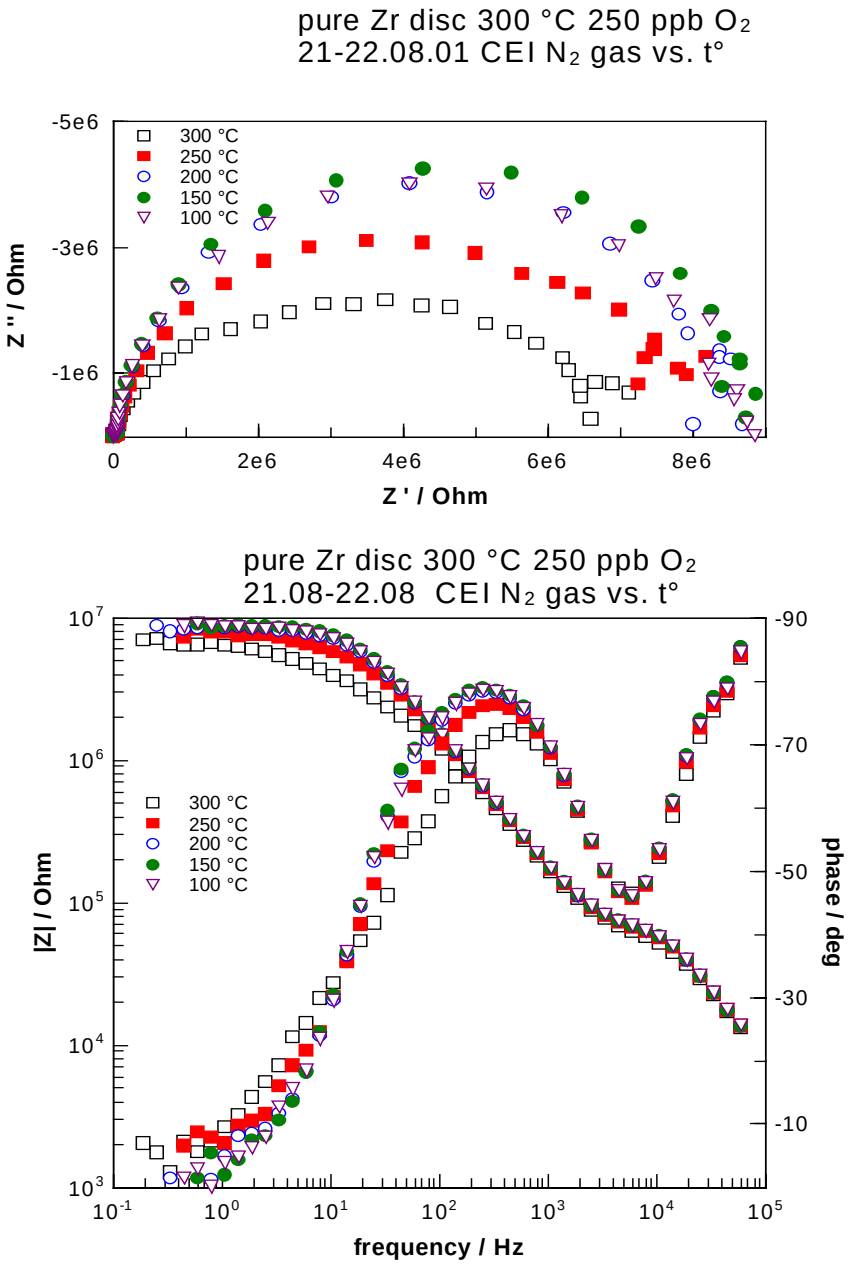

Figure 7. A complex plane presentation (above) and a Bode-plot presentation (below) of the contact electric impedance (CEI) spectra of the Zr specimen. Measurements were performed in nitrogen atmosphere at various temperatures after a 4-day exposure to the high temperature water. Contact pressure of the Ir tip applied to the Zr specimen was 4 MPa.

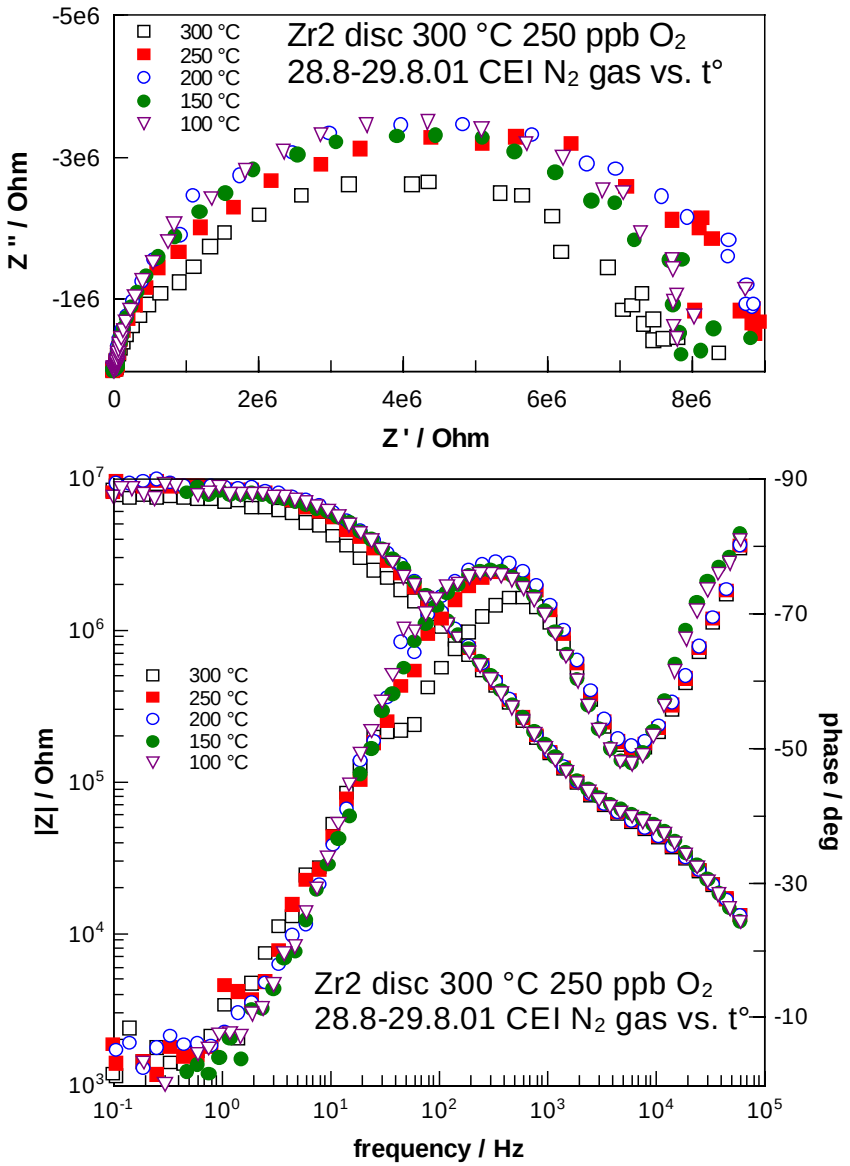

Figure 8. A complex plane presentation (above) and a Bode-plot presentation (below) of the contact electric impedance (CEI) spectra of the Zircaloy-2 specimen. Measurements were performed in nitrogen atmosphere at various temperatures after a 4-day exposure to the high temperature water. Contact pressure of the Ir tip applied to the Zr specimen was 4 MPa).

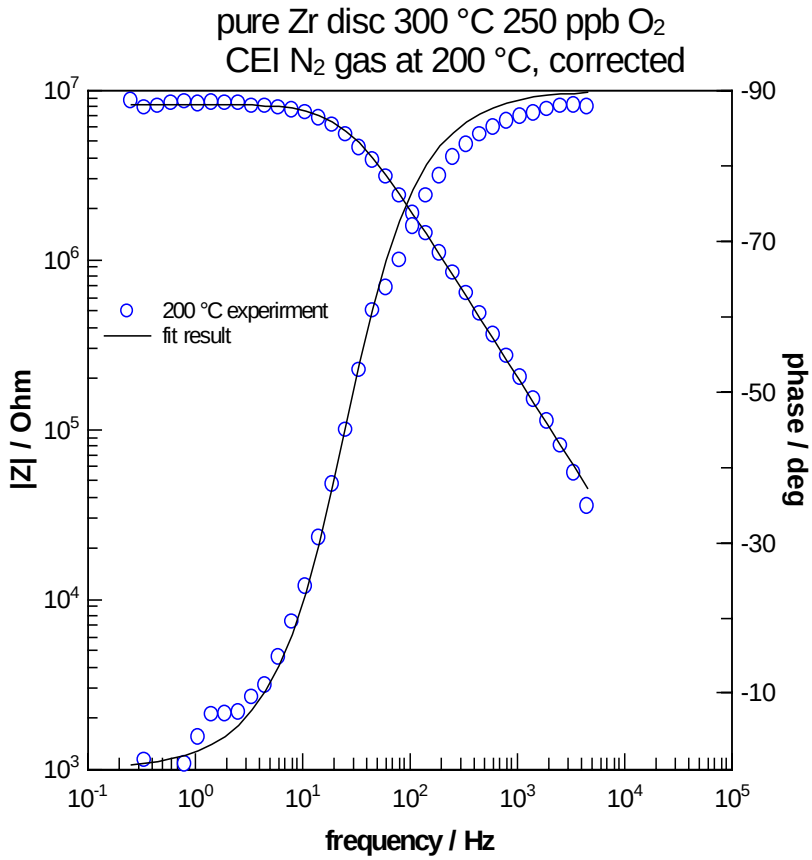

Figure 9. Corrected impedance spectrum for pure Zr disc measured at 200°C in nitrogen gas: points – experimental values, lines - fit to a simple R-C parallel circuit.

A fit to a simple R-C parallel circuit shown in the same figure with solid lines demonstrates the possibility of such a circuit to accurately describe the corrected experimental spectrum. The resistance R can be related to the electronic conductivity of the zirconia layer σ:

$R = (L / \sigma S)$, where L is the layer thickness and S is the contact area. The capacitance C is related to the zirconia film thickness and its dielectric permittivity ε: $C = \varepsilon\varepsilon_0 S / L$, where ε is close to 20, $\varepsilon_0 = 8.85 \times 10^{-14}$ F cm^{-1}. Thus, the product RC, or the time constant of the zirconia film τ, is given by $\varepsilon\varepsilon_0/\sigma$, and an estimate of the conductivity of the zirconia layer $\sigma = \varepsilon\varepsilon_0 / \tau$ can be obtained when assuming that $\varepsilon = 20$. These calculations indicate that the time

constant determined for the spectrum shown in Fig. 13 is $\tau = 6.56$ ms and, therefore, the conductivity of the zirconia is of the order of $\sigma = 3 \times 10^{-10}\ \Omega^{-1}cm^{-1}$. The value is within an order of magnitude of the values determined by Howlader et al. for zirconia films formed on Zircaloy-2 in 400 to 500°C steam [3].

4. Conclusions

The impedance measurements performed up to now in the contact mode in the simulated BWR coolant conditions have turned out to be comparatively well reproducible for both flat and the new disc shaped specimens. Therefore, the contact impedance measurements will be used also in the future to assess the in-situ corrosion mechanism of zirconium alloys in simulated BWR coolant conditions. Results obtained with the disc shaped Zircaloy-2 imply that the new specimen is suitable for measurements in a poorly conductive simulated BWR coolant. Since the specimens made of pure Zr have exhibited exceptionally poor corrosion properties it was decided that this material will not be used in the future experiments.

The last results show that the contribution of the oxide film properties on the CEI spectra of the zirconium alloys can be distinguished from the contribution of the corrosion reactions by performing the measurements in an inert gaseous environment. As a result, the zirconia films of the specimens measured in N_2 exhibit contact impedance spectra with their magnitudes approximately 300 times higher than the respective spectra measured in the simulated BWR water. These results have been found to be compatible with those performed using solid, liquid and evaporated metal contacts reported in literature. Such measurements provide a chance to obtain a correlation between the impedance parameters, film thickness and corrosion rate of Zircaloy-2. However, the difference between the contact impedance spectra of the two different specimens made of Zircaloy-2 and Zr measured in the water and in N_2 was not larger than the accuracy of these measurements. Since the work in this experiment consisted of only two separate measurements, it is not possible to draw any further conclusions before more data is available.

Acknowledgements

This presentation is prepared for a joint Finnish industry group in a project on Structural operability and plant life management (RKK). The project funding by the National Technology Agency (Tekes) and Teollisuuden Voima Oy (TVO) is gratefully acknowledged. The discussions with Mr. Lunabba of TVO and other partners in the project were of great help in planning and execution of this work.

References

1. Bojinov, M., Hansson-Lyyra, L., Laitinen, T., Mäkelä, K., Saario, T. and Sirkiä, P. Zircaloy-2 cladding materials – Effect of microstructure on corrosion properties. Development of the structural integrity of nuclear power plants, Results in 2000. Espoo: VTT Manufacturing Technology. Research Report BVAL62-001086. 24 p.

2. Bojinov, M., Hansson-Lyyra, L., Laitinen, T., Mäkelä, K., Saario, T. and Sirkiä, P. Testing and verification of electrochemical techniques to study oxide films on fuel cladding materials, Results in 2001. Espoo: VTT Manufacturing Technology. Research Report BVAL62-013060. 24 p.

3. Howlader, M. M. R., Shiyama, K., Kinoshita, C., Kutsuwada, M. and Inagaki, M. 1998. The electrical conductivity of Zircaloy oxide films. Journal of Nuclear Materials, 1998, Vol. 253, No. 1–2, pp. 149–155.

4. Levy, M., Foultier, J. and Kleitz, M. Model for the electrical conductivity of reduced stabilized zirconia. Journal of the Electrochemical Society, 1988. Vol. 135, No. 6, p. 1584.

Vacancy generation in electrochemical oxidation / dissolution of copper in $NaNO_2$ solutions and its role in SCC mechanism

Pertti Aaltonen[1], Yuriy Yagodzinskyy[2], Oleksandr Tarasenko[2]
and Hannu Hänninen[2]
[1] VTT Industrial Systems, Espoo, Finland
[2]Helsinki University of Technology, Espoo, Finland

Abstract

Interaction of copper with the oxide layers growing on it at various potentials during electrochemical polarization in $NaNO_2$ solution was studied. It was shown that anodic oxidation/dissolution of copper is accompanied with generation of vacancies at the oxide/metal interface, when cuprous oxide, partially coherent to copper substrate, becomes unstable. The ingress of vacancies into substrate results in a significant rearrangement of dislocation substructure and relaxation of stresses in the plastically deformed copper substrate. If the anodic oxidation/dissolution of annealed pure copper is continued in the absence of effective annihilation mechanisms for the generated vacancies, i.e., diffusion or dynamic plastic deformation, dislocation sources, such as Bardeen-Herring sources, start to operate close to the film substrate interface, which results in measurable plastic strain.

The influence of anodic oxidation/dissolution on dynamic straining conditions of pure copper at various temperatures was also studied. The potential and current density for anodic dissolution in $NaNO_2$ solution were higher if the substrate was simultaneously dynamically strained. It was shown that excessive vacancies were generated under constant current anodic oxidation/dissolution at the potential of about 100 mV_{SCE}, which led to a significant increase in the steady state creep rate. In order to measure the strain introduced by electrochemical oxidation/dissolution in $NaNO_2$ solution, plastic deflection of copper strips in one-sided oxidation was studied. Deflection is due to plastic relaxation of elastic stresses stimulated by annihilation of vacancies near the surface layer, i.e.,

rearrangement of dislocation assemblies. The influence of oxidation/dissolution processes on dislocation substructures in copper was confirmed by low-temperature internal friction measurements and TEM. High-purity copper was used in the above mentioned experiments. The results are discussed with a possible model developed for TGSCC based on electrochemical oxidation/ dissolution of copper, where the major influence of vacancies generated at the crack tip on crack initiation and growth is described.

1. Introduction

Understanding the role of vacancies in the mechanism of environmentally assisted cracking (EAC), has increased through various observations. Active dissolution of the metal surface in acidic environment [1], selective dissolution of the alloy surface [2], growth of the passivating oxide film [3] and hydrogen absorption to the metal due to the cathodic reaction [4] have been proposed to be accompanied with the vacancy generation in the surface layer of the material. There is indirect evidence confirming assumptions concerning generation of excessive amounts of vacancies compared to their thermal equilibrium content in the metal. Continuous generation of vacancies can cause changes in the dislocation behavior contributing deformation of materials, i.e., creep properties have been observed to change [5]. An example of that is a significant increase observed in the creep rate of copper during dissolution in aqueous acetate solution of pH 3.7, when no film is present on the metal. In externally unstressed materials deformation, indicated by deflection, has been observed [6] during one-sided oxidation conducted at high temperatures in gaseous environments for thin strip specimens. Selective anodic dissolution of zinc in brass exposed to tap water has been shown to provide excessive amounts of vacancies in the substrate [7]. In a bimetallic sample, made of silver deposited with copper, diffusion at the Cu/Ag interface has been observed when the copper side was subjected to anodic dissolution in 1N H_2SO_4 solution [8]. In many studies concerning stress corrosion cracking behavior of copper, fast straining electrode tests have been applied to verify the effect of dynamic straining on re-passivation kinetics and on the anodic peak current density in certain environments [9]. In order to model and understand EAC it should also be studied how much oxidation/dissolution reactions provide deformation itself and how this rather slow, dynamic deformation accelerates corrosion on the other hand. As an attempt to visualize

the interrelationship between deformation, dissolution, vacancy generation and stress an EAC tetrahedron is presented in Fig. 1.

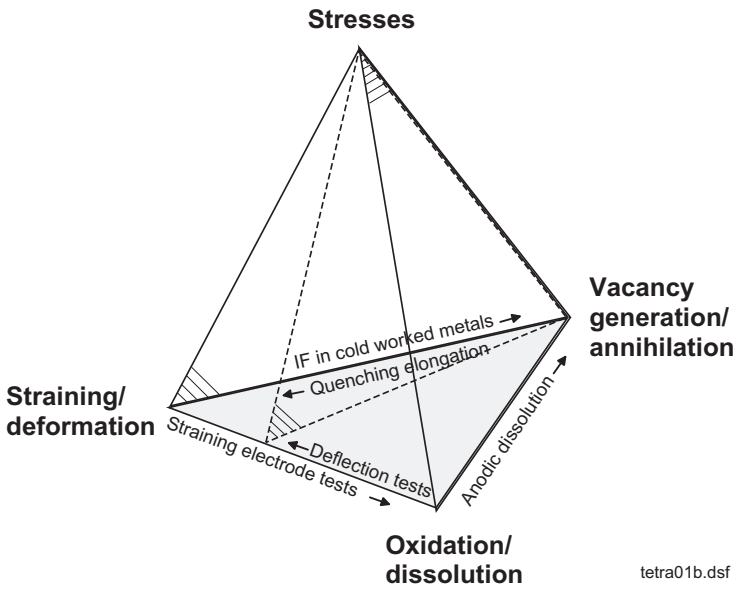

Figure 1. EAC tetrahedron describing associated reactions included in material/environment/loading interactions.

The interdependence of bottom plane reactions in the tetrahedron, i.e. corrosion-deformation-interactions, including vacancy generation, is verified in this study by using different test methods.

Deflection measurements at ambient temperature during one-sided anodic oxidation/dissolution were applied to verify corrosion-induced deformation. Internal friction (IF) measurements after anodic oxidation/dissolution prove generation of vacancies due to corrosion and IF after cold deformation indicates vacancy generation caused by plastic deformation. Straining electrode tests have been reported widely in the literature showing deformation-enhanced corrosion and historical dilatometric measurements of elongation in quenched materials have verified strain (elongation) caused by vacancy generation. Traditional dynamic SCC laboratory tests combine strain and oxidation/dissolution in different environments. Depending on material homogeneity and loading

parameters, the amounts of corrosion or deformation vary. The main purpose of this study is to show that anodic oxidation/dissolution provides deformation of the substrate and that dynamic deformation enhances corrosion of copper in $NaNO_2$ environment.

2. Experimental

2.1 Test material

Test material used in this study were pure copper (99.998%) containing only 1.2 ppm oxygen. In order to simulate the material at the tip of stress corrosion crack it was cold deformed by rolling with appropriate intermediate anneals to produce 0.98 mm thick plate. The specimens were manufactured from the plate by using electric discharge machining.

2.2 Deflection measurements in $NaNO_2$ solution

In order to study the deformation caused by oxidation/dissolution reactions taking place at different potentials at ambient temperature, deflection of pure copper caused by one-sided oxidation/dissolution was measured. The metal strip specimens ($0.5\times5\times40$ mm^3) were instrumented with strain gauges on one side and the opposite side of the specimen was exposed to the electrolyte, 0.3 M $NaNO_2$ solution. By using compensation strain gauge, the effects of temperature fluctuations were eliminated. Sample surface was polarized starting from the potential of -150 mV_{SCE} with a scan rate of 1 mV/min up to 150 mV_{SCE}. Additional deflection measurements using cold-worked and annealed specimens were conducted at different temperatures, in $NaNO_2$ solutions with various concentrations and varying specimen thickness, under constant potentials and currents as well as during dynamic potential sweeps.

2.3 Anodic current densities and dynamic straining

Current densities related to repassivation during rapid straining tests in specific environments have been reported for copper and brass to be orders of magnitude higher than those recorded for static surfaces [9, 10]. Slow dynamic straining of pure copper substrate has also an effect on dissolution current density and potential needed for reaction. Polarization curves measured using flat strip specimens oxidized one-sided or oxidized symmetrically on both sides have been obtained. Relaxation of misfit stresses during oxidation/dissolution conducted on one side only provides slow dynamic straining of the substrate. In the case of symmetrically oxidized strip specimens relaxation by deflection could not be measured with the applied test arrangement.

2.4 Internal friction measurements

Internal friction measurements were conducted after oxidation/dissolution in 0.3 M $NaNO_2$ solution at ambient temperature and were used to follow rearrangements in the dislocation structure after exposure of the test material to electrochemical conditions known to provide SCC in pure copper, i.e., 0.3 M $NaNO_2$ solution at the potential of 100 mV_{SCE}. Internal friction was also measured for cold deformed pure copper in as-received condition after six months storage of material at ambient temperature. IF measurements were carried out with an inverted torsion pendulum in the temperature range of 80–500 K with the heating rate of 1.5 K/min. The oscillation frequency was about 1 Hz and the amplitude of deformation was of the order of 10^{-6}. Samples with dimensions of about $40\times2\times0.5$ mm^3 were polished with 800 grit emery paper.

2.5 Creep tests

Creep tests at various temperatures were conducted in order to evaluate the enhancement caused by anodic oxidation/dissolution current of 1 mA/cm^2 on the strain rate of pure copper. Tests were conducted using dead weight loading (~660 kN) and the specimen gauge length ($0.4\times9\times25$ mm^3) was exposed to 0.3 M $NaNO_2$ electrolyte. When steady state creep was obtained, anodic current was switched on. The enhancement in the creep rate due to anodic current was

recorded for one hour and by switching the current off creep caused by mechanical control only continued. Based on the enhancement observed in the creep rate apparent activation energies for mechanical deformation and for the corrosion enhancement were determined.

2.6 TEM and micro-hardness measurement

Transmission electron microscopy (TEM) studies of the specimens in the original cold deformed condition and after exposure to 0.3 M $NaNO_2$ solution at the potential of 100 mV_{SCE} were conducted to confirm the observations of oxidation/dissolution behavior of pure copper obtained with one-sided and two-sided specimens. Additionally, micro-hardness measurements were used for the same purpose.

3. Results

3.1 Deflection measurements

An example of the recorded strains caused by oxidation/dissolution reactions and the anodic polarization current on the opposite side of the cold worked copper strip specimen at different potentials at room temperature as a function of time is shown in Fig. 2. Negative strains measured on the counter side of the oxidizing strip specimen surface indicate oxidation introduced compressive stress in the oxide and tensile stress in the substrate near the interface. Independent of the potential, initial stress starts to relax in the thin strip specimen. Accelerated deflection can be observed first after the current density starts to increase at the potential above 50 mV_{SCE}. Tests carried out at temperatures up to 60°C showed the same behavior. If the material was annealed before oxidation/dissolution, initial compressive strains were smaller, Fig. 3, and the specimen starts to deflect similarly to the cold deformed specimens when the anodic current increased due to dissolution.

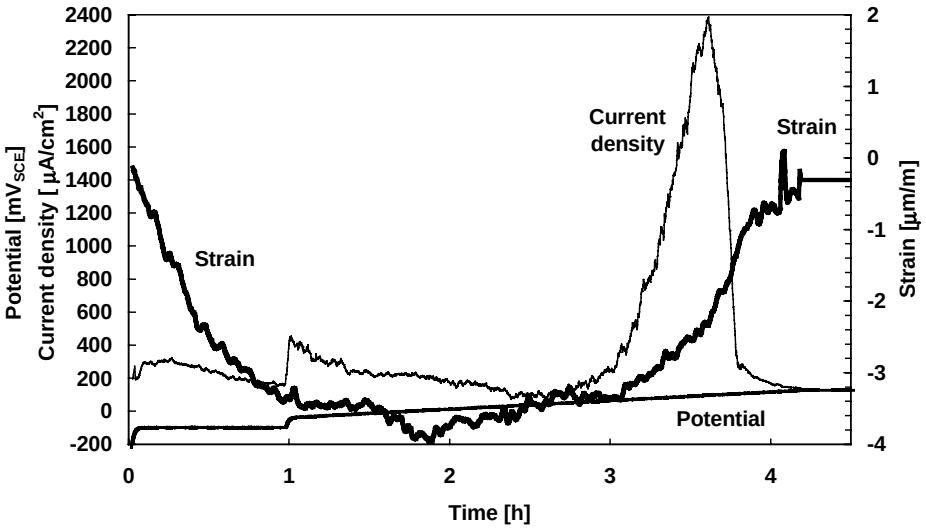

Figure 2. Deflection of cold deformed copper specimen during anodic polarization with scan rate of 1 mV/min in 0.3 M $NaNO_2$ solution.

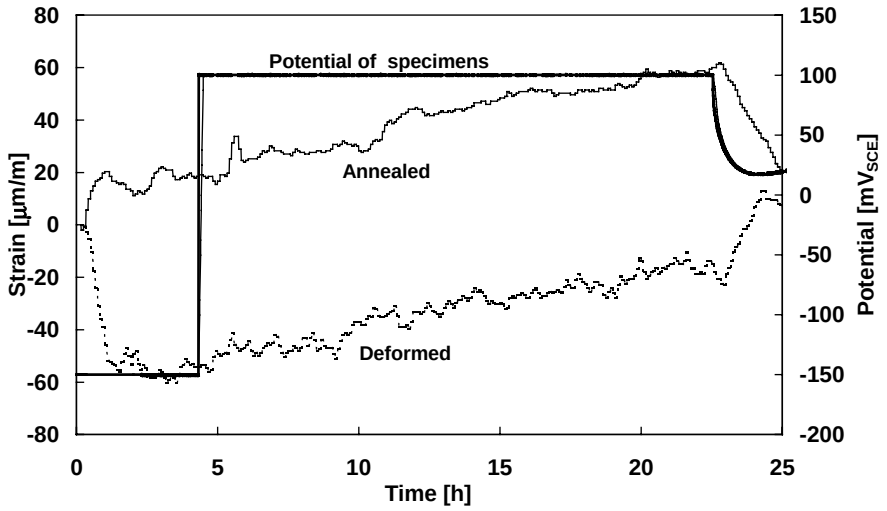

Figure 3. Deflection curves for cold deformed and annealed pure copper specimens oxidized/dissolved in 0.3 M $NaNO_2$ solution at 100 mV_{SCE}.

3.2 Oxidation/dissolution of pure Copper in 0.3 M $NaNO_2$ solution

Polarization curves for pure copper obtained with a scan rate of 1 mV/min at room temperature are shown in Fig. 4. The current densities were measured using one-sided and two-sided specimens. Peak current densities for one-sided specimens were systematically higher than those measured for two-sided specimens, where corrosion/deformation interaction obviously is symmetrical and does, thus, not result in relaxation of the dissolving substrate.

Anodic dissolution peak in the case of symmetrical two-sided specimen occurs at the potential of 50 mV_{SCE} and the potential needed for anodic dissolution for one-sided specimen is higher, occurring at the potential of about 100 mV_{SCE}. The difference in the current density at the potential of 100 mV_{SCE} between the two-sided and one-sided specimens is more than one order of magnitude. In the case of one-sided specimen, the anodic dissolution starting at the potential of about 100 mV_{SCE} continues over a wide potential range. This means that the amount of dissolved metal ions can become much higher than those in the symmetrical oxidation/dissolution.

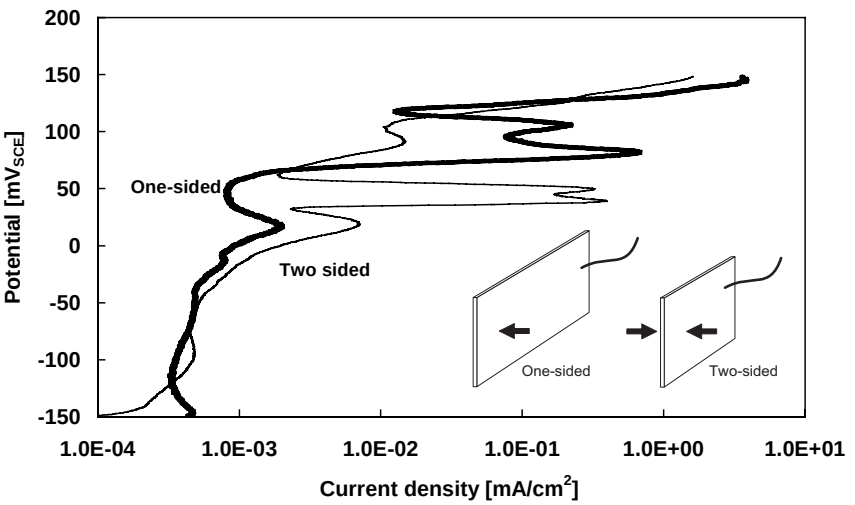

Figure 4. Anodic polarization curves for one-sided and two-sided copper specimens exposed to 0.3 M $NaNO_2$ solution at room temperature.

3.3 Internal friction

Temperature dependencies of IF of copper in as-received state and after oxidation/dissolution at the potential of 100 mV_{SCE} in 0.3 M $NaNO_2$ solution at 306 K are shown in Fig. 5. Three distinct IF peaks in the vicinity of 150 K, 200 K and 250 K appear as a result of oxidation/dissolution, while only little humps are visible at close temperatures in as-received state of studied copper. Temperature positions of the peaks observed after oxidation/dissolution correspond to those which are typical for so-called Hasiguti peaks observed in irradiated pure copper [11]. It was well established that Hasiguti peaks are caused by interaction between dislocations and vacancies or their complexes produced by irradiation [11]. Based on such a similarity one can conclude that IF peaks at 150 K, 200 K and 230 K observed after oxidation/dissolution of copper are a result of vacancy generation at the oxide/metal interface and their ingress into the metal during oxidation of copper. Since observed IF peaks are caused by mechanical energy loss in the bulk or subsurface layer of copper, it is an evidence that vacancies generated during oxidation/dissolution produce changes in the dislocation structures of copper substrate.

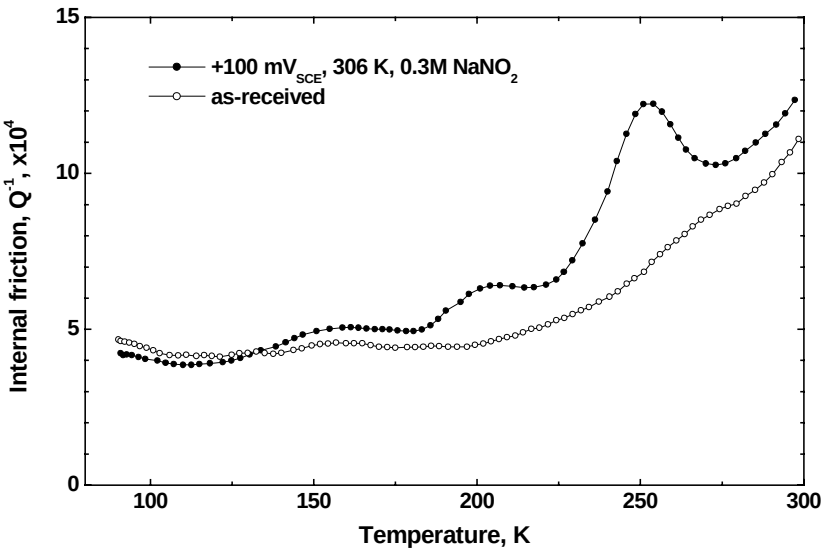

Figure 5. IF peaks observed for pure copper after cold deformation and after exposure for 2 hours to 0.3 M $NaNO_2$ solution at 100 mV_{SCE} at room temperature.

3.4 Creep

The creep curves for pure copper exposed to 0.3 M $NaNO_2$ solution obtained at temperatures 20, 40, 60 and 80°C using 180 N/mm^2 constant load are shown in Fig. 6. During the initial phase, before the creep rate has stabilized, the specimens were polarized to –100 mV_{SCE}. After the creep rate stabilized, anodic current in the range of 1 mA/cm^2 was applied, which accelerated the creep rate almost immediately. The potential of pure copper specimens during creep tests in 0.3 M $NaNO_2$ solution under anodic current control was about 100 mV_{SCE} and remained stable for the whole one hour period. Switching off the applied anodic current decreased the measured creep rate with some delay, Fig. 7. Based on the creep rate curves obtained at different temperatures apparent activation energies for the mechanical component of pure copper creep and for the oxidation/dissolution enhancement of the creep rate were calculated. The apparent activation energy for the mechanical component was 0.23 eV. For the oxidation/dissolution enhancement apparent activation energy was 0.16 eV.

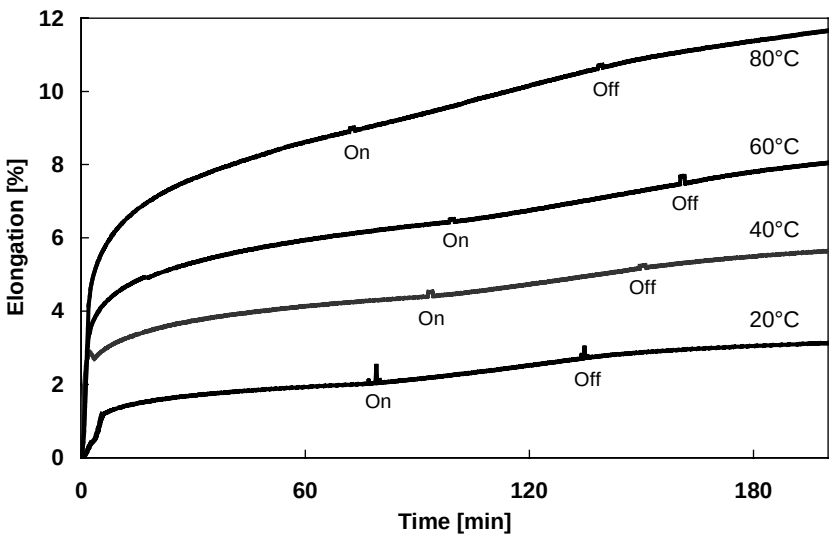

Figure 6. Creep curves of pure copper obtained using dead weight loading (180 N/mm^2) in 0.3 M $NaNO_2$ solution at various temperatures at anodic current density of 1 mA/cm^2 to accelerate the creep rate.

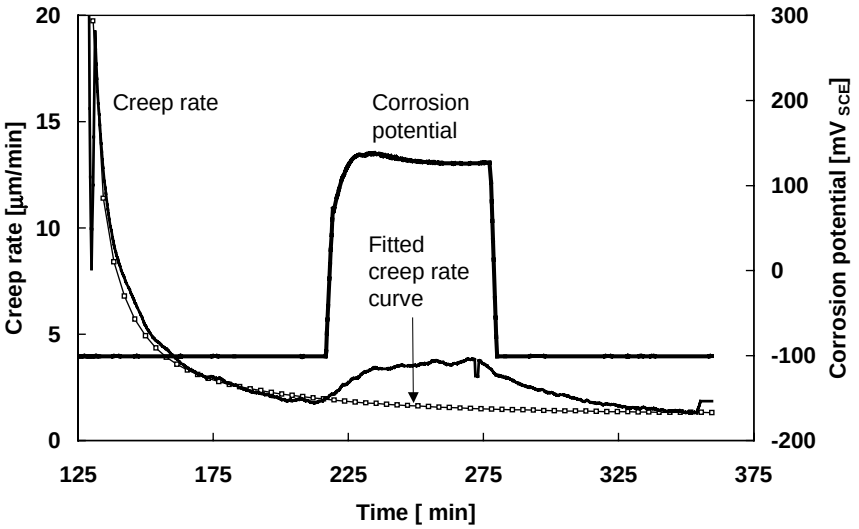

Figure 7. Creep rate of cold deformed pure copper loaded with 180 N/mm^2 at 40 ℃. Starting at 215 min an anodic current density of 1 mA/cm^2 was applied for one hour.

3.5 Transmission electron microscopy

Transmission electron microscopy revealed recovery in the initially cold worked dislocation structure caused by oxidation/dissolution during anodic polarization with sweep rate of 1 mV /min at room temperature in 0.3 M $NaNO_2$ solution. The one-sided specimen showed clearly recovered dislocation microstructure, Fig. 8a. The microstructure in the two-sided oxidized/dissolved specimen was quite similar to the cold-worked microstructure and showed only local recovered areas, Fig. 8b.

Micro-hardness measurements confirmed the trends of TEM observations. The hardness in the cold deformed pure copper was in the range of 120–125 HV and due to one-sided oxidation/dissolution of the 1 mm thick specimen in 0.3 M $NaNO_2$ solution hardness was reduced slightly to the value of 118 HV. In two-sided oxidized/dissolved specimen hardness was 120 HV.

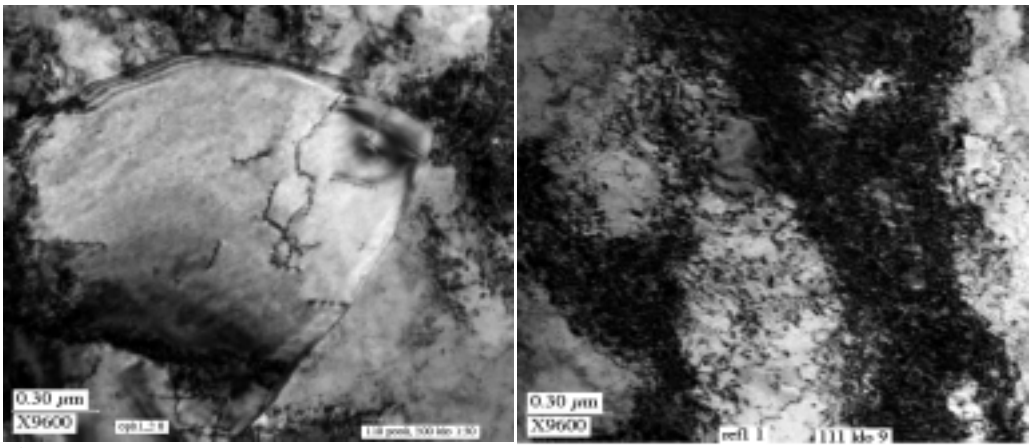

a) *b)*

Figure 8. TEM pictures of highly deformed pure copper after anodic oxidation/ dissolution conducted in 0.3 M $NaNO_2$ solution at room temperature one-sided (a) and two-sided (b).

4. Discussion

The involvement of vacancies in EAC is not easy to show because the prerequisite for environmental enhancement is that they must annihilate in order to continue the environment crack tip interaction. However, there are many indirect demonstrations that without vacancies the interactions between deformation and oxidation/dissolution shown in the EAC tetrahedron can not take place. The reasonable explanation, how the crack tip anodic dissolution provides strain, Fig. 1, and strain accelerates corrosion, can be made using vacancies.

The formula used to describe crack tip strain rate, in general, consists of the mechanical creep component and the corrosion induced addition [12]:

$$\dot{\varepsilon}_{CT} = A \times \dot{\varepsilon}_{creep} + B \times \dot{\varepsilon}_{corrosion} \qquad (1)$$

Oxidation/dissolution generated vacancies have to be annihilated in order to further continue oxidation/dissolution. Missing interfacial annihilation of corrosion generated vacancies prevents further oxidation/dissolution [13].

Annihilation of vacancies provides dynamic strain of the substrate and consequent rearrangement of the dislocation structure. These two reactions can take place in different positions near the crack tip: deformation in the bulk material in the crack tip plastic zone and corrosion along the crack surfaces behind the crack tip. The inertia of dissolution-deformation interactions, mainly due to vacancy annihilation reactions, can be the reason for observed intermittent crack growth typical for EAC. Based on the conducted measurements for pure copper in $NaNO_2$ solution it is clear that dynamic straining is necessary to maintain intimate contact between the oxide film on copper and the substrate. Strain necessary to accelerate oxidation/dissolution is very small and does not lead to break-down of the oxide film. However, combined straining and oxidation/dissolution in a specific environment, i.e., in $NaNO_2$ solution provides continuous generation of vacancies in the substrate [14]. The role of a specific environment is obviously to take care of dissolved ions, e.g., by forming complex ions, and by that way to prevent concentration polarization at the electrolyte/oxide interface. The generated vacancies annihilate close to the crack tip mainly by reacting with the dislocation pile-ups formed at crack tip by mechanical loading providing, thus, a reaction to relax the stress. The applied loading can, thus, strain further the crack tip material, which again is the prerequisite for further oxidation/dissolution.

The activation energies defined for the mechanical enhancement of crack growth, i.e., creep was 0.23 eV and for anodic oxidation/dissolution enhancement, i.e., corrosion 0.16 eV, respectively. The mechanical component is increasing as a function of temperature, but the corrosion related component is inversely related to temperature. Using these energies and the crack growth rates reported for pure copper in $NaNO_2$ solution at room temperature obtained with strain rates of 10^{-4}/s and 10^{-6} /s [9] the combined effect of mechanical loading and the environment on crack growth rate of pure copper can be described as shown in Fig. 9.

Crack growth obtained with the higher strain rate of 10^{-4} /s at room temperature is mainly controlled by mechanical deformation at the crack tip. By reducing the strain rate to a value of 10^{-6}/s or lower oxidation/dissolution becomes more important until the temperature exceeds 325 K when the crack growth is mainly controlled by mechanical straining. The rate-determining reaction in the oxidation/dissolution can be relaxation of the substrate by annihilation of

generated vacancies. The apparent activation energy reported for the surface layer relaxation of copper by a surface layer removal method was about the same as obtained in this study for oxidation/dissolution enhancement in creep, i.e., 0.16 eV [15].

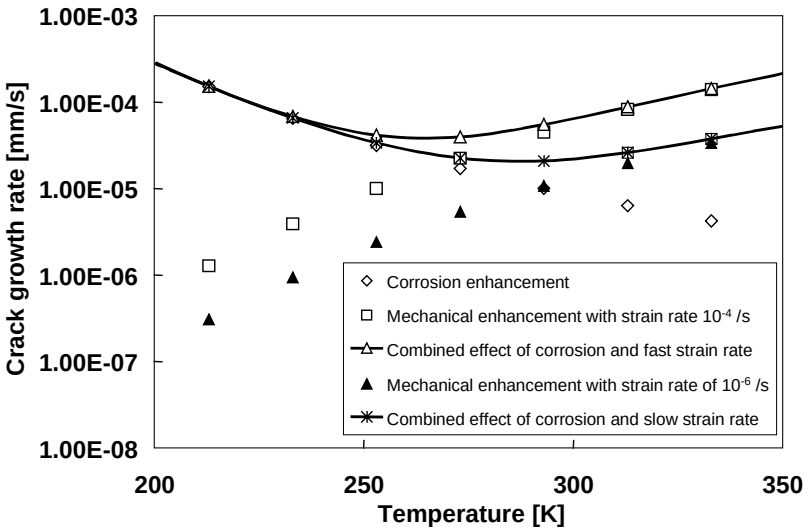

Figure 9. Crack growth rates for pure copper as a function of temperature in 1 M $NaNO_2$ solution at 100 mV_{SCE} ; mechanical loading rate 10^{-4} or 10^{-6} /s [9].

5. Conclusions

- Annihilation of vacancies generated by oxidation/dissolution in pure copper takes place by plastic deformation.

- Annihilation of vacancies provides relaxation of the dislocation structure close to the oxide /substrate interface.

- Relaxed substrate maintains contact with the growing oxide and pronounced oxidation/dissolution of pure copper in 0.3 M $NaNO_2$ solution at room temperature at the potential of 100 mV_{SCE} is able to continue.

- Continued vacancy generation can relax effectively the dislocation structures maintained by external loading of the material at the crack tip.

Acknowledgements

This presentation is based on work performed jointly in Helsinki University of Technology and VTT within the Research Program on Operational Safety and Structural Integrity (FINNUS) and partially also the RKK project. The financial support from the Finnish Ministry of Trade and Industry and the Radiation and Nuclear Safety Authority (STUK) as well as Technical Research Center of Finland (VTT) for the FINNUS program is acknowledged. The support from Outokumpu Poricopper providing test material is also acknowledged.

References

1. Pickering, H. W. and Wagner, C. Electrochemical Science, 114 (1967), 698.

2. Sieradzki, K. and Newman, R.C. Philosophical Magazine A, 51 (1985), 95.

3. McDonald, D. D. Journal of the Electrochemical Society, 139 (1992), 3434.

4. Birnbaum, H. K., Buckley, C., Zeides, F., Sivois, E., Rozenak, P., Spooner, S. and Lin, J.S. Journal of Alloys and Compounds, 253–254 (1997), 260.

5. Revie, R.W. and Uhlig, H.H. Acta Metallurgica, 22 (1974), 619.

6. Jaenicke, X. Leistikow, S. and Stadler, A. Journal of the Electrochemical Society, 111 (1964), 1031.

7. Aaltonen, P., Jagodzinski, Yu., Tarasenko, A., Smouk, S. and Hänninen, H. Acta Materialia, 46 (1998), 2039.

8. Jones, D. A. Metallurgical Transactions, 16A (1985), 1133.

9. Yu, J. and Parkins, R. N. Corrosion Science, 27 (1987), 159.

10. Alvarez, M. G., Manfredi, C., Giordano, M. and Galvele, J. R. Corrosion Science, 24 (1984), 769.

11. Nowick, A. S. and Berry, B. S. Anelastic Relaxation in Crystalline Solids. New York: Academic Press, 1972. 677 p.

12. Ford, P. Environment-induced Cracking of Metals. Eds. R. P. Gangloff and M. B. Ives. Houston, TX: NACE, 1990. 139 p.

13. Andrieu, E., Pieraggi, B. and Gourgues, A.F. Scripta Materialia, 39 (1998), 579.

14. Aaltonen, P., Jagodzinski, Yu., Tarasenko, A., Smouk, S. and Hänninen, H. Corrosion Science, 40 (1998), 903.

15. Kramer, I. R. Trans. Met. Soc., 230 (1964), 991.

Effects of dynamic strain aging on environment-assisted cracking of low alloy pressure vessel and piping steels

Hannu Hänninen[1], Hans-Peter Seifert[2], Yuriy Yagodzinskyy[1],
Ulla Ehrnstén [3], Oleksandr Tarasenko[1] and Pertti Aaltonen[3]
[1]Helsinki University of Technology, Espoo, Finland
[2]Paul Scherrer Institut, Villigen, Switzerland
[3]VTT Industrial Systems, Espoo, Finland

Abstract

Strain aging occurs in alloys containing solutes that segregate strongly to dislocations. In low-alloy steels (LAS) static strain aging is a process where aging takes place after pre-straining and results in return of Lüders strain. Dynamic strain aging (DSA) is a process where aging is sufficiently rapid to occur during straining and it produces inhomogeneous deformation, serrated yielding. DSA occurs at temperatures of 150–350 °C, where stress-strain curves show serrations, being most marked at 250 °C depending on strain rate. The mechanism of DSA in LAS is explained based on the interstitial (N, C, H) interactions with dislocations and their immobilization. The important role of the accumulation of vacancies, which are diffusion vehicles for the solute atoms, is also considered in case of EAC. In general, activation energy of DSA in LAS is equal to that of N/C diffusion in ferrite. The effects of DSA of LAS are evaluated based on peaks in UTS, hardness and strain hardening rate in the DSA temperature range and minimum of ductility (A, Z) and temperature of peaks decreases with decreasing strain rate. DSA causes an increase in the ductile-to-brittle transition temperature following plastic deformation in the DSA temperature range, lowering of the ductile fracture resistance (decrease of tearing modulus) at temperatures within the DSA temperature range, as well as ductile crack instabilities (crack jumps) in the DSA temperature range, decreases low-cycle fatigue resistance and the susceptibility of LAS to EAC coincides with DSA behavior, in terms of temperature and strain rate ranges. The present knowledge of DSA on above mentioned properties of LAS is reviewed and DSA susceptibility of some pressure vessel steels is demonstrated by internal friction method and slow-strain rate tensile testing.

1. Introduction

Strain aging occurs in alloys (typically dilute alloys) containing solutes that segregate strongly to dislocations resulting in strong elastic interactions between solutes and the stress-strain fields of dislocations and in strong dislocation pinning. Static strain aging is a process where aging takes place after pre-straining and results in a return of Lüders strain. Dynamic strain aging (DSA) is a process where aging is sufficiently rapid to occur during straining and it produces a variety of inhomogeneous deformations which are characterized by terms such as Portevin-le Chatelier effect, serrated yielding, jerky or serrated flow, blue brittleness, etc. The serrations observed in stress-strain curves are generally classified to A–E types (from regular to more irregular) depending on the amount of strain and strain rate. In low alloy steels (LAS) DSA occurs at temperatures within 150–350°C, where the stress-strain curves show serrations, being most marked at 250°C, depending, however, on strain rate. Yield drops of even 30% due to large amplitude serrations can be obtained in the stress-strain curve. The effect of strain rate on DSA temperature range is related to the diffusing atoms to keep pace with the moving dislocations during deformation allowing to form atmospheres around dislocations generated throughout the whole stress-strain curve. Other materials in addition to LAS relevant to light water reactors (LWR) known to cause discontinuities in deformation related to DSA include, e.g., Ni-base alloys including superalloys (due to C and in H-charged condition), austenitic stainless steels (due to both interstitial and substitutional alloying elements) as well as Zr-alloys (due to H, C, N and O).[1-5]

Dynamic strain aging has some detrimental effects on LAS. It results in a peak in ultimate tensile strength (UTS), hardness, and strain hardening rate in the DSA temperature range, a minimum of ductility (elongation to fracture, A and reduction of area, Z) and results in negative strain rate sensitivity. Yield strength is affected by static strain aging rather than DSA resulting in plateau or a small peak in yield strength in the temperature range of DSA. The temperature of the peak effect decreases with decreasing strain rate. In general, the hardening effect of DSA may be better characterized by the tensile properties, rather than only based on the observation of serrations in the stress-strain curve alone. Ultimate tensile strength highlights the hardening effect best and distinguishes the effects of strain rate most clearly. Strain localization and shear bands on the surface of the specimens appear as a result of DSA and intensified acoustic emission is

often related to dislocation multiplication events. Dynamic strain aging results in an increase in the ductile-to-brittle transition temperature following plastic deformation in the DSA temperature range as well as a lowering of the ductile fracture resistance (decrease of tearing modulus) at temperatures within the DSA temperature range.[6–9] A reduction of low-cycle fatigue resistance of LAS in air and water environment is observed as the loading strain rate is decreased – the reduction being much larger in water environments. The role of DSA in environment-assisted cracking (EAC) has not been studied much. However, the EAC data strongly suggest that the susceptibility of LAS to EAC coincides with DSA behavior, in terms of T and strain rate.[10–12] In EAC, DSA is especially important in dynamic crack tip plasticity behavior such as dynamic loading or development of creep strain.

All effects of static and dynamic strain aging are explained in terms of either segregation of solute atoms to dislocations to form condensed Cottrell atmospheres or precipitates, or Snoek (stress-induced) ordering of solute atoms in the dislocation core structure. In ferrite C and N are producing a nearly identical lattice misfit strain, which they can reduce by moving to the dislocation core regions, resulting in an overall reduction in the total strain energy. In ferrite N and C have similar diffusion coefficients and, thus, these two elements are expected to produce nearly similar DSA effects in LAS. Therefore, in general, the effects produced by C and N can be considered as additive. For example, with a typical dislocation density of $10^8/cm^2$ in Fe a C concentration of 10^{-6} wt-% is sufficient to provide one interstitial C atom per atomic plane along all the dislocation lines present. Thus, very small C and N contents are sufficient to form condensed atmospheres on dislocations in ferrite and cause yield point phenomena. At room temperature, the residual solubility of N in ferrite is about 100 times greater than that of C – N solubility in steel is higher at all temperatures than that of C. It is generally assumed that N, rather than C, is mainly responsible for DSA. However, at higher temperatures in the DSA range the increasing solubility of carbon may cause DSA even in the absence of N. Aluminum (or V, Ti) is a strong nitride former and reduces the N content in solution to a low level. Solid state precipitation of aluminum nitride is also important in limiting the austenite grain growth. Thus, Al content (being low generally in weld metals and in welds Al is first combined with O) is also of importance in DSA susceptibility of various steels. In general, in BCC metals interstitial solute atoms cause DSA, while in FCC metals it may also be caused

by substitutional solute atoms. In austenitic stainless steels Cr is thought to be the reason at higher temperatures, but N and C and their pairs with vacancies are important at lower temperatures.

If a steel susceptible to DSA is plastically deformed in the DSA temperature range an unusually high dislocation density is observed coupled with immobilization of many of the dislocations by N and/or C atmospheres. Large yield drops are related, thus, to generation of a large number of new dislocations. The precise mechanism of this is related to the effectiveness of the locking of pre-existing dislocations, which substantially will raise the stress necessary to cause dislocation movement, e.g., inside the crack tip plastic zone. If the pinning is weak, then the yield point effect can also arise as a result of unpinning and break away of dislocations of their C and N atmospheres. When the pre-existing dislocations are strongly locked, either by interstitial atmospheres or precipitates, the yield point effect and serrations result from a rapid generation of new dislocations. Under DSA conditions the C and N atmospheres form continuously also on newly-generated dislocations resulting in a markedly higher density of dislocations to complete the deformation, e.g., in the crack tip plastic zone or heat-affected zones (HAZ) of the welds. This can be seen, e.g., in the HAZ of the welds due to development of shrinking strains during the thermal cycle of welding as well as in later loading in the DSA temperature range.

Deformation induced vacancies ("vacancy model"), which are the diffusion vehicles for the solute atoms, can play also an important role in the DSA process especially in FCC alloys. However, strain-induced vacancies are not expected to accelerate diffusion of interstitial atoms. Therefore, the importance of prior strain in inducing serrated flow has been explained as follows: vacancies form interstitial-vacancy pairs, which order in the stress-strain fields of dislocations and if substitutional-interstitial complexes are involved, vacancies are necessary to increase the mobility of substitutional atoms. Recently, deformation-induced generation of vacancies and their clustering has been considered to be promoted by hydrogen and to play a primary role in hydrogen trapping and HE susceptibility in many FCC and BCC metals and alloys. A substantial density of vacancies can be expected in plastic strain of steels under presence of hydrogen, which is stabilizing the vacancies. Hydrogen is lowering the formation energy of vacancies by the amount of binding energies of trapped hydrogen atoms. Formation of vacancy-solute complexes (such as H, C and N in steels) elevates

the annihilation temperature of vacancies up to 200ºC and higher.[13, 14] Due to the low migration energy of vacancies in Fe (53 kJ/mol) marked diffusion distances in the crack tip regions are attainable in short time. Extra vacancies are introduced in the crack tip plastic zone region in addition due to hydrogen in EAC by oxidation reactions producing vacancies at the oxide metal interface, which are injected into the base metal in the crack tip region, as well. The extra vacancies produced by hydrogen uptake and oxidation due to their agglomeration to clusters and small voids may be more important in causing the brittle-like EAC fracture than hydrogen itself as was already proposed in Reference 15. It has also been observed that if steels susceptible to HE are tested in conditions, which promote DSA, the ductility decreases remarkably by the simultaneous effects of DSA and HE.[16]

In LAS, activation energy for DSA obtained normally from onset temperature of serrated flow with the change of strain rate is equal to that of N/C diffusion in ferrite. Based on the temperature of disappearance of serrations it should correspond to that of a sum of activation energy for diffusion and binding energy of an interstitial atom to the dislocation core.[2] However, the observations for LAS for this explanation to be always true show often too high activation energy values.

Implications of DSA in fracture toughness of LWR pressure vessel and piping steels can especially be expected in as-welded welds. The low post-weld heat treatment (PWHT) temperature is also found to be detrimental. The contents of total and soluble (free) N are typically not known for welds, but can be expected to be in the range of 100 and 10 ppm, respectively. These values should be determined for both base and weld metals, in general, together with the contents of Al. When LAS are used in environments, which promote DSA and EAC including hydrogen embrittlement (HE), the ductility of the steel may decrease remarkably in SSRT, low-cycle fatigue and slow strain rate fracture mechanics tests in LWR environments. Dynamic strain aging is known to affect the upper-shelf ductile cracking as measured by both J_{IC} and tearing modulus (seen to decrease by about 30–40% at the reactor operating temperature region) (e.g., see References 6–9). At the moment there are DSA screening criterion for fracture instability (hardness ratio, BHN (288°C)/BHN (RT), >1.09 crack jumps are likely to occur at 288°C, < 0.91 crack jumps in concert with stable cracking are not expected to occur at 288°C) for leak-before-break analysis corresponding to

seismic dynamic loading at normal plant operation temperature. It may also be possible to develop these kinds of criteria for EAC susceptibility, which is known to be greatest in LAS at around 200–250°C. Additionally, DSA has been manifested in studies of radiation effects on LAS, where interstitial atoms migrate to the radiation-induced point defects or defect clusters at which they are trapped and cause hardening by acting as barriers to slip dislocation motion. Thus, the susceptibility to DSA can be reduced with increasing radiation exposure. In fatigue the DSA effects are similar to those in tensile tests: serrations occur in the hysteresis loops, increased cyclic hardening takes place, negative strain rate sensitivity effect is observed, plastic strain localization and enhanced planar deformation are present.

The temperature for occurrence of DSA increases with increasing strain rate and the peak hardening stress due to DSA decreases linearly with increase of strain rate. The measured activation energy for the onset of serrations in the stress-strain curve is not sensitive to the microstructure or composition of steel. The exemption being the Mn content which seems to influence the diffusion process of N and C by forming Mn-N and Mn-C pairs increasing thus the activation energy for the diffusion process[17]. Large differences in the activation energy for the disappearance of DSA reported suggest that it is also a function of steel composition. The reported values of activation energy for the onset of DSA are in the range of 75–85 kJ/mol being comparable to the common values for N and C diffusion in α-iron, 65–85 kJ/mol (the activation energy for diffusion is higher for C than for N)[2]. Activation energy for the disappearance of serrations can be interpreted as the sum of activation energy for interstitial diffusion in α-iron and the binding energy between dislocations and interstitial solutes. The activation energy of disappearance of serrations (DSA) is quite similar to that for the Snoek-Köster (cold work) internal friction (IF) peak in iron, which suggests that these two processes are related. This can be interpreted as follows: as the dislocation moves, the solute atoms jump between positions in the dislocation core and adjacent to the core, which yields an activation energy equal to the sum of the activation energy for solute diffusion and the binding energy between a solute and dislocation. The binding energies of N and C to dislocations in LAS are not well known at present, but the binding energy between a dislocation in iron and a C atom and a N atom is 0.75–0.85 eV. At present aging is proposed not to occur always during the free motion of the dislocations (motion of dislocations is in general a discontinuous process), but rather during the period

when the dislocations are temporarily held up at local obstacles such as the forest dislocations in the glide plane. The waiting time, t_w, is directly related to the strain rate[18]. A possible mechanism is the draining of solutes from the forest dislocations by pipe diffusion. Disappearance of serrated flow occurs when localized flow changes to homogeneous flow.

Dynamic strain aging in LAS is associated with diffusion of interstitial species such as C and N atoms. The internal friction technique is suitable for evaluation of the amounts and behavior of free C and N atoms in the lattice and their interactions with dislocations. In a common internal friction spectrum of LAS a Snoek peak associated with redistribution of free C and N between equivalent octahedral sites in the lattice is expected at above RT. This peak may be asymmetric resulting from overlapping of C peak (located at around 39°C in α-Fe) and N peak (located at around 24–25°C in α-Fe). The other important thing in LAS compared to pure Fe is the presence of alloying elements (such as Cr, Mo and V) affecting especially the diffusivity (jump process) of N and C and thus reducing markedly the Snoek peak height. The Snoek peak height can give a measure of free randomly distributed N or C content in the lattice. Generally a linear relationship between Snoek peak height and free interstitial content is assumed[19]. This allows a correlation between the observed ductility loss of LAS in tensile tests to Snoek peak height in internal friction measurements to obtain a measure for DSA sensitivity of steel. The broad Snoek-Köster (cold work) peak observed between 150–250°C is due to the mobility of interstitial atoms in the dislocation stress-strain fields. The exact mechanism of this relaxation is still to be clarified. Correlation between internal friction results and tensile and fracture mechanical data would allow a better understanding of the role of DSA in EAC of LAS. In the following this is tried for the first time for LAS.

2. Materials and experimental methods

The materials used in this study are a 20 MnMoNi 5 5 steel similar to SA508 Cl. 3, SA533 B Cl. 1 steel and a reactor pressure vessel (RPV) circumferential girth weld metal. The chemical compositions of these steels are reported in Table 1. The O_2-contents of the steels were 140 (20 MnMoNi 5 5), 20 (SA533 B Cl. 1) and 260 (RPV weld) ppm. The heat treatment conditions are given in Table 2. The mechanical properties of the studied materials at room temperature and at

288ºC are shown in Table 3. More detailed information of the materials is given in Reference 20.

Table 1. The chemical compositions (in wt.-%, N_{tot} and N_{free} in ppm) of the studied RPV steels.

Steel	C	Si	Mn	P	S	Cr	Mo	Ni	V	Al	Cu	N_{tot}*	N_{free}*
20 MnMoNi 5 5	0.21	0.25	1.26	0.004	0.004	0.15	0.5	0.77	0.008	0.013	0.06	70, 80	30
SA 533 B Cl. 1	0.25	0.24	1.42	0.006	0.018	0.12	0.54	0.62	0.007	0.03	0.15	60, 70	<1
RPV weld	0.05	0.17	1.19	0.013	0.007	0.04	0.55	0.94	0.006	0.0053		110, 100	16

∗For N_{tot} results of two independent laboratories are shown in ppm.

Table 2. The heat treatment conditions of the studied RPV steels (WQ: Water quenched, FC: Furnace cooled, AC: Air cooled).

Steel	**Heat treatment**
20 MnMoNi 5 5	**Q+T:** 910°C – 920°C / 6 h / WQ / 640°C – 650°C / 9.5 h / FC
SA 533 B Cl. 1	**Q+T**: 915°C / 12 h / 860°C / 12 h / WQ / 635°C / 12 h / FC
RPV weld	**PWHT:** 540°C – 555°C / 59 h / 465°C / 590°C – 610°C / 21 h / 465°C / 590°C – 605°C/ 11.5 h/ AC

Table 3. The mechanical tensile properties (according to DIN 50145) of the studied steels at room temperature and at 288ºC (direction of gauge length: T).

Steel	**25°C**				**288°C**			
	$R_{P0.2}$ MPa	R_m MPa	A_5 %	Z %	$R_{P0.2}$ MPa	R_m MPa	A_5 %	Z %
20 MnMoNi 5 5	485	648	19.3	72.1	418	572	12.9	70.0
SA 533 B Cl. 1	467	605	18.2	71.9	400	578	16.2	69.5
RPV weld	553	624	17.4	73.1	473	569	9.7	67.7

Internal friction experiments were performed in the temperature range of 77–1000 K on an inverted torsion pendulum with an applied strain of 5×10^{-6} and heating rate of 1.5°C/min. The samples (1.5×0.8×50 mm) were machined in rolling direction of the original plates. The materials were also studied in cold worked conditions (cold rolling up to 40% reduction) to reveal the Snoek-Köster internal friction peaks and after hydrogen charging, which was applied at room temperature in 1 N H_2SO_4 aqueous solution with a 5 mg/l addition of $NaAsO_2$ with a current density of 10 mA/cm^2 for 20 h to reveal the possible hydrogen DSA interactions.

3. Results

As DSA refers to the attractive interaction between diffusing solute atoms and the mobile dislocations during straining, tensile testing as functions of temperature and strain rate was performed. The mechanical property variation with temperature is exhibited in Fig. 1 for studied steels. Ultimate tensile strength (UTS) values show maximum and reduction of area (Z) values show minimum in the tested temperature range indicating DSA behavior. This is also manifested by the strain rate dependence of these values at 200ºC. Typical stress-strain curves of 20 MnMoNi 5 5 steel at 200ºC exhibiting serrations at slow strain rates are presented in Fig. 2. The serrations start almost immediately on yielding (small critical strain) and exhibit after irregular beginning a saw-tooth appearance combined with small serrations (type A + B). The stress drops associated with the serrations vary up to as high as 20 MPa. In general, the magnitude of the stress drops increases with decreasing the strain rate. Based on the small number of tests it was not possible to determine the activation energy values for the onset and disappearance of the serrations in these steels separately. With the appearance of serrations there is a marked increase in the strain hardening rate and UTS and a loss of ductility. Furthermore, the strain rate sensitivity of the flow stress becomes negative during DSA. The peak stress regions of the stress-strain curves are not associated with the serrations and the stress peak is shifted to a higher temperature and the increase of UTS is smaller at higher strain rates. Based on changes in UTS and Z, the susceptibility to DSA of studied three steels decreases in the order: 20 MnMoNi 5 5 > SA533 B Cl. 1 > RPV weld.

The EAC behavior of the studied RPV steels has been examined in simulated clean and transient BWR conditions by SSRT, low-cycle corrosion fatigue and constant load tests in the temperature range of 150–288°C. Maximum susceptibility to EAC in SSRT tests was observed at 250°C and at slow strain rates. Steel 20 MnMoNi 5 5 showed at 200 and 250ºC (but not at 288°C) sustained stress corrosion crack growth in constant load crack growth tests in simulated BWR water conditions but the other materials were not susceptible to constant load EAC. In low-cycle fatigue tests the materials behaved very similarly in simulated BWR water conditions showing high crack growth rates at low frequencies in the studied temperature range.[21]

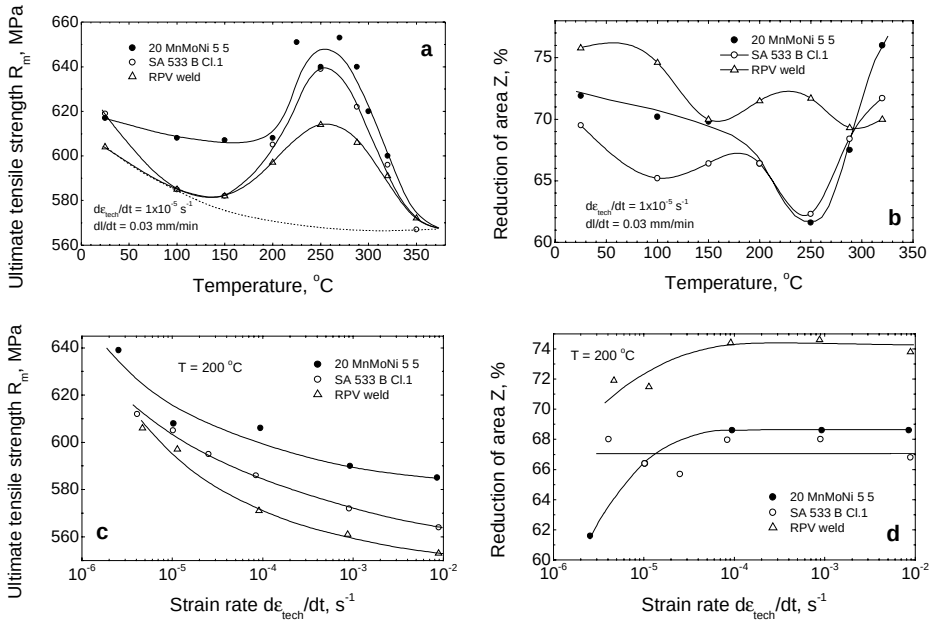

Figure 1. Ultimate tensile strength (a) and reduction of area (Z) (b) as a function of tensile test temperature for studied steels with strain rate of 1×10^{-5} s^{-1}. UTS (c) and Z (d) as a function of strain rate at 200ºC for the studied steels (direction of gauge length: T).

The internal friction results are shown in Figs 3–7. Snoek peaks resulting from free C and N redistribution between octahedral sites in the ferrite lattice are not visible in the spectra of as-received steels, except the RPV weld metal which shows a small Snoek peak. This indicates that in the RPV weld metal the content

of free interstitials in solid solution is the highest. The results indicate also that the C and N contents are not in the solid solution at the detection limit of the present IF technique (estimated to be 10 ppm). The weak peak observed in 500 K temperature region corresponds to the Snoek-Köster (cold work) (S-K) peak and is due to the interaction between interstitials, C and N, and dislocations. The higher height of S-K peak of 20 MnMoNi 5 5 steel is apparently due to the higher C content of this steel compared to the weld metal. The S-K peak height is related to the density of mobile dislocations and the interstitial content in the vicinity of dislocations. In order to study S-K interaction more closely the density of fresh dislocations was markedly increased by cold rolling (up to 40 % reduction). It can be seen in Fig. 3a that already 5% tensile strain in the DSA temperature range (280ºC) results in a well-defined S-K peak as well as a Snoek peak. A correlation with S-K peak height (30% strain at RT) and interstitial content is presented in Fig. 3b. This result suggests that the influence of C masks totally the effects of N. Thus, it seems that free C content (not known exactly) is of crucial importance in correlation between IF S-K peak height and interstitial content. Carbon and nitrogen interaction parameters with dislocations were evaluated with 35% cold rolled 20 MnMoNi 5 5 steel, Fig. 4. The activation parameters of the C/N S-K relaxation obtained by frequency shift of IF peak maxima for 20 MnMoNi 5 5 steel are the following: $H = 1.67$ eV and $\tau_0 = 3.7\times10^{-18}$ s. Activation enthalpy of S-K relaxation can be expressed as $H_{S\text{-}K} = H_D + H_B$, where H_D is enthalpy of C/N diffusion in solid solution and H_B is enthalpy of C/N binding to dislocations. Using $H_D = 0.84$ eV [22], H_B can be evaluated to be 0.83 eV in this case.

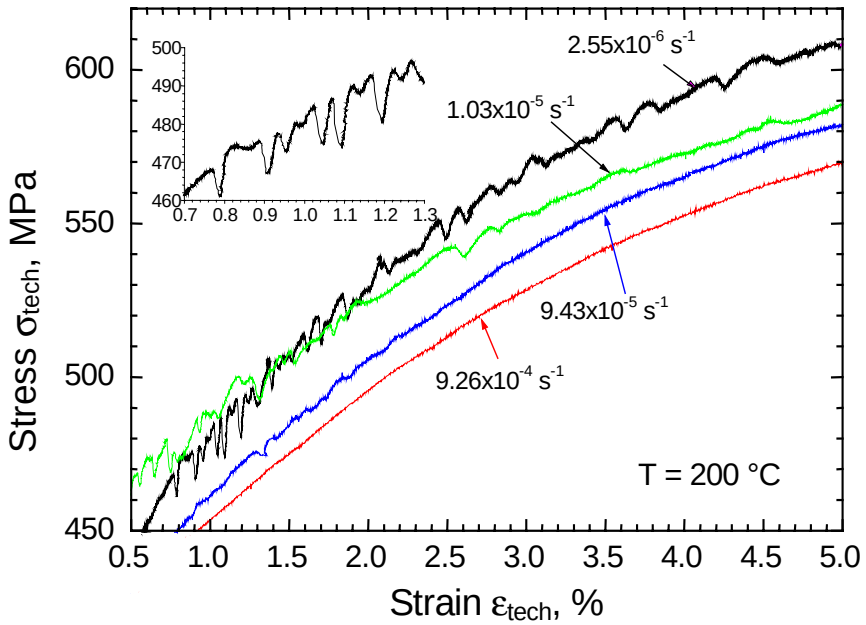

Figure 2. Stress-strain curves for 20 MnMoNi 5 5 steel at 200ºC in air obtained with different strain rates.

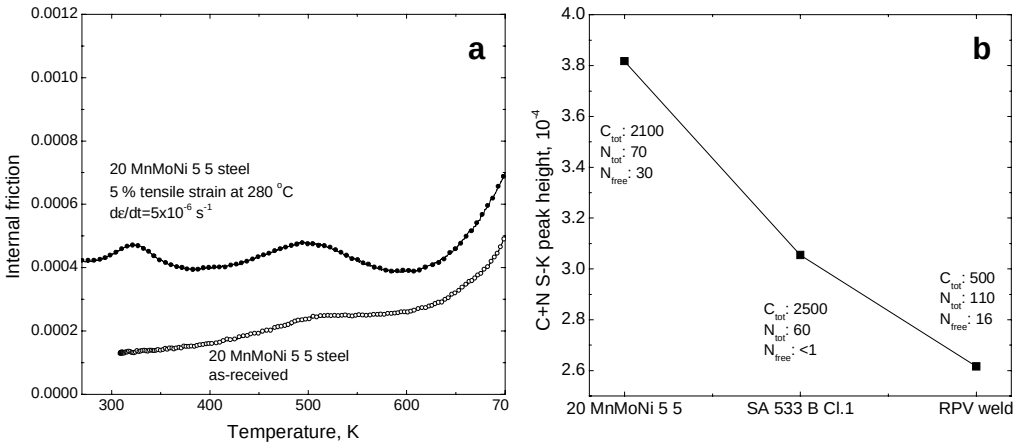

Figure 3. (a) Internal friction spectra of 20 MnMoNi 5 5 steel in as-received condition and after 5% tensile strain at 280ºC. (b) S-K peak heights for studied steels (30% strain at RT) related to their C+N contents (wt. ppm).

Internal friction spectra were also studied after hydrogen charging, Fig. 5, with cold deformed materials to simulate the hydrogen uptake conditions in the crack tip plastic zone. Hydrogen dislocation interaction causes a two-component IF peak in the temperature range of 100–200 K. Study of hydrogen S-K-1 peak allows to determine the enthalpy of hydrogen interaction with dislocations. S-K-2 peak is probably related to evaporation of hydrogen Cottrell atmospheres on dislocations. In all deformed materials a so called γ-peak is present at around 320 K. This peak reflects a process of kink-pair nucleation on screw dislocations[22]. This peak is observed after cold work without hydrogen charging, even though it is often claimed that hydrogen enhances kink-pair formation. Peak at 500 K is the C/N S-K peak, which was discussed earlier. All of these peaks except C/N S-K peak at 500 K vanish after heating to 500 K exhibiting the transient characteristics of hydrogen and γ-peaks. The parameters of hydrogen dislocation interactions were also evaluated based on the frequency shift of the hydrogen IF peak maximum both for 20 MnMoNi 5 5 steel and the RPV weld metal, Figs 6 and 7. The activation parameters for the S-K relaxation are for 20 MnMoNi 5 5 steel H = 0.44 eV and $\tau_0 = 6.5\times10^{-15}$ s and for weld metal H = 0.46 eV and $\tau_0 = 1.1 \times 10^{-14}$ s, respectively.

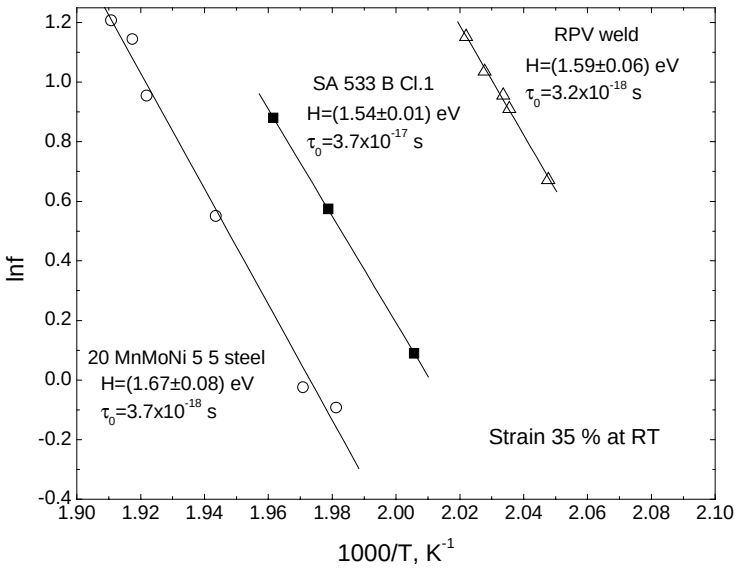

Figure 4. Arrhenius plots for C/N S-K peaks of 35% deformed (cold rolling) 20 MnMoNi 5 5 steel, SA 533 B Cl.1 steel and RPV weld metal. Activation parameters are obtained for C/N S-K relaxation from frequency shift of peak maximum.

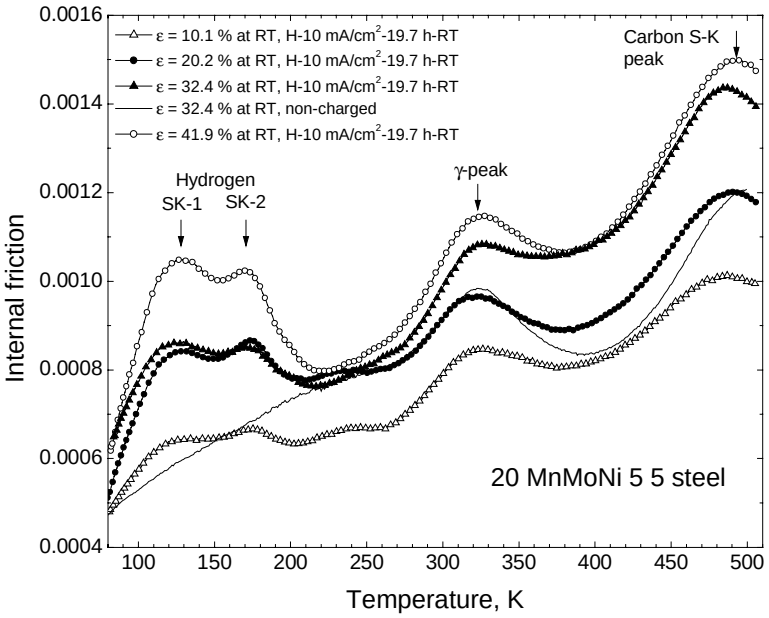

Figure 5. IF spectra of 20 MnMoNi 5 5 steel after cold deformation and hydrogen charging as indicated in the plot.

The mechanical test data of studied materials is summarized in Figs 8–10 in strain rate – temperature coordinates. Generally, four regions are observed: yield plateau, yield plateau + few serrations, serrations, no plateau and no serrations. Boundaries for onset and disappearance of serrations (dotted lines) have been drawn rather approximately supposing that the boundary is described by Arrhenius type of dependence. Solid lines are calculated using the values of activation enthalpies of S-K peaks obtained from IF measurements. There is a very good agreement between calculated curve (based on IF data) and boundary of disappearance of serrations for studied RPV steels. Boundary of serration disappearance is not clear for RPV weld in Fig. 10 due to a small amount of experimental data. These results clearly confirm the main role of interaction between mobile interstitials and dislocations in the development of DSA in LAS.

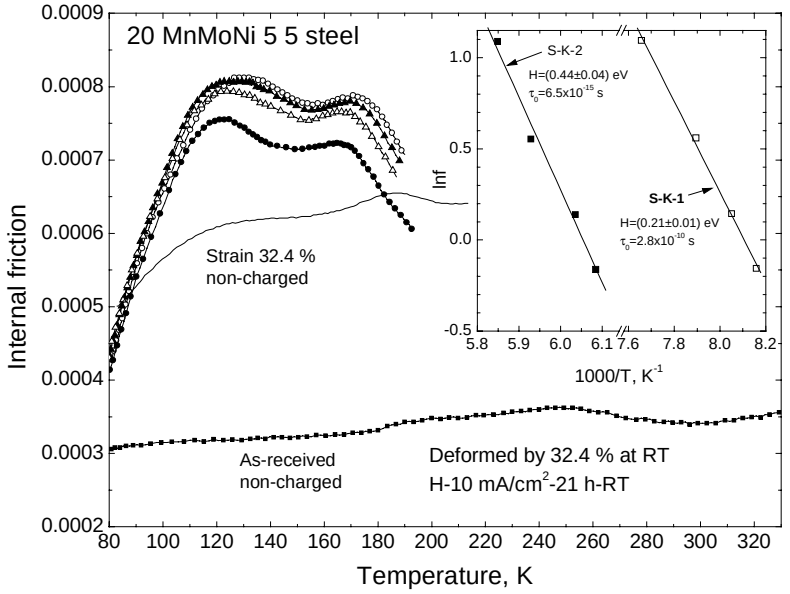

Figure 6. IF spectra and evaluated activation parameters for hydrogen S-K peaks of 20 MnMoNi 5 5 steel after 32% cold work.

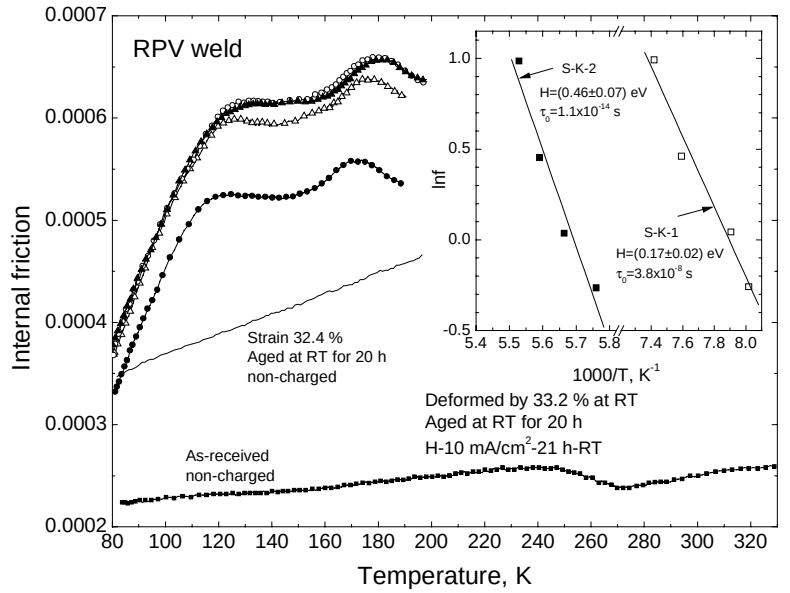

Figure 7. IF spectra and evaluated activation parameters for hydrogen S-K peaks of RPV weld metal after 33% cold work.

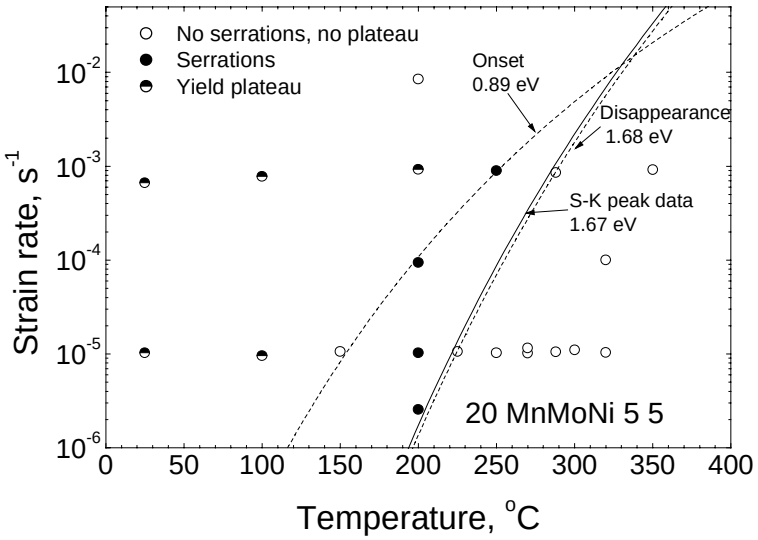

Figure 8. Map of presence of serrations in stress-strain curves of 20 MnMoNi 5 5 steel. Dotted lines present the onset and disappearance of serrated flow. Solid line is plotted using the activation enthalpy for S-K IF peak.

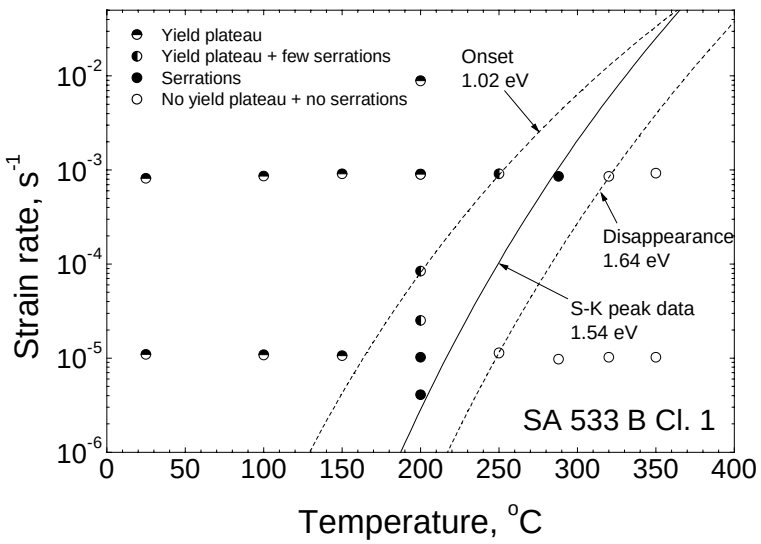

Figure 9. Map of presence of serrations in stress-strain curves of SA533 B Cl. 1 steel. Dotted lines present the onset and disappearance of serrated flow. Solid line is plotted using the activation enthalpy for S-K IF peak.

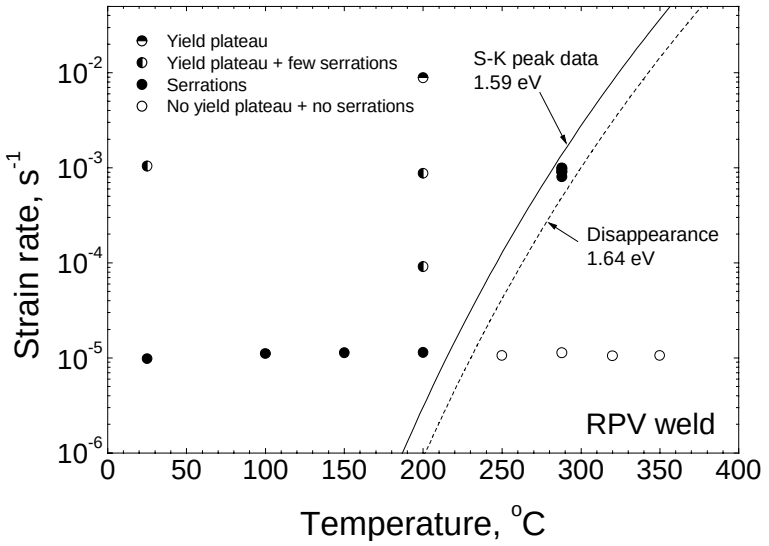

Figure 10. Map of presence of serrations in stress-strain curves of RPV weld. Dotted line presents disappearance of serrated flow. Solid line is plotted using the activation enthalpy for S-K IF peak.

4. Discussion

Environment-assisted cracking behavior of LAS is controlled by various parameters that affect the crack initiation and crack propagation such as the mechanical, material, and environmental parameters. These all effects affect the yield strength, strain hardening exponent and creep rate, which are important factors affecting the crack tip strain rate in EAC. Since DSA is mainly caused by diffusion of interstitial atoms to dislocations and locking them, it is thus evident that possible embrittlement caused by DSA depends on both the strain rate and temperature. The activation energies of diffusion of C and N in α-iron do not differ markedly. Therefore it is not possible to identify only based on the activation energy value obtained from mechanical testing or IF measurements, which interstitial atom is responsible for the occurrence of DSA. Thus, also the chemistry of the steel has to be carefully determined and heat treatments to be considered.

The absence of Snoek internal friction peak at about 40°C does not allow any conclusions to be made between free interstitials and mechanical properties of

these steels. It has been observed in general that when the S-K (cold work) peak is present the Snoek peak decreases. The broad S-K internal friction peak at 500 K increases in height with degree of cold work, i.e., with the dislocation density. This peak has been proposed to be due to the movement of dislocations either in the presence of an atmosphere of interstitial atoms or small particles of carbide (Schoeck's theory). It has also been proposed that the basic mechanism of S-K relaxation is the reorientation of interstitials in the immediate vicinity of dislocations (Köster's theory) or the formation of kink-pairs in the presence of mobile interstitial atoms (C, N, O) (Seeger's theory). Analogous mechanisms should be related at lower temperatures to hydrogen dislocation interaction.[23]

An internal friction peak, called γ-peak is observed typically in BCC metals after plastic deformation and it has been attributed to the thermally assisted generation of kink-pairs on screw dislocations. Consequently the Peierls-Nabarro stress can be estimated from the activation energy of γ-peak (0.6–0.7 eV). Even small amounts (20–30 at. ppm) of C and N in solution are able to suppress this peak. The existence of this peak, thus, supports the non-existence of Snoek peak in these steels.

The binding energy of hydrogen to dislocations obtained in this study (0.44–0.46 eV) is in agreement with the values obtained normally for α-Fe (0.42–0.56 eV) depending on the model assumed. The obtained activation energy values for hydrogen diffusion, 0.17–0.21 eV, are higher than reported for α-Fe in the literature (e.g., 0.13 eV). Concerning the role of vacancies related to hydrogen charging in these steels causing high concentration of excess vacancies, no clear conclusive evidence of their possible contribution to internal friction could be observed. However, it is clear that the heights of both γ-peak and the S-K peak increase markedly in the case of hydrogen charging of cold worked steels. This may be related to increased vacancy concentration in these cases, since vacancies enhance kink-pair formation and they form interstitial-vacancy pairs, which cause enhanced S-K relaxation. The hydrogen and γ-peaks anneal out at temperatures above their maximum temperature and after heating to 500 K only S-K peak was present. This is because of hydrogen outgasing from the sample and relaxation of dislocation structures.

The commonly observed incubation strain (critical strain) before the onset of serrated flow has been explained by the threshold concentration of vacancies

created by plastic deformation, which results in an enhanced diffusion coefficient of the solute atoms through the lattice responsible for DSA. The critical strain is also dependent on strain rate. In these steels this type of critical strain was not observed. The rapid onset of serrated plastic deformation is a result of rapid dislocation multiplication, unpinning or a combination of these causing large yield drops. The stress amplitude of serrations increases with decreasing strain rate, increasing solute content and with plastic strain accumulation (higher pinning because of higher diffusivity associated with increased vacancy content and high obstacle density allows longer waiting time for dislocation pinning). All these events can be considered to take place inside the plastic zone of the crack tip, where strain occurs as a result of highly localized deformation in DSA conditions. The region of localized deformation, i.e. Lüders band, is bordered to non-deformed (during the event) regions by Lüders front. Lüders strain refers to the strain associated with the passage of a single deformation band of localized deformation without strain hardening. Each serration in the stress-strain curve is produced by a propagation of a separate Lüders band. DSA of dislocations at the Lüders front can also take place and halt its passage and during reloading DSA causes a new deformation band formation event.

Prior deformation inside the crack tip plastic zone produces a high forest dislocation density. Dislocations are not mobile due to DSA and can not be broken away from their solute clouds. Thus, the rapid accumulation of a dense dislocation structure causes the high work hardening rate. The high production rate of dislocations due to repeated yielding together with solute restricted dynamic recovery processes associated with dislocation annihilation may not be able to operate. Inside plastic zone in the pre-strained material static strain aging is, thus, occurring, but it will have a dynamic component as well as the crack tip plastic zone undergoes slow strain due to crack extension or creep. The freshly formed dislocations are then able to form solute atmospheres and become completely pinned or move slowly depending on whether the dislocation atmosphere is condensed or dilute. All this is resulting in more localized plastic deformation especially at the crack tip conditions, when serrated flow is occurring and mobile dislocations are strongly pinned. The high concentration flux of vacancies at the crack tip will facilitate the plastic deformation to occur inside the deformation band ahead of the crack tip.

The synergistic interactions between EAC and DSA in dynamic monotonic loading (SSRT or slow strain rate fracture mechanics test) and in fatigue at elevated temperature water environment may be rationalized as follows. Hydrogen and vacancies produced by the corrosion reactions at the crack tip region enter the steel and hydrogen diffuses to the strong trapping sites inside crack tip maximum hydrostatic stress region ahead of the crack tip such as to MnS inclusions. These sites are normally the initiation sites for local quasi-cleavage events as well as void formation. The microcracks link with the main crack. Dynamic strain aging occurs in steels both in air and water environments at a given temperature lowering the ductility and toughness of the steel mainly due to enhanced strain localization. Hydrogen and possibly very high vacancy concentrations are available only in certain water environments triggering the brittle-like quasi-cleavage events that lower the value of J and enhance EAC and cyclic crack growth rate in fatigue. Thus, dynamic strain aging is not the only contributor to EAC, such as reduction of fatigue life with decreasing strain rate, enhanced corrosion fatigue crack growth rate or stress corrosion cracking under dynamic and sometimes static (of these materials 20 MnMoNi 5 5 steel was shown to exhibit static crack extension at 200°C in 8 ppm O_2 containing BWR water at high stress intensity levels[21]) loading conditions. However, DSA in its temperature range makes typically a marked additional contribution to EAC susceptibility, which needs much more studies to be understood mechanistically, in detail.

5. Conclusions

Occurrence of dynamic strain aging in low alloy pressure vessel and piping steels was reviewed and two RPV steel base metals and one RPV weld metal were studied experimentally by slow strain rate tensile testing in air. Additionally, internal friction method was used for evaluating the parameters of interaction between interstitial atoms (C, N, H) and dislocations. DSA was clearly associated to the reduction of ductility and increasing strain hardening and UTS of the steels. Internal friction measurements confirmed the interstitial (C/N, H) interactions with dislocations in cold worked steels simulating the material microstructures inside the plastic zone ahead of the EAC cracks. The effects of hydrogen uptake to the deformed steels were discussed based on the

suggested high vacancy concentration related to hydrogen in solution and on possible effects of vacancies on EAC mechanism.

Acknowledgements

This study was funded by Tekes (Finland) within the MVM-RKK project as well as the Swiss Federal Nuclear Safety Inspectorate (HSK) and Swiss Federal Office for Energy (BFE) (Switzerland). Mr. H. Hänninen is also grateful for Visiting Scientist scholarship of JRC Petten, The Netherlands.

References

1. Hall, E. O. Yield Point Phenomena in Metals & Alloys. Macmillan, Australia, 1970. 296 p.

2. Keh, A. S., Nakada, Y. and Leslie, W. C. Dynamic Strain Aging in Iron and Steel. Dislocation Dynamics. Eds. A. R. Rosenfield et al. McGraw–Hill Book Co., 1967. Pp. 381–408.

3. Baird, J. D. Dynamic Strain Aging. The Inhomogeneity of Plastic Flow. ASM, Metals Park, Ohio, 1973. Pp. 191–222.

4. Dingley, D. J. and McLean, D. Components of the Flow Stress of Iron. Acta Metall., 1967, 15 (5), pp. 885–901.

5. Robinson, J. M and Shaw, M. P. Microstructural and Mechanical Influences on Dynamic Strain Aging Phenomena. International Materials Reviews, 1994, 39 (3), pp. 113–122.

6. Miglin, M. T., Van Der Sluys, W. A., Futato, R. J. and Domian, H. A. Effect of Strain Aging in the Unloading Compliance J Test. Elastic-Plastic Fracture Test Methods. The User's Experience. ASTM STP 856, E. T. Wessel and F. J. Loss (Eds.) American Society for Testing and Materials, 1985. Pp. 150–165.

7. Kang, S. S. and Kim, I. S. Dynamic Strain-Aging Effect on Fracture Toughness of Vessel Steels. Nuclear Technology, 1992, 97(3), pp. 336–343.

8. Mohan, R. and Marschall, C. Cracking Instabilities in a Low-Carbon Steel Susceptible to Dynamic Strain Aging. Acta Mater., 1998, 46 (6), pp. 1933–1948.

9. James, L. A. and Porr, W. C. The Effect of an Elevated Temperature Aqueous Environment upon the J-controlled Tearing of a Low-Alloy Steel. Int. J. Pressure Vessels and Piping, 1999, 76, pp. 769–779.

10. Atkinson, J. D. and Yu, J. The Role of Dynamic Strain-Ageing in the Environment Assisted Cracking Observed in Pressure Vessel Steels. Fatigue Fract. Engng Mater. Struct., 1997, 20 (1), pp. 1–12.

11. Lee, S. G. and Kim, I. S. Strain Rate Effects on the Fatigue Crack Growth of SA508 Cl.3 Reactor Pressure Vessel Steel in High-Temperature Water Environment. J. Pressure Vessel Technology, 2001, 123 (1), pp. 1–6.

12. Solomon, H. D. and De Lair, R. E. The Influence of Dynamic Strain Aging on the Low-cycle Fatigue Behavior of Low Alloy and Carbon Steels in High Temperature Water.

13. Iwamoto, M. and Fukai, Y. Superabundant Vacancy Formation in Iron under High Hydrogen Pressures: Thermal Desorption Spectroscopy. Mat. Trans. JIM, 1999, 40 (7), pp. 606–611.

14. Nagumo, M., Yagi, T. and Saitoh, H. Deformation-Induced Defects Controlling Fracture Toughness of Steel Revealed by Tritium Desorption Behaviors. Acta Mater., 2000, 48, pp. 943–951.

15. Oriani, R. A. A Mechanistic Theory of Hydrogen Embrittlement of Steels. Ber. Bunsen-Ges. Phys. Chem., 1972, 76 (8), pp. 848–857.

16. Kikuta, Y., Araki, T. and Yoneda, M. Hydrogen Embrittlement and Dynamic Strain Aging in Steel at Elevated Temperature. Third Int. Congress on Hydrogen and Materials, Paris, France, 1982. Pp. 599–604.

17. Li, C.-C. and Leslie, W. C. Effects of Dynamic Strain Aging on the Subsequent Mechanical Properties of Carbon Steels. Met. Trans., 1978, 9A (12), pp. 1765–1775.

18. McCormick, P. G. Theory of Flow Localization due to Dynamic Strain Ageing. Acta Metall., 1988, 36 (12), pp. 3061–3068.

19. Wagner, D., Moreno, J. C. and Prioul, C. Dynamic Strain Aging Sensitivity of Heat Affected Zones in C-Mn Steels. J. Nuclear Mat., 1998, 252, pp. 257–265.

20. Heldt, J. and Seifert, H. P. Stress Corrosion Cracking of Low-Alloy, Reactor-Pressure-Vessel Steels in Oxygenated, High-Temperature Water. Nuclear Engineering and Design, 2001, 206, pp. 57–89.

21. Seifert, H. P. Unpublished results, 2001.

22. Richie, I. G., Dufresne, J. F. and Moser, P. Internal Friction of Deformed Pure Iron. Phys. Stat. Sol. (a), 1978, 50, pp. 617–626.

23. Nowick, A. S. and Berry, B. S. Anelastic Relaxation of Crystalline Solids. Academic Press, New York, 1972. 677 p.

24. Seeger, A. A Theory of the Snoek-Köster Relaxation (Cold Work Peak) in Metals. Phys. Stat. Sol. (a), 1979, 55, pp. 457–468.

Effects of water chemistry transients on crack growth rate of nickel-based weld metals

Aki Toivonen, Pekka Moilanen, Pertti Aaltonen and Laura Taivalaho
VTT Industrial Systems, Espoo, Finland
Erkki Muttilainen
Teollisuuden Voima Oy, Olkiluoto, Finland

Abstract

Stress corrosion crack growth rates of Alloy 182 and 82 weld metals in thermally aged (400°C/200 h) conditions have been measured in simulated BWR conditions. The effects of water chemistry impurity concentration transients on crack growth rate and cracking morphology have been studied. The time for onset of accelerated crack growth due to impurity / conductivity transient was measured when the conductivity of the coolant was adjusted by additions of sulphate as H_2SO_4 in the range of 10–100 ppb. Crack growth was monitored using potential drop method during slow rising displacement testing applied to 10×10 mm^2 cross section, fatigue pre-cracked, three point bend specimens. The delay in crack growth rate slow down after returning to high purity water was also measured.

In the tests an increase in the crack growth rate became visible in Alloy 182 within 25–45 h after sulphate was introduced into the bulk water. Although there is no reason or consistent data to support a permanent increase in crack growth rate caused by a sulphate transient, the measured crack growth rate did not return back to the level prevailing prior to the transient. In Alloy 82 no crack growth was observed with any of the applied conditions of this study. Crack growth rates were measured also for cold deformed AISI 316NG and furnace sensitised AISI 304 stainless steels, as reference.

1. Introduction

The effect of sulphate on crack initiation and propagation rate in BWR environment of Alloy 182 weld metal has been investigated in many studies, and an accelerating effect of sulphate on crack growth rate has been found in the investigations. Initiation is also enhanced, if the sulphate concentration is high enough to change the pH value from near neutral to acidic. However, the amount of sulphate addition has mostly been high, of the order of 1 ppm [1, 2, 3], and only few results are available on the effect of small amounts, i.e., 30 ppb of sulphate, relevant to the possible ion exchange resin intrusion induced concentrations in a real BWR plant. In the surveyed literature, no data was found on the effect of sulphate concentrations at the level of 10 ppb or less.

Sulphate guideline values for cold shutdown, hot standby and power operation corresponding to three different action levels are given in Table 1. According to the EPRI BWR Water Chemistry Guidelines – 1993 Revision [4], for the action level 2, meaning the initiation of unit shutdown within 24 h; the level of sulphate ion concentration (>20 ppb) is established for crack growth rates of approximately 10 times higher than those at the median concentration level, and this requires corrective actions as soon as practicable. The median level of sulphate in BWRs in the United States given in Water Chemistry Guidelines – 1993 Revision [4] was only 2 ppb.

Table 1. Sulphate concentration in reactor water (ppb), EPRI BWR Water Chemistry Guidelines – 1993 Revision [4].

Action level	1	2	3
	Sulphate concentration (ppb)		
Cold Shutdown	> 100	---	---
Hot Standby	---	> 100	> 200
Power Operation	> 5	> 20	> 100

The presence of anionic impurities has been shown to enhance the crack growth rate even at low temperatures. The decrease of the corrosion potential, e.g., by HWC, reduces the crack growth rate and therefore tends to offset the effect of impurities. However, with increasing temperature, the crack growth rate can be

significant even in de-aerated water, i.e., at low corrosion potentials at high temperatures, if the anion concentration is high [5, 6].

Stress corrosion cracking in Alloy 182 is interdendritic, and uneven crack propagation is common. The accuracy of the commonly used crack length measurement method, Potential Drop (PD) method, is sensitive to the unevenness of the crack extension. The uneven crack propagation and remaining uncracked ligaments behind the crack tip may result in a considerable difference between the crack extension measured using PD and actual physical crack extension observed on the fracture surface.

The critical sulphate ion level required to accelerate crack growth depends on the flow conditions and the duration of the transient. In tests conducted in Studsvik two sulphate extrusions of short duration (<14 h) were needed before measurable acceleration in the crack growth rate was observed [7]. On the other hand, the decrease in the crack growth rate after returning to low impurity level in the bulk environment can be prolonged up to >100 hours.

2. Experimental procedures

Test materials were weld metals Alloy 182 and 82 in thermally aged condition. The thermal aging was conducted by 200 h annealing at 400^{o}C. The chemical compositions of the studied test materials are presented in Table 2. The specimens were pre-fatigued three point bend specimens with 10x10 mm^2 cross section. In addition to the weld metals Alloy 182 and 82, sensitised AISI 304 and cold worked AISI 316NG stainless steel specimens were tested for reference purpose. Thermally sensitised AISI 304 and cold worked AISI 316NG are known to be susceptible to intergranular stress corrosion cracking (IGSCC) in BWR conditions [8].

Table 2. Chemical compositions, w%, of the test materials, weld metals Alloy 182 and 82, sensitised AISI 304 and cold worked AISI 316NG. The compositions of Alloy 182 and 82 and AISI 316NG are given by the material suppliers. The composition of AISI 304 is a typical composition, not a measured one [9].

	Fe	C/N	Cr	Mn	Si	S	Ti/Mo	Ni
Alloy 182	8.07	0.03/-	15.24	7.57	0.52	0.001	0.52/-	Bal.
Alloy 82	0.71	0.036/-	20.23	2.92	0.05	0.001	0.38/-	Bal.
AISI 304	Bal	< 0.08/-	18-20	< 2.0	< 1.0	< 0.03	-/-	8-12
AISI 316NG	Bal	0.013/0.056	16.96	1.86	0.28	0.004	-/2.55	10.5

The test method applied was very slow rising displacement rate (2×10^{-8} mm/s) three point bending test (3PB). Six specimens were loaded simultaneously in the same autoclave using separate loading frames and instrumentation for each specimen. The test environment was simulated BWR environment: temperature 273^{o}C and outlet oxygen content 300 ppb. Diluted H_2SO_4 pre-mixture solution was added into the high temperature and pressure autoclave inlet water by a liquid chromatograph pump. The flow rate of the injection solution was used to adjust the concentration of SO_4^{2-} in the water. The outlet flow was purified with ion exchangers before returning the water into the re-circulation. The re-circulation flow volume through the autoclave was 0.3 l/min, which means that the autoclave water was refreshed in every 20 min. The water flow rate inside the autoclave was increased by constricting the inlet flow. The water chemistry parameters for the outlet water and inlet water (pH, conductivity and dissolved oxygen content) were continuously measured at ambient temperature. Corrosion potential was measured using an Ag/AgCl-electrode with 0.01 M KCl-electrolyte.

Crack lengths were monitored by reversing direct current potential drop method during the tests. The crack lengths were calculated using the closed form expression for potential drop calibration presented in standard ASTM E 1737-96, and after that by applying linear correction to fit the calculated crack extension to physical crack extensions measured using an optical microscope.

J-integral levels were calculated by following the procedures presented in standard ASTM E 1737-96. After the J-integral levels were calculated, the J-integral values were converted into K-values by using the relation [10]:

$$K_J = \sqrt{\left[J * E / \left(1 - \nu^2\right)\right]} \qquad (1)$$

where ν = Poisson's ratio and E = Young's modulus.

The crack growth rates of this study are presented as a function of K_J obtained using equation (1).

3. Results

Fig. 1 shows an example of a typical load-displacement curve of a thermally aged Alloy 182 3PB specimen during testing with sulphate intrusions. The load starts to decrease quickly after sulphate is injected into the autoclave inlet water. When the sulphate intrusion is finished, the load decrease rate begins to slow down immediately.

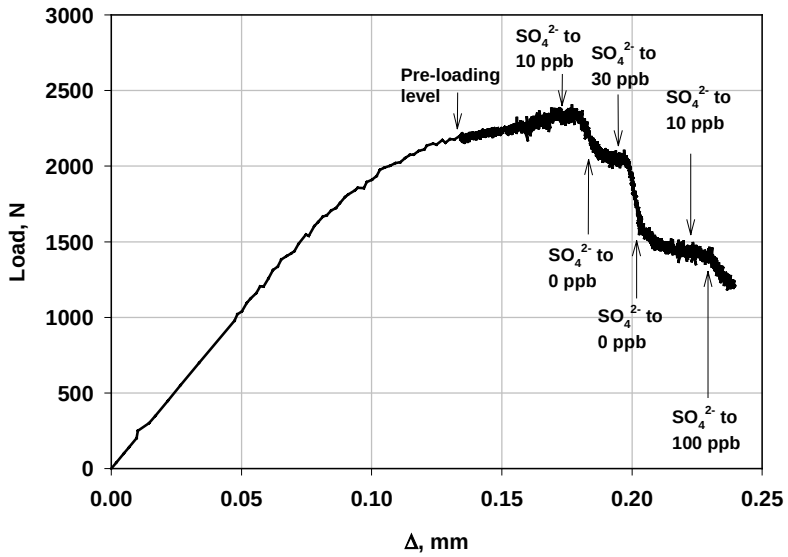

Figure 1. A typical load-displacement curve showing the effect of sulphate induced acceleration of crack growth rate in thermally aged Alloy 182.

The crack extension measured by PD and calculated using the closed form expression remained below the physical crack extension due to the uneven crack growth leaving uncracked ligaments behind the crack tip in Alloy 182. The difference between the crack extension calculated using the measured PD data and the extension measured on the fracture surface was up to 50%, depending on the specimen. The PD data was linearly corrected to average physical crack extension measured on the fracture surface of each specimen. The crack propagation rates obtained during the test using this method are presented in Fig. 2 for thermally aged Alloy 182 and cold worked AISI 316NG stainless steel specimens. The outlet water conductivity is also shown. The lowest crack growth rates were measured in pure water prior to the first sulphate transient. Injection of a small amounts of sulphate, producing a minor increase in the conductivity of the outlet water, affected the measured crack growth rate considerably. The increase in the crack growth rate was most pronounced due to the first impurity transients, when the sulphate content of the water was increased to 10 ppb in the beginning of the test. However, the enhancement caused by small additions of sulphate later during the test are still clearly detectable.

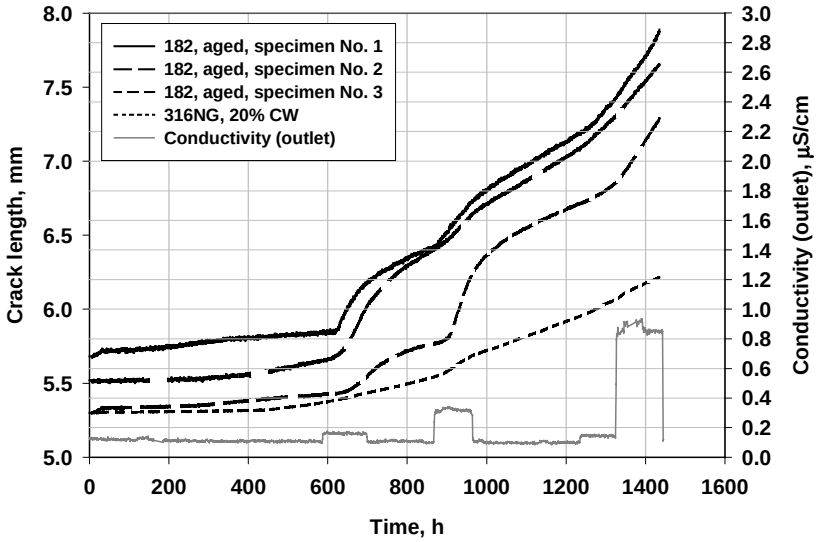

Figure 2. Changes in crack growth rate in Alloy 182 due to water chemistry transients.

After the sulphate concentration was reduced back to 0 ppb, the crack growth rate never reached the initial value measured prior to the first sulphate transient in pure water, at least not within the duration of the pure water, sulphate-free, sequence applied, i.e., within a few hundred hours.

The effect of increased sulphate concentration on the crack growth rate became visible after a 25–45 h incubation period, Fig. 2. On the other hand, purification of the water started to decrease the crack growth rate immediately, but the decrease took place slowly and at least several hundred hours was needed to reduce the crack growth rate to the level where it was before the first sulphate transient in the case of Alloy 182. The effect of the sulphate transient on the crack growth rate of cold worked AISI 316NG and sensitised AISI 304 stainless steels was not as pronounced as in Alloy 182, but the incubation periods were similar.

The crack growth rate measured for Alloy 182 weld metal in aged condition in simulated BWR environment with various low sulphate concentrations is shown in Fig. 3 as a function of K_J. The crack growth rate measured in sulphate-free bulk water after the first sulphate transient had been introduced and water purified is indicated by the circled data points.

Similar trends for the acceleration of crack growth rate resulting from sulphate additions, but not as pronounced as in the case of Alloy 182, were observed for cold worked AISI 316NG and sensitised AISI 304 stainless steels, Figs 4 and 5, respectively. No crack growth was observed in thermally aged Alloy 82 at any of the applied loading levels, K_J = 35–60 MPa$\sqrt{m}$, and with any of the applied water chemistry parameters, 0–100 ppb sulphate.

The measured crack growth rate values for Alloy 182 weld metal are presented in Fig. 6 as a function of sulphate concentration for two loading levels. Thermally aged Alloy 182 weld metal shows a clear increase in the crack growth rate with increasing sulphate concentration at both applied loading levels. Also, in Fig. 6, the circled data points refer to sulphate-free bulk water, obtained after sulphate transients in the re-circulation water.

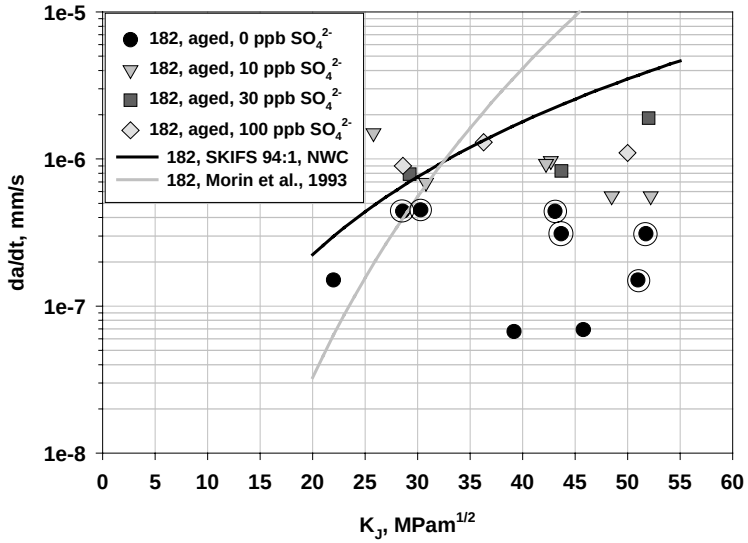

Figure 3. Crack growth rates of Alloy 182 weld metal in aged condition obtained with various sulphate contents in BWR environment.

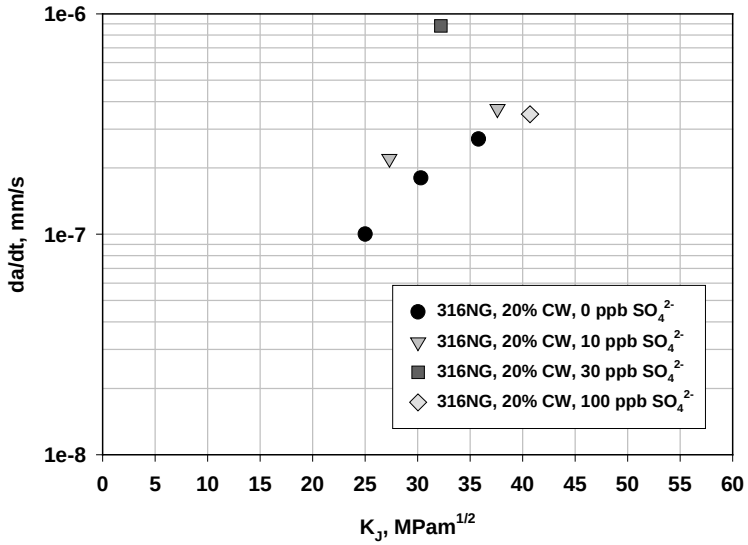

Figure 4. Crack growth rates of cold worked AISI 316NG stainless steel obtained with various sulphate contents in BWR environment.

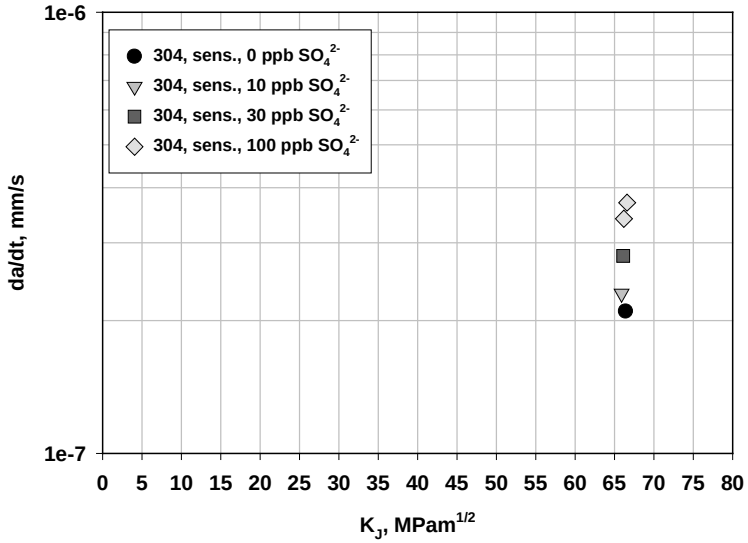

Figure 5. Crack growth rates of sensitized AISI 304 stainless steel obtained with various sulphate contents in BWR environment.

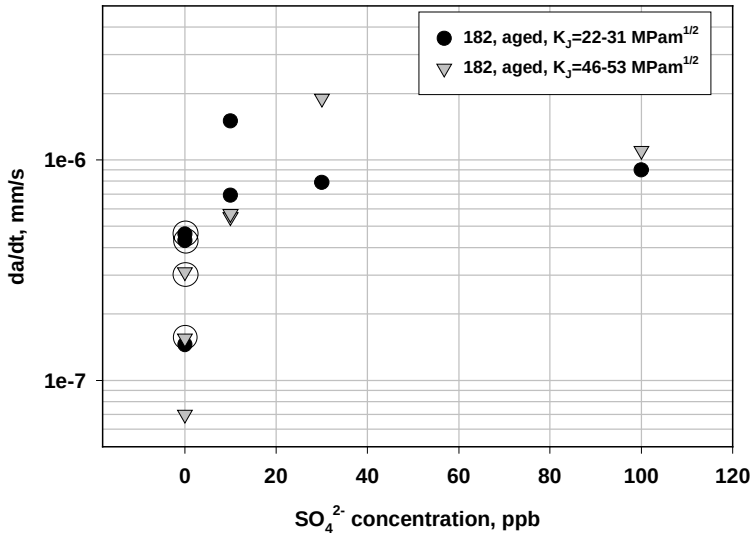

Figure 6. Crack growth rates of aged Alloy 182 weld metal in simulated BWR environment as a function of sulphate concentration.

Water chemistry parameters for one autoclave cycle when six specimens were simultaneously exposed to simulated BWR environment are shown in Fig. 7. Typical initial corrosion and redox potential values prior to the first sulphate transient were +100 mV_{SHE} and +275 mV_{SHE}, respectively, and the measured conductivity was ~0.1 µS/cm. When the first sulphate transient of 10 ppb was introduced, an immediate increase in the conductivity up to 0.18 µS/cm was observed and the corrosion potential of the specimens decreased about 50 mV. During the following water purification period, after the sulphate injection was interrupted, the conductivity decreased back to ~0.1 µS/cm level and the corrosion potential increased to a level corresponding to the initial pure water condition. No changes in redox potential (Pt electrode) due to sulphate transients were observed. The changes in corrosion potential and conductivity were reproducible, when recurrent sulphate concentration transients were introduced.

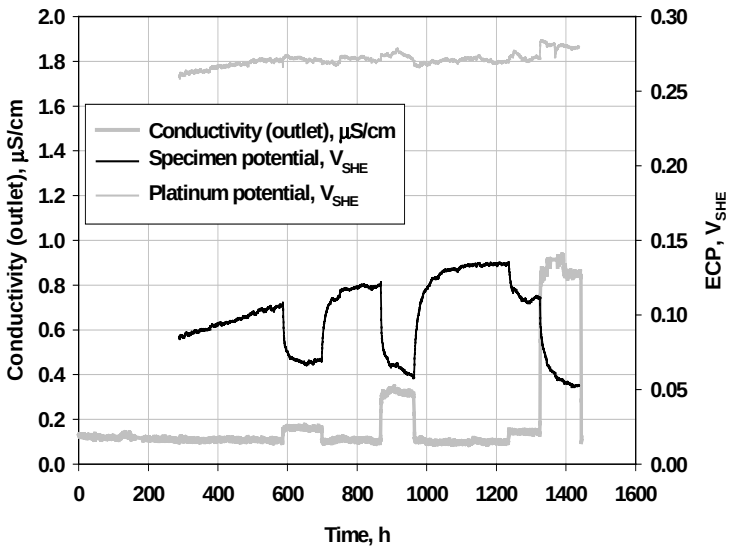

Figure 7. Water chemistry parameters during crack growth rate measurements with 10, 30 and 100 ppb sulphate transients in BWR environment.

Fracture surfaces of Alloy 182 weld metal specimens showed typically irregular crack fronts already after pre-fatigue in air, Fig. 8. During the rising displacement tests the cracks continued to propagate unevenly, leaving uncracked ligaments behind the crack tip. The fracture morphology of Alloy 182 was interdendritic, Fig. 9. In the cold worked AISI 316NG, Fig. 10, and in the sensitised AISI 304 stainless steel the fracture morphology was intergranular.

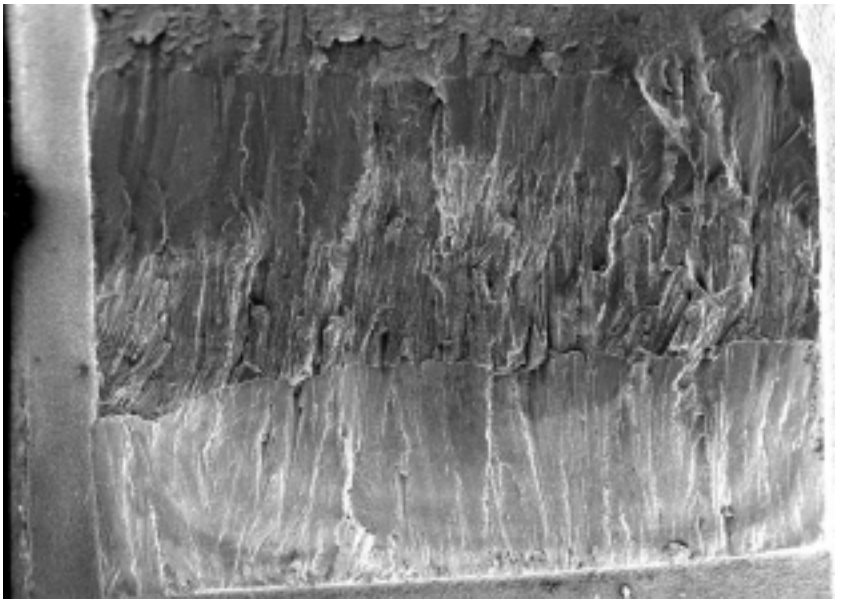

Figure 8. Fracture surface of one of the Alloy 182 specimens showing pre-fatigue crack, crack extension during the test, and post-test fatigue.

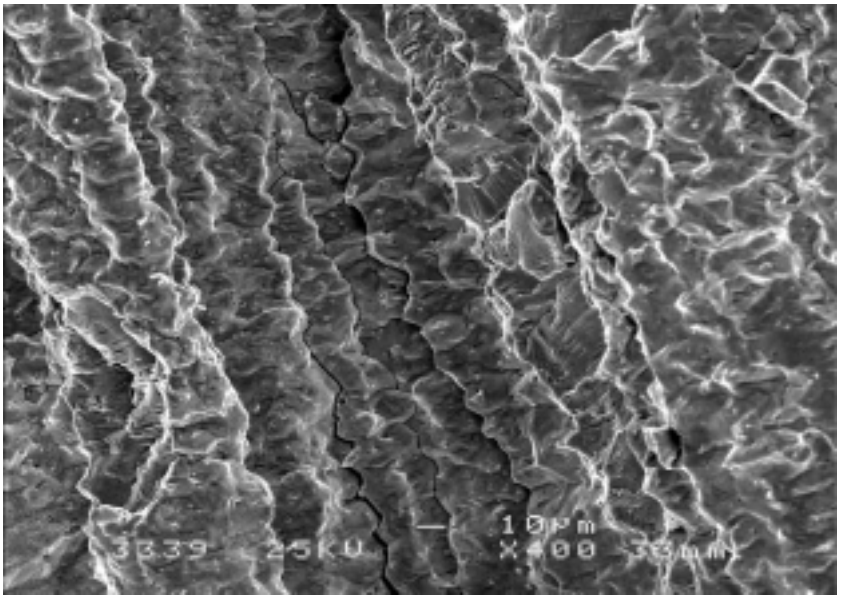

Figure 9. A detail of the fracture surface 8 showing interdendritic fracture.

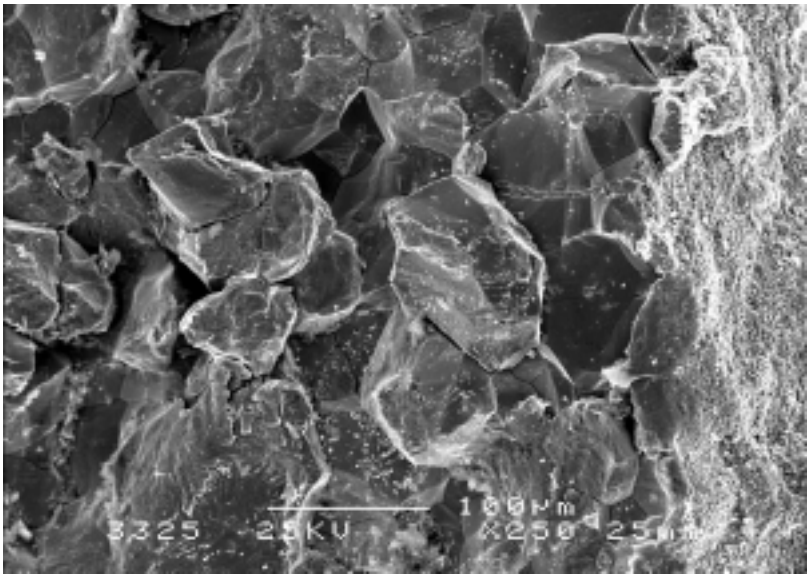

Figure 10. Intergranular fracture in cold worked AISI 316NG stainless steel.

4. Discussion

Sulphate addition in BWR water resulted in an increase in the crack growth rate in Alloy 182 weld metal, cold worked AISI 316NG and sensitised AISI 304 stainless steels after an incubation period of about 25–45 h in the slow rising displacement tests. Increased crack growth rate was sustained for longer periods after the sulphate injection was stopped, although the environment became clean after a 1–2 h period according to the measured conductivity. The observed rapid load reduction in the load-displacement curve after sulphate injection is a result of the change in the crack growth rate. The reduced load level, in the purified water after the fast crack growth, is a result of the reduced dimensions of the remaining ligament of the specimen. For the aged Alloy 182 weld metal even the smallest increase in the sulphate content in the water, i.e., 10 ppb, provided about 8 times higher crack growth rate (from 7×10^{-8} to 5.5×10^{-7} mm/s) at a stress intensity level of about 50 $MPam^{1/2}$, Fig. 6. These values are within the range reported in the literature, since the crack growth rate data shows large scatter. The measured crack growth rates for Alloy 182, in general, remain lower than the reference curves indicated in Fig. 3 [11, 12]. Only exceptions are observed at the lowest loading levels, where crack growth rates slightly exceed the lines.

In the aged Alloy 82 weld metal no crack initiation took place during the conducted slow rising displacement tests and, thus, the effects of sulphate on crack growth could not be observed.

The weak dependence between the crack growth rates and the increasing K_J level is a phenomenon possibly resulting from overestimated crack tip loading. The K_J levels are based on the area under the load-displacement curve. However, during the tests, the uncracked ligaments remaining behind the crack front in Alloy 182 weld metal specimens may carry a considerable part of the load, especially if the ligaments are far behind the crack front. On the other hand, this does not explain the slightly inverse dependence between the crack growth rate and K_J level in the three studied Alloy 182 specimens in the beginning of the tests before the first 10 ppb sulphate intrusion. The originally uneven pre-fatigue crack fronts may have an impact on this.

The dependence between the crack propagation rate and K_J level in the cold worked AISI 316NG stainless steel seems reasonable, especially since the crack propagation mode was intergranular as shown in Fig. 10. The crack propagation rate at the 100 ppb sulphate concentration level seems to be unexpectedly low when compared to the other sulphate levels. It may be a deviation resulting from a too high elastic-plastic loading level. The crack growth rate at the 100 ppb sulphate concentration level was measured in the end of the test when the load line displacement was large. The large load line displacement may have resulted in large crack opening angle and, thus, in dilution of the occluded cell chemistry in the crack. Diluted crack chemistry may also be a reason for the measured rather low dependence between the crack growth rate and the sulphate concentration level in the case of sensitised AISI 304.

Stress corrosion cracking is supposed to be controlled by crack tip strain rate. One measure related to the crack tip strain rate is crack tip opening displacement rate. Rice et al. [13] suggested a near tip expression for the crack opening displacement rate in a growing crack:

$$d\delta/dt = \alpha * \frac{dJ/dt}{\sigma_0} + \beta * \frac{\sigma_0}{E} * da/dt * \ln\left(\frac{R}{r}\right), \qquad (2)$$

where
α and β are dimensionless constants (α depends on σ_0/E and strain hardening exponent n, and β = 5.08) [10], R is a size which scales approximately with the size of the plastic zone, and r is a distance behind the propagating crack tip.

The crack growth rate results reported in this paper were measured using very slow rising displacement tests during which the term dJ/dt in equation (2) was very close to zero. Based on equation (2), it was estimated that the contribution of dJ/dt to the crack tip opening displacement rate was in the range of 12–22% of the total crack tip opening displacement rate in the case of the tests on AISI 304. The following parameters were used for the estimation: α = 0.5, R/r = 100, dJ/dt = $4x10^{-4}$ J/m^{2}s, σ_0 = 160 MPa, E = 170 GPa, da/dt = $2–4\times10^{-10}$ m/s.

This indicates that the part of equation (2) which includes the size R and crack growth rate dominates the crack tip opening displacement rate (and thus crack tip strain rate) in these tests. However, Rice et al. [13] suggest that at general yielding the size R should saturate to some fraction of the dimension of the remaining ligament, after which J (and thus K_J) level has no influence on the crack tip opening rate. This indicates that there is a specimen size/yield strength dependent K_J-level above which the crack growth rate shows a plateau and the crack growth at the plateau depends on the applied loading rate. Indeed, this kind of behaviour has been reported elsewhere [14]. In this study the measured crack growth rates for Alloy 182 and cold worked AISI 316NG was found to be relatively independent of K_J when it became higher than about 35 MPa$\sqrt{m}$. It can be concluded that so far the elastic-plastic K_J-levels reported in this paper corresponds [5] closely to linear-elastic K_I. Application of elastic plastic 3PB testing method gives reasonable crack growth rate results for Alloy 182 weld metal. However, more work is needed to better understand the relation between the elastic-plastic crack tip loading parameter K_J and linear-elastic loading parameter K_I in stress corrosion crack growth tests.

Water chemistry parameters reacted rapidly on the changes in the sulphate concentration in high temperature water. Obviously small amounts of sulphate, i.e., less that 100 ppb, did not change the pH value in high temperature water which is indicated by the stable platinum potential, but they were absorbed on existing oxide films reducing slightly the electrochemical potential. By this way it can be possible that small amounts of sulphate did not enhance the crack

initiation thought to be accelerated by acidic pH. Crack initiation in Alloy 82 in dynamic rising displacement test even with slow displacement rate may require higher sulphate concentrations than applied in this study.

5. Conclusions

- Small amounts of sulphate in BWR water accelerate crack growth rate in aged Alloy 182 weld metal as well as in sensitised AISI 304 and in cold worked AISI 316NG stainless steel.

- Sulphate up to 100 ppb did not change the high temperature pH value of simulated BWR water.

- In aged Alloy 82 weld metal cracks did not initiate during applied slow rising displacement tests and this alloy did not show any environmental cracking under the applied loads.

- Accelerated crack growth was observed after an incubation period of minimum 25 h and delay in the decrease in crack growth rate was several hundred hours.

- Small amounts of sulphate did not change pH value, but decreased slightly the corrosion potential.

- Increase in conductivity of the water showed the risk for enhanced crack growth rate in Alloy 182, but incubation times and delay must also be accounted.

Acknowledgements

This presentation is prepared within the project Structural operability and plant life management (RKK), which is coordinated by Teollisuuden Voima Oy. The work has been funded by the National Technology Agency (Tekes), Teollisuuden Voima Oy (TVO), Fortum Power and Heat Oy, Fortum Nuclear Services Ltd., FEMdata Oy, Neste Engineering Oy, Fortum Oil and Gas Ltd. and VTT. Their funding is gratefully acknowledged.

References

1. McMinn, A. and Page, R. A. Stress Corrosion Cracking of Inconel Alloys and Weldments in High Temperature Water – The Effect of Sulfuric Acid Addition. Corrosion 1988, 44 (4), pp. 239–247.

2. McMinn, A. and Page, R. A. Stress Corrosion Cracking of Inconel Alloys and Weldments in High Temperature Water – The Effect of Sulfuric Acid Addition. Corrosion `87, Paper No. 173, March 9–13, 1987, Moscone Center, San Francisco, California. 22 p.

3. McMinn, A. and Page, R. A. Stress Corrosion Cracking Resistance of Alloys 600 and 690 and Compatible Weld Metals in BWRs. EPRI Project 1566-1. Final Report EPRI NP-5882M, July 1988.

4. EPRI BWR Water Chemistry Guidelines – 1993 revision.

5. Andresen, P. Effects of Dissolved Oxygen, Solution Conductivity and Stress Intensity on the Interdendritic Stress Corrosion Cracking of Alloy 182 Weld Metal. Corrosion '87, Paper No 85. March 9–13, 1987. Moscone Center, San Francisco, California. 12 p.

6. Ljungberg, L. and Stigenberg, M. Stress Corrosion Cracking Propagation in Low-Strength Nickel-base Alloys in Simulated BWR Environment. 8th International Symposium on Environmental Degradation of Materials in Nuclear Power Systems – Water Reactors, August 10–14, 1997, Amelia Island Plantation, Florida. Pp. 704–711.

7. Lidar, P. Influence of Sulphate Transients on Crack Growth in Type 304 Stainless Steels in Water at 288^{o}C. 7th International Symposium on Environmental Degradation of Materials in Nuclear Power Systems – Water Reactors, August 7–10, 1995, Breckenridge, Colorado. Pp. 597–607.

8. Ehrnsten, U., Aaltonen, P., Nenonen, P., Hänninen, H., Jansson, C. and Angeliu, T. Intergranular Cracking of an AISI 316NG Stainless Steel Material in BWR Environment. To be presented in 10th International Symposium on Environmental Degradation of Materials in Nuclear Power Systems – Water Reactors, August 5–9, 2001, Lake Tahoe, Nevada.

9. Metals Handbook. Desk Edition (Second Edition). ASM International, Materials Park, 1998.

10. Anderson, T. L. Fracture Mechanics, Fundamentals and Applications, Second Edition. Department of Mechanical Engineering, Texas A&M University, College Station, Texas, CRX, 1995.

11. SKIFS 1994:1. Statens kärnkraftsinspektions föreskrifter om mekaniska anordningar i kärntekniska anläggningar. SKI, 1994.

12. Morin, U., Jansson, C. and Bengtsson, B. Crack Growth Rates for Ni-base Alloys with the Application to an Operating BWR. 6th International Symposium on Environmental Degradation of Materials in Nuclear Power Systems – Water Reactors, August 1–5, 1993, San Diego, California. Pp. 373–377.

13. Rice, J. R., Drugan, W. J. and Sham, T.-L. Elastic-Plastic Analysis of Growing Cracks, Fracture Mechanics: Twelfth Conference, ASTM STP 700, American Society for Testing and Materials, 1980. Pp. 189–221.

14. Toivonen, A., Moilanen, P., Pyykkönen, M., Tähtinen, S. and Rintamaa, R. The Feasibility of Small Size Specimens for Testing of Environmentally Assisted Cracking of Irradiated Materials and of Materials Under Irradiation in Reactor Core. Nuclear Engineering and Design, 1999, 93, pp. 309–316.

Investigations on aged Ti-stabilised stainless steels

Ulla Ehrnstén[1], Päivi Karjalainen-Roikonen[1], Pertti Nenonen[1],
Ritva Korhonen[2], Boris T. Timofeev[3] and Alexandr A. Bloomin[3]
[1] VTT Industrial Systems, Espoo, Finland
[2] Fortum Nuclear Services, Vantaa, Finland
[3] ZNIIKM, St. Petersburg, Russia

Abstract

Mechanical and microstructural properties of cast material of type O8X8H10TL and wrought and welded stainless steel pipe material of type O8X8H10T have been determined, aged at NPP operation temperature for about 100 000 h and 200 000 h, respectively. The mechanical properties were determined using tensile testing, impact energy determination and fracture resistance testing. The microstructures were studied using optical, scanning and transmission electron microscopy.

The mechanical properties of the cast Ti-stabilised stainless steel material are evaluated to be only slightly affected by long term (~100 000 hours) operation at NPP operation temperature. Also the effect of even longer (~200 000 hours) operation on wrought Ti-stabilised pipe material is very small, as the properties of the aged material are within the normal range of as-manufactured material. The mechanical properties of the Mo-alloyed stainless steel weld metal after ~200 000 hours of operation are still good, although indications of changes due to thermal ageing were observed.

1. Introduction

Cast austenitic stainless steels are materials used for valves and pumps in nuclear power plants. The composition of cast stainless steels is adjusted to achieve a microstructure containing austenite (γ) with a small amount of δ-ferrite, which improves the casting, welding and strength properties of the

material. Typically the amount of δ-ferrite is less than 20% in non-stabilised cast stainless steels and typically less than 10% in cast stabilised stainless steels.

The properties of cast non-stabilised stainless steels are known to degrade during long term ageing at nuclear power plant (NPP) operation temperatures as low as 250°C.[1–6] Much less is known about the behaviour of Ti-stabilised cast stainless steel during long term operation. In non-stabilised stainless steel castings, the degradation of mechanical properties due to thermal ageing is known to be due to spinoidal decomposition in the δ-ferrite phase, which results in an increased hardness of the δ-ferrite and reduced toughness of the whole material. Investigations have shown that the degradation of the mechanical properties due to spinoidal decomposition can be recovered by short time annealing at 550°C, typically for 1 hour.[2] The properties of cast stainless steels during long term operation can further be influenced by growth of carbides and/or nitrides, especially at the δ-ferrite austenite phase boundaries and in the δ-ferrite and by precipitation of the silicon and nickel rich G-phase. Similar changes can also occur in weld materials, which also have an γ-δ-microstructure.[7]

The aim of this investigation is to determine the mechanical and microstructural properties of Ti-stabilised cast and wrought stainless steel materials as well as of Mo-alloyed weld metal after long term ageing.

2. Experimental

2.1 Materials

The materials included in this investigation are cast as well as wrought and welded Ti-stabilised stainless steel pipe material of type O8X18H10T(L). The cast valve material and wrought pipe material had been in operation at about 270°C for about 100 000 hours and 200 000 hours, respectively. The weld of the pipe section had been welded by Shielded Metal Arc Welding (SMAW) using a Mo-alloyed stainless steel filler material. The chemical compositions of the materials are presented in Table 1.

Table 1. Chemical compositions of the materials investigated.

material	C	Si	Mn	S	P	Cr	Ni	Mo	Ti
Cast material	0.07	0.52	1.60	0.010	0.023	18.0	8.4	0.06	0.62
Wrought material	0.08	0.41	1.20	0.014	0.025	17.3	10.6	0.20	0.56
Weld metal	0.04	0.25	1.41	0.015	0.024	18.4	11.3	2.30	0.11

2.2 Test methods

The amount of δ-ferrite was determined with a Feritscope. Microstructural investigations were performed using optical, scanning and transmission electron microscopy. In the TEM-investigations special emphasis was put on features typical for thermal ageing, e.g. spinoidal decomposition and precipitation of G-phase in the δ-ferrite.

Impact tests were conducted mainly using a computerised conventional 300 J instrumented pendulum with an impact velocity of 5.4 m/s. The Charpy-V specimen preparation and the testing were carried out according to DIN 50115 standard. The cast material was Charpy tested at temperatures between -196°C and +100°C in plant aged condition and after solution annealing and water quenching. The weld metal was tested in plant aged condition at room temperature and at 280°C. The impact energy at room temperature was additionally determined for the weld metal after recovery annealing at 550°C/1h.

The tensile properties of the cast valve material and of the wrought pipe material were determined at room temperature and at 350°C. Tensile tests were additionally performed for the coarse grained heat affected zone (CGHAZ) and weld metal of the pipe section using subsize tensile test specimens.

Fracture resistance tests (J-R curves) of the cast stainless steel and of the weld metal of the pipe section were determined using Charpy size 10x10x55 mm specimens at room temperature.

The hardness of the material was determined as Vickers hardness numbers using a load of 5 kp or 1 kp. A load of 10 p was used for Vickers microhardness measurement of the δ-ferrite in cast material. The size of the δ-ferrite islands in the weld metal was too small for hardness measurements.

3. Results

3.1 Microstructure and amount of δ-ferrite

The microstructure of the Ti-stabilised cast stainless steel is austenitic, with about 10 % δ-ferrite. The amount of δ-ferrite in the ferritic-austenitic weld metal is bout 6 %. The base metal of the pipe section is fully austenitic with inclusions and precipitates typical for Ti-stabilised stainless steels, i.e. large titanium sulphides, titanium carbides and titanium carbo-nitrides, as well as numerous Ti-C precipitates of submicron size. These were the only precipitates also in the HAZ, i.e., no chromium carbides were detected.

Spinoidal decomposition could neither be detected in the δ-ferrite of the plant aged Ti-stabilised cast stainless steel material nor in the δ-ferrite of the plant aged Mo-alloyed weld metal. In the δ-ferrite of the weld metal, clustering of elements typical for the G-phase (Ni, Si and Mo) was observed. Additionally, coarse chromium carbides precipitates were observed at the δ-γ-phase boundaries. Sigma phase was not detected; not in the cast material, nor in the weld metal. Clustering of elements indicating G-phase was not observed in the δ-ferrite of the cast stainless steel material, where some other type of Ni-rich precipitate originating from manufacturing, containing also Al, Mn and Ti, was observed.

3.2 Impact Toughness

The impact test results of the cast stainless steel material, i.e., the impact energies together with the transition curves, using fitting with a tanh function, are presented in Fig. 1. Impact toughness values for both the cast valve material and the weld metal is summarised in Table 2. The results reveal, that the impact toughness of plant aged cast stainless steel material is relatively low and about half the values of solution annealed cast stainless steel material. The low value is

close to the minimum nominal value (59 J/cm^2). The impact toughness at room temperature of the plant aged weld metal is relatively high. It was still increased about 20% after recovery heat treatment at 550°C/1h. The fracture mode was ductile in all cases.

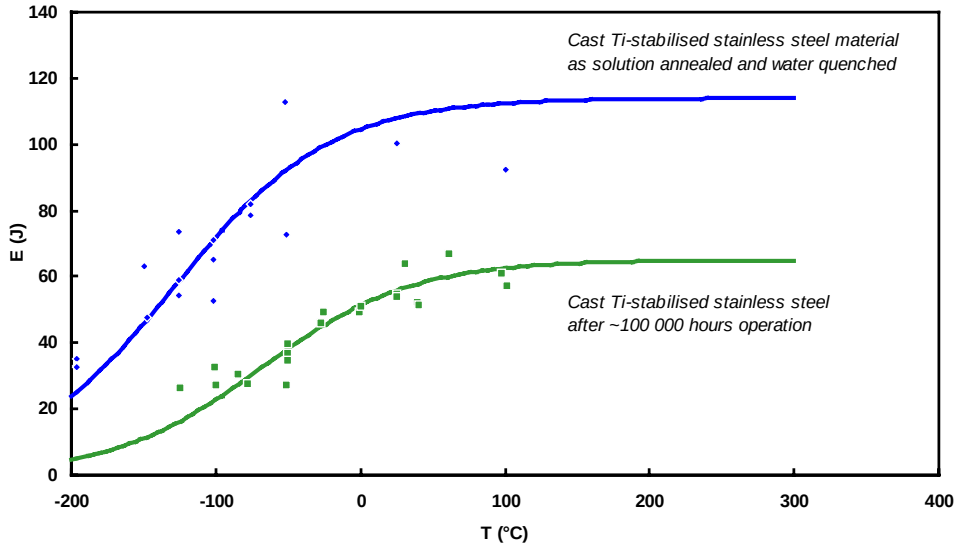

Figure 1. Charpy test results for cast Ti-stabilised stainless steels O8X18H19TL.

Table 2. Charpy impact energy values at room temperature and high temperature for cast Ti-stabilised stainless steel and Mo-alloyed weld metal.

Material	Room temp. [J]	Upper shelf [J]
Cast steel after ~100 000 h operation	55	57 (100°C)
Cast steel, solution annealed and water quenched	100	92 (100°C)
Weld metal after ~200 000 h operation	135	255 (280°C)
Weld metal after ~200 000 h operation and recovery heat treated 550°C/1h	165	not determined

3.3 Tensile properties

The tensile properties of the materials are presented in Table 3. The strength values of the cast stainless steel are lower than those of wrought stainless steel material, according to expectations. The strength values of the CGHAZ (Coarse Grained HAZ) of the pipe material is higher than that of the weld metal and base metal, both at room temperature and at elevated temperature. Recovery heat treatment at 550°C/1h results in a small decrease of the strength values.

Table 3. Tensile properties at room temperature(RT) and 350°C

Material	**$R_{p0.2}$ (RT) N/mm^2**	**R_m (RT) N/mm^2**	**$R_{p0.2}$ (350°C) N/mm^2**	**R_m (350°C) N/mm^2**
Cast Ti-stabilised stainless steel after ~100 000 h operation	250	510	190	320
Mo-alloyed weld metal after ~200 000 h operation	360	590	270	430
Mo-alloyed weld metal ~200 000 h operation + 550°C/1h	340	570	n.d.	n.d.
Wrought Ti-stabilised stainless steel after ~200 000 h operation	330	600	240	390
CGHAZ in welded Ti-stabilised steel after ~200 000 h operation	420	630	380	490
Nominal properties of Ti stabilised cast material (min)	200	450	130	-
Nominal properties of weld metal (min)	350	550	280	-
Nominal properties of wrought 08X18N10T (min)	215	510	180	410

3.4 Fracture resistance tests (J-R curves)

The initiation fracture toughness values are presented in Table 4. The fracture toughness of the plant aged cast stainless steel material is relatively high, and that of the aged pipe material and weld metal is very high > 700 kJ/m^2.

Table 4. Summary of fracture toughness values for cast and wrought Ti-stabilised stainless steel and Mo-alloyed weld metal.

Material	J_{IC} (RT) [kJ/m^2]
Cast Ti-stabilised stainless steel after ~100 000 h operation	190
Wrought Ti-stabilised stainless steel after ~200 000 h operation	780
Mo-alloyed weld metal after ~200 000 h operation	770

3.5 Hardness

The material history had a clear influence on the δ-ferrite microhardness in the cast material, while the influence in the macrohardness is much smaller, Table 5. The hardness of the δ-ferrite in the plant aged cast stainless steel is between that of solution annealed and that of artificially aged (410°C/1350h)[7].

Table 5. Summary of macrohardness and ferrite microhardness measurements for cast and wrought Ti-stabilised stainless steels and Mo-alloyed weld metal.

Material	Hardness HV1 or HV5	δ-ferrite HV0.01
Cast stainless steel, plant aged	160	390
Cast stainless steel, plant aged and additionally artificially aged	190	430
Cast stainless steel, solution annealed	144	266
Wrought stainless steel, base material	190	*
Weld metal, filler passes	190	**

* the base metal does not contain any δ-ferrite

4. Discussion

In non-stabilised stainless steels degradation of cast and weld material properties are known to occur due to spinoidal decomposition[1–8]. Spinoidal decomposition results in elemental redistribution in the nanometer scale and formation of Fe-rich α and Cr-rich α' regions. Precipitation of G-phase has been observed in materials with spinoidal decomposition, with a probable synergistic effect.[8] In this investigation, spinoidal decomposition in the δ-ferrite was not observed; not in the cast Ti-stabilised stainless steel material nor in the Mo-alloyed weld metal.

In the Mo-alloyed weld metal, clustering of G-phase elements were observed, indicating a preprocess for G-phase precipitation. As it is reasonable to assume, that spinoidal decomposition and element clustering are simultaneous events, weak microstructural changes due to thermal ageing in the weld metal are possible, i.e. spinoidal decomposition and element clustering preceding G-phase precipitation. Also the improvement of the impact energy (and decrease of tensile strength values) of the weld metal after recovery heat treatment at 550°C/1h indicates changes due to thermal ageing of the weld metal. However, the mechanical properties of the Mo-alloyed stainless steel weld metal after about 200 000 hours operation at NPP operation temperature are still good, and

the possible effect of thermal ageing is small. The mechanical properties of the wrought Ti-stabilised stainless steel pipe material are also very good. This is in accordance with expectations, as long term ageing at ~270°C is not considered to change the mechanical properties of the austenitic material. Growth of nucleated precipitates as well as segregation due to diffusion is possible in the temperature range in question. However, these are not expected to result in large changes in the mechanical properties.

Results from investigations on artificially aged Ti-stabilised cast stainless steel material show, that thermal ageing can occur resulting in remarkable degradation of mechanical properties [8–10]. Artificial ageing result in an increase in the microhardness of the δ-ferrite and in a decrease especially in the upper shelf impact energy. The evaluation of the influence of thermal ageing on impact toughness values as well as other mechanical properties is complicated by the lack of as-manufactured data on the very same material as investigated in aged condition. Depending on the manufacturing process details, e.g. wall thickness, cooling rate, heat treatments etc., the as-manufactured properties can obviously vary within a large range. However, based on the investigations performed it is evaluated, that the effect of thermal ageing after ~100 000 hours operation at NPP operation temperature on the mechanical properties of the investigated Ti-stabilised cast stainless steel material is small.

5. Conclusions

The mechanical and microstructural properties of Ti-stabilised cast and wrought stainless steel as well as of Mo-alloyed stainless steel weld material after ~100 000 hours operation (cast) and ~200 000 hours operation (wrought pipe material and weld metal) were determined. The following conclusions can be made based on the results:

- No remarkable degradation of the mechanical properties of the investigated materials aged at NPP operation temperature were detected. The following materials were considered:
  - cast Ti-stabilised stainless steel of type O8X18H10TL after 100 000 hours of operation,
  - Mo-alloyed weld metal after ~200 000 hours of operation, and

  - Ti-stabilised pipe material of type O8X18H10T after ~200 000 hours of operation.

- The mechanical properties of all above mentioned materials are good

- No spinoidal decomposition could be detected in the weld metal after ~200 000 hours operation, but indications of thermal ageing were obtained, i.e., clustering of G-phase elements and increased impact toughness after a recovery heat treatment known to restore ductility after thermal ageing.

Acknowledgements

This presentation is prepared for a joint Finnish industry group in a project on Structural operability and plant life management (RKK). The project funding by the National Technology Agency (Tekes), Teollisuuden Voima Oy (TVO), Fortum Power and Heat Oy, Fortum Nuclear Services Ltd., FEMdata Oy, Neste Engineering Oy, Fortum Oil and Gas Ltd. is gratefully acknowledged.

References

1. Chung, H. M. Aging and Life Prediction of Cast Duplex Stainless Steel Components. Int. J. Pres. Ves & Piping, 1992, 50**,** pp. 179–213.

2. Chung, H. M. and O. K. Chopra, O. K. Long-term Embrittlement of Cast Austenitic Stainless Steels-Mechanisms and Kinetics. Properties of Stainless Steels in Elevated Temperature Service, ed. M. Prager, The Materials Properties Council, Inc., MPC, Vol. 26, The American Society of Mechanical Engineers, NY 1987. Pp. 17–34.

3. Massoud, J.-P., Auger, P., Danoix, F., Rezakhanlou, R. and Van Duysen, J.-C. Evaluation of the Thermal Ageing of Duplex Stainless Steels. Sixth International Symposium on Environmental Degradation of Materials in Nuclear Power Systems – Water Reactors, ed. By R. G. Gold and E. P. Simonen. The Minerals, Metals & Materials Society, 1993.

4. Jansson, C. Degradation of Cast Stainless Steel Elbows after 15 Years in Service. Fontrevaud II International Symposium, Royal Abbey of Fontrevaud, France, 10–14 September, 1990.

5. Chopra, O. K. Thermal Aging of Cast Stainless Steels: Mechanisms and Predictions. Fatigue, Degradation and Fracture, 1990. Ed. By Bamford, W. H. et al., AMES, PVP, Vol. 195, MPC, Vol. 30. Pp. 193–214.

6. Massoud, J. P., Bethmond, M. and Champredonde, J. Long term aging of cast duplex stainless steels between 300 and 400 °C. Relationship between toughness properties and metallurgical parameters. Duplex Stainless Steels,´91, October 28–29, 1991, Beaune Bourgogne, France. Pp. 93–100.

7. Alexander, K. B., Miller, M. K. and Nanstad, R. K. Microscopical Evaluation of Low Temperature Aging of Type 308 Stainless Steel Weldment. Materials Science and Technology, March 1990, Vol. 6., pp. 314–320.

8. Mateo, A., Llaned, L. and Anglada, M. Characterization of the Intermetallic G-phase in an AISI 328 Duplex Stainless Steel. Journal of Materials Science 1997, 32, pp. 6544–4540.

9. Ehrnstén, U., Karjalainen-Roikonen, P., Aaltonen, P., Ahlstrand, R., Timofeev, B. and Bloomin, A. The Effects of Long-term Operation on Properties of Cast Titanium Stabilized Stainless Steel. Eight International Symposium on Environmental Degradation of Materials in Nuclear power Systems – Water Reactors. August 10–14, 1997, Amelia Island Plantation, Florida USA. Pp. 1023–1030.

10. Ehrnstén, U., Karjalainen-Roikonen, P., Nenonen, P., Ahlstrand, R., Hietanen, O., Timofeev, B. T. and Bloomin, A. A. Properties of Cast Ti-stabilised Stainless Steel after Long-term Ageing. Proc. of the Sixth Internation Conference on Material Issues in Design, Manufacturing and Operation of the Nuclear Plant Equipment. St. Petersburg, 19–23 June 2000. Pp. 104–112.

Thermal ageing of ferrite in stainless steel

Pertti Nenonen
VTT Industrial Systems
Espoo, Finland

Abstract

The changes in the microstructure and composition of ferrite in two types of cast duplex stainless steels and in an austenitic-ferritic weld metal after long term thermal ageing has been studied using analytical transmission electron microscope (FEGTEM). A cast test steel containing Mo was investigated first as a reference material in three different conditions: as solution annealed, aged at 300^{o}C and aged at 400^{o}C. This investigation was carried out to gain experience of how EDS analyser and TEM can bee used to study elemental unhomogeneity, which is usually investigated with an atom probe (APFIM). The two other materials, an austenitic-ferritic weld metal and a cast duplex Ti-stabilised stainless steel used for long time at NPP operation temperature were investigated using the experience obtained with the test steel.

The results showed that analytical TEM can be used to investigate elemental unhomogeneity of ferrite, but there are several important things to be taken into account when the spectra for this purpose are collected. These kind of things are, such as the thickness of the specimen, probe size, contamination rate, "elemental background" of the spectrum and possible enrichment of certain alloying elements in the surface oxide layer of the TEM-specimens. If minor elements are also analysed, it may increase the scattering of the results.

1. Introduction

Long term thermal ageing of duplex stainless steel is known to cause elemental unhomogeneity, i.e. spinodal decomposition of ferrite and finally precipitation of intermetallic G-phase in ferrite. The spinodal decomposition leads to the formation of a sponge-like network of Cr-rich α'- and Fe-rich α-phases. G-phase

is an intermetallic compound Ni16X6Si7, where X can be alloying elements, such as Cr, Mo, Fe or Mn. The structure is fcc with a lattice constant of 1.09–1.12 nm depending on the composition. G-phase has cube on cube orientation relationship with ferrite [1, 2]. The ageing induced changes in the microstructure have been usually studied with a transmission electron microscope (TEM) and the elemental unhomogeneity with an atom probe (APFIM), [1 to 4]. A X-ray analyser (EDS) has not been commonly used to study the elemental unhomogeneity. The main purpose of this work was to investigate with TEM and EDS a reference material characterised earlier with APFIM and to gain experience of how the investigations must be done. In addition to the reference material two other steels affected by long term use at NPP operation temperature were examined in the similar way.

2. Experimental

The cast duplex stainless test steel (Steel E) used in this study as a reference material was delivered by EDF, France in three different conditions:

1. Solution annealed at 1100^{o}C and water quenched.

2. Aged for 10 000 h at 300^{o}C, which corresponds to 100 000 h at 270^{o}C.

3. Aged for 30 000 h at 400^{o}C, containing precipitates of intermetallic G-phase and a high level of spinodal decomposition in ferrite.

The other examined steels were an austenitic-ferritic weld metal used for 201 500 h at 270^{o}C (Steel S) and a cast duplex Ti-stabilised stainless steel used for 106 000 h at 270^{o}C (Steel K). These materials were provided by The central research institute for structural materials ZNIIKM Prometey. The SOL-state (start of life) of Steel K is not known and that of Steel S is as after welding. The chemical compositions and ferrite contents of the investigated steels are presented in Table 1.

Table 1. Chemical compositions and ferrite contents of the steels investigated.

Material	ferrite %	C	Cr	Ni	Mn	Si	S	P	Mo	Ti	N
Steel E	30	0.033	21.10	9.70	0.88	1.07			2.51	<0.01	0.052
Steel S	6	0.04	18.40	11.30	1.41	0.25	0.015	0.024	2.30	0.11	
Steel K	10	0.07	18.0	8.40	1.60	0.52	0.010	0.023	0.06	0.62	

The transmission electron microscope investigations were carried out with Philips CM200 FEG-STEM microscope and Gatan MSC CCD camera was used for recording the micrographs. Elemental analyses were made using Noran Voyager thin window EDS analyser, which detects boron (B) and elements heavier than that. Real collection time was always 30 seconds and quantitative results were calculated using MBTS correction program.

Because the plain elemental unhomogeneity does not necessarily cause any visible contrast in TEM, it was investigated by measuring the contents of different elements in ferrite using point analyses and comparing the results obtained for the different samples. Spectra for this purpose were collected from random points with different specimen thickness using ϕ 1.2–2.8 nm probe. Variation of probe size and specimen thickness was necessary, since the magnitude of possible unhomogeneity was not known. Probe size and specimen thickness are always some kind of compromise between spatial resolution, count rate, carbon contamination and resolution/detecting limit. A combination of small intensive probe and a thin specimen gives a good spatial resolution but high contamination rate and poor counting rate and statistic. Thicker specimen and larger probe increase counting rate, which improves statistic, but decreases spatial resolution. The thickness of the TEM specimen was estimated by comparing the locations of contamination marks of the point analyses and first thickness fringes of certain reflection after the analysis.

The point analysis spectrum may contain information collected outside the probe. The level of this "elemental background" depends on the type of the specimen and in Philips series CM200 microscope on the aperture used to limit the beam size. In this investigation the probes smaller than 2.4 nm were produced by limiting the beam size with condencer 2 aperture, which increases so called hole count rate.

TEM-specimens were prepared by punching and grinding the materials to $\phi 3 \times 0.1$ mm discs, which were finally thinned in a twin jet electropolishing equipment at -35°C. The electrolyte was 30% nitric acid solution in methanol. As usual the polishing rates of austenite and ferrite were different. In this case ferrite phase was always thinner than parent austenite, which caused some difficulties discussed later.

3. Results

3.1 Microstructure of Steel E

Microstructure of the test steel was a typical solidification structure consisting of long and narrow ferrite grains between austenite. The real grain size was so coarse, that in many cases the whole transparent area of a TEM specimen contained only one orientation of ferrite and austenite. The dislocation density of both phases was low and there were no precipitates in austenite but ferrite contained variable amounts of coarse plate like precipitates, often existing in small groups, Figure 1. These precipitates were analysed to be titanium carbides containing some nitrogen. The presence of nitrogen may explain why these precipitates have not been dissolved during the solution annealing. Small titanium carbides were found also at phase boundaries.

The microstructures of the solution annealed specimen and at 300°C aged specimen were similar and the only visible change after ageing at 400°C was the very dense precipitation of G-phase in ferrite, Figure 2. The G-phase precipitates seemed to be incoherent and the contrasts of them were often week and overlapping because the density of the precipitates was very high. It was found that in a bright field image a reasonably good contrast between the matrix and the precipitates could be achieved around the first dark thickness fringe with [110] reflection of matrix, Figure 3. In this figure the average size of the precipitates is 6 to 7 nm. When imaged in the dark field mode these precipitates were not seen as solid grains, Figure 4. Interpretation of the corresponding diffraction pattern revealed that the precipitates are internally twinned, Figure 5.

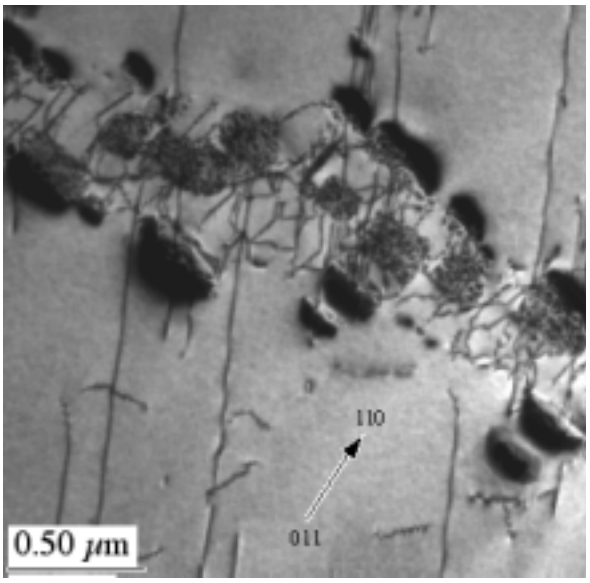

Figure 1. Steel E, solution annealed. Titanium carbides and typical straight screw dislocations in ferrite.

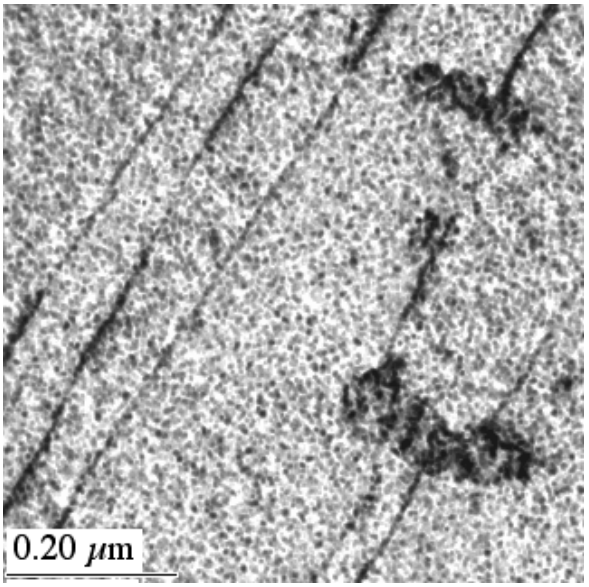

Figure 2. Steel E, aged at 400℃. G-phase precipitates, titanium carbides and straight screw dislocations in ferrite.

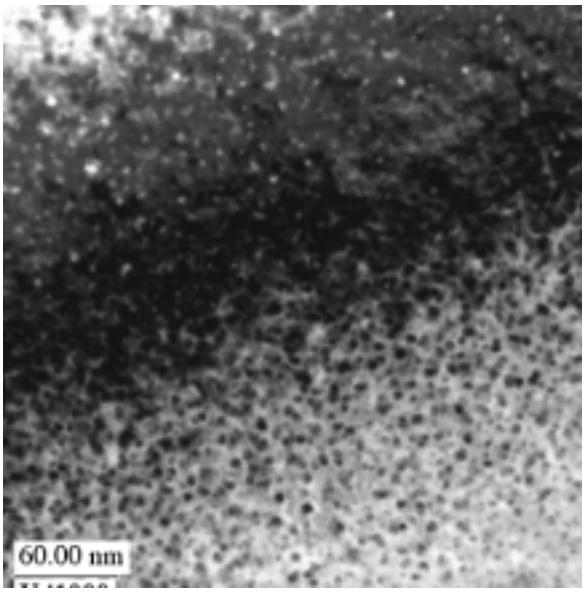

Figure 3. Steel E, aged at 400℃. G-phase precipitates in ferrite. First dark thickness fringe at the edge of the specimen. Thickness of the dark area is 17 nm.

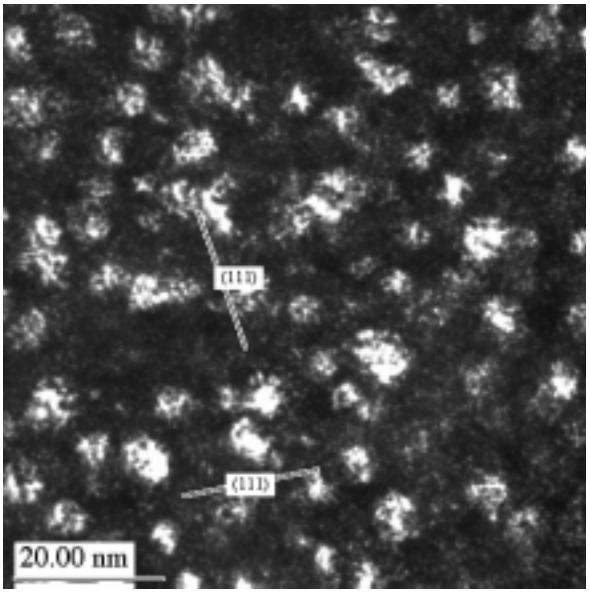

Figure 4. Steel E, aged at 400℃. Dark field image of internally twinned precipitates. (333)-type reflection of G-phase. Traces of twinning planes have been marked on the picture.

This explains the features seen in the dark field images. The quite complex diffraction pattern in Figure 5 contains [110] patterns of matrix and precipitate, as well as double reflections of the precipitates from each matrix point. In addition, there are spots, which can be explained with twins in the precipitates. The fcc [110] zone axis contains two possible twining planes. Traces of these planes have been marked in Figure 4, where substructure parallel with them is seen. The very thin edge of ferrite showed that the changes caused by thermal ageing affect polishing rate of ferrite in a very fine scale, Figure 6. The thickness of the specimen varied slightly in very fine scale and, as a consequence, the edge was rough and partly perfored. On the other hand the dark field images showed that all the contrasts, seen in the bright field images, are not G-phase precipitates. This feature was used to select the places for point analyses.

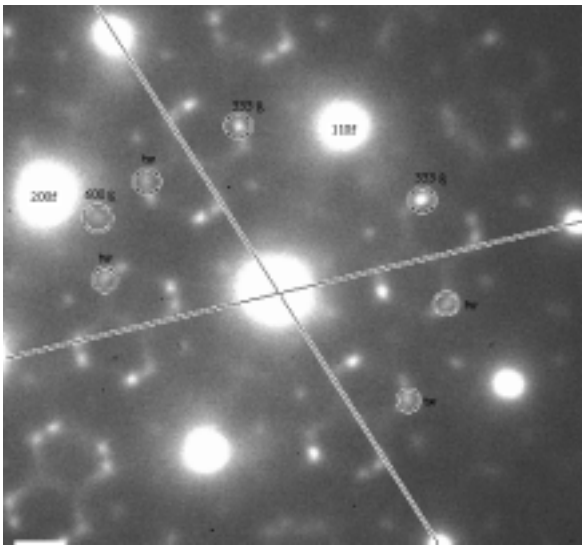

Figure 5. Steel E, aged at 400℃. [011] diffraction pattern of ferrite and G-phase. Complex pattern is caused by twinning and double reflections from matrix spots. Types of some reflections and twinning planes have been marked on the picture.

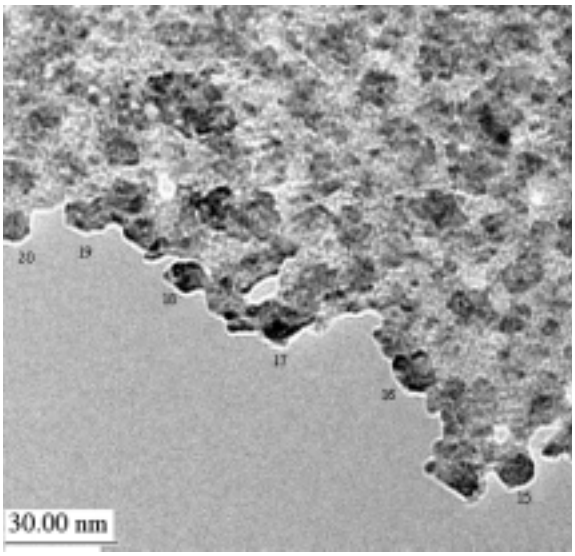

Figure 6. Steel E, aged at 400℃. Thin edge of ferrite. Some places of point analyses from contrasts have been marked with numbers. Nanoprobe mode, under focused image without objective aperture.

3.2 Composition of ferrite in Steel E

The material aged at 400°C containing visible changes was analysed first. Several point analyses spectra were collected from the dark contrasts on the edge of the specimen, from the places between them, as well as from the G-phase precipitates, Figure 6. Dark field mode was used to localise the precipitates. The precipitates were analysed with 2.8 nm probe and other targets with 1.6 nm probe. Summary of the average results of the point analyses and the averages obtained from thick and thin ferrite are shown in Table 2.

The results show that the precipitates and the contrasts on the edge of the specimen contain increased amounts of Ni, Mo and Si. These results also show that the Cr and Mo contents increase (also the Si content, as shown later) with decreasing specimen thickness. This is caused by enrichment of these elements in the oxide layer on the surfaces of the specimen. Standard deviations of the results increase in the following order: places between contrasts, contrasts and precipitates. The relative standard deviations of the Ni, Mn, Mo and Si contents are quite high. One must note that all of the analysed places are thinner than 17 nm, especially the places between the contrasts. The sum of the presented

results is less than 100% because minor elements, such as Cu, P, S and Nb, were originally also analysed. The differences between the targets and the real scatter of the results are revealed better when the results are plotted point by point like in a line analysis, Figure 7. This presentation shows that there are large variations in the Fe and Cr contents and also in the sum of Ni, Mn, Mo and Si contents. It can also be concluded that two of the analysed dark contrasts (points 21 and 31) are most probably precipitates.

Table 2. Steel E, aged at 400 ℃. Summary of the average results of the point analyses collected from different places in ferrite, weight %.

Target	Fe	Cr	Ni	Mn	Mo	Si	Ni+Mn+Mo+Si	Sum
Av. of ferrite thick	61.93	24.63	6.92	1.24	3.84	1.10	13.10	99.66
17 nm	60.23	26.83	6.22	0.61	4.74	1.08	12.65	99.71
Betw. contrasts average	49.62	32.19	7.27	1.49	5.03	2.07	15.86	97.66
st dev	3.05	2.50	1.70	0.88	1.28	0.70	2.78	
Contrasts average	44.79	30.92	9.28	1.87	6.57	4.37	22.08	97.79
st dev	4.57	3.78	3.00	0.99	1.84	1.50	5.31	
Precipitates average	37.87	27.88	13.92	2.21	8.04	7.65	31.82	97.57
st dev	7.07	4.86	4.10	1.24	1.86	3.68	6.02	

Since Ni content is not dependent on the specimen thickness, it can be used as a reference element when assessing the relationship between Ni, Mn, Mo and Si contents without the effect of thickness, Figure 8. This figure shows that these elements have a tendency to gather together and finally form precipitates without a clear stoichiometric composition. The contrasts seen on the edge of the specimen are mainly clusters of these elements preceding the real precipitation of G-phase. Some of these clusters already contained very small nuclei of precipitates, which was seen in the dark field images. The relationship between iron and chromium contents can be depicted in the similar way, Figure 9. The wide scatter of the results is most probably caused by spinodal decomposition of ferrite, even a certain part of scatter can be explained by thickness variations and clustering of other elements. The contrasts of the clusters and precipitates prevent to see, whether the spinodal decomposition itself causes any kind of contrast in TEM-image.

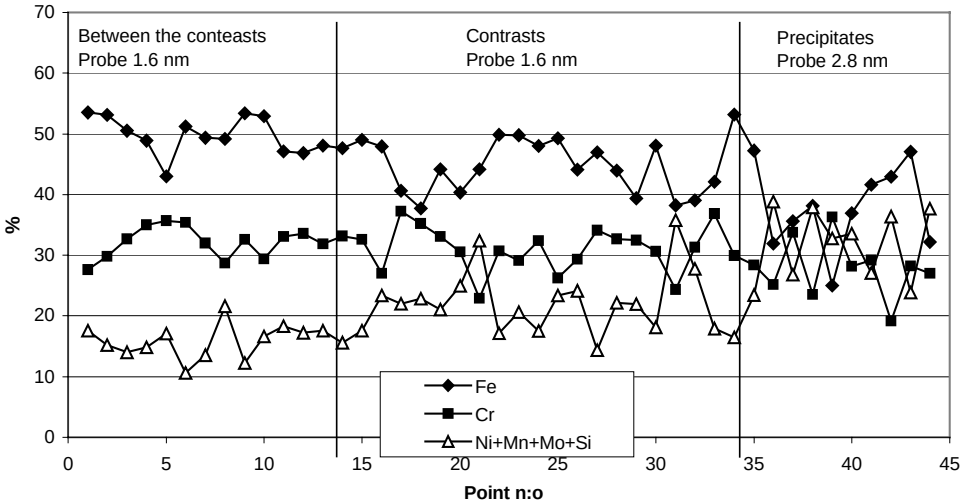

Figure 7. Steel E, aged at 400℃. Results of the point analyses from different targets in thin ferrite.

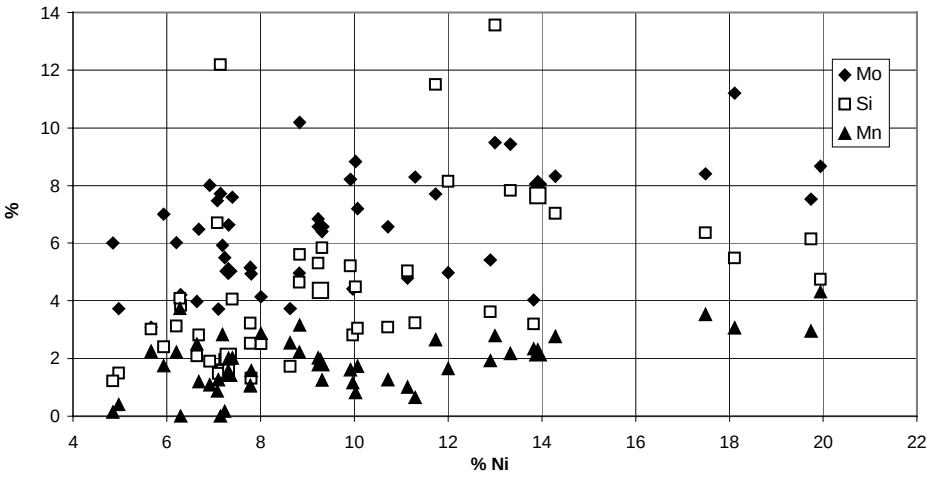

Figure 8. Steel E, aged at 400℃. Results of the point analyses from thin ferrite. Mo, Si and Mn contents as a function of Ni content. Averages in Table 2 have been marked with enlarged symbols.

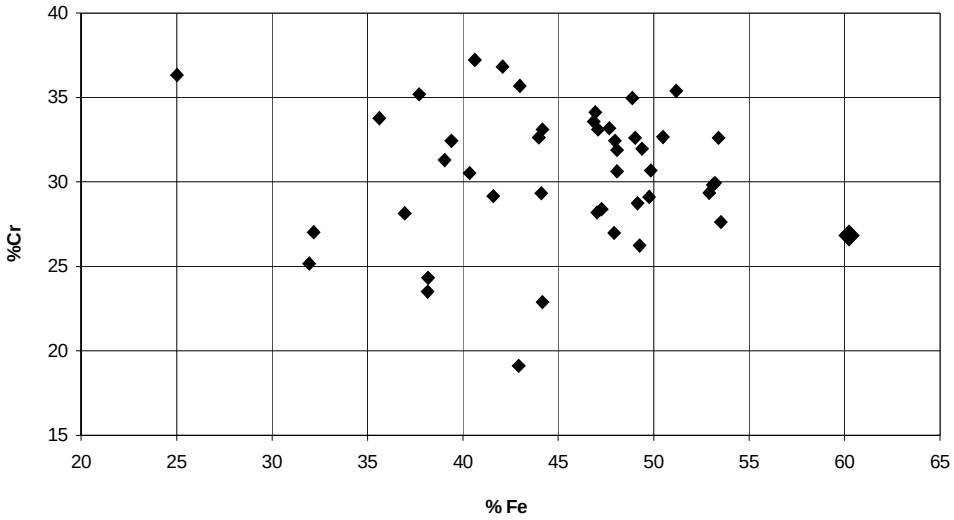

Figure 9. Steel E, aged at 400℃. Results of the point analyses from thin ferrite. Cr content as a function of Fe content. Average of 17 nm thick ferrite has been marked with an enlarged symbol.

To obtain reference data for the material aged at 400°C, the results of the solution annealed Steel E are presented next. The thin edge of ferrite in the TEM-specimen of the solution annealed material was smooth and the observed weak contrasts are most probably caused by defects in the oxide layer, Figure 10. The point analyses were collected from ferrite with different thickness using probe sizes of 1.6 and 2.8 nm. The variation of the thickness inside the chosen thickness areas was small.

Summary of the average results of the point analyses of the solution annealed material is shown in Table 3. These results clearly show how Cr, Mo and Si contents increase with the decreasing specimen thickness. All standard deviations are much smaller than in the case of the material aged at 400°C. Especially in this specimen, small thin ferrite grains were always surrounded by much thicker austenite. This caused a high hole count rate with the smaller probe size (when the beam was limited by lower condenser aperture).

Table 3. Steel E, solution annealed. Summary of the average results of the point analyses collected from different places in ferrite, weight %. .

Target	Fe	Cr	Ni	Mn	Mo	Si	Ni+Mn+Mo+Si	Sum
Thick ferrite	62.75	26.03	6.05	0.71	3.36	0.96	10.37	99.86
Thickness >25nm								
Probe size 1.6 nm	60.04	26.44	6.23	1.21	3.85	1.19	12.48	98.97
st dev	0.97	1.16	0.52	0.5	0.88	0.13	0.75	
Thickness ≥10nm								
Probe size 1.6 nm	57.68	27.53	7.43	0.91	4.17	1.32	13.82	99.03
st dev	1.86	1.37	0.92	0.87	1.46	0.28	1.55	
Thickness <10nm								
Probe size 2.8 nm	53.94	29.94	6.87	0.68	4.02	2.71	11.29	98.17
st dev	2.08	1.54	0.83	0.65	1.07	0.39	1.43	

The material aged at 300°C was examined in the similar way as the solution annealed one. The thin edge of ferrite was smooth and revealed no thickness variations, Figure 11. The point analyses were collected near the edge using different probe sizes and varying specimen thickness. Summary of the average results of the point analyses is presented in Table 4. Based on the Cr contents, the real differences between the average thickness of the analysed places are smaller than in the case of the solution annealed specimen and maybe there are no differences at all. Results collected using 1.2 nm probe show high standard deviations, because the total amounts of collected counts are the lowest. In this specimen the thickness variation between the different phases was smaller and the hole count rate with the small probe was clearly lower than that measured for the solution annealed specimen. The level was same as in the case of the specimen aged at 400°C.

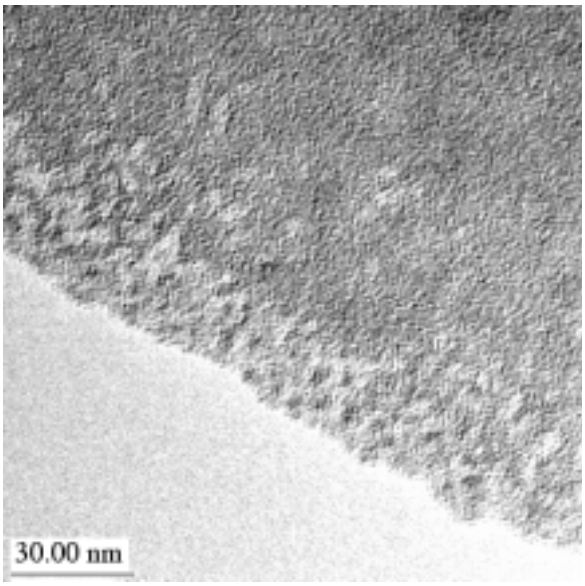

Figure 10. Steel E, solution annealed. Thin edge of ferrite. Nanoprobe mode. under focused image without objective aperture.

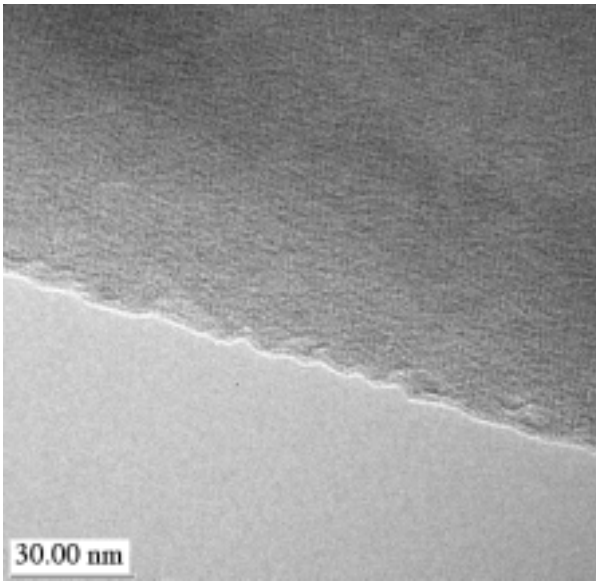

Figure 11. Steel E, aged at 300℃. Thin edge of ferrite. Nanoprobe mode, under focused image without objective aperture.

Table 4. Steel E, aged at 300℃. Summary of the average results of the point analyses collected from different places in ferrite, weight %.

Target	Fe	Cr	Ni	Mn	Mo	Si	Ni+Mn+Mo+Si	Sum
Thickness 17-20 nm								
Probe size1.4 nm	60.07	25.56	7.03	1.28	3.79	1.28	13.38	99.01
st dev	1.61	1.08	0.69	0.67	0.96	0.42	1.29	
Thickness 17-20 nm								
Probe size1.2 nm	59.36	25.54	6.36	0.95	4.44	1.22	12.98	97.88
st dev	3.04	2.17	1.13	1.07	1.51	0.33	1.65	
Thickness 15 nm								
Probe size2,4 nm	60.74	25.11	6.96	0.88	3.67	1.55	13.06	98.90
st dev	1.23	0.87	0.76	0.47	0.76	0.20	0.96	

All the results of the point analyses of the solution annealed and at 300°C aged materials are shown in Figures 12 to 15 in the similar way as those of the material aged at 400°C. The results of the solution annealed specimen reveal a scatter typical of EDS analyses based on quite limited amount of total counts. Figure 12 shows that Ni, Mn and Si contents vary independently from each other, but Mo content seems to decrease slightly with an increasing Ni content. Figure 14 shows how the specimen thickness affects the relationship between the iron and chromium contents. The results of the material aged at 300°C are quite similar to those of the solution annealed material. A somewhat thicker specimen and a smaller thickness variation decrease the scatter of the iron and chromium contents. Figure 13 shows decreasing Mo content with increasing Ni content, similar to the solution annealed material. This is opposite to what was found in the case of the material aged at 400°C. It can be concluded that the clustering of Ni, Mn, Mo and Si has not begun after ageing for 10 000 h at 300°C and, that there is no evidence of the beginning of spinodal decomposition of ferrite. This is in good agreement with the results published in the literature [5]. Ageing for 10 000 h at 300°C does not change the mechanical properties of the studied Steel E.

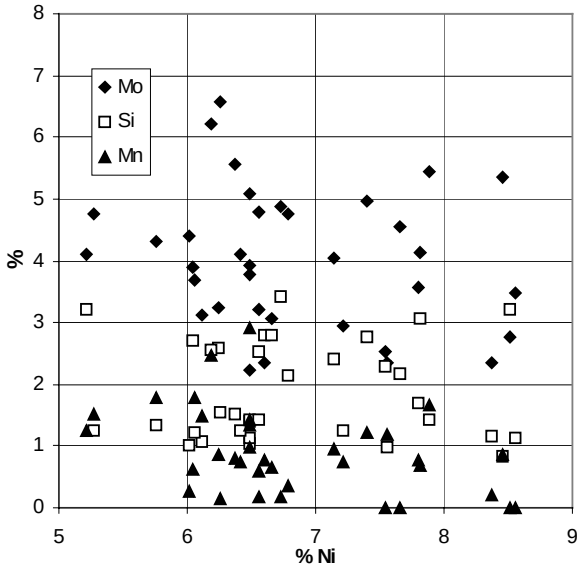

Figure 12. Steel E, solution annealed. Results of the point analyses from thin ferrite. Mo, Mn and Si contents as a function of Ni content.

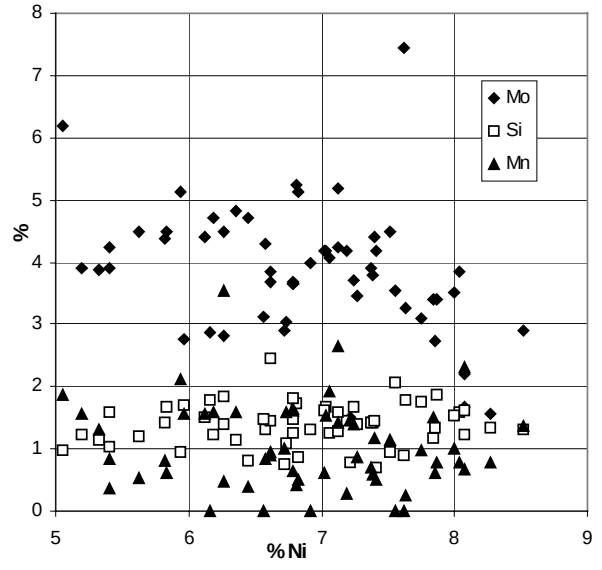

Figure 13. Steel E, aged at 300 °C. Results of the point analyses from thin ferrite. Mo, Mn and Si contents as a function of Ni content.

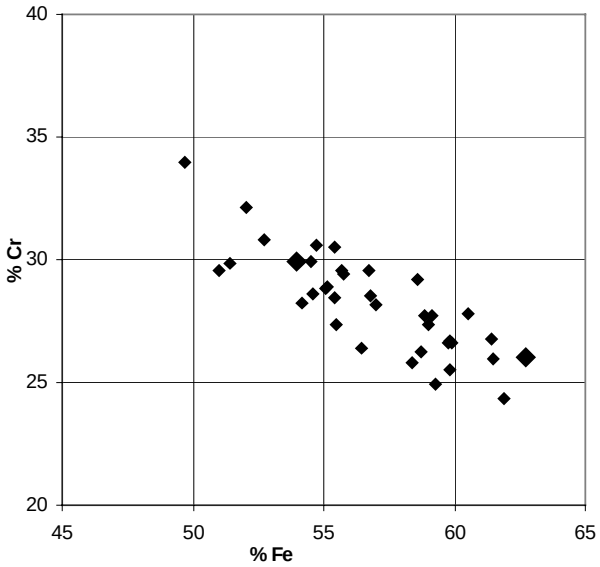

Figure 14. Steel E, solution annealed. Results of the point analyses from ferrite. Cr content as a function of Fe content. Averages of thick and thin (< 10 nm) ferrite have been marked with enlarged symbols.

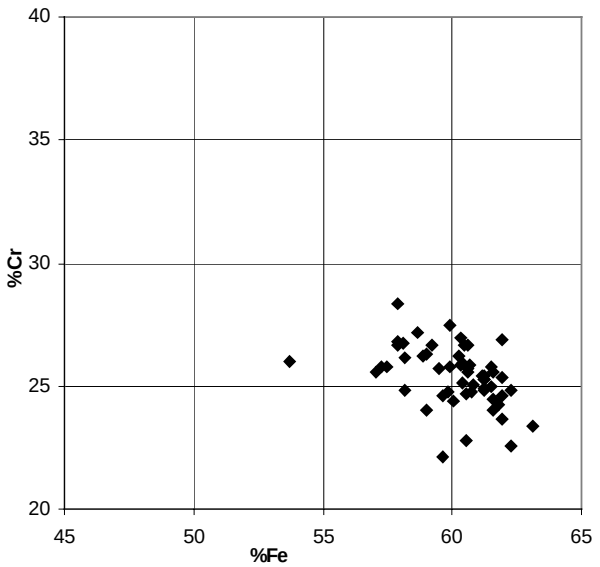

Figure 15. Steel E, aged at 300 °C. Results of the point analyses from thin ferrite. Cr content as a function of Fe content.

3.3 Steel S and Steel K

Steels S and K have been used for long time at temperature of 270°C. The composition of the ferrite phase of them was examined in the similar way as Steel E. The experience obtained with Steel E was partly available during examinations. Steel S was an austenitic-ferritic weld metal containing small amount of elongated irregular ferrite grains often decorated with chromium carbides at the phase boundaries. The point analyses spectra were collected from thin ferrite using 2.8 nm probe so, that one half of the results represent thickness slightly over 10 nm and the other half slightly less than 10 nm. Summary of the average results of the point analyses and the average obtained from thick ferrite are presented in Table 5. Also these results show that especially Cr but also Mo and Si enrich in the surface oxide of the specimen, but Ni and Mn do not. The sum of the contents shown in Table 5 is less than 100%, because minor elements, such as Al, Cu, S, P and Ti were originally also analysed. The relationship between Ni, Mn, Mo and Si contents is shown in Figure 16 and the relationship between Cr and Fe in Figure 17. Figure 16 reveals that Ni, Mo and Si have slightly clustered replacing manganese. This is probably the beginning of the process preceding the precipitation of G-phase. The thin edge of ferrite is shown in Figure 18. The clustering of Ni, Mo and Si may cause the roughness of the edge. It is not obvious, why manganese behaves in a different way than in Steel E. The scatter of the results in Figure 17 is mainly due to the thickness of the specimen and clustering of Mo, Si and Ni. There is no clear evidence about spinodal decomposition of ferrite. On the other hand the results shown in Figure 17 do not exclude the beginning of spinodal decomposition.

Table 5. Steel S. Summary of the average results of the point analyses collected from ferrite, weight %.

Target	Fe	Cr	Ni	Mn	Mo	Si	Ni+Mn+Mo+Si	Sum
Thick ferrite	64.57	25.47	4.31	1.28	3.67	0.42	9.68	99.72
Thickness > 10 nm	58.60	28.59	4.46	1.13	3.97	1.60	11.16	98.35
st dev	1.63	0.73	0.68	0.67	1.01	0.27	1.49	
Thickness < 10 nm	54.90	31.23	4.12	1.31	4.68	2.10	12.21	98.33
st dev	2.04	1.38	1.03	0.87	1.26	0.51	1.97	

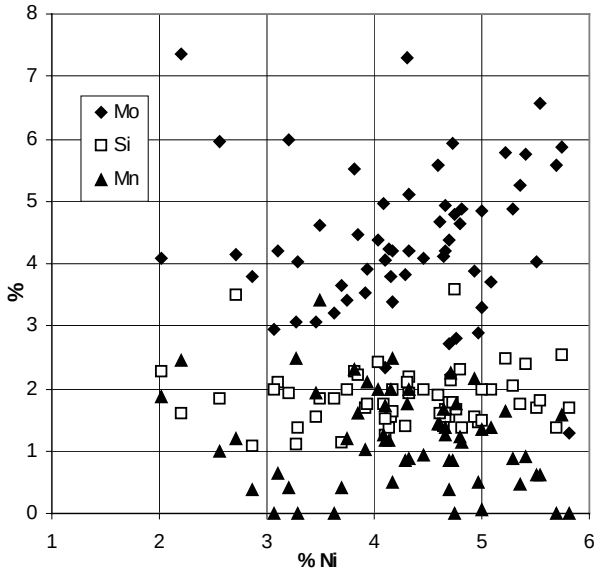

Figure 16. Steel S. Results of the point analyses from ferrite. Mo, Si and Mn contents as a function of Ni content.

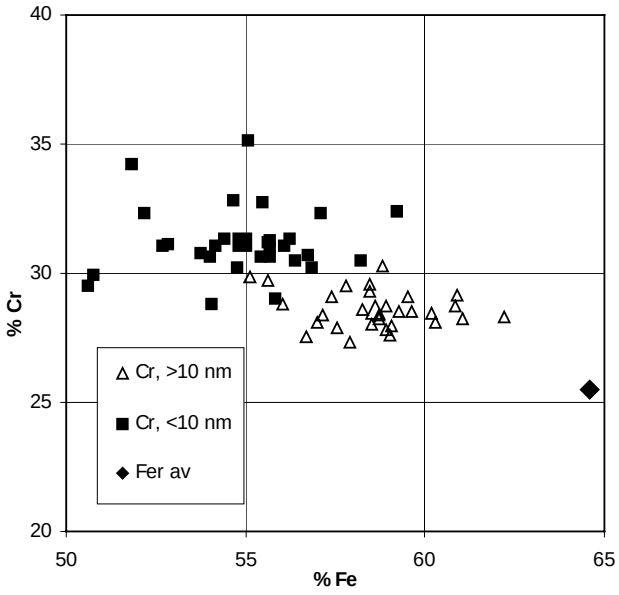

Figure 17. Steel S. Results of the point analyses from thin ferrite. Cr content as a function of Fe content. The averages of both groups have been marked with enlarged symbols.

Steel K was a cast duplex Ti-stabilised stainless steel. The SOL-state of this material was not known, but based on the microstructure the material has not been in the solution annealed condition. Austenite contained plenty of (Ti, Fe, Ni)-phosphides as long, thin needle like precipitates, which most probably have not precipitated at 270°C, Figure 19. Ferrite contained small semi-coherent precipitates, which were analysed to contain Ni, Al, Mn and Ti, Figure 20. Probably these precipitates also originate from the SOL-state. The relationship between iron and chromium in ferrite was examined by collecting point analyses spectra from the thin ferrite matrix between the precipitates. One group of the results represents specimen thickness slightly over about 15 nm and the other group slightly less than 15 nm. These spectra were collected using 2.8 nm probe and without analysing minor elements. Summary of the average results of the point analyses, typical composition of a precipitate and the average obtained from thick ferrite are presented in Table 6. The results show again slight enrichment of Cr and Si in the surface oxide. In Figure 21 Cr content is shown as a function of Fe content. The sum of Cr and Fe contents is nearly constant and quite high. The scatter of the results obtained from thinnest ferrite (<15 nm) is rather wide, which is partly caused by variation of the thickness. On the other hand, it may indicate some degree of spinodal decomposition taken place together with precipitation, because the thickness variation inside this group of results was quite small.

Table 6. Steel K. Summary of the average results of the point analyses collected from different places in ferrite, weight %.

Target	Fe	Cr	Ni	Mn	Si	Al	Ti
Precipitate	35.74	13.84	28.71	5.20	1.41	6.90	5.90
Thick ferrite	68.18	25.06	3.66	1.64	0.55	0.43	0.12
Thickness >15 nm	68.16	25.95	3.10	1.39	0.86	0.30	0.04
st dev	1.20	1.09	0.81	0.34	0.09	0.16	0.05
Thickness <15 nm	65.98	28.04	2.97	1.49	1.09	0.38	0.04
st dev	1.60	1.51	0.42	0.27	0.13	0.16	0.06

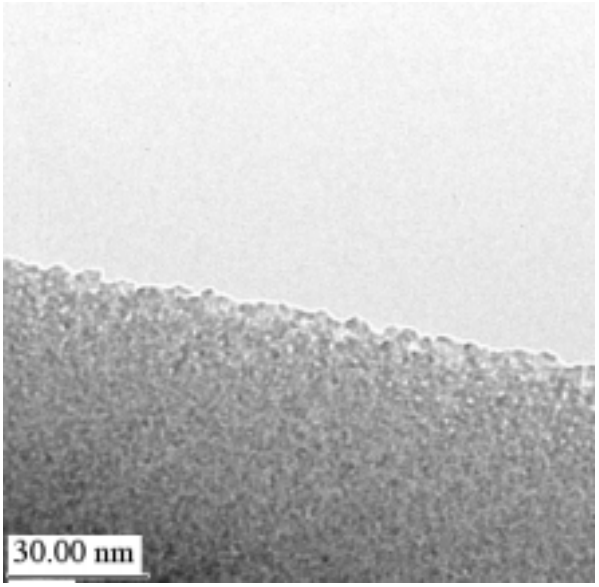

Figure 18. Steel S. Thin edge of ferrite. Nanoprobe mode, under focused mage without objective aperture.

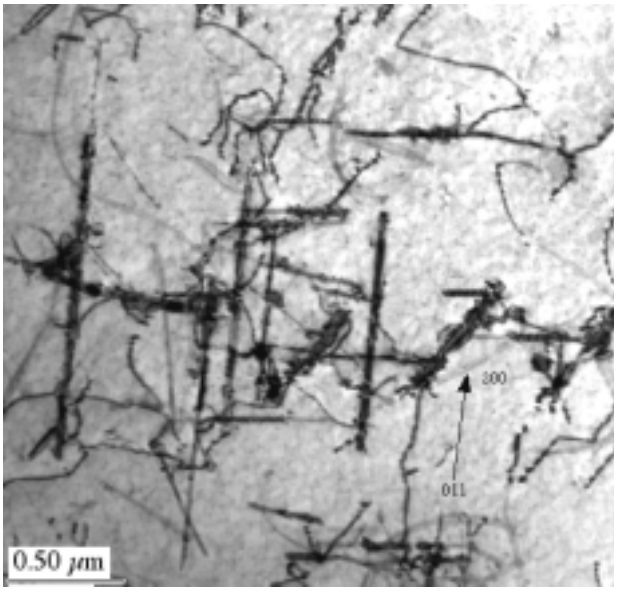

Figure 19. Steel K. Needle like phosphide precipitates in austenite.

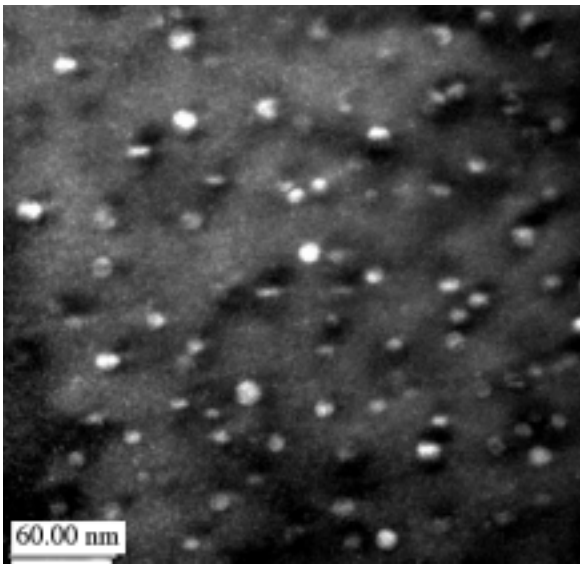

Figure 20. Steel K. Semi-coherent precipitates containing Ni, Al, Mn andTi in ferrite.

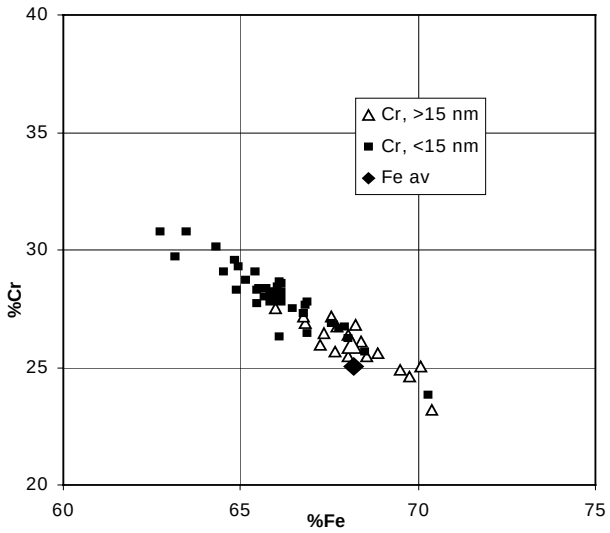

Figure 21. Steel K. Results of the point analyses from thin ferrite between precipitates. Cr content as a function of Fe content. The averages of both groups have been marked with enlarged symbols.

4. Conclusions

Based on the results obtained using FEGTEM and EDS analyser, both are, as supposed, very capable tools to investigate decomposition of ferrite after thermal ageing causing clear structural changes. Results of this study also revealed that there are certain limitations and things to be considered, especially if beginning of the decomposition is investigated with EDS at a stage in which visible changes are not present, yet:

- Elements, such as Cr, Mo and Si have a tendency to enrich in the surface oxide of the specimen during the electropolishing with the used electrolyte.
- Low number of total counts seems to increase the average sum of minor elements. This is probably caused by errors due to rough background of the spectrum since no systematic enrichment has been found. This increases the scatter of major elements.
- Low number of total counts itself also increases the scatter of major elements.
- Use of condencer 2 aperture in order to limit the beam size in Philips CM200 microscope increases the information collected outside the probe. This increases the detection limits of real differences of local compositions. (Depending on TEM-type this problem may be always present).
- High contamination rate may decrease the amount of net counts of analysed elements.

The above mentioned features can be avoided, or the effects of them can be limited as follows:

- Condenser 1 aperture is used as a beam limiting aperture. The smallest useful probe size is 2.4–2.8 nm, which seems to be small enough and offers a high count rate, clean spectrum and low contamination rate.
- Plasma cleaning of the specimen just before point analyses reduces the contamination rate for next 2 to 3 working hours.
- Minor elements are not analysed and in the case of spinodal decomposition, perhaps only Cr and Fe are analysed or their concentrations are later recalculated without taking into account the other elements.
- If the enrichment of chromium can not be eliminated by using some other electrolyte, each group of spectra or true line analyses must be collected

from places with equal thickness. As a compromise of several things a suitable thickness of the specimen seems to be 10 to15 nm.

These conclusions should be confirmed by investigating sample/samples aged to the stage in which the beginning of spinodal decomposition has been identified with some other methods.

Acknowledgements

This work is a part of the project on Structural operability and plant life management (RKK). The project funding by the National Technology Agency (Tekes), Teollisuuden Voima Oy (TVO), Fortum Power and Heat Oy, Fortum Nuclear Services Ltd., FEMdata Oy, Neste Engineering Oy, Fortum Oil and Gas Ltd. in Finland is gratefully acknowledged.

References

1. Auger, P., Danoix, F., Menand, A., Bonnet, S., Bourgoin, J. and Guttman, M. Atom probe and transmission electron microscopy study of aging of cast stainless steel. Material Science and Technology, March 1990, Vol. 6, pp. 301–313.
2. Mateo, A., Llanes, L., Anglada, M., Redjaimia, A. and Metauer, G. Characterization of intermetallic G-phase in an AISI 329 duplex stainless steel. Journal of Materials Science, 1997, Vol. 32, pp. 4533–4540.
3. Danoix, F., Bas, P., Massoud, J. P., Guttman, M. and Auger, P. Atom probe and transmission electron microscopy study of reverted duplex stainless steels. Applied Surface Science, 1993, Vol. 67, pp. 348–355.
4. Alexander, K. B., Miller, M. K., Alexander, D. J. and Nanstad, R. K. Microscopical evaluation of low temperature aging of type 308 stainless steel weldments. Materials Science and Technology, March 1990, Vol. 6, pp. 314–320.
5. Grisot, O. and Massoud, J. P. Proceedings of 5th International Conference on Nuclear Engineering, May 26–30, 1997, Nice, France.

Properties and IASCC susceptibility of austenitic stainless steel 08X18H10T

Aki Toivonen, Pertti Aaltonen, Pertti Nenonen, Ulla Ehrnstén and Arvo Käki
VTT Industrial Systems, Espoo, Finland
Ossi Hietanen
Fortum Nuclear Services, Vantaa, Finland

Abstract

A study on an irradiated titanium stabilised 08X18H10T stainless steel from Loviisa NPP absorber element bottom end was initiated in 1999. The aim was to characterise the changes in mechanical properties and the susceptibility to IASCC in VVER environments by laboratory tests. Results showed that material properties had changed as a result of neutron irradiation, but not to the extent expected on the basis of estimated neutron fluences. Yield strength, tensile strength, and dislocation loop density were all lower and ductility much higher than expected.

Initially calculated neutron fluence of the material varied between 1×10^{21} and 2.6×10^{21} n/cm^2, E > 1 MeV (1.5 and 4 dpa, respectively). The newest calculations using Monte Carlo simulations indicate that the real fluences are clearly lower, 0.5×10^{21} and 1×10^{21} n/cm^2, E > 1 MeV (0.7 and 1.5 dpa, respectively) and below the assumed threshold for IASCC in PWR environment.

1. Introduction

Irradiation assisted stress corrosion cracking of reactor core components is a topic of interest in the international nuclear materials research community. 15 partners from USA, Japan and Europe have joined together in an international group of Co-operative Irradiation Assisted Stress Corrosion Cracking Research Program (CIR) coordinated by the Electric Power Research Institute (EPRI). VTT is participating in the CIR programme through in-kind information exchange.

The Finnish research contribution to CIR is partly realised within this RKK subproject. The objective of this subproject is to investigate whether irradiation assisted stress corrosion cracking can occur in PWR reactor core conditions in titanium stabilised austenitic stainless steel. This presentation is based on a report, which describes the third year status of the subproject.

1.1 Irradiation assisted stress corrosion cracking

Irradiation assisted stress corrosion cracking, IASCC, has been reported to occur as intergranular cracking in austenitic stainless steels in BWR environments at neutron fluences above 5×10^{20} n/cm^2 (E > 1 MeV), corresponding to about 0.7 dpa (displacements per atom). The threshold fluence for increased risk of intergranular irradiation assisted cracking in PWR environment is suspected to be clearly higher, 3 dpa or more.

In oxidising BWR environment, the role of corrosion in IASCC is evidently important, but in hydrogen containing PWR environment corrosion should not be as decisive. Possible additional factors promoting intergranular cracking are radiation-induced hardening, radiation-induced creep and segregation together with hydrogen embrittlement. Also swelling, formation of helium bubbles and radiation-induced precipitation may become an issue, especially at higher irradiation temperatures or at higher neutron fluences.

1.2 Background

Failure of a fuel assembly spacer grid sleeve created the motivation to this subproject. The fuel assembly spacer grid sleeve was made of Ti-stabilised austenitic stainless steel 06X18H10T. It had failed after three years of operation in a VVER-440 PWR reactor. Irradiation assisted stress corrosion cracking was suspected and a careful failure analysis was performed [1].

The fuel rod spacer grid is clamped to the central tube with the spacer grid sleeve ($\phi13\times0.55$ mm). The estimated irradiation temperature was 300°C, and the fluence of the failed spacer grid sleeve after three years of exposure was calculated to be 4.6×10^{21} n/cm^2, E > 1 MeV, i.e., about 7 dpa.

1.3 Objectives

The objective was to investigate whether irradiation assisted stress corrosion cracking can occur in PWR reactor core conditions in titanium stabilised austenitic stainless steels. Verified evidence was still missing at the time when this project was launched. An absorber element bottom end, which had been used in the Loviisa NPP, was assumed suitable test material for this purpose.

The material type is similar to the spacer grid sleeve material. The main differences are a bit lower neutron fluence, 1.5–4 dpa according to initial calculations, and higher carbon content, 0.08 wt%. However, the production history of neither the spacer grid sleeve nor the absorber element bottom end are not accurately known.

The test program aimed to characterise the mechanical properties, microstructure and IASCC susceptibility in PWR environments of this Loviisa NPP absorber element.

2. Experimental

The study was planned to begin with characterisation of mechanical properties and microstructure followed by determination of IASCC susceptibility in environments relevant to VVER 440 power plants.

2.1 Test material

Test material is titanium stabilised austenitic stainless steel 08X18H10T, which is one of the main construction materials used in the reactor of Loviisa NPP, Table 1. The irradiated material originates from the bottom end of an absorber element, Fig. 1. The initially calculated fluences were ~1×10^{21} n/cm^2 in the thickest part in the middle of the component and ~2.6×10^{21} n/cm^2, E > 1 MeV, in the lowest part of the component, i.e., about 1.5 and 4 dpa, respectively. These calculations were based on the locations of the element in the core and on the vertical positions as registered by the process computer. Estimated irradiation temperature is 300^{o}C.

Table 1. Nominal composition of the test material 08X18H10T, wt%.

Fe	C	Cr	Ni	Mn	Si	Ti
Bal.	0.08	17–19	10–11	1.0–2.0	< 0.8	5xC–0.7

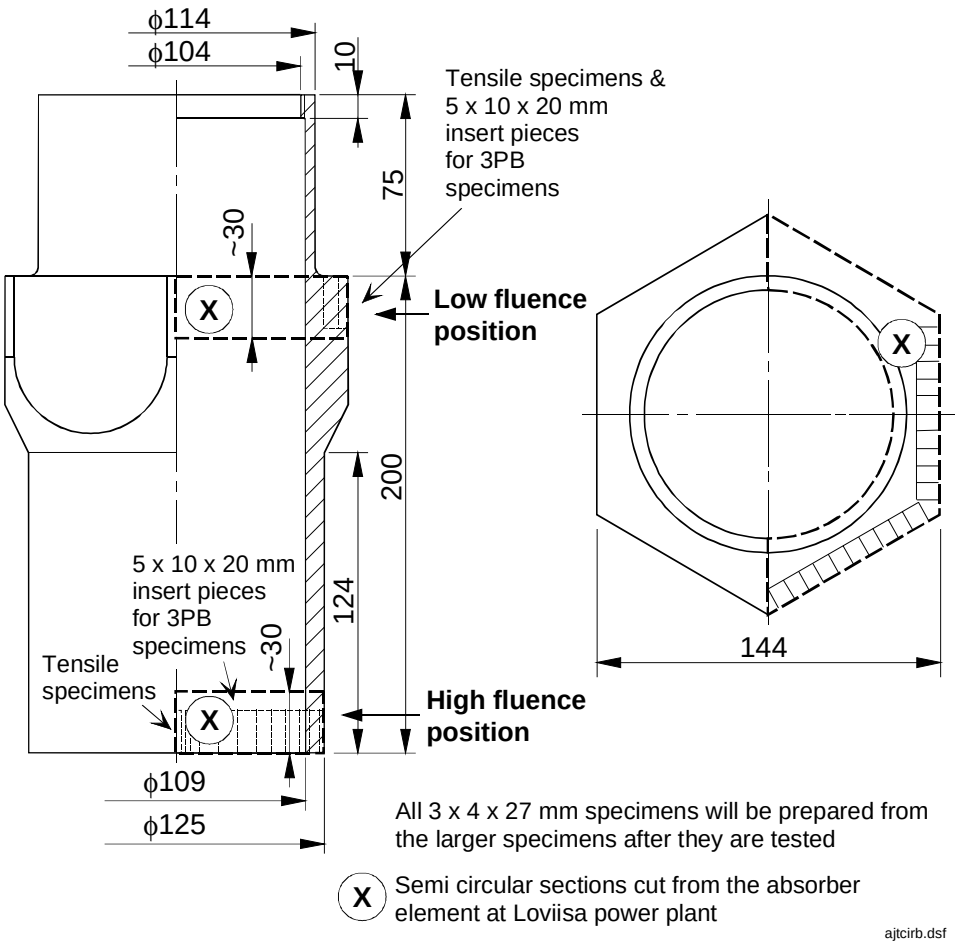

Figure 1. Bottom end of the absorber element and location of test samples.

2.2 Material characterisation

Mechanical characterisation consists of tensile, hardness, fracture resistance (J-R), and impact tests. Microstructural characterisation is conducted using optical and transmission electron microscopes.

2.2.1 Tensile and hardness tests

Tensile tests of the irradiated material for both fluence levels were conducted at room temperature, 100°C, 200°C and 300°C. The specimens for the tensile tests were small electric discharge machined plate type specimens with cross section of 2×1 mm and gauge length of 8 mm, Fig. 2. The tests were conducted according to the standard SFS-EN 10 002-1.

The hardness of the material at both fluence levels was determined using Vicker's microhardness measurements.

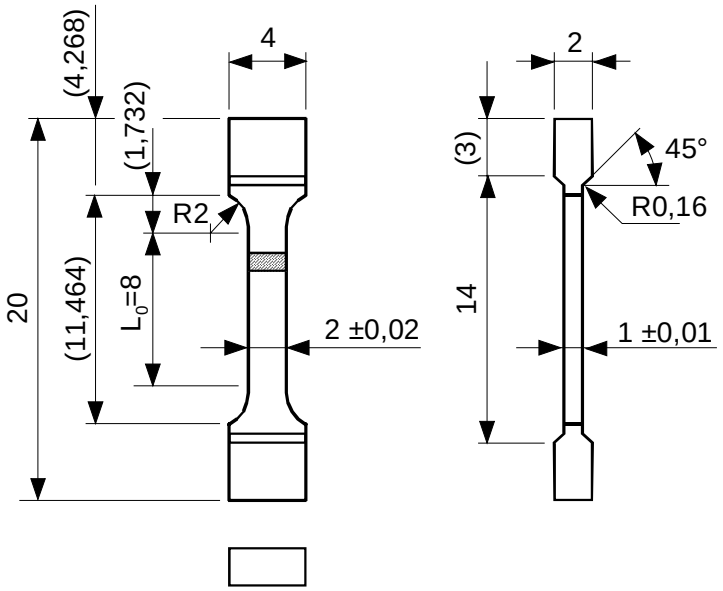

Figure 2. Tensile specimen geometry.

2.2.2 Fracture resistance measurements and impact tests

Fracture resistance measurements, i.e., J-R tests for the lower fluence material are conducted on 10×10×55 mm^3 three point bend (3pb) specimens. This J-R test specimen geometry is presented in Fig. 3. Because the higher fluence section of the absorber element bottom end has a wall thickness less than 5 mm, specimen size 4×10×55 mm^3 is used for the higher fluence material. J-R tests are conducted and analysed according to the standard ASTM E 1737-96.

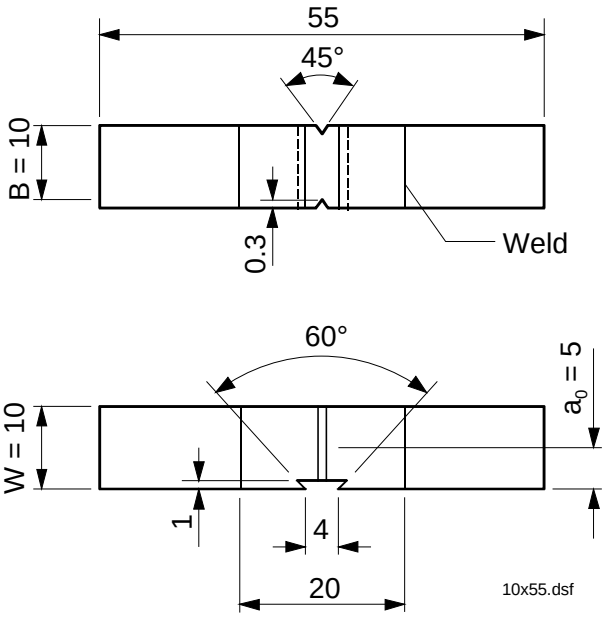

Figure 3. Reconstitution welded and pre-fatigued 10×10×55 mm^3 three point bend specimen with an irradiated insert piece in mid section of the specimen. The 4×10×55 mm^3 specimen is similar, except the B-dimension (4 mm) and side groove depths (0.4 mm).

J-R tests for the lower fluence material have been conducted at room temperature and 100°C. The J-R test series will be continued by tests at 175 and 300°C on the lower fluence material and by tests at room temperature, 100, 175 and 300°C on the higher fluence material.

The J-R tests at the temperatures up to 175°C are conducted using the partial unloading compliance method for crack growth measurement. The tests at 300°C have to be conducted using the Potential Drop (PD) technique.

Impact tests will be conducted at room temperature. The impact specimens are notched 3×4×27 mm^3 specimens of KLST geometry, Fig. 4.

J-R- and impact specimens are cut in L-C orientation. All J-R and impact specimens are prepared by electric discharge machining. Reconstitution technique is used to minimise material consumption.

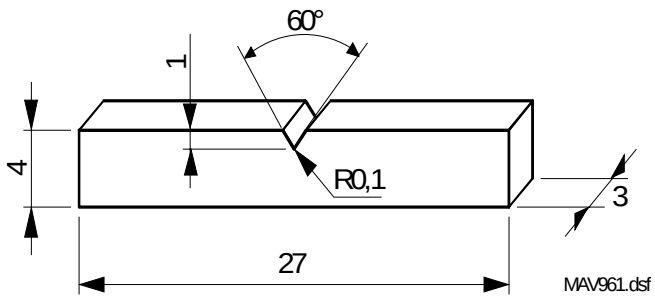

Figure 4. KLST impact specimen for impact tests.

2.2.3 Microstructural characterisation

Philips CM 200 Field Emission Gun Scanning Transmission Electron Microscope (FEGSTEM) was used to analyse the defect density of the material and segregation of alloying elements at the grain boundaries. The defect density was analysed from bright field images. FEGSTEM samples were cut from the same locations as the tensile specimens. Optical microscopy was used to determine the grain size.

2.3 Characterisation of IASCC susceptibility

IASCC susceptibility was planned to be studied by tests in simulated normal operation and shutdown water chemistries of VVER 440 plants. Start of these tests was postponed as the initial neutron fluence estimates were questioned after

receiving the first results of material characterisation. The aim was to modify the test matrix, if necessary after re-calculation of the neutron fluences. At time of writing this presentation newest results on neutron fluence indicate that IASCC cannot be reasonably expected to occur in the planned tests.

However, an autoclave and two pneumatic servo-controlled loading frames for specimen loading have been prepared ready for these IASCC tests. Similar loading frames have been successfully utilised in earlier stress corrosion crack growth tests at VTT. Slow rising/constant displacement tests on pre-fatigued ~4×10×55 and 10×10×55 mm^3 three point bend specimens were planned to be conducted during the project year 2002. The specimens are similar to the specimens as used in the J-R tests for mechanical characterisation. Crack growth rates as a function of K_J will be determined from the tests data. Fracture morphologies will be studied using a scanning electron microscope, SEM, if the tests will be realised.

3. Results

After the third year of the project the mechanical properties, defect structures and grain boundary segregation have been characterised by tensile tests, hardness measurements, and FEGSTEM analysis. Metallographic properties have been studied by optical microscopy.

The autoclave test have not been started. They were postponed in order to clarify the significance of initial results first. Namely, the initial neutron fluence estimates were questioned on the basis of the results of material characterisation. Much time and effort was used in assessment of the results and fluence calculations. Alternative dosimetric techniques have been explored and more detailed fluence calculations have been recently performed.

3.1 Mechanical characterisation

Tensile and hardness test results of the absorber element are summarised in Table 2. Averages of two repeated tests are shown together with the minimum tensile properties and hardness of unirradiated material according to material supplier, and also the hardness measured from the spacer grid sleeve.

Table 2. Tensile properties and hardness of the absorber element bottom end and spacer grid materials. Initially calculated fluences (E > 1 MeV) are given.

Fluence n/cm^2 & dpa	**Temp.** ^{o}C	**$R_{p0.2\%}$** MPa	**R_m** MPa	**A_g** [1] %	**A_t** [1] %	**Hardn.** HV
0	23	196 [2]	490 [2]		38 [2]	156 [2]
	350	176 [2]	352 [2]		25 [2]	
1×10^{21} [3]	23	367	658	49	64	210
(1.5 dpa)	101	333	553	33	43	
	200	301	503	27	35	
	300	294	472	25	32	
2.6×10^{21} [3]	23	453	692	43	65	228
(4 dpa)	101	408	602	29	43	
	200	391	550	23	34	
	300	387	537	23	31	
4.6×10^{21} (7 dpa)	23					347 [4]

[1] A_g = uniform elongation; A_t = elongation to failure.

[2] Minimum values according to the material supplier.

[3] Fluences were later found smaller than these initial estimates.

[4] Fuel assembly spacer grid sleeve. Grain size was clearly smaller than in the absorber element bottom end.

Fig. 5 shows an example of the measured load-elongation curves, which all showed ductile behaviour of the material. Figs 6 to 9 show the trends in yield strength, ultimate tensile strength, elongation to fracture and uniform elongation.

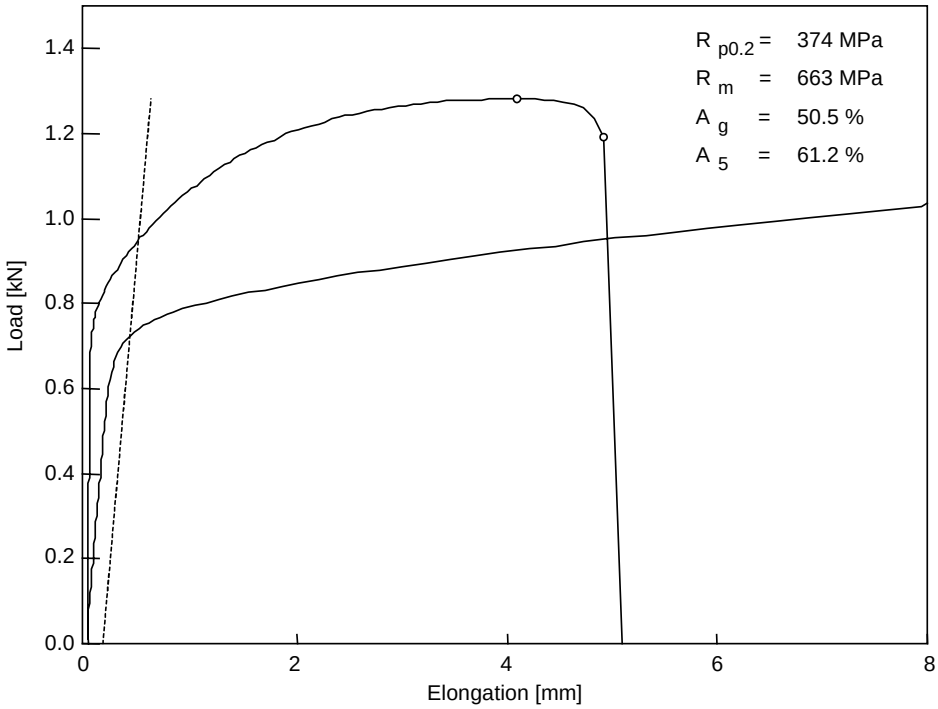

Figure 5. Load-elongation curve of the lower fluence material (initially calculated fluence 1×10^{21} n/cm^2, E > 1MeV, ~1.5 dpa) measured at 23^{o}C. Specimen size: cross section 0.97×1.99 mm^2, L_0 8.0 mm.

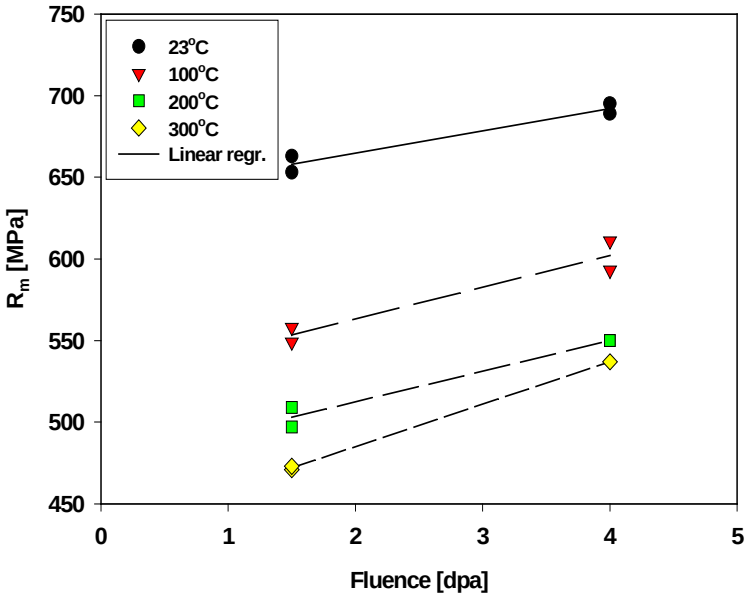

Figure 6. Yield strength ($R_{p0,2}$) at room temperature, 100°C, 200°C and 300°C at two fluences. The fluences are initially calculated values.

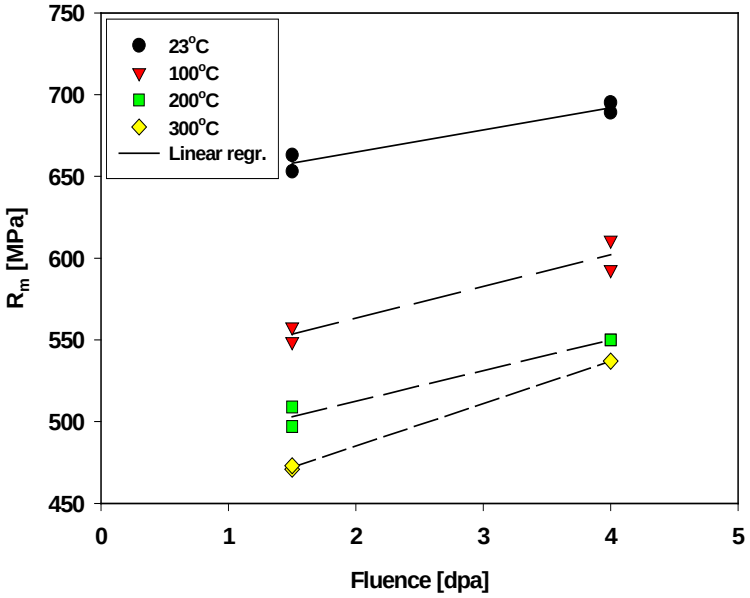

Figure 7. Ultimate tensile strength (R_m) at room temperature, 100°C, 200°C and 300°C at two fluences. The fluences are initially calculated values.

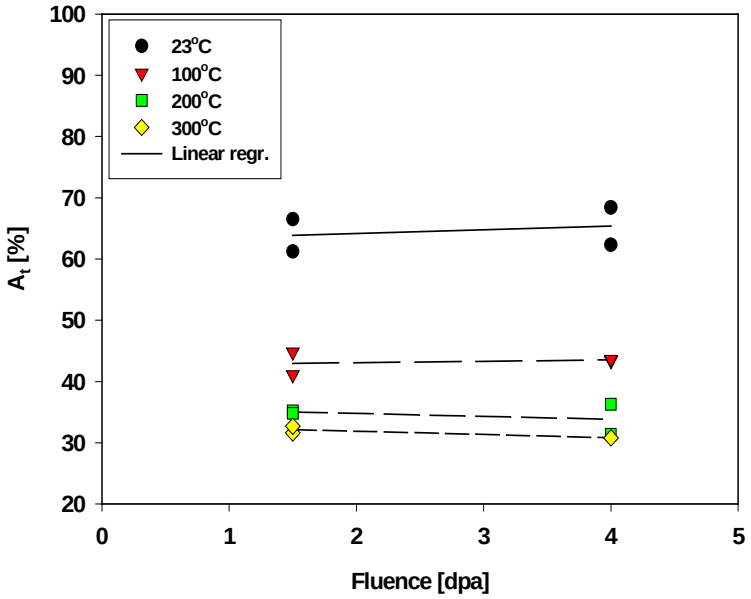

Figure 8. Elongation to fracture (A_t) at room temperature, 100°C, 200°C and 300°C at two fluences. The fluences are initially calculated values.

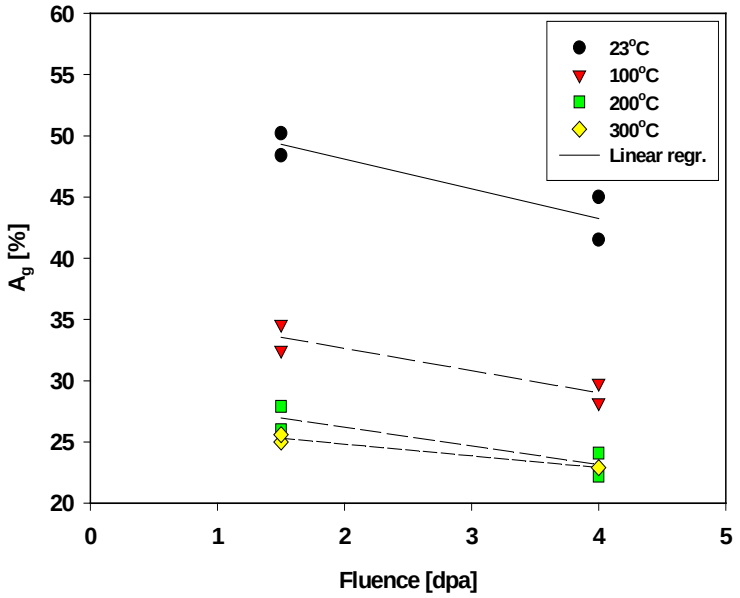

Figure 9. Uniform elongation (A_g) at room temperature, 100°C, 200°C and 300°C at two fluences. The fluences are initially calculated values.

3.2 Microstructural characterisation

3.2.1 Defect structure

Transmission electron microscopy samples were cut from the same locations as the tensile specimens and they represent two levels of neutron fluence. For the lower fluence material, initially calculated to 1×10^{21} n/cm^2, E > 1 MeV, 1.5 dpa, FEGSTEM results reveal that the defect structure consists mainly of black dots and faulted interstitial loops with the average size of 4.2 nm, Fig. 10. The loop density of this lower fluence material is 4.5×10^{22} m^{-3}.

The defect structure of the higher fluence material, initially calculated to 2.6×10^{21} n/cm^2, E > 1 MeV, 4 dpa, is otherwise similar to the defect structure of the lower fluence material except that the average loop size is 5.9 nm and density 5.5×10^{22} m^{-3}, Fig. 11. Besides the black dots and loops, this material possibly contains also small (~2 nm) voids.

The loop densities and loop sizes inside the grains, close to the grain boundaries and close to the Ti-carbides were carefully compared. Examples of these different locations in the higher fluence material are shown in Figs. 11 to 14. No significant differences were found between the grain boundaries and interiors, see Figs. 11 and 12.

Close to the Ti-carbides, the loop density is clearly higher than elsewhere. The loops around the carbides are also larger than elsewhere in the matrix, 8.1–8.2 nm in average. The size of the carbides varies between ~10 nm and ~1 μm. A general view showing the effect of a Ti-carbide cluster on the defect density is presented in Fig. 13. Similar carbide clusters as seen in Fig. 13 are here and there both in the matrix and at the grain boundaries. A detail showing the defect structure around a Ti-carbide is presented in Fig. 14.

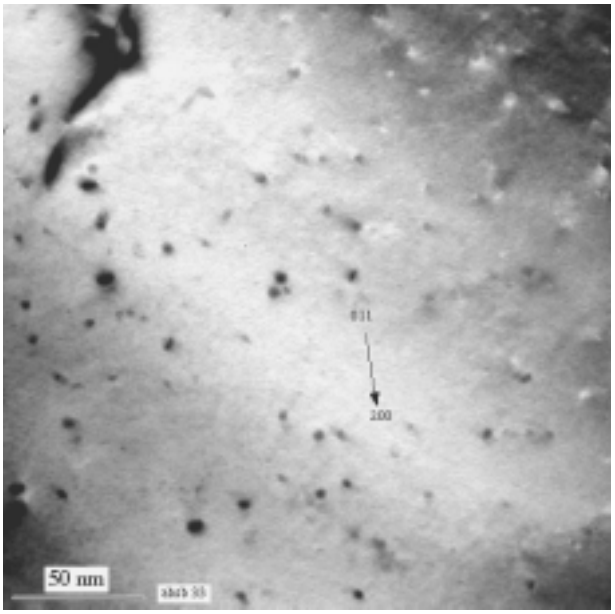

Figure 10. A bright field image showing the defect density in the matrix of the lower fluence material (initially calculated 1.5 dpa). Sample thickness is 37 nm.

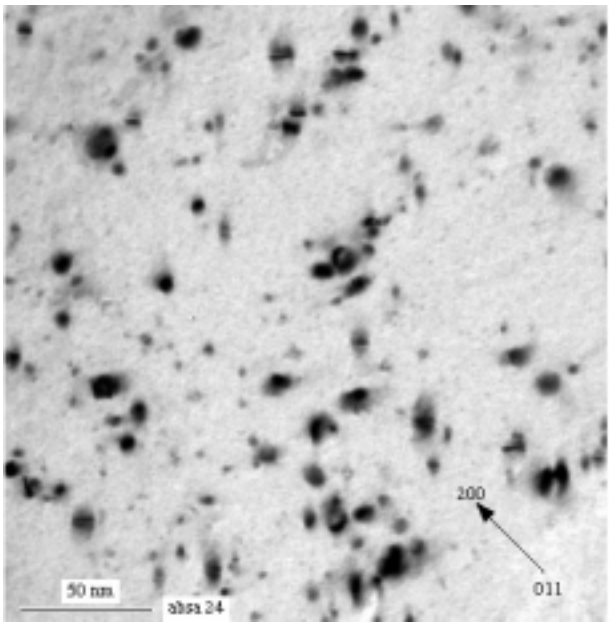

Figure 11. A bright field image showing the defect density in the matrix of the higher fluence material (initially calculated 4 dpa). Sample thickness is 37 nm.

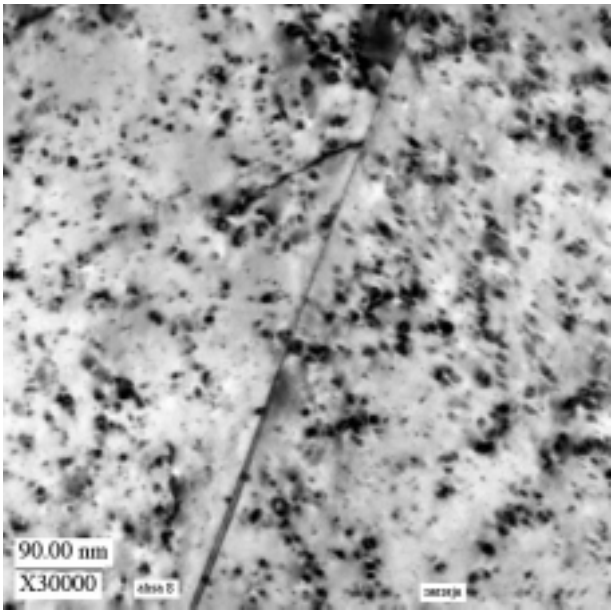

Figure 12. Overview of the loop density close to a grain boundary in the higher fluence material.

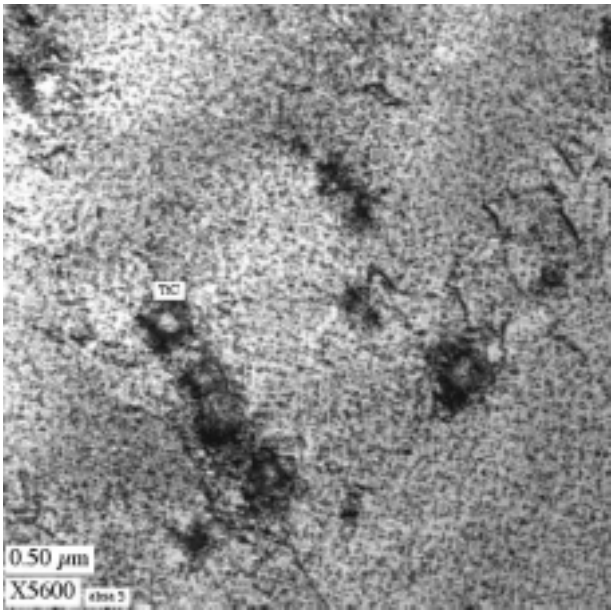

Figure 13. A bright field image shoving the average matrix defect density and increased density close to Ti-carbides in the higher fluence material.

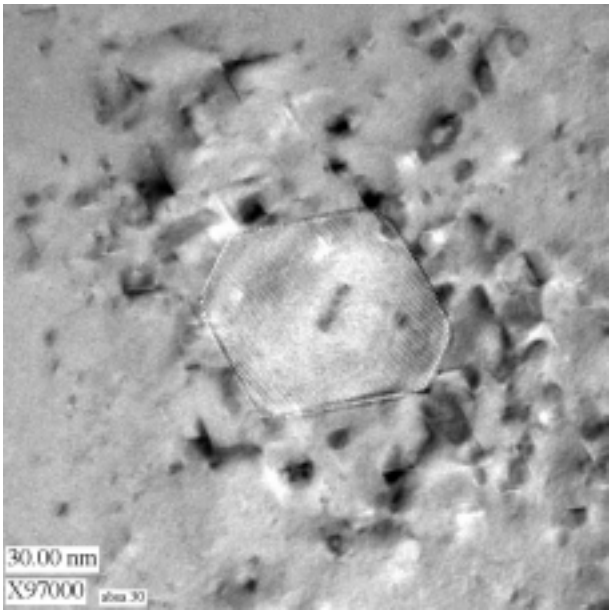

Figure 14. A bright field image shoving the increased defect density around a single Ti-carbide in the higher fluence material.

1.1.2 Grain boundary segregation

Radiation induced grain boundary segregation could not be measured from the 3 mm diameter disc shaped samples, which are commonly used in TEM studies. Energy dispersive x-ray analysis was prevented by a high gamma dose rate from the sample. To overcome this problem, a new specimen preparation method was developed. An 1 mm diameter irradiated insert disc was attached into a hole in the centre of a 3 mm disc.

After the new specimen preparation method was developed, grain boundary and matrix compositions were analysed using 1.2 and 20 nm diameter beams, respectively. The grain boundary analyses are averages of four grain boundaries and the matrix analyses are averages of both matrices adjacent to the grain boundaries. The analyses were conducted from locations where there were no carbides.

The results showed that there was Fe and Cr depletion and Ni, Si, P, Mo and Ti enrichment in grain boundaries, Table 3.

Table 3. Matrix and grain boundary compositions (wt%) and segregation of different elements in irradiated absorber element material at two fluence levels.

Fluence / location	Fe	Cr	Ni	Mn	Si	P	Mo	Ti
1.5 dpa (initial calc.)								
Grain boundary	64.41	17.93	12.12	2.04	1.45	0.41	0.36	0.60
Matrix	66.68	18.39	11.34	1.98	0.77	0.01	0.28	0.26
Segregation	-2.27	-0.46	+0.78	+0.06	+0.68	+0.40	+0.08	+0.34
4 dpa (initial calc.)								
Grain boundary	64.47	18.27	10.39	3.77	1.13	0.44	0.35	0.74
Matrix	66.12	19.21	9.20	3.37	0.93	0.11	0.24	0.31
Segregation	-1.65	-0.94	+1.19	+0.40	+0.20	+0.33	+0.11	+0.43

1.1.3 Metallography

Microstructure of the absorber element lower end material is shown in Figs 15 and 16. Fig. 15 represents the lower fluence part and Fig. 16 the higher fluence part. The ASTM grain sizes are 4–4.5 and 5, respectively. The structures are typical austenitic structures with twins and small amount of probably δ-ferrite, seen as long horizontal bands in Fig. 16. The samples were etched by $HF+HNO_3$+glycerol after mechanical polishing.

Figure 15. Optical micrograph of the lower fluence material, initially calculated 1.5 dpa. Grain size ASTM 4–4.5. (100X).

Figure 16. Optical micrograph of the higher fluence material, initially calculated 4 dpa. Grain size ASTM 5. (100X).

4. Discussion

4.1 Fluence calculations

The test material is taken from the bottom end of an absorber element, which is periodically moved in vertical direction during operation. The locations of the element in the core are registered by the process computer. The vertical positions are recorded in certain intervals and this data was used for estimating the neutron fluences. The initially calculated neutron fluences were ~1×10^{21} n/cm^2 in the thickest part in the middle of the component and ~2.6×10^{21} n/cm^2, E > 1 MeV, in the lowest part of the component, i.e., about 1.5 and 4 dpa, respectively. Irradiation temperature is estimated to 300^{o}C.

The initial neutron fluence estimates were questioned when the measured mechanical properties and defect structures were compared to material properties of other irradiated stainless steels reported in the literature. In tensile tests, the elongations were much larger than expected and yield and tensile strengths were lower. The densities and sizes of defects as observed by TEM were lower than expected. Similar data was not available to the exactly same steel, but on the other hand, the observed differences could not be explained by effects of titanium stabilisation and the current knowledge on the irradiation damage mechanisms.

These findings resulted in a decision to perform re-calculation of the fluences and to investigate possibilities for new measurements to verify the fluence calculations. In this phase it was noted that the absorber element lower end operates in a high gradient area of neutron flux and the vertical position increments needed to be refined for a more realistic fluence estimate.

Recent calculations confirm that the fluences were notably lower than initially estimated. Monte Carlo simulations using refined flux distribution data resulted in fluences of 1×10^{21} n/cm^2, E > 1 MeV (~1.5 dpa) for the higher fluence material and 5×10^{20} n/cm^2, E > 1 MeV (~0.7 dpa) for the lower fluence material. Estimation of fluence is beyond the scope of this project and will be reported separately in near future.

4.2 Mechanical properties

At typical LWR irradiation temperatures, ~300°C, mechanical properties of austenitic stainless steels change under irradiation. Yield strength and ultimate tensile strength increase, material ductility and strain hardening capability reduce and, usually at relative low fluences, fracture mechanism in tensile tests changes from ductile to "channel fracture" in which deformation localises to a very narrow zone where irradiation induced defects disappear as a result of plastic deformation [2, 3, 4]. This deformation localisation results in very small uniform elongations, in the range of < 1%. "Channel fracture", i.e., dislocation channeling, has been reported to occur typically at fluences above 1 dpa, for example, at 1.5 dpa in AISI 304 stainless steel tested and irradiated at 277°C [3].

Tensile tests after irradiation at higher irradiation temperatures often result in intergranular failure mode and even lower ductility because of helium embrittlement [2]. Helium, which is a transmutation product, migrates to the grain boundaries and forms bubbles.

Irradiation of austenitic stainless steels at lower temperatures, e.g., at 60°C, usually results in smaller changes in yield and tensile strengths than at higher temperatures. Strain hardening capability is also better than in austenitic stainless steels irradiated at higher temperatures [4].

The tensile test results in this study show that the material has remained very ductile even though the yield and tensile strengths have increased when compared to the minimum values given by the material supplier for similar unirradiated material. The room temperature elongation to fracture of the irradiated material is even larger than the minimum value in unirradiated condition. The uniform elongation decreases along with increasing fluence at every test temperature although it stays notably larger than usually in austenitic stainless steels irradiated to similar fluences.

The yield strengths vs. the square root of the fluence (both initial and new calculations) are presented in Fig. 17 along with the values of several other studies. The results of the other studies are for stainless steel grades without Ti-stabilisation irradiated and tested at around 300°C. As can be seen, the yield strength of the 08X18H10T steel is much lower than in the non-stabilised and

Nb-stabilised steels at the initially estimated fluences, but the newly calculated fluence values would place the results at the lower end of the scatter band.

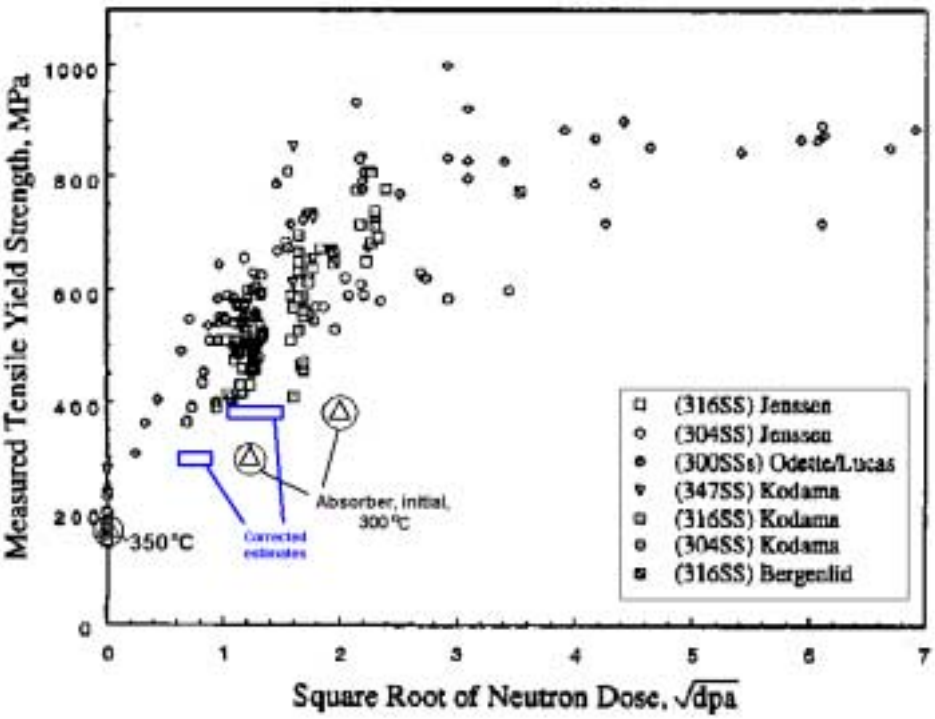

Figure 17. Comparison of measured yield strengths with other data [5]. Test and irradiation at ~300°C, but yield strength for unirradiated 08X18H10T at 350°C according to material supplier. Results are plotted with both the initially and newly estimated fluences.

The Vicker's microhardness measurement results also show that the hardness increases along with the increasing fluence, though the relative increase is not as large as the increase in the yield strength. The increase in the hardness of the absorber element material, even if the fluence is taken into account, seem to be lower than in the chemically comparable spacer grid sleeve material. The difference can, at least partially, be explained by a difference in the grain sizes, which are ASTM 4–5 in the absorber and ASTM 9 in the spacer grid material.

4.3 Microstructure

The overall outlook of the microstructure of the absorber material is typical to austenitic stainless steels with twins and δ-ferrite. The structure also contains Ti-carbides of various sizes.

4.3.1 Defects caused by irradiation

At low temperatures, 20–250°C, irradiation of 300 series austenitic stainless steels usually results in small (<4 nm) defect clusters, black dots, which are interstitial or vacancy clusters, and interstitial loops. Also 4–20 nm faulted interstitial Frank loops are common [5]. At higher temperatures, 250–300°C, the density of black dots begins to decrease rapidly and the size of Frank loops begins to increase [2]. At higher temperatures, above 300°C, irradiation produces large loops, dislocation networks and cavities, Fig. 18 [2, 5]. Pre-irradiation cold work has been observed to reduce loop density at least at irradiation temperatures under 250°C [2].

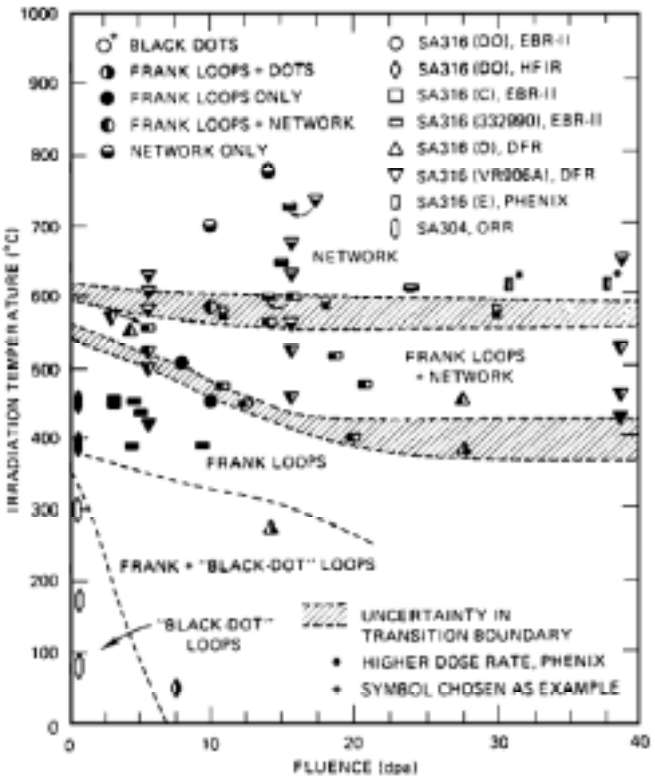

Figure 18. Typical defects produced by neutron irradiation at different temperatures [2].

4.3.2 Defect density and size

At temperatures around 300°C Frank loop density saturates usually at fluences below 1 dpa. Frank loop sizes increase rapidly along with increasing fluence until about 1 dpa after which they continue to grow slowly [5].

The measured loop densities and sizes both for this absorber element lower end material and the earlier studied spacer grid material are presented in Fig. 19 together with values for austenitic stainless steels in several other studies irradiated at around 300°C [5]. The dislocation loop densities in both higher and lower fluence material are smaller than densities observed in other 300 series austenitic stainless steels. The dislocation loop densities are also clearly lower

than in the spacer grid sleeve material which is also titanium stabilised 0X18H10T stainless steel.

Also the dislocation loop sizes were smaller than expected for both higher and lower fluence materials when compared to densities and sizes observed in other irradiated 300 series stainless steels and in the spacer grid sleeve made of the same steel. However, the updated fluence estimates bring the results much closer to the literature data.

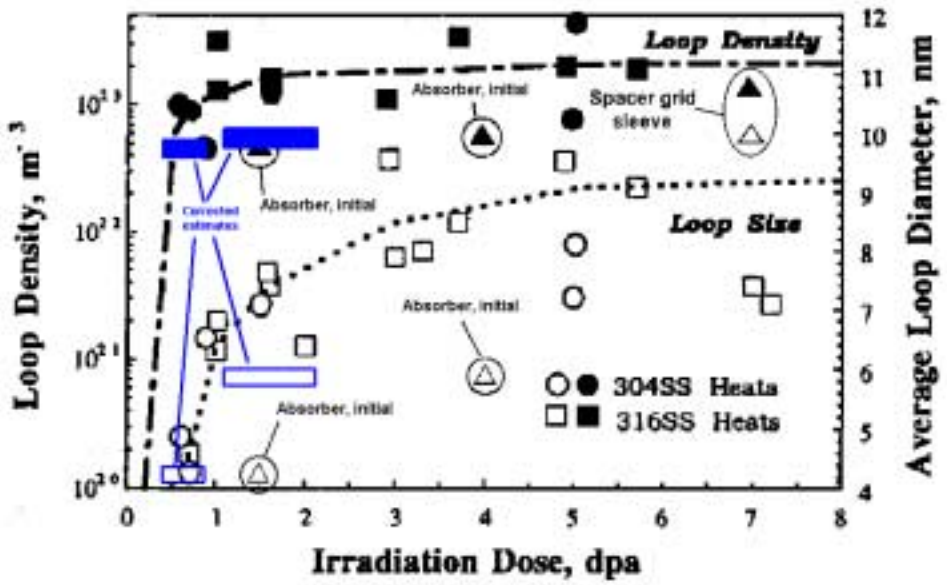

Figure 19. Measured loop densities and sizes for the absorber element bottom end and the spacer grid materials with data from several other studies [5].

4.3.3 Defects and hardening

The irradiation induced change in yield strength is usually attributed to the increased number of obstacles preventing dislocation movement. Typical obstacles are black dots, Frank loops, and precipitates. The change in the yield strength caused by each type of obstacle can be expressed as [6]

$$\Delta\sigma_{YS}=M\alpha\mu b(Nd)^{1/2}$$

where M is Taylor factor (=3.06), α is barrier strength of the obstacle (=0.5 for Frank loops and 0.146 for black dots), μ is shear modulus of the matrix (=$58x10^3$ MPa), b is Burger's vector of moving dislocation (b=a/2x[110] used here, lattice constant a=0.359 nm), N is number density of the obstacles and d is mean diameter of the obstacles.

If all observed defects are assumed to be Frank loops, increases of 310 MPa for 1.5 dpa and 406 MPa for 4 dpa in yield strength would be predicted. The measured increases were ~118 and 211 MPa, respectively, when 176 MPa is used for the unirradiated yield strength. At these fluences and at the irradiation temperature of 300^{o}C some of the defects are probably black dots, not Frank loops. The average barrier strength of the obstacles is lower than it would be for Frank loops alone.

4.3.4 Effect of titanium carbides

Loop density close to the Ti-carbides was clearly higher than elsewhere in the absorber element material. A difference in loop density may result of the stress-strain field caused by the precipitation or of an eventual gradient in alloying element concentration close to the carbides.

Another possible reason for the higher loop density and size close to the carbides could be the effect of the Ti-carbides on collision cascades and thus on defect development. The collision cascades are a result of elastic collisions of neutrons on atoms. Linear momentum and kinetic energy are preserved and the energy of the primary knock on atom (PKA) after neutron collision depends on the mass of the atom. The lighter the PKA is, the larger the kinetic energy of the PKA is after the collision with the neutron. Carbon and titanium atoms, which form the carbides, are lighter than iron which is the most common element in the matrix.

The possible existence of the alloying element concentration gradient close to the titanium carbides should be further studied using FEGSTEM. Comparison of the possible concentration gradients to the results of the model alloy studies presented in literature could prove fruitful in understanding the influence of the minor alloying elements on the properties of the absorber element bottom end material.

4.4 Irradiation induced segregation

Radiation in LWR conditions results in depletion of Cr and Fe and enrichment of Ni, Si and P in grain boundaries of 300 series austenitic stainless steels. Usually IASCC sensitivity is attributed to grain boundary segregation and irradiation hardening. It is also proposed [3] that IASCC susceptibility is linked to the tendency to dislocation channeling in the material, not to the irradiation hardening intrinsically. Irradiated stainless steels become IASCC susceptible when grain boundary Cr concentration drops by 1–2 wt% units [5]. Typically Cr-depletion is around 1–3 wt% units at 1 dpa and 5–8 wt% units at 5 dpa. Most analytical measurement data show exponential decrease in Cr content down to ~13 wt% with increasing fluence, Fig. 20. Consequently, grain boundary Cr segregation and prevention of it is of great interest. The effects of Ti, Nb and C on the Cr segregation have been studied, for example, by Dumbil et al. [7].

Energy dispersive x-ray analysis of this study showed that there was depletion of grain boundary Fe and Cr and enrichment of Ni, Si, P, Mo and Ti. On the other hand, segregation is not very significant. For example the depletion of Cr is less than one percent even in the higher fluence sample of the absorber element material whereas in the spacer grid sleeve it was 4.2% at fluence of 7 dpa.

As in previous comparisons, Figs 17 and 19, the reduced fluence estimates bring our results closer to literature data. For irradiation induced segregation this is demonstrated in Fig. 20.

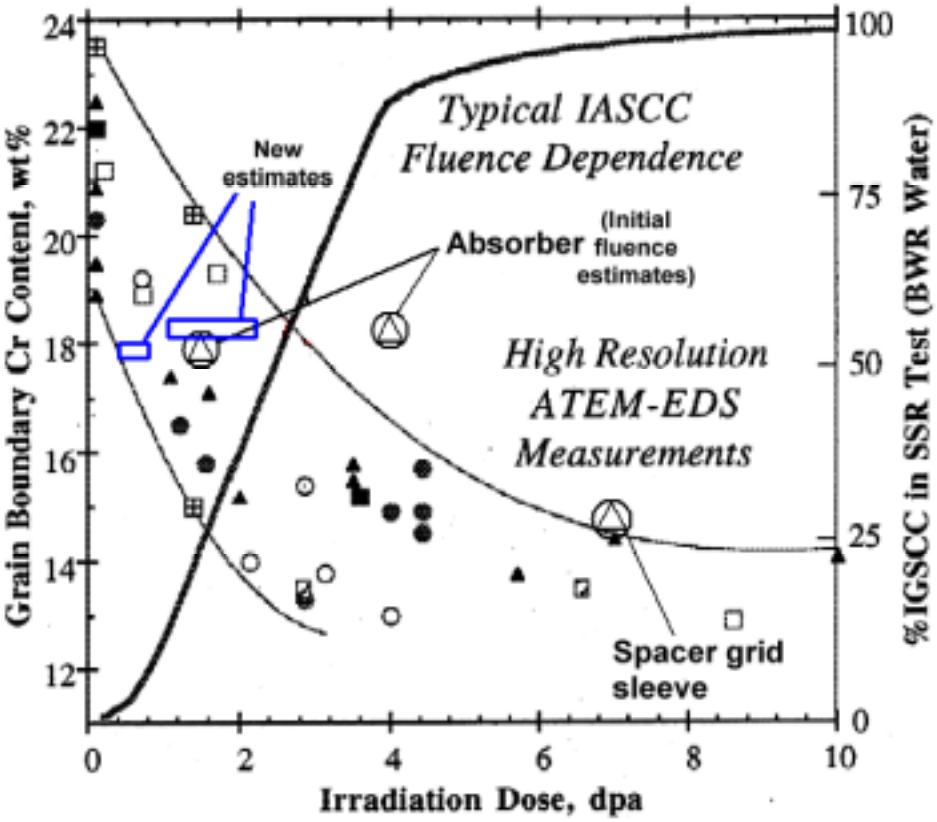

Figure 20. Comparison of measured grain boundary Cr contents and typical values in 300 series stainless steels irradiated at around 300°C [5].

4.5 Effects of minor alloying elements

The absorber element bottom end material may react to neutron irradiation in a different manner than stainless steels without Ti-stabilisation. FEGSTEM results of the spacer grid sleeve do not support this kind of assumption, but minor alloying elements are known to change the response of material properties to irradiation. This response also depends on the form in which the alloying elements are in the metal. This further depends on the manufacturing process and thermal history. The manufacturing processes and thermal treatments of the absorber element bottom end material and the spacer grid sleeve are not clearly known.

Studies on model alloys and modified austenitic stainless steels have shown that minor alloying elements like Ti, C, Nb, Si etc. have an influence on the micro-structural development and mechanical properties during irradiation. It has been reported [2] that

- strain hardening capability is preserved in Ti modified AISI 316 at all fluences when irradiated and tested at 390^{o}C,
- Nb and Ti enhance IASCC resistance, and
- C, Ti, and Si reduce tendency to swelling.

On the other hand, it has been also reported that an alloy of type Fe-0.06C-0.5Si-1.8Mn-14Cr-16Ni-2Mo-0.24Ti irradiated at 200^{o}C to 10 dpa show no strain hardening capability in tensile tests at the irradiation temperature [8].

T. Tsukada et al. [9] studied the effects of Si, P, S, C and Ti on the IASCC susceptibility of high purity type 304 alloy (Fe-18Cr-12Ni-1.4Mn). They performed slow strain rate tensile tests in oxygenated (32 ppb) water at 300^{o}C. The materials were irradiated to 6.7×10^{20} n/cm^{2}, E > 1 MeV (~1 dpa) at 240^{o}C. Elongation to fracture increased in the following order:

- HP304 + 0.03% S
- HP304 + 0.1% C
- HP304 + 0.1% C + 0.3% Ti
- HP304
- HP304 + all elements (A_g~12%)
- HP304 + 0.017% P
- HP304 + 0.7% Si (A_g~18%).

Uniform elongation was ~0% in alloys with no Si. In HP304 + Si the yield strength was ~250 MPa while in others it was 400–700 MPa. In HP304 + all it was ~600 MPa. Considerable amount of IGSCC was observed only on the fracture surfaces of the specimens with no C as an alloying element. The results of Tsukada et al. indicate that the irradiated HP304 doped with Si and doped with all elements would be ductile also in tensile tests. The composition of the

HP304 + all is close to the composition of the absorber element bottom end material. The Si content of the spacer grid sleeve was also similar [1].

Y. Miwa et al. [10] studied microstructures of high purity model alloy of type 316 doped with C, Ti, P, Si and S alone or together, and high purity 304. Materials were irradiated to 1 dpa at 513 K (240^{o}C). They observed that in HP304 the loop density was 6.6×10^{22} m^{-3} with average diameter of 11.2 nm and in HP316 1.7×10^{22} m^{-3} and 9.2 nm, respectively. Carbon doping into HP316 increased the loop density almost one order of magnitude to 13×10^{22} m^{-3} and decreased the average loop diameter to 7.9 nm. Titanium doping in addition to carbon doping decreased the loop density only slightly and increased the average loop size. They observed also that silicon doping in every case when carbon and other doping elements were present decreased the loop density drastically and decreased also the average loop diameter. In HP316 doped with 0.063% C, 0.76% Si, 1.42% Mn, 0.018% P, 0.037% S and 0.30% Ti the Frank loop density was 5.7×10^{22} m^{-3} and the average loop diameter was 5.9 nm. They considered that in Ti-doped alloys the titanium was dissolved (no stabilisation treatment was performed before the irradiation) and that the dissolved titanium does not affect the influence of carbon on the Frank loop development.

According to reference [2], Ti does not have influence on total dislocation density. On the other hand, Si and Ti is reported to enhance the formation of Frank loops [11].

H. Watanabe et al. [12] conducted irradiation experiments at 427–600^{o}C on model alloys Fe-16Cr-17Ni, with and without P (up to 0.1%) and Ti (up to 0.18%), and Fe-15.27Cr-15.80Ni-2.66Mo-0.24Ti. The irradiation fluences were up to 60 dpa. They observed that void swelling and dislocation density decreased with increasing P + Ti content. P and Ti together suppressed swelling more effectively than Ti alone. Swelling resistance of Ni rich alloys is attributed usually to fine-grained coherent precipitates homogeneously distributed in the matrix [13]. According to reference [13], carbide forming elements like Ti and Nb form fine grained carbonitrides, which are coherent with the matrix when their diameters are <5 nm at fluences up to 10 dpa. The authors state that the second phase precipitates intensify the recombination of vacancies and interstitial atoms created by the irradiation [13].

C, Nb, and especially Ti have been reported to decrease irradiation induced grain boundary segregation by forming trapping sites for point defect flux to the grain boundaries [7]. Dumbil and Hanks [7] concluded that C, Ti, and Nb were in solution form in the matrix in their study. They observed that the effectiveness, as ΔCr depletion / at% in solution, of the alloying elements were 5.77, 7.11, and 10.48 for C, Nb, and Ti, respectively. The studied samples were irradiated at 450^{o}C to the fluence of 1.11×10^{20} n/cm^{2}, E >0.1 MeV.

5. Conclusions

Properties of the studied titanium stabilised 08X18H10T stainless steel have changed as a result of neutron irradiation. However, initial results indicated that either the material response to neutron irradiation differs significantly from the response of other austenitic stainless steels, the neutron fluences were overestimated, or both.

The loop densities, loop sizes, yield strengths, ultimate tensile strengths and hardnesses were lower than expected and uniform elongations and elongations to fracture were higher than expected for the irradiated absorber element material when initial fluence estimations were used.

The alloying elements in 08X18H10T steel and the manufacturing history might have explained at least part of the observations. However, results presented in literature do not unambiguously show that the alloying elements, e.g. Ti, would decrease the irradiation response of the mechanical properties and microstructures as much as the initial results of this study indicated.

New calculations indicate that real fluences are lower than initially estimated. Based on the new fluence values, the results correspond fairly well to literature.

Possible existence of the alloying element concentration gradients close to the titanium carbides should be verified and the results compared to results of the model alloy studies presented in literature to enhance understanding on influence of minor alloying elements on the properties of the absorber element bottom end material.

None of the properties characteristic to IASCC susceptible materials were observed in the absorber element bottom end material. Such indicators would be Cr depletion by more than 1 wt% at the grain boundaries, high irradiation hardening or dislocation channeling as a deformation mechanism.

Postponing of IASCC testing in autoclaves was well justified and continuation according to original test matrix is not recommended. The plans should be reconsidered as soon as a final report on fluence calculations is available.

Acknowledgements

This presentation is prepared within the project Structural operability and plant life management (RKK), which is coordinated by Teollisuuden Voima Oy. The work has been funded by the National Technology Agency (Tekes), Teollisuuden Voima Oy (TVO), Fortum Power and Heat Oy, Fortum Nuclear Services Ltd., FEMdata Oy, Neste Engineering Oy, Fortum Oil and Gas Ltd. and VTT. Their funding is gratefully acknowledged.

References

1. Ehrnstén, U., Nenonen, P., Aaltonen, P., Teräsvirta, R. and Hietanen, O. Intergranular Cracking of an Irradiated Ti-stabilized Austenitic Stainless Steel Spacer Grid Sleeve from a VVER-440 reactor. Presented at 9th Int. Conf. Environm. Degradation of Materials in Nuclear Power Systems – Water Reactors. Newport Beach, CA, USA, Aug. 1–5, 1999.

2. Effect of Irradiation on Water Reactors Internals. Report available at http://ie.jrc.cec.eu.int/publ/EUR17694EN.pdf (13.3.2002).

3. Bailat, C., Almazouzi, A., Baluc, N., Schäublin, R., Gröschel, F. and Victoria, M. The effects of irradiation and testing temperature on tensile behaviour of stainless steels. Journal of Nuclear Materials 283–287 (2000), pp. 446–450.

4. Hashimoto, N., Zinkle, S. J., Rowcliffe, A. F., Robertson, J. P. and Jitsukawa, S. Deformation mechanisms in 316 stainless steel irradiated at 60oC and 330oC. Journal of Nuclear Materials 283–287 (1993), pp. 528–534.

5. Bruemmer, S. M., Simonen, E. P., Scott, P. M., Andresen, P. L., Was, G. L. and Nelson, J. L. Radiation-induced material changes and susceptibility to intergranular failure of light-water-reactor core internals. Journal of Nuclear Materials 274 (1999), pp. 299–314.

6. Hashimoto, N., Wakai, E. and Robertson, J. P. Relationship between hardening and damage structure in austenitic stainless steel 316LN irradiated at low temperature in the HFIR. Journal of Nuclear Materials 273 (1999), pp. 95–101.

7. Dumbil, S. and Hanks, W. Strategies for the moderation of chromium depletion at grain boundaries in irradiated steels. 6th International Symposium on Environmental Degradation of Materials in Nuclear Power Systems – Water Reactors. The Minerals, Metals & Materials Society, 1993. Pp. 521–528.

8. Ioka, I., Naito, A., Shiba, K., Robertson, J. P., Jitsukawa, S. and Hishinuma, A. Effects of annealing on the tensile properties if irradiated austenitic stainless steel. Journal of Nuclear Materials 258–263 (1998), pp. 1664–1668.

9. Tsukada, T., Miwa, Y. and Nakajima, H. Stress corrosion cracking of neutron irradiated type 304 stainless steel. 5th International Symposium on Environmental Degradation of Materials in Nuclear Power Systems – Water Reactors. Pp. 1009–1018.

10. Miwa, Y., Tsukada, T., Tsuji, H. and Nakajima, H. Microstructures of type 316 model alloys neutron-irradiated at 513 K to 1 dpa. Journal of Nuclear Materials 271&272 (1999), pp. 316–320.

11. Maziasz, P. J. Overview of microstructural evolution in annealed austenitic steels, Journal of Nuclear Materials 205 (1993), pp. 118–145.

12. Watanabe, H., Muroga, T. and Yoshida, N. The temperature dependent role of phosphorus and titanium in microstructural evolution of Fe-Cr-Ni alloys irradiated in FFTF. Journal of Nuclear Materials 228 (1996), pp. 261–274.

13. Turkin, A. A. and Bakai, A. S. Recombination mechanism of point defect loss to coherent precipitates in alloys under irradiation. Journal of Nuclear Materials 270 (1999), pp. 349–356.

Re-embrittlement of annealed pressure vessel, IAI_1-material condition of a Loviisa irradiated weld

Matti Valo and Tapio Planman
VTT Industrial Systems
Espoo, Finland

Abstract

The re-irradiated (IAI_1) material condition data of a VVER-440 weld, which is part of the contribution of Fortum Nuclear Services Ltd. to the IAEA research programme, are given in summary. The data were created with the lower half of the Loviisa NPP re-irradiation chain 12K3 using specimen reconstitution. The second re-irradiation fluence will be created with the upper half of the same chain later on. The tests include tensile tests, ISO Charpy-V impact tests, Charpy-V impact tests of 5 mm × 5 mm and 3 mm × 4 mm cross-sectional specimens and fracture toughness tests of 10 mm × 10 mm and 5 mm × 5 mm cross-sectional specimens. The baseline, I and IA-condition data have been reported earlier. The joint analyses of the test results including earlier Loviisa data as well as a short comparison to an irradiation in Halden are given.

1. Introduction

The Fortum contribution to the IAEA co-ordinated round robin exercise ("Round robin exercise on WWER-440 RPV weld metal irradiation embrittlement, annealing and re-embrittlement") was started in 1997 by installing three irradiation chains into the surveillance positions of the Loviisa reactor. The Loviisa reactors are operated with reduced cores and hence the chains were irradiated until summer 2000 when the chains for the I- and IA-material conditions (irradiated and irradiated + annealed) were removed from the reactor. At the same time the remaining chain 12K3 was annealed at the plant and re-installed into the reactor.

The specimens were irradiated in the standard surveillance position of the Loviisa-2 reactor. The I- and IA-material conditions were created with two irradiation chains (12K1 and 12K2), both including 12 irradiation capsules. The chains were irradiated during years 1997–2000 (18th–20th reactor cycles). The IAI- material condition was created with the six lowest capsules cut away from chain 12K3. The re-irradiation was performed during 2000–2001 (21st reactor cycle). Only the average neutron fluence values of the whole chains (Table 1) were used in the analyses. The single capsule average fluence values deviated from the chain average values by +5% to -14% for chains 12K1 and 12K2 and by ±1% for chain 12K3. The neutron fluence values are based on PREVIEW calculations. The fluence values are given in units [10^{19} n/cm^2, E > 1 MeV] if not otherwise indicated.

Table 1. The irradiation parameters for the I_1, I_1A and I_1AI_2 -material conditions.

Cycle	T_{irr} °C	Neutron fluence [10^{19} n/cm^2]				Fluence rate [10^{12} n/cm^{2}s]	
		E > 1 MeV	E > 0.5MeV	dpa	E < 0.1 eV	E > 1 MeV	E > 0.5 MeV
I_1	265	2.6	5.7	0.049	4.1	0.3	0.6
I_2	265	1.0	2.0	0.017	1.5	0.3	0.6

Two separate re-irradiation fluences were to be realised with the single re-irradiation chain. Hence, during the summer outage 2001 the chain was cut into two halves and the lower half was removed from the reactor. Irradiation of the IAI_2-condition material continued until summer 2002. The IAI_1-condition material characterisation was made using specimen reconstitution. In the report the IAI_1-condition data and the results from the joint analysis of the new and old data are given in summary.

The weld material used in the programme was acquired directly from the CRISM "Prometey" by Fortum Nuclear Services Ltd. The specimens were removed and prepared and the tests performed at VTT.

2. Material and experimental data

2.1 Material, specimens and tests

The material tested for the programme is a VVER-440 type reactor pressure vessel weld denoted by "weld 502, block 6". The chemistry profile and the mechanical properties of the block number 6 of weld 502 have been reported in ref. [1].

The tensile tests were conducted with small proportional (round ϕ 3 mm or flat 1*2 mm^2 cross section) specimens. Normal and sub-size Charpy-V (CH-V) specimens were used for dynamic testing (Figures 1–2). Fracture toughness was measured using Charpy size (10 mm × 10 mm) or smaller (3 mm × 4 mm or 5 mm × 5 mm) 3-point bend specimens. The small fracture mechanics specimens were prepared mainly like the Charpy-V specimens (Figures 1–2) except that the 1 mm deep crack initiation notches were prepared with the ϕ 0.25 mm electric discharge wire and the support span used in the tests was 4 × specimen width. No clip gauge seats were made to these specimens. All fracture toughness specimens were pre-fatigued by using stress intensity factor $K_{max} \approx 10$ MPa√m with load ratio R ($R = K_{min}/K_{max}$) between $0 < R < 0.1$. The specimens were pre-fatigued before side-grooving. The side grooves of 2 × 10% were used for all fracture toughness specimens.

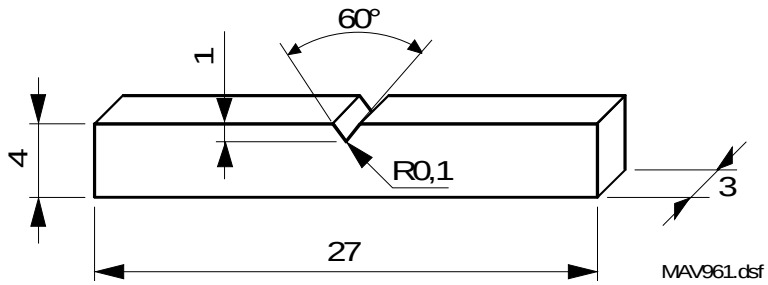

Figure 1. The 3 mm ×4 mm CH-V specimen (KLST). Span S = 22 mm.

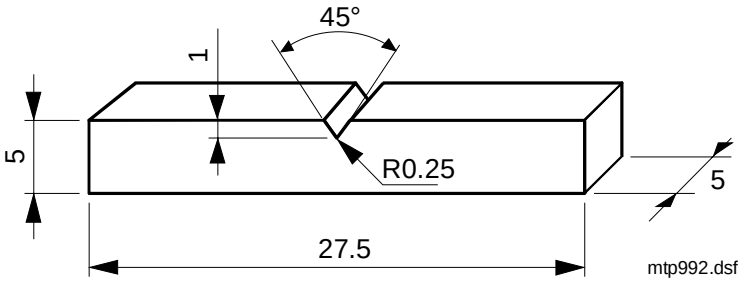

Figure 2. The 5 mm ×5 mm CH-V specimen. Span S = 20 mm.

The number of tests performed for different material conditions are given in Table 2.

Table 2. Tests performed for the IAEA programme. The additional tests given in parenthesis will be performed later.

Specimen		Number of tests				
Type	Size	R	I	IA	IAI_1	IAI_2
CH-V	10×10	15	15	12	15	(15)
CH-V	5×5	15	15	15	15	(15)
FT	10×10	15	15	15	15	(15)
T	ϕ 3 ×15	6	6	6	6	(6)
CH-V*	3×4	15	15	15	15	(15)
FT *	5×5	15	12	12	12	(12)
FT*	3×4	15	(15)	(15)	(15)	(15)

* Tests additional to the IAEA programme.

The orientation of all irradiated specimens, i.e. the 10×10, 5×5 and 3×4 CH-V specimens and the 10×10 and 5×5 fracture toughness specimens, is T-L (Figure 3). The irradiated 3×4 specimens have not been tested yet. The orientation of the unirradiated specimens was T-L, except the 5×5 and 3×4 fracture toughness specimens which had orientation T-S.

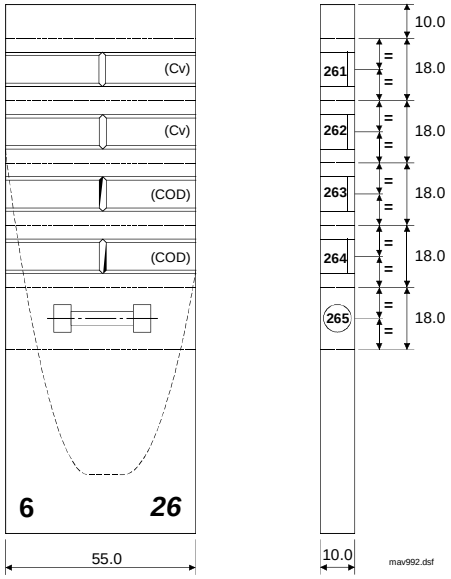

Figure 3. The T-L specimen orientation in the weld. The CH-V specimens of all sizes, tensile specimens and CH size fracture toughness specimens had this orientation.

2.2 Test methods

2.2.1 Tensile and Charpy tests

The tensile tests were performed with a servohydraulic testing machine. Elongation was measured between the upper and lower specimen heads.

The ISO CH-V tests (10×10 specimen) were performed with a 300 J hammer and the 3×4 and 5×5 CH-V specimen tests with a 51 J hammer. Both hammers had a DIN type impact tup and all tests were performed as instrumented. The impact velocity of the 300 J hammer was 5.4 m/s and that of the smaller hammer 3.85 m/s.

2.2.2 Fracture toughness tests

The fracture toughness tests were performed and the data analysed following ASTM E 1152-87 (Standard Test Method for Determining J-R Curves) as far as possible.

The unloading compliance technique was used in the tests of the 10×10 specimens. In the small specimen (5×5 and 3×4) tests only the load and load-point deflection were measured. If small crack growth (Δa) was noticed in the small specimen before cleavage fracture initiation, a crack growth correction according to (1) was made to the critical J-value (J^C).

$$J_{corrected} = J^C \times (1 - \frac{0.5 \times \Delta a}{W - a_0}) \quad (1)$$

where W is specimen width and a_0 the initial crack length.

The data were analysed basically following ASTM E 1921-97 (Standard Test Method for Determination of Reference Temperature, T_0, for Ferritic Steels in the Transition Range).

The small specimen K_{Jc} values were size-corrected to B = 25 mm specimen (thickness) values by the relationship

$$K_{B2} = K_{min} + (K_{B1} - K_{min}) * \left(\frac{B_1}{B_2} \right)^{0.25} \quad (2)$$

where B_1 and B_2 are the specimen thickness values and K_{B1} and K_{B2} the corresponding K_{Jc} values. K_{min} = 20 MPa√m was used. The maximum likelihood estimation formula and the standard specimen size criterion were used to determine the values of T_0.

3. Results

3.1 Tensile tests

The measured tensile test data are given in Table 3. Only room temperature tensile tests were performed for the IAI_1-material condition.

Table 3. Tensile test results (0.2% proof and tensile strength, uniform and total elongation). The IAI-data have been measured with flat and the other with round specimens.

Specimen	State	T	$R_{p0.2\%}$	R_m	A_g	A_5
		°C	MPa	MPa	%	%
average	*ref.*	*23*	*470*	*604*	*8*	*16*
average	*I*	*23*	*625*	*720*	*6*	*15*
average	*IA*	*23*	*499*	*612*	*7*	*17*
254	IAI	23	546	643	9	18
254	IAI	23	516	626	10	18
254	IAI	23	540	642	9	17
254	IAI	23	525	625	10	20
average	*IAI*	*23*	*532*	*634*	*10*	*18*

3.2 ISO Charpy-V tests

The absorbed energy vs. temperature transition curve for the IAI-material condition is shown in Figure 4. The transition curve based on the 4 kN crack arrest load is given in Figure 5.

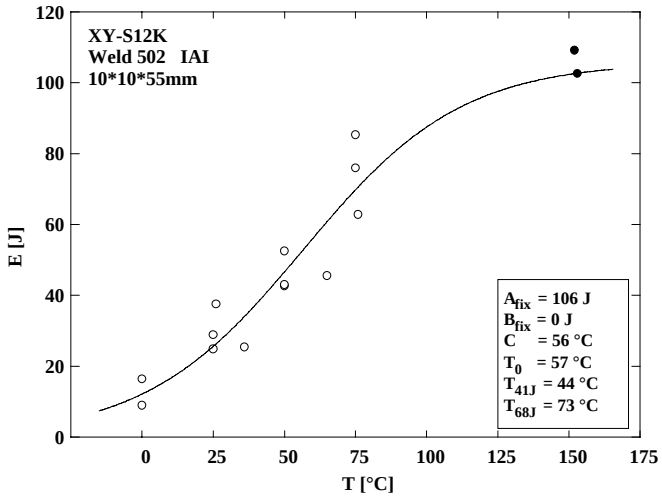

Figure 4. Impact energy transition curve, ISO CH-V test, IAI_I-material condition.

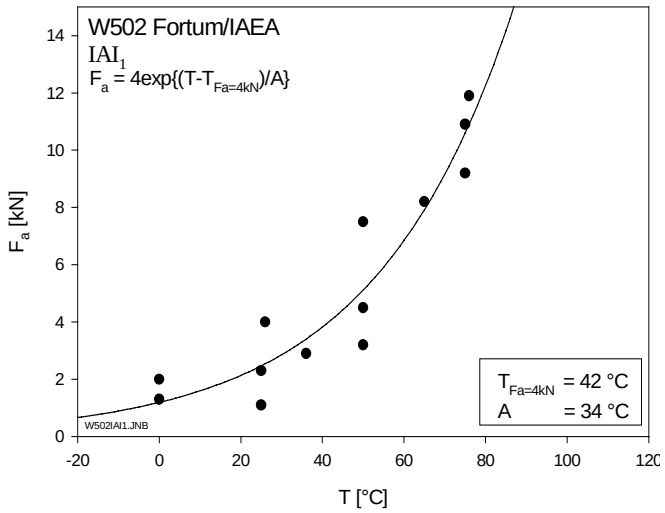

Figure 5. Crack arrest load based transition curve, ISO CH-V test, IAI_I-material condition.

3.3 Charpy-V tests with 5 mm x 5 mm specimens

The absorbed energy vs. temperature transition curve for the IAI-material condition is given in Figure 6.

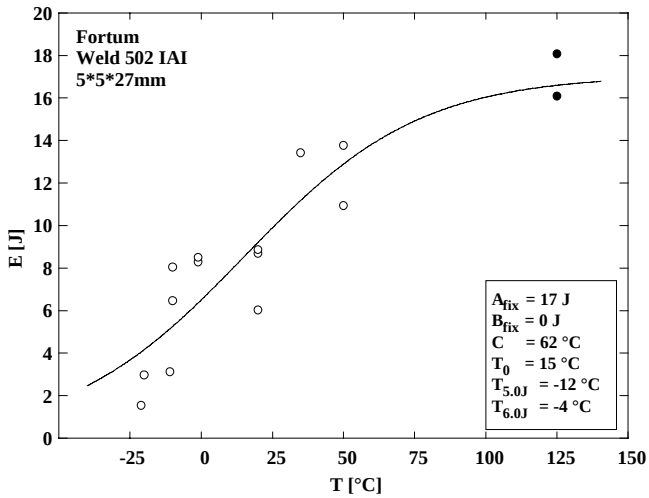

Figure 6. Impact energy transition curve, 5×5 specimen CH-V test, IAI_1-material condition.

3.4 Charpy-V tests with 3 mm x 4 mm specimens

The absorbed energy vs. temperature transition curve for the IAI-material condition is given in Figure 7.

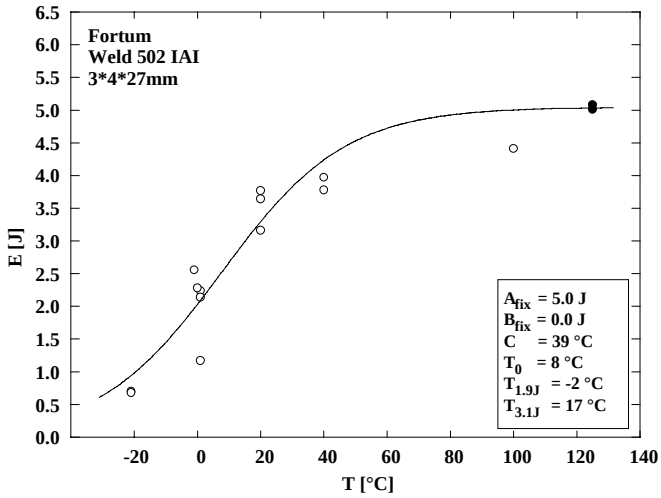

Figure 7. Impact energy transition curve, 3×4 specimen CH-V test, IAI_I-material condition.

3.5 Fracture toughness tests

The fracture toughness vs. temperature curves measured with 10×10 and 5×5 mm specimens are given in Figure 8.

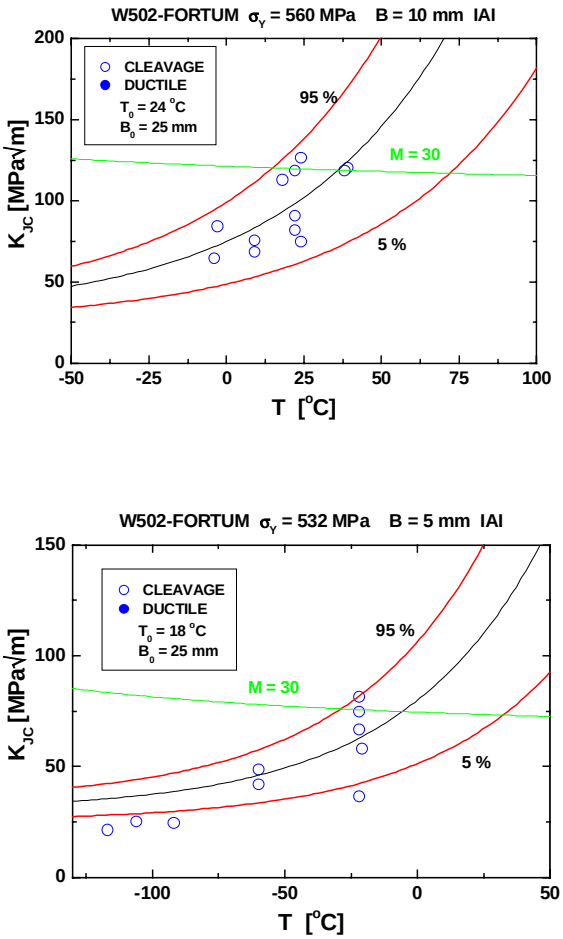

Figure 8. Fracture toughness data for the IAI$_1$-material condition measured with B = 10 mm specimens (left) and B = 5 mm specimens (right). The measured data, fracture probability curves and upper validity limits are shown.

4. Discussion

4.1 Background

4.1.1 The Russian norm

The Russian norm, which is based on ISO CH-V data, describes the upper limit behaviour of irradiation embrittlement by

$$\Delta T = A_f * \left(\frac{\Phi t}{10^{18}} \right)^{1/3}, \text{ where} \quad (3)$$

ΔT is the transition temperature shift, Φt is the neutron fluence and A_f is the chemistry factor (^{o}C). The Russian norm gives an estimation formula (4) for A_f.

$$A_{f,\ norm,\ E>0.5MeV} = 800 * (P+0.07*Cu) \quad (4)$$

where P and Cu are the phosphorus and copper contents (wt-%).

The norm procedure is in reality more complicated as it includes the acceptance criteria and the conditional choices of impact energy or lateral expansion transition temperature criteria in the determination of T_k-values. In the report, fixed transition temperature criteria are used and the behaviour is compared to predictions (3) and (4).

4.1.2 The re-irradiation models

The re-irradiation behaviour is conventionally described by phenomenological, descriptive models which are derived from the initial irradiation embrittlement behaviour. The models are described by formulas (5)–(7) and they are shown qualitatively in Figure 9.

$$\Delta T_2^{con} = A * (\Phi_2)^n \quad \text{(conservative shift)} \quad (5)$$

$$\Delta T_2^{lat} = A * \left[\left(\frac{\Delta T_{Res}}{A} \right)^{\frac{1}{n}} + \Phi_2 \right]^n - \Delta T_{Res} \quad \text{(lateral shift)} \tag{6}$$

$$\Delta T_2^{ver} = A * \left(\Phi_a + \Phi_2 \right)^n - A * \Phi_a^n \quad \text{(vertical shift)} \tag{7}$$

where

ΔT_2	transition temperature shift during re-irradiation
Φ_2	neutron fluence in re-irradiation
Φ_a	neutron fluence during the initial irradiation
ΔT_{res}	residual shift after annealing (embrittlement shift not recovered in annealing)
A,n	parameters of the initial embrittlement function.

The upper limit of the residual shift is often assumed to be $\Delta T_{res,\,max} = 20\ ^{o}C$.

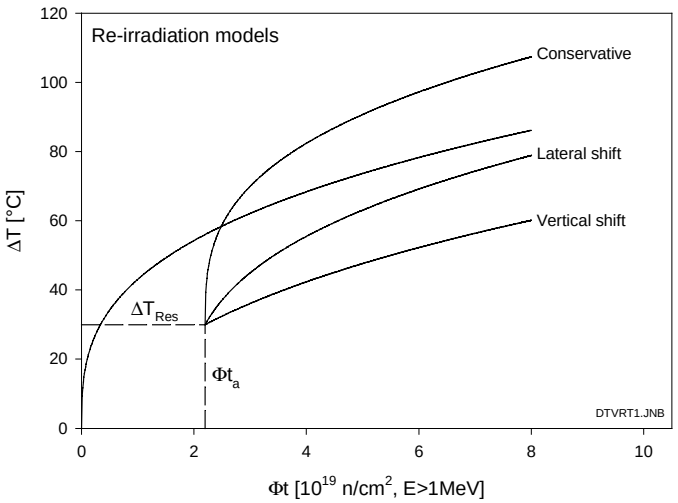

Figure 9. The re-irradiation models.

4.1.3 The neutron fluence units

In the Russian norm the neutron fluence unit [E > 0.5 MeV] is used. The numerical value of the chemistry factor A_f depends on the neutron fluence unit as follows:

$$A_{f,E>1MeV} = \left(\frac{\Phi t_{E>0.5MeV}}{\Phi t_{E>1MeV}} \right)^n * A_{f,E>0.5MeV} \quad (8)$$

where n is the exponent of the embrittlement function.

In the Loviisa surveillance position the ratio

$$\frac{\Phi t_{E>0.5MeV}}{\Phi t_{E>1MeV}} \approx 2.11 \quad (9)$$

If n=1/3 is assumed, the relation between the A_f-coefficients will be

$$A_{f,E>1MeV} = 1.28 * A_{f,E>0.5MeV} \quad (10)$$

The values of the A_f -coefficients, which are given later in the report, are based on the unit [E > 1 MeV], if not otherwise indicated.

4.2 Summary of test data

The transition temperatures and the transition temperature shifts are given in reports [1] and [2]. The values based on the T_0 temperature are summarised together with the new data in Table 4.

Table 4. Transition temperatures (T_0) and their shifts for the reference, I, IA and IAI -material conditions.

Condition/	I_1	I_2	Master Curve T_0 and ΔT_0 / [^oC]		
Shift			B = 10 mm	B = 5 mm	B = 3 mm
ref.	-	-	-42	-49	-43
I	2.6	-	+54	+48	-
IA	2.6	-	-30	-47	-
IAI	2.6	1.0	+24	+18	
ΔT_{irr}	2.6	-	+96	+97	-
ΔT_{anneal}	2.6	-	-84	-95	-
ΔT_{res}	2.6	-	+12	+2	-
$\Delta T_{re\text{-}irr}$	2.6	1.0	+54	+65	-
$\Delta T_{IAI\text{-}ref}$	2.6	1.0	66	67	-
ΔT_{irr} (I_1+I_2) *	2.6	1.0	107	108	-
$\Delta T_{residual}$%	2.6	-	*13%*	*3%*	-
	2.6	-	*8%*		-
ΔT_{IAI}%	2.6	1.0	*62%*	*62%*	-
	2.6	1.0	*62%*		-

*) The irradiation shift calculated for fluence $I_1+I_2 = 3.6$.
$\Delta T_{residual}$ % $= 100*(\Delta T_{residual} / \Delta T_{irradiation})$
ΔT_{IAI} % $= 100*(T_{re\text{-}irradiated}-T_{unirradiated}) / \Delta T_{irradiation}(I_1+I_2)$.

4.3 The measured versus norm based embrittlement

The average composition of weld 502 according to VTT measurements [2] is: P = 0.027% and Cu = 0.124%. According to (4) this gives for $A_{f,\ E>0.5MeV}$ = 28.5^{o}C. The value for $A_{f\ E>1MeV}$ = 36.5^{o}C according to formula (10).

The irradiation embrittlement shift calculated from the norm prediction will be

$$\Delta T(\Phi t = 26) = A_f * \left(\frac{\Phi t}{10^{18}}\right)^{n=1/3} = 108^o C \qquad (11)$$

The measured chemistry factors are given and compared to the norm based factors in Table 5. In one case the norm based chemistry factor is slightly exceeded.

Table 5. The norm-based versus measured irradiation embrittlement chemistry factors (^oC).

Criterion	$A_{f,\ E>1MeV}$		$A_{f,\ E>0.5MeV}$		$A_{f,meas}/A_{f,norm}$
	measured	norm	measured	norm	
ISO CH-V					
T_{42J}	27.6	36.5	21.6	28.5	76%
T_{68J}	38.5	36.5	30.1	28.5	106%
$T_{0.89mm}$	32.3	36.5	25.2	28.5	88%
$T_{50\%FA}$	24.6	36.5	19.2	28.5	67%
T_{Fa4kN}	15.1	36.5	11.8	28.5	41%
5x5 CH-V					
T_{6J}	21.2	36.5	16.6	28.5	58%
$T_{0.35mm}$	21.2	36.5	16.6	28.5	58%
3x4 CH-V					
$T_{3.1J}$	20.9	36.5	16.3	28.5	57%
$T_{0.3mm}$	22.6	36.5	17.7	28.5	62%
FT					
T_0 - B10	32.3	36.5	25.2	28.5	88%
T_0 - B5	32.7	36.5	25.5	28.5	89%

4.4 The re-irradiation behaviour

The re-irradiation shifts based on the lateral shift model were compared to the measured re-irradiation shift values. In the evaluation it was assumed that the original embrittlement is described by the fluence exponent n = 1/3. The transition temperatures measured and calculated for the irradiated, annealed and re-irradiated materials are shown in Figures 10–17. With the 3×4 CH-V specimens the measured shifts slightly exceed the lateral shift prediction but for

other toughness parameters the lateral shift model is conservative. The crack arrest behaviour T_{Fa4kN} is not in line with the descriptions of other parameters.

In the figures the measured transition temperatures, the A_f-coefficients, which describe the behaviour during the original irradiation, and the lateral shift model description for re-irradiation based on the measured original irradiation are shown.

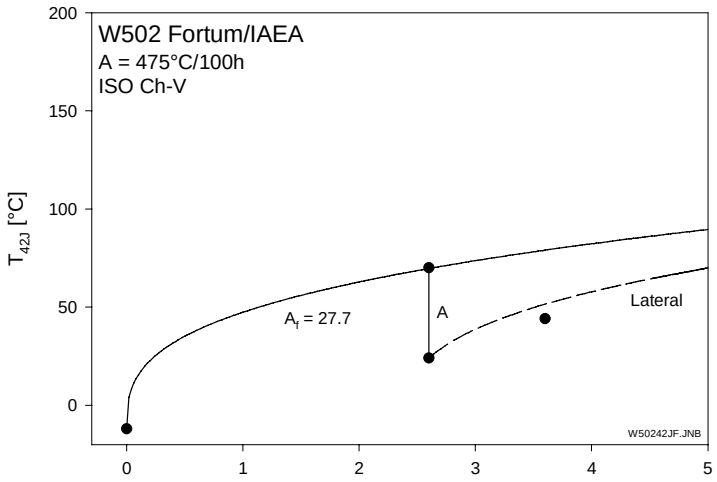

a)

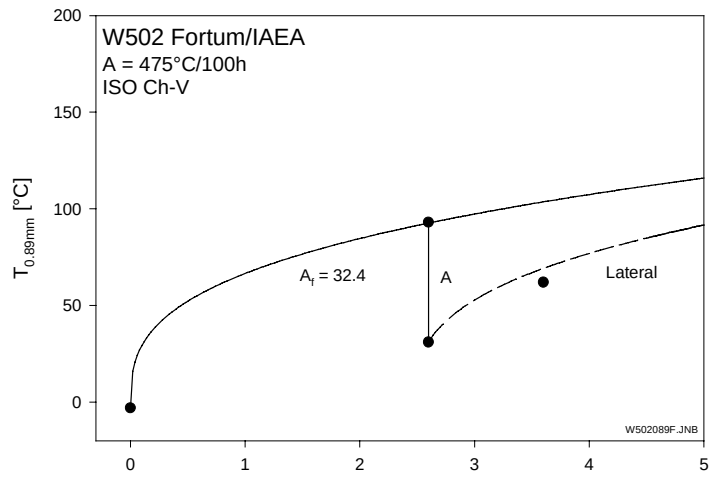

b)

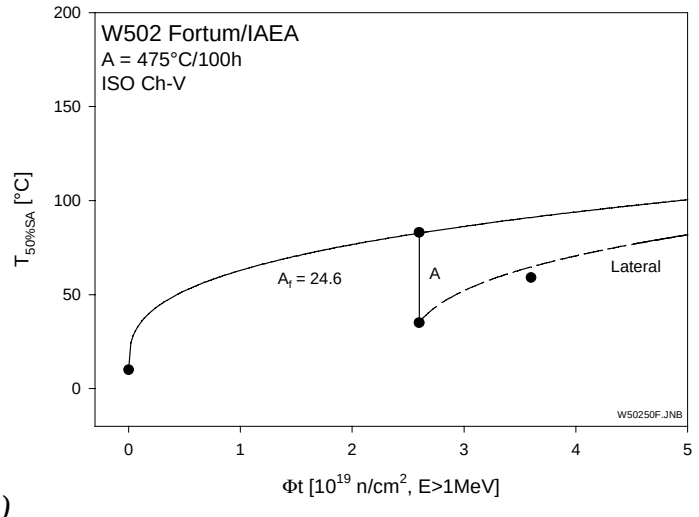

c)

Figure 10. The I-, IA- and IAI-behaviour of weld 502 irradiated in the Loviisa reactor. Lateral shift model is shown in the figures, ISO CH-V specimens, T_{42J}, $T_{0.89mm}$ and $T_{50\%FA}$ transition temperatures (Figures a–c).

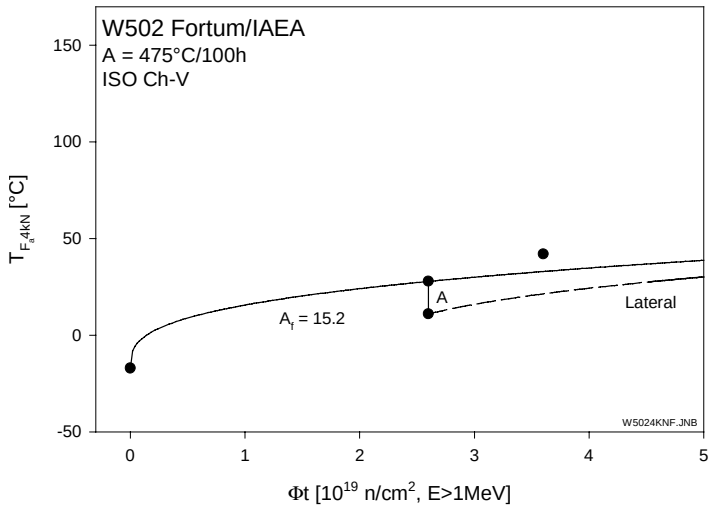

Figure 11. The I-,IA- and IAI-behaviour of weld 502 irradiated in the Loviisa reactor. Lateral shift model is shown in the figure, ISO CH-V specimens, T_{Fa4kN} transition temperature.

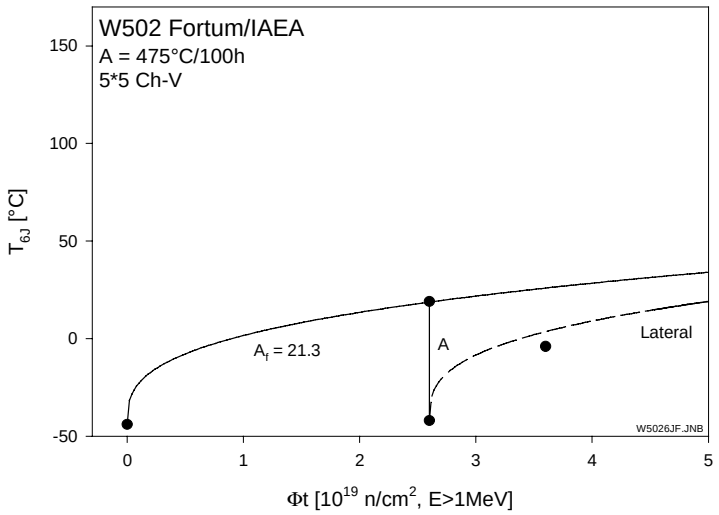

Figure 12. The I-, IA- and IAI-behaviour of weld 502 irradiated in the Loviisa reactor. Lateral shift model is shown in the figure, 5x5 CH-V specimens, T_{6J} transition temperature.

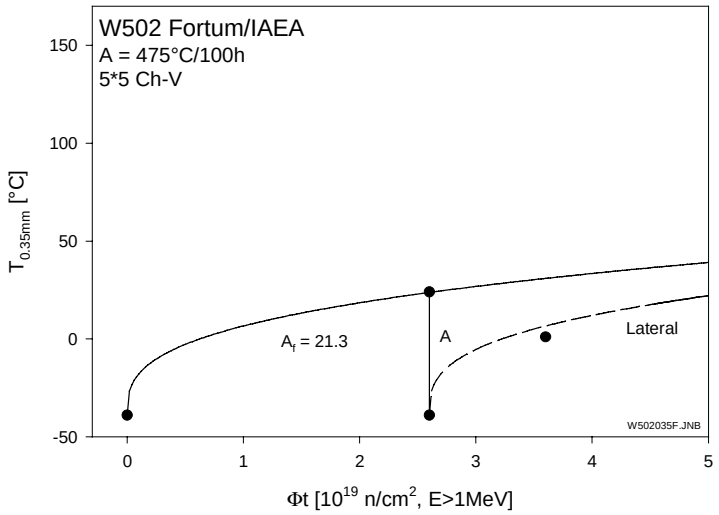

Figure 13. The I-, IA- and IAI-behaviour of weld 502 irradiated in the Loviisa reactor. Lateral shift model is shown in the figure, 5x5 CH-V specimens, $T_{0.35mm}$ transition temperature.

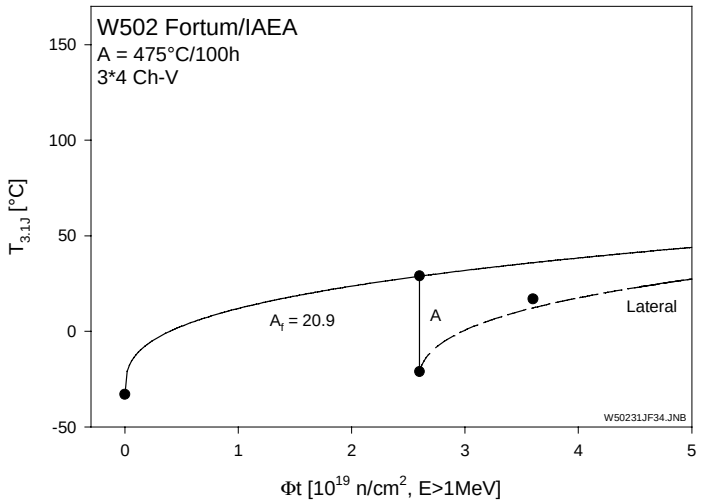

Figure 14. The I-, IA- and IAI-behaviour of weld 502 irradiated in the Loviisa reactor. Lateral shift model is shown in the figure, 3x4 CH-V specimens, $T_{3.1J}$ transition temperature.

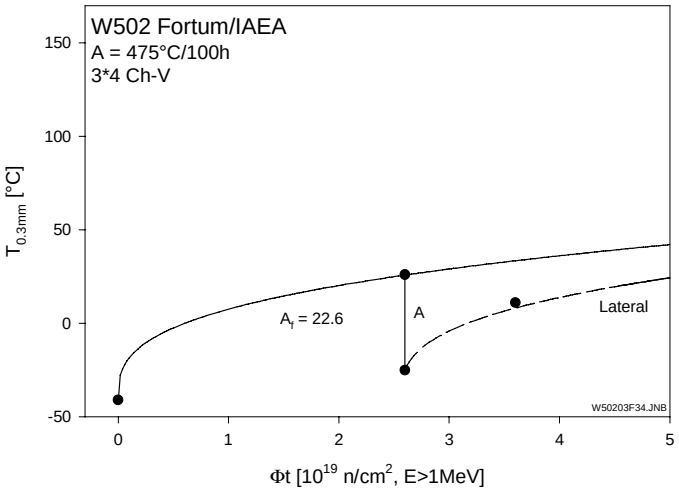

Figure 15. The I-, IA- and IAI-behaviour of weld 502 irradiated in the Loviisa reactor. Lateral shift model is shown in the figure, 3x4 CH-V specimens, $T_{0.3mm}$ transition temperature.

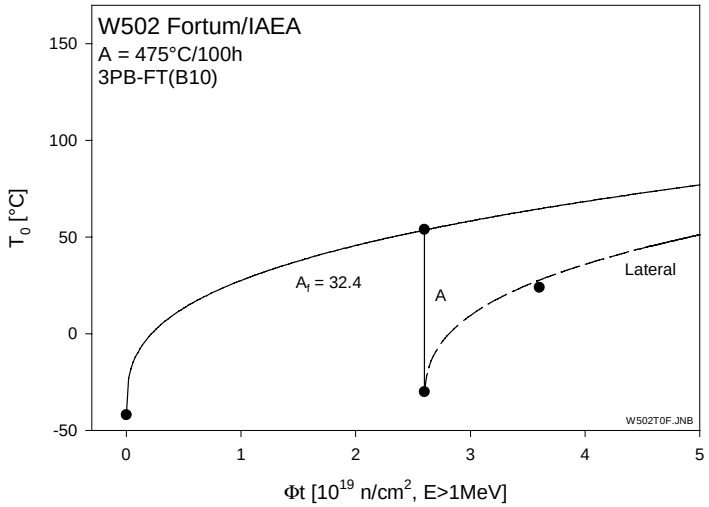

Figure 16. The I-, IA- and IAI-behaviour of weld 502 irradiated in the Loviisa reactor. Lateral shift model is shown in the figure, fracture toughness B = 10 mm specimens, Master Curve T_0 transition temperature.

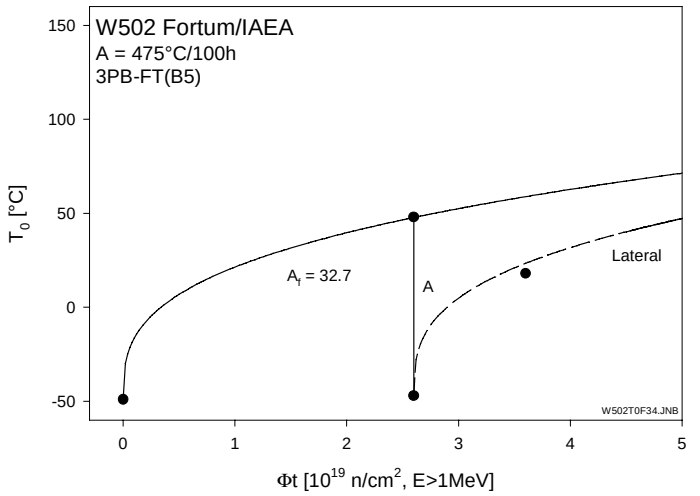

Figure 17. The I-, IA- and IAI-behaviour of weld 502 irradiated in the Loviisa reactor. Lateral shift model is shown in the figure, fracture toughness B = 5 mm specimens, Master Curve T_0 transition temperature.

4.5 Material response to irradiation, annealing and re-irradiation according to different toughness parameters

The irradiation, annealing and re-irradiation shifts measured with different types and sizes of specimens are shown in Figures 18–22. The shifts measured with the 5×5 and 3×4 CH-V specimens are clearly lower that the shifts measured with the ISO CH-V or fracture toughness specimens. It is to be noted that the 5×5 CH-V specimen orientation is T-S in the reference condition and T-L in the I-, IA- and IAI-conditions (the orientation refers to the weld seam). It is not expected that orientation has any major effect on toughness in welds but this point will be experimentally checked later on.

The lower sensitivity of the 5×5 and 3×4 CH-V based toughness parameters to material condition changes means that small specimen CH-V data and other toughness data should not be cross-utilised, i.e. the shifts measured with 5×5 CH-V specimens should not be set equal to the shifts measured with larger specimens.

The values of the proportional parameters $\Delta T_{residual}$ % (the ratio of the residual shift to the irradiation shift) and ΔT_{IAI} % (the ratio of $[T_{re\text{-}irradiated}\text{-}T_{unirradiated}]$ to $[\Delta T_{irradiation}\ (I_1+I_2)]$) based on single types of specimens were determined. The ISO CH-V specimens gave a relatively high value and FT and 3×4 CH-V specimens a relatively low value for parameter $\Delta T_{residual}$ %. Parameter ΔT_{IAI} % compares the total shift due to irradiation-annealing-reirradiation procedure to the situation, where the material has experienced only two irradiations, i.e. $I_{total} = I_1+I_2$. These parameter values varied from 56% to 72%, i.e. the benefit from annealing is relatively constant when measured with different types of specimens.

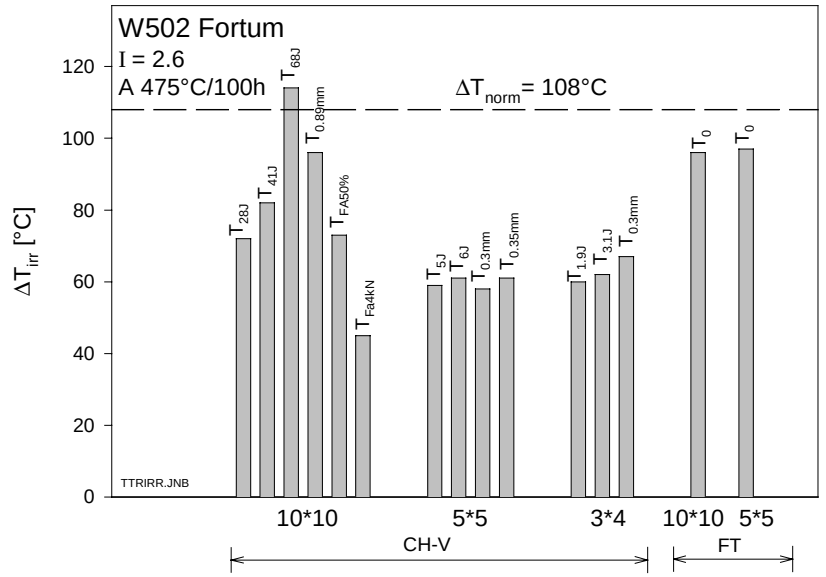

Figure 18. Comparison of measured irradiation shifts evaluated with different types and sizes of specimens and transition temperature criteria.

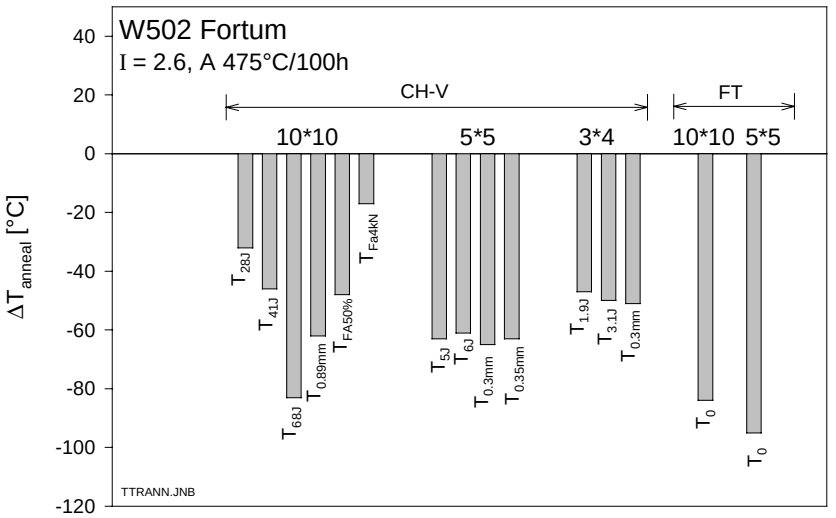

Figure 19. Comparison of measured annealing shifts evaluated with different types and sizes of specimens and transition temperature criteria.

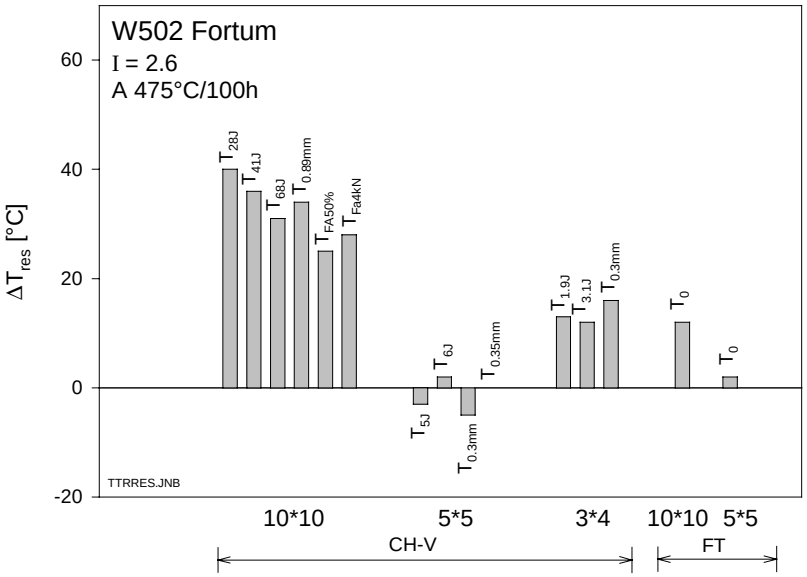

Figure 20. Comparison of measured residual shifts evaluated with different types and sizes of specimens and transition temperature criteria.

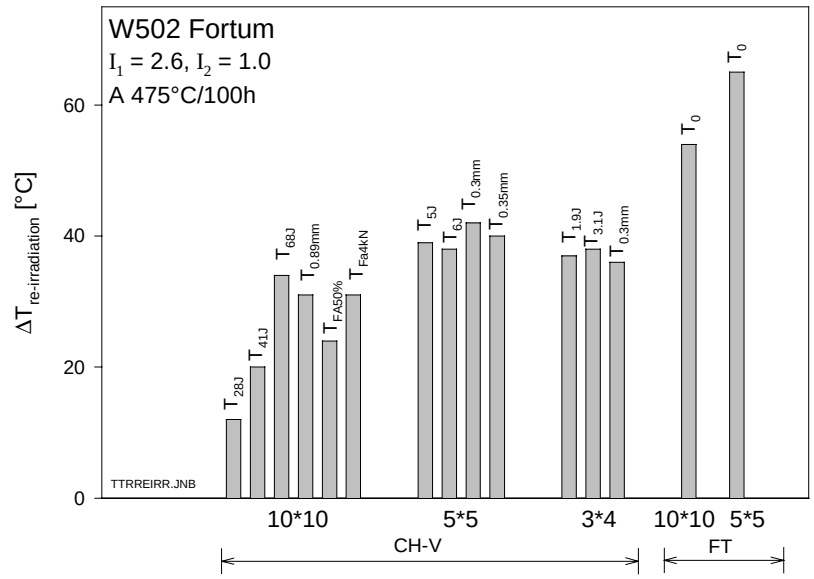

Figure 21. Comparison of measured re-irradiation shifts evaluated with different types and sizes of specimens and transition temperature criteria.

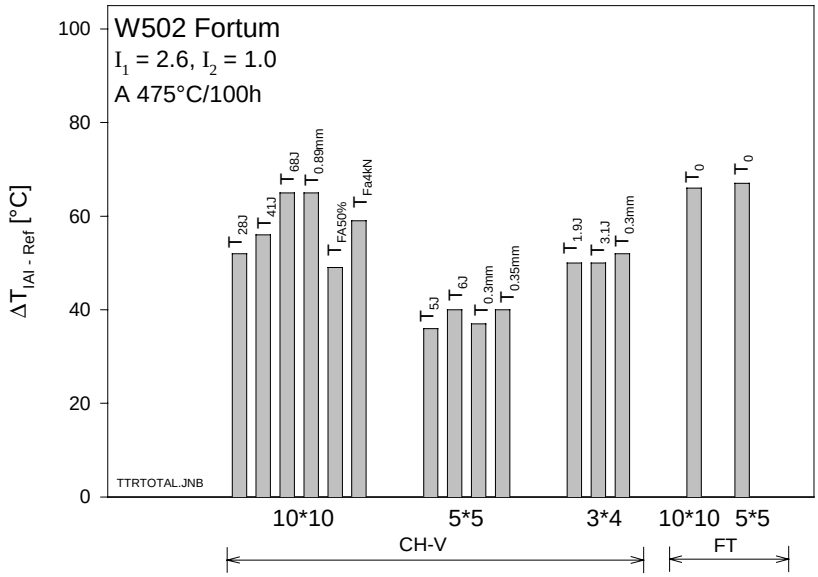

Figure 22. Comparison of measured total (T_{IAI} -$T_{reference}$) transition temperature shifts, i.e. the total response to the IAI-treatment evaluated with different types and sizes of specimens and transition temperature criteria.

4.6 The CH-V upper shelf behaviour

The proportional changes of CH-V upper shelf toughness values are shown in Figure 23. Different size specimens are not identified in the figure, as the behaviour is relatively independent of specimen size. The figure indicates that the upper shelf over-recovers in annealing and the drop of upper shelf is faster during re-irradiation than during original irradiation.

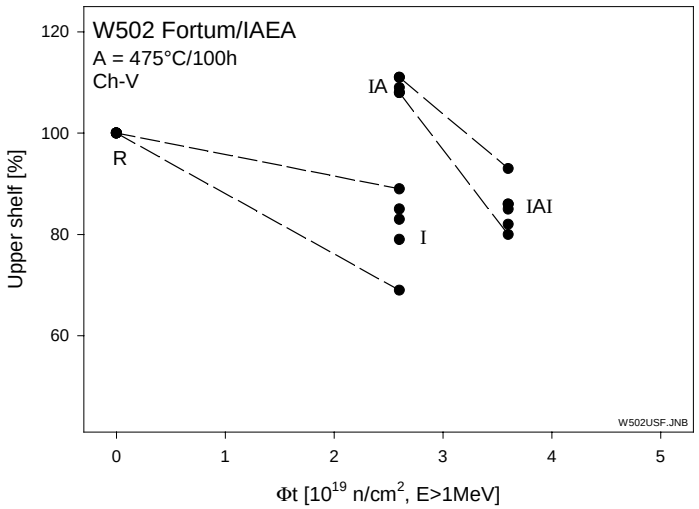

Figure 23. CH-V impact energy and lateral expansion upper shelf values in I-, IA- and IAI-material conditions. Unirradiated condition data is used as a reference (100%), US_E and US_{LE} parameters measured with 10x10, 5x5 and 3x4 CH-V specimens are given.

4.7 Comparison of material data from Loviisa and Halden reactor irradiations

In the comparisons it is assumed that re-irradiation behaviour depends only on the re-irradiation fluence I_2, not on the original irradiation fluence I_1. This allows to start the re-irradiation curves from the same point in the fluence axis.

Specimens were re-irradiated into different neutron fluences in the Loviisa and Halden reactors [3]. The neutron spectra in Loviisa and Halden reactors differ clearly as is indicated by the values of the fluence ratio, i.e. I (E > 0.5 MeV) / I (E > 1.0 MeV) is 2.11 for the Loviisa and 1.45 for the Halden reactor. This leads to a cut-off energy dependent irradiation and re-irradiation descriptions, if joint data is used. The ratios of the re-irradiation fluences are given in Table 6.

Table 6. The ratios of Halden and Loviisa re-irradiation fluences I_2 given in different fluence units.

Fluence unit	$I_2^{HRP} / I_2^{Loviisa}$
E > 1MeV	2.60
E > 0.5MeV	1.90
dpa	2.65

In the comparisons the irradiation embrittlement functions based on the Loviisa and Halden irradiation data are shown separately but the re-irradiation functions are based on joint data. As the re-irradiation data consists in practice only of three data points, i.e. two shift values, the parameters of the re-irradiation functions can be easily derived from

$$n = \frac{\ln(\Delta T_1 / \Delta T_2)}{\ln(\Phi_1 / \Phi_2)} \tag{12}$$

$$A_f = \frac{\Delta T_1}{\Phi_1{}^n} \tag{13}$$

The derived re-irradiation functions are shown in Figures 24–27. The CH-V upper shelf behaviour is shown in Figures 28 and 29. The functional re-irradiation descriptions based on the units [E > 1 MeV] and dpa were nearly the same as can be expected from the fluence ratio values given in Table 6. The descriptions based on the unit [E > 0.5 MeV] deviate considerably from the other descriptions. The CH-V upper shelf behaves nearly in a similar manner in the Loviisa and Halden irradiations and re-irradiations as indicated by Figures 28–29.

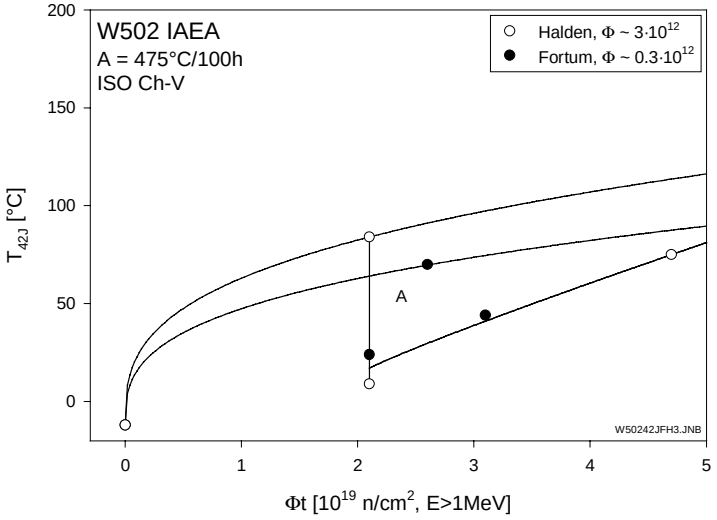

Figure 24. Comparison of ISO CH-V T_{42J} transition temperatures measured with Loviisa and Halden irradiated specimens, neutron fluence unit [E >1 MeV].

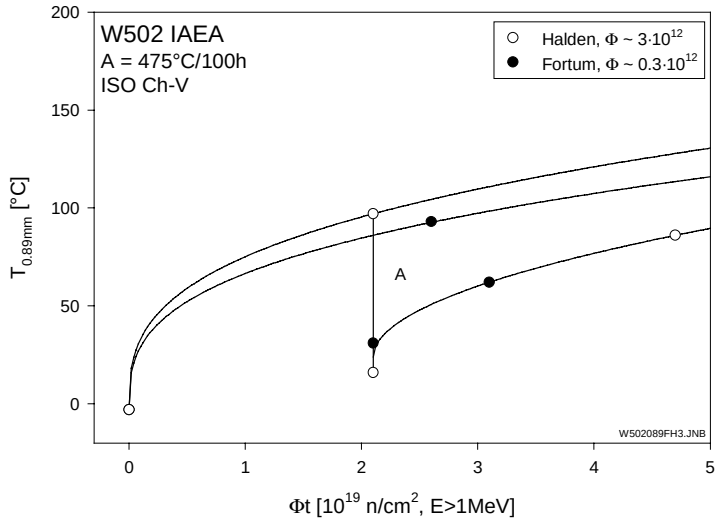

Figure 25. Comparison of ISO CH-V $T_{0.89mm}$ transition temperatures measured with Loviisa and Halden irradiated specimens, neutron fluence unit [E>1 MeV].

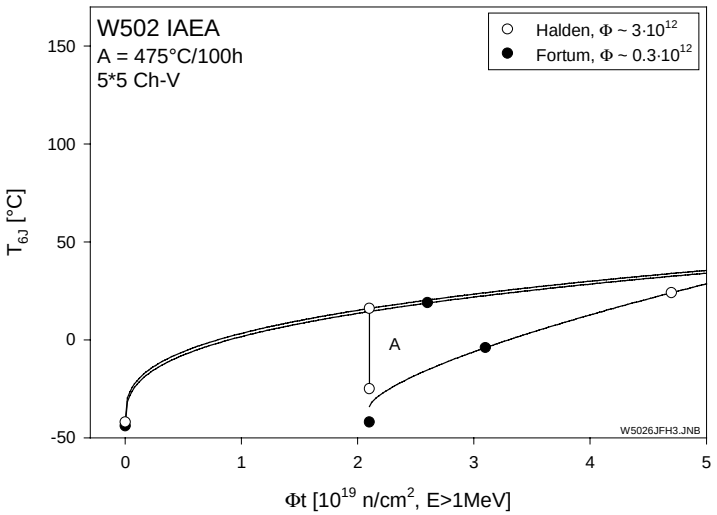

Figure 26. Comparison of 5x5 CH-V T_{6J} transition temperatures measured with Loviisa and Halden irradiated specimens, neutron fluence unit [E >1 MeV].

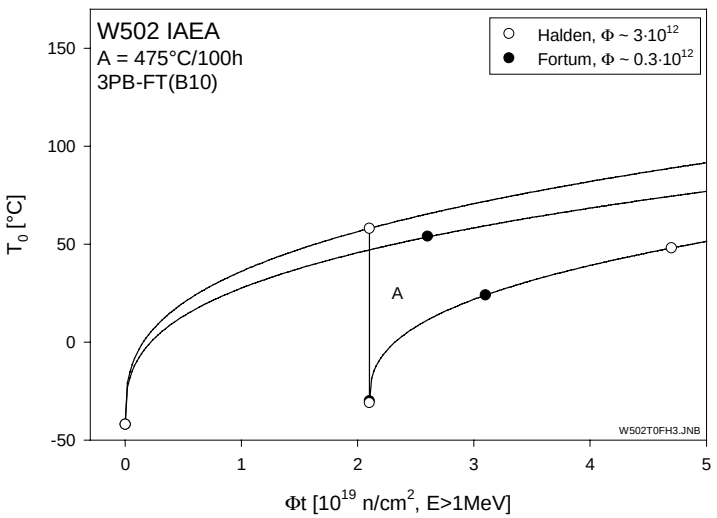

Figure 27. Comparison of fracture toughness T_0 transition temperatures measured with Loviisa and Halden irradiated specimens, neutron fluence unit [E>1 MeV].

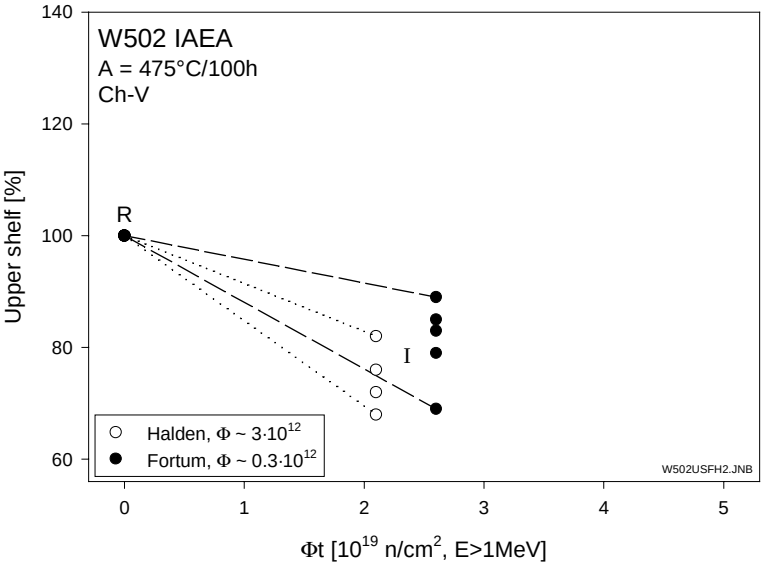

Figure 28. Comparison of CH-V upper shelf values measured with Loviisa and Halden irradiated specimens. Reference and I-material conditions.

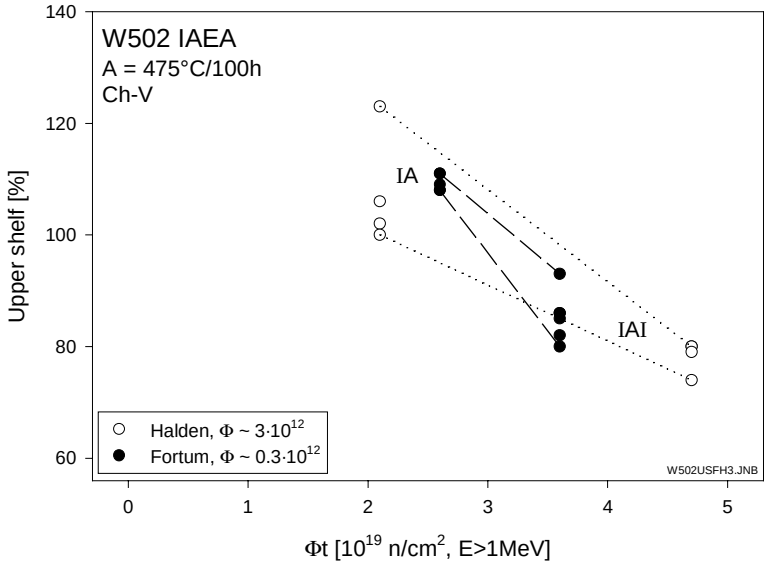

Figure 29. Comparison of CH-V upper shelf values measured with Loviisa and Halden irradiated specimens. US_E and US_{LE} values measured with 10x10, 5x5 and 3x4 (Fortum only) specimens are included. IA- and IAI-material conditions.

5. Summary and conclusions

The VVER-440 weld (weld 502) was irradiated, annealed and re-irradiated in the Loviisa reactor in order to fulfil the co-ordinated IAEA programme requirements. As an additional contribution a second re-irradiation fluence will be realised later.

In the report, the IAI_1-condition data are given and a full analysis of the whole data including the previously reported unirradiated, irradiated and irradiated-annealed conditions is performed. In addition, the Loviisa and Halden irradiation data are compared in the report. The data allow the following conclusions:

- Irradiation embrittlement rate of the Loviisa irradiated weld 502 is in general clearly lower than the prediction of the Russian norm. The T_{68J} embrittlement slightly exceeds the norm value, but this can be attributed to the relatively low upper shelf value (85 J) in the I-condition.

- Re-irradiation embrittlement remains in general clearly below the prediction of the lateral shift model based on the best fit embrittlement description. The data of 3×4 CH-V specimens exceed slightly the lateral shift prediction. The large deviation of the T_{Fa4kN} data from the lateral shift estimation (small absolute shifts) is probably due to statistical uncertainties, the curve fitting procedure, or the different physical event (initiation/arrest).

- The response of parameters based on small CH-V specimens is in general smaller than the response of ISO CH-V and fracture toughness specimens to irradiation, annealing and re-irradiation. Hence, small CH-V specimens may lead to non-conservative embrittlement, annealing and re-irradiation estimations.

- CH-V upper shelf has a tendency to over-recover slightly in annealing as is indicated by the parameter $\Delta T_{residual}$ %. The drop of upper shelf seems to be faster in re-irradiation than in the original irradiation.

- The comparison of the Halden and Loviisa irradiated data shows clearly that care should be taken when comparing data created in different neutron spectra. The use of neutron correlation units [E > 1 MeV] and dpa gives

nearly the same predictions but the prediction based on the unit [E > 0.5 MeV] deviates clearly from the others. In the comparison the two-parameter model was fitted to the two re-irradiation shifts and hence all uncertainties (transition temperature values, neutron parameters) were interpreted in a deterministic way, which tends to emphasise the differences in the behaviour.

- CH-V upper shelf behaviour is nearly the same in the Halden and Loviisa irradiated materials.

Acknowledgements

This presentation is prepared for a joint Finnish industry group in a project on Structural operability and plant life management (RKK). The project funding by the National Technology Agency (Tekes), Teollisuuden Voima Oy (TVO), Fortum Power and Heat Oy, Fortum Nuclear Services Ltd., FEMdata Oy, Neste Engineering Oy, Fortum Oil and Gas Ltd. is gratefully acknowledged. The work has been planned together with Dr. Jyrki Kohopää of Fortum Nuclear Services Ltd. The herein summarised results have been separately reported in more detail.

References

1. Valo, M. IAEA Co-ordinated Research Programme: Round robin exercise on WWER-440 RPV weld metal irradiation embrittlement, annealing and re-embrittlement, The unirradiated material data. Espoo: VTT Manufacturing Technology, 1999. Research Report VALC583.

2. Valo, M. IAEA Co-ordinated Research Programme: Round robin exercise on WWER-440 RPV weld metal irradiation embrittlement, annealing and re-embrittlement, I-and IA-material condition of Loviisa irradiated weld 502. Espoo: VTT Manufacturing Technology, 2001. Research Report VAL63-001963.

3. Valo, M., Østensen Lauvstad, G., Beere, W. H. and Kim, J.-C. IAEA Co-ordinated Research Programme "Round robin exercise on WWER-440 RPV weld metal irradiation embrittlement, annealing and re-embrittlement", I-, IA- and IAI-material condition data of Halden irradiated weld 502. Espoo: VTT Manufacturing Technology, 2001. Research Report BVAL63-021201.

Risk informed plant life management – application of the Master-Curve approach for hydrotreating reactors in an oil refinery

Kim Wallin, Anssi Laukkanen and Pekka Nevasmaa
VTT Industrial Systems
Espoo, Finland

Abstract

Classically, surveillance of hydrogen cracking reactors has been based solely on the Charpy-V impact test. This study introduces and verifies a new, risk informed, fracture mechanics based surveillance procedure for hydrotreating reactors and quantifies the present safety margins and life expectancy for the reactors included in the study. The results validate the new advanced surveillance procedure and verify the safety of the reactors at least until the year 2010.

1. Introduction

Classically, the surveillance of hydrotreating reactors has been based solely on the Charpy-V impact test. The empiricism in the test has led to difficulties in quantifying the safety margins and life expectancy of the reactors. Technological development in the field of fracture mechanics has opened up the possibility of introducing new fracture mechanics based advanced surveillance procedures to these types of reactors. In principle, the new procedures are similar to the advanced surveillance procedures, currently being introduced for nuclear pressure vessel applications [1]. The new procedures, called the Master Curve methodology, have been developed at VTT over the last 15 years and have resulted in a revolution in brittle fracture assessment thinking. The basic Master Curve method has been standardized in the ASTM standard E1921 [2], the first standard that accounts for the statistical specimen size effect and variability in brittle fracture toughness.

2. Case study on hydrotreating reactors

This study focussed on the introduction and verification of a new fracture mechanics based surveillance procedure for hydrotreating reactors and on quantifying the present safety margins and life expectancy for the reactors included in the study.

The study targeted two specific thick walled reactors, currently in use. The research consisted of a study of the reactors initial properties, prior surveillance results and new surveillance tests, including both tensile, standard Charpy-V tests and advanced fracture toughness tests. Additionally, a fracture mechanics based elastic plastic FEM analysis of the reactors was performed so that a quantitative safety assessment was achieved.

2.1 The reactors and studied locations

The reactors are of the stand-up type. Their inside diameter is 3.2 m and the overall height is 18.0 m. The reactors are lined with a thin stainless cladding, which was not analysed in the assessment. A schematic of the reactors is presented in Fig. 1.

The analyses focused on safety assessments for vessel shell, sphere and nozzle areas under hydro-testing and operational transient conditions. Shutdown and start-up were considered as operational transients. "Shell" refers to the basic cylindrical part of the vessel, while the transition to the discontinuity between the spherical and cylindrical parts of the vessel is referred to as "sphere". The "nozzle" is that of the inlet diffuser.

A hypotetic crack was postulated in the assessments. The crack postulate was a semi-elliptical surface flaw with a depth of 30 mm and width of 150 mm. This crack specification was attained as a conservative upper bound flaw based on NDT detection limits and it is close to the 1/4 thickness flaw prescribed by the ASME code. It has a safety factor of approximately 10 with respect to observed indication sizes, related to slag inclusions, in the reactors.

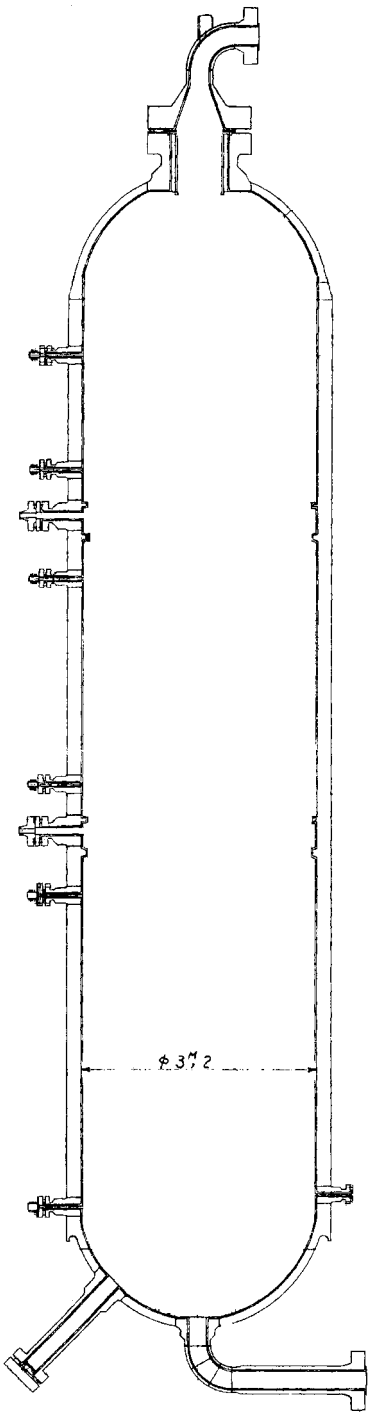

Figure 1. Schematic of the investigated hydrotreating reactors.

2.2 Experimental

The tensile tests were performed to determine the present yield and ultimate strength of the material. True stress-strain curves were correlated based on the yield- and ultimate strength information [4]. The Charpy-V impact tests were performed instrumented so, that in addition to standard Charpy-V values, information regarding the materials crack arrest properties were obtained. Specimens of two different size were used for the fracture toughness tests. A 5x10 mm bend specimen was used as reference specimen, since the validity of the specimen geometry has been well verified [3]. The 5x5 mm bend specimen geometry was used to check the applicability of such miniature specimens for fracture toughness testing of this kind of materials. The fracture toughness testing was performed and analyzed in accordance with ASTM E1921-2002 [2] .

2.3 Numerical methods

Numerical finite element analyses were carried out using the FEACrack and WARP3D software. Three-dimensional models were generated for different representative areas of the reactor. The analyses aimed on determining the stress intensity factor for vessel shell, sphere and nozzle areas under hydro-testing and operational transient conditions.

Automated finite element mesh generation was used to generate the crack models in three dimensions. An example mesh along with numerical results for stress contours are presented in Fig. 2a. Mesh sizes ranged from 2000 to 12000 quadratic 20 node elements. Geometry was specified according to vessel drawings. Computations were carried out incorporating elastoplasticity and finite deformations.

3. Results and assessment

3.1 Stress analysis

The hydro-test conditions and operational shutdown and start-up transients were all considered pressure transients only because of low rates of temperature changes. The numerical results shown in Figs 2 to 4 are contours of equivalent von Mises stress, describing the characteristics of the stress distribution in different cracked geometries.

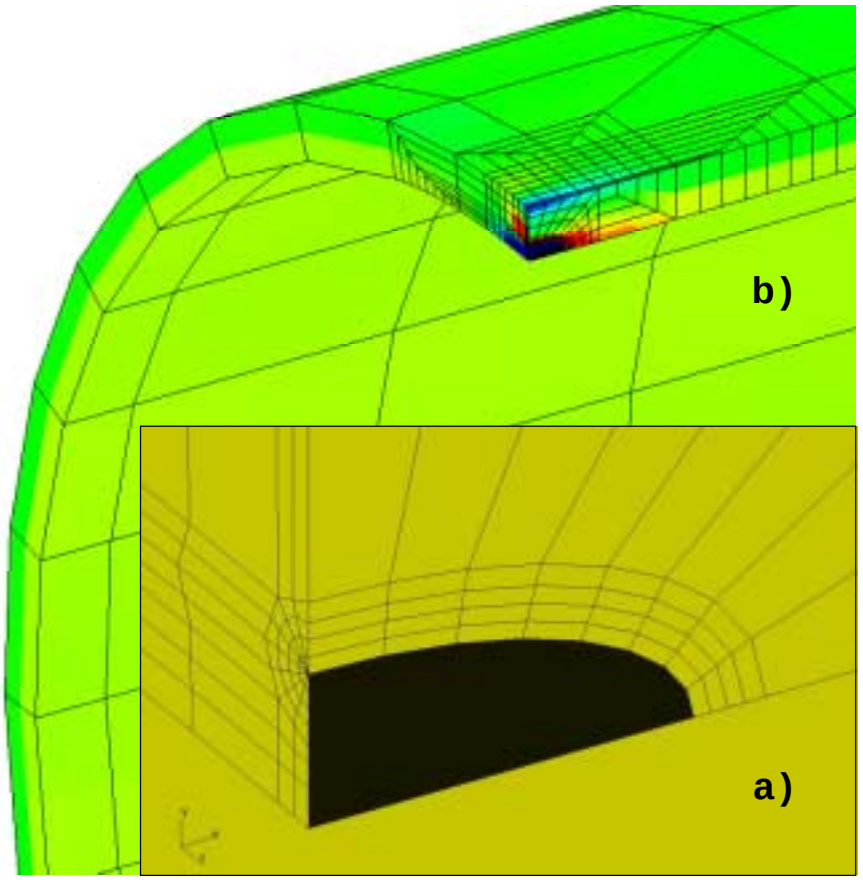

Figure 2. Finite element analysis results for the cylindrical shell. a) Crack postulate and mesh, b) equivalent von Mises stress distribution in the shell.

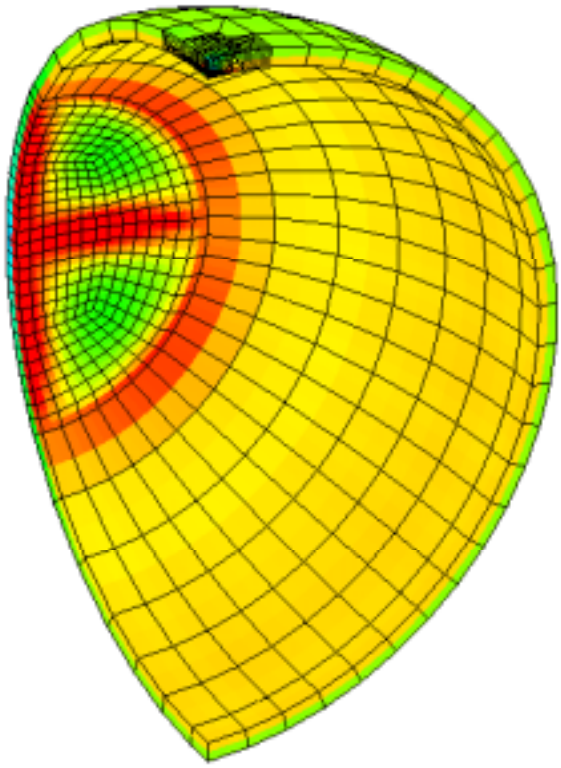

Figure 3. Equivalent von Mises stress distribution in sphere.

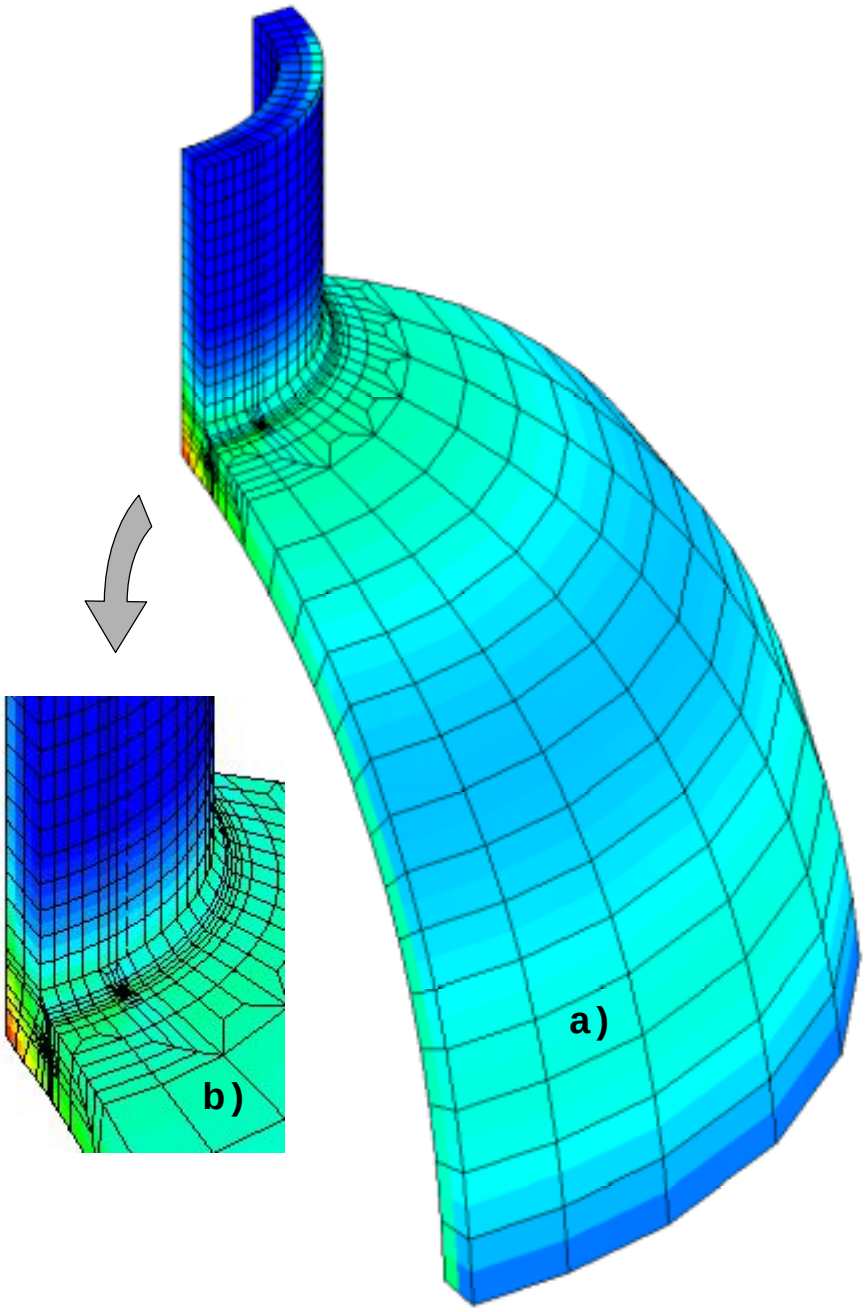

Figure 4. Equivalent von Mises stress distribution in a nozzle: a) general distribution, b) local distribution.

3.2 Assessment of hydro-test

Hydro-test computational results for different cases are presented in Fig. 5 for the shell, sphere and nozzle regions. Shell refers to the basic cylindrical part, while the transition to the discontinuity between the spherical and cylindrical parts of the vessel is referred to as "sphere". For the shell part, additional computation was performed using the aged material property data, referred to as "shell", aged. The inlet nozzle region was assessed for two crack configurations, one with a crack located as a corner crack on the inside of the vessel and another where a toe crack was located at the transition of the sphere and nozzle on the outside of the cylinder.

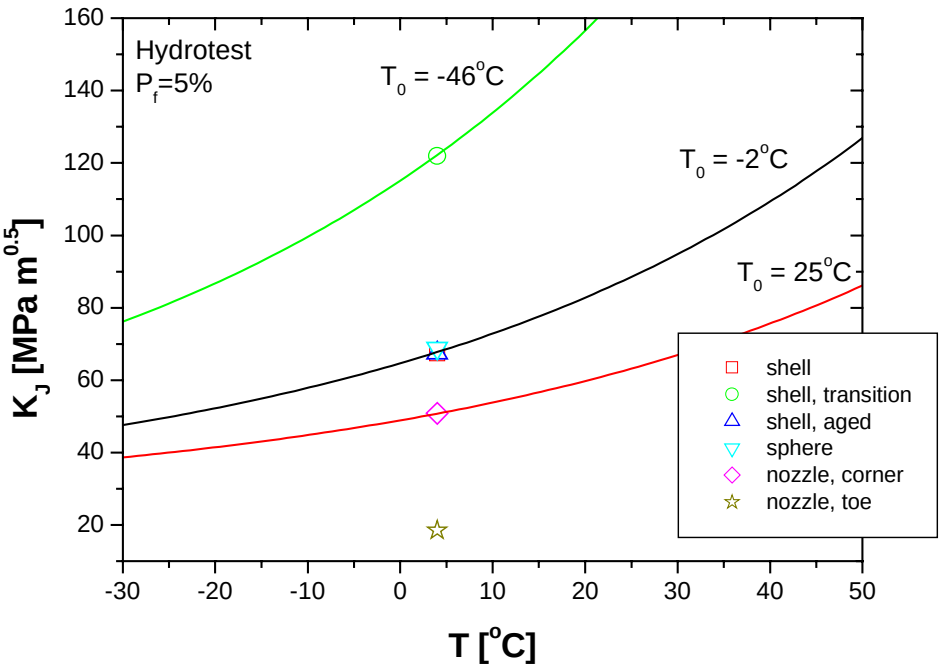

Figure 5. Hydro-test analysis results.

The hydro-test analysis results indicate that the regions of the vessel most susceptible to crack initiation are the shell and sphere regions. This appears imminent based solely on the nominal dimensions specified in the nozzle regions. The analyses for the sphere and shell regions with nominal and aged

material properties produced results very close to each other, within a few percents. The configuration producing the highest crack driving force was the transition area between the shell and sphere, which was analysed conservatively by neglecting the effects of the transition region between the shells.

In order to specify fracture toughness requirements, Master Curves with a 5% total failure probability have been added to Fig. 5. The nozzle region is seen to require a T_0 of only 25°C, while the requirements for the shell and sphere regions are -2°C. The conservative analysis for the transition region produces a T_0 requirement of -46°C.

3.3 Operational transients

Based on hydro-test analysis results, the start-up and shutdown transients were computed for the cylindrical shell and sphere and their transition region. For operational conditions, the requirements set to Master Curve reference temperature are far more lenient.

3.4 Ageing

The tensile test results indicate no changes since 1989. The embrittlement seems to have occurred during the first five years of operation. This was supported by the fracture toughness results, but not entirely by the Charpy-V tests. The CVN transition temperatures for the reactors are compared in Fig. 6. Unfortunately, lack of material did not allow the determination of the CVN properties after a 5 year use (1989 condition), but the 1993 and 1997 test results do indicate a deterioration of the CVN properties.

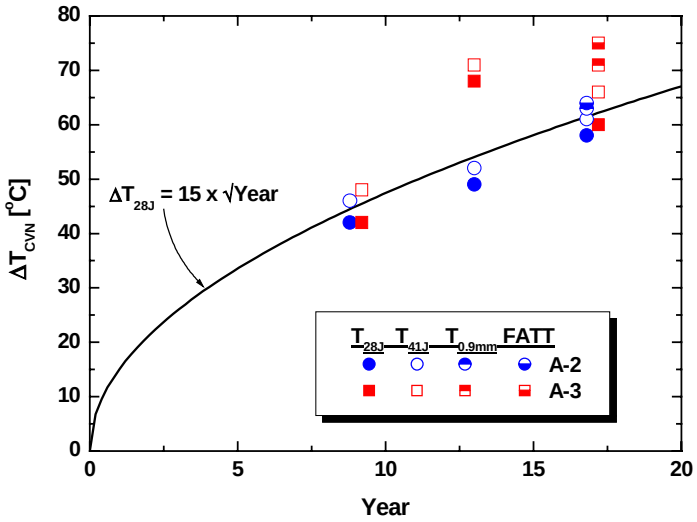

Figure 6. Comparison of CVN transition temperatures for reactors A-2 and A-3.

Fig. 6 contains a power law curve fit to the T_{28J} transition temperature data. This additionally describes satisfactorily the other determined transition temperature shifts. This CVN based embrittlement estimate is combined with the fracture toughness results in Fig. 7. The CVN shift was adjusted to correspond to the fracture toughness properties of 1989. The result is clearly a conservative estimate of the fracture toughness properties of 2001 for all investigated materials. This means that the CVN embrittlement estimate constitutes a conservative estimate in predictions beyond 2001. The results indicate that the T_0 value in 2010 will remain below -60ºC.

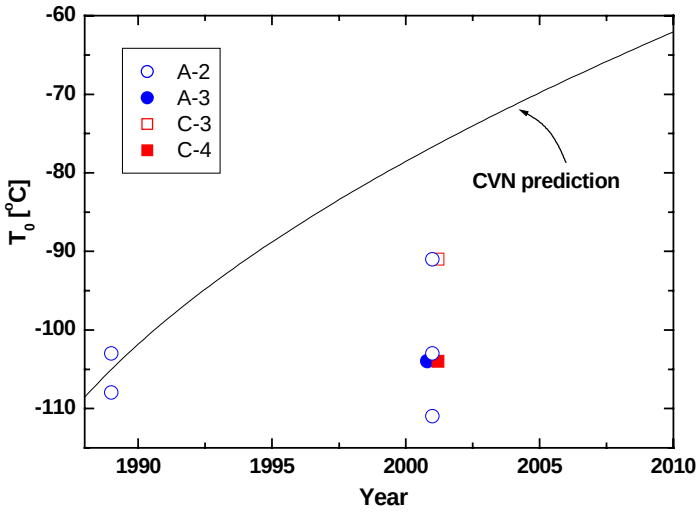

Figure 7. Comparison of embrittlement predicted by CVN and fracture toughness results.

4. Discussion

Welds were not included in the reactor's surveillance programs. The original CVN data indicate roughly a 20ºC difference between weld and plate. The aging response was similar for both weld and plate. Thus, the T_0 for the welds by the year 2010 should be better than -40°C.

The lowest critical T_0 value determined in the numerical analysis was -46ºC. This would constitute a critical condition for the weld in 2010. However, the value corresponded to a hydro-test loading and contained an extremely conservative treatment of the transition region between shell and sphere. A more realistic analysis result is reflected in the results for shell and sphere ($T_{0critical}$ = -2ºC). This means that even for a hydro-test, the materials' toughness is sufficient in 2010. For normal operating conditions, brittle crack initiation is not possible.

5. Conclusions

Based on the studies relating to the hydrotreating reactors, the following conclusions can be made:

- Direct measurement of the materials fracture toughness for these types of materials is possible using the Master Curve method.

- The smallest examined specimens, 5x5 mm, were found to produce reliable fracture toughness values for the materials.

- The two reactors have essentially identical material properties.

- The Charpy-V impact test results indicate a deterioration of toughness with time, but tensile tests and fracture toughness tests indicate practically no changes after 1989.

- A detailed elastic-plastic finite element analysis, combined with the new fracture toughness based surveillance data, indicates no brittle fracture initiation possibility before 2010, even considering a hydro-test.

Acknowledgements

This presentation is prepared for a joint Finnish industry group in a project on Structural operability and plant life management (RKK). The project funding by the National Technology Agency (Tekes), Teollisuuden Voima Oy (TVO), Fortum Power and Heat Oy, Fortum Nuclear Services Ltd., FEMdata Oy, Neste Engineering Oy and Fortum Oil and Gas Ltd. is gratefully acknowledged. The discussions with Ms. Tiina Hakonen and Ms. Kirsi Rintamäki of Fortum were of great help in planning and execution of this work.

References

1. Rintamaa, R., Wallin, K., Keinänen, H., Planman, T. and Talja, H. Consistence of fracture assessment criteria for the NESC-1 thermal shock test. Int J Pres Ves Piping 2001, 78, pp. 125–135.

2. American Society for Testing and Materials. E1921-02 Standard test method for determining of reference temperature, T_0, for ferritic steels in the transition range. Annual Book of ASTM Standards 2002, 03.01. Pp. 1139–1157.

3. Wallin, K., Planman, T., Valo, M. and Rintamaa, R. Applicability of miniature size bend specimens to determine the Master Curve reference temperature T_0. Engng Fract Mech 2001, 68, pp. 1265–1296.

4. Auerkari, P. On the correlation of hardness with tensile and yield strength. VTT Tutkimuksia – Forskningsrapporter – Research Reports 416, Technical Research Centre of Finland, Espoo, 1986. 20 p.

Paint coatings and rubber linings in seawater service pipelines

Irina Aho-Mantila and Reima Lahtinen
VTT Industrial Systems
Espoo, Finland

Abstract

Studies for paint coatings and rubber linings are part of the operational reliability research of seawater piping systems. Failure analyses and immersion tests of seawater pipe coatings were made in order to determine the lifetime limiting factors. Based on the operational experience as well as coating and corrosion experience quality control guidelines for coating were developed. Cleanliness and carefulness are extremely important in the coating process. Short lifetime of the pipe material without coating makes it important to control the quality of the coating and the pipe within certain intervals. Draft of the guidelines for the repair of the coating of the used pipes were also given.

1. Introduction

Seawater pipe lines are made of large diameter carbon steel pipe coated with rubber or epoxy. Pipe material itself corrodes in seawater and is therefore protected by the coating. For assurance of operational reliability of seawater piping typical coating failures, guidelines for high quality coating, condition of the pipes and coating repair possibilities of the used pipes are presented in four reports. Some of the results are briefly shown in this paper.

2. Experimental methods and results

In the study several types of specimens were examined. E.g., the condition of coating and pipe materials were examined from pipes having outside diameters 220 mm and 420 mm, Fig. 1. Rubber coating was heavily blistered and paint coating had failures. Corrosion had caused perforation in the painted pipe, Fig. 2.

Figure 1. Flanged seawater pipes having outside diameter of 220 mm and 420 mm were examined.

Even if the rubber was heavily blistered or thin coating clearly destroyed the steel under the coating was not always heavily corroded. Steel surface under the blister is shown in Fig. 3. Coating repair is possible if the unevenness of the surface is less than 3 mm. Because of the possibility of breakthrough holes the pipes have to be cleaned and examined before their reuse.

Figure 2. Painted seawater pipe having a breakthrough hole adjacent to the flange.

Figure 3. Surface of the steel under the large rubber blisters is not heavily corroded.

In the examination of loosened paint particles it was obvious that painting was done on the unclean surface. Also lacking temperature control during painting was evident because paint surface contained unmelted particles. To show the effect of good coating practice immersion tests for both rubber and epoxy coatings having weld, bad cleaning and oil dirt on the steel surface were performed. Oil smear on the steel surface destroys the coating in immersion test, Fig. 4.

Draft of the guidelines for the selection of the coating and coating repair were given. The emphasis is on the careful execution of the painting process.

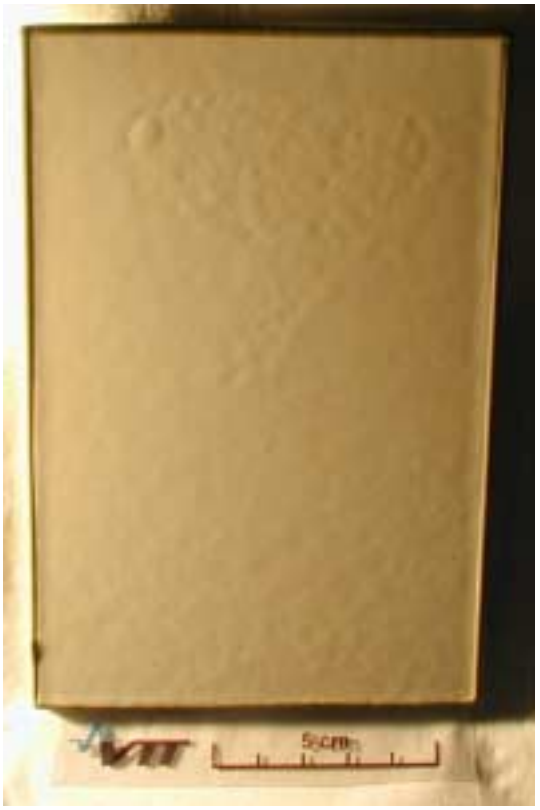

Figure 4. Oil smear on the steel surface destroys the coating in the immersion test. Oil smear area can be seen in the upper part of the specimen where also one large blister is seen.

3. Conclusions

1. Failure analyses showed the importance of cleanliness and carefulness especially in paint coating process. E.g., oil smears, dust particles, salts and other chemical substances on the steel surface can cause the failure of coating. The coating thickness must be carefully controlled, too.

2. Breakthrough holes were found in the painted steel pipes used in seawater service.

3. Coating conditions as well as pipe conditions need to be controlled regularly.

4. Relining or coating of used pipes is possible when local corrosion damages are shallow.

5. Draft of the guidelines for the selection of the coating and coating repair were given.

Acknowledgements

This presentation is prepared for a joint Finnish industry group in a project on Structural operability and plant life management (RKK). The project funding by the National Technology Agency (Tekes), Teollisuuden Voima Oy (TVO), Fortum Power and Heat Oy, Fortum Nuclear Services Ltd., FEMdata Oy, Neste Engineering Oy, Fortum Oil and Gas Ltd. is gratefully acknowledged. The discussions with Mr. Ossi Hietanen, Ms. Ritva Korhonen and Mr. Erik Westerlund of Fortum and other partners in the project were of great help in planning and execution of this work. The work of laboratory personnel is also gratefully acknowledged.

Published by

VTT

Series title, number and report code of publication

VTT Symposium 227
VTT–SYMP–227

Author(s)
Jussi Solin (editor)

Title

Plant Life Management

Progress for structural integrity

Abstract

A joint project cluster of industry, VTT and other R&D suppliers is dealing with managing of lifetime of critical structures and components in energy and process industry. The research topics include systematic component lifetime management, data management, integrity and lifetime of pressure bearing components, non-destructive inspection, interactions of coolant and materials, environmentally assisted cracking and ageing of reactor internals.

This Symposium is a compilation of selected papers describing an intermediate status of the projects after three years of research and development.

Keywords
service life, plant life, management, NPP, nuclear power plants, materials testing, ultrasonic testing, pipe vibrations, BWR, corrosion, pressure vessels, thermal ageing, stainless steel

Activity unit
VTT Industrial Systems, Kemistintie 3, P.O.Box 1704, FIN–02044 VTT, Finland

ISBN	Project number
951–38–6280–1 (soft back ed.) 951–38–6281–X (URL: http://www.inf.vtt.fi/pdf/)	H2SU00363

Date	Language	Pages	Price
March 2003	English	361 p.	H

Name of project	Commissioned by
Rakenteiden käytettävyys ja käyttöiän hallinta	TVO, Fortum

Series title and ISSN	Sold by
VTT Symposium 0357–9387 (soft back ed.) 1455–0873 (URL: http://www.inf.vtt.fi/pdf/)	VTT Information Service P.O.Box 2000, FIN–02044 VTT, Finland Phone internat. +358 9 456 4404 Fax +358 9 456 4374

This Symposium is a compilation of selected papers describing the progress of research and development dealing with estimating and managing lifetime of critical structures and components in energy and process industry. The research topics include

- non-destructive inspection,
- piping vibrations and integrity,
- monitoring of water chemistry,
- mechanisms of corrosion and environmentally assisted cracking,
- ageing of materials and components in nuclear reactors,
- management of materials ageing, and
- integrity of pressure bearing components.

Tätä julkaisua myy
VTT TIETOPALVELU
PL 2000
02044 VTT
Puh. (09) 456 4404
Faksi (09) 456 4374

Denna publikation säljs av
VTT INFORMATIONSTJÄNST
PB 2000
02044 VTT
Tel. (09) 456 4404
Fax (09) 456 4374

This publication is available from
VTT INFORMATION SERVICE
P.O.Box 2000
FIN–02044 VTT, Finland
Phone internat. +358 9 456 4404
Fax +358 9 456 4374

ISBN 951–38–6280–1 (soft back ed.)
ISSN 0357–9387 (soft back ed.)

ISBN 951–38–6281–X (URL: http://www.inf.vtt.fi/pdf/)
ISSN 1455–0873 (URL: http://www.inf.vtt.fi/pdf/)